

Shear Load Transfer and Relaxation in Bolted Joints with Fractured Surfaces

DISSERTATION

vorgelegt von
Diplom-Ingenieur
Peter Lyszczan
aus Stuttgart

Von der Fakultät V – Verkehrs- und Maschinensysteme
der Technischen Universität Berlin
zur Erlangung des akademischen Grades
Doktor der Ingenieurwissenschaften
- Dr.-Ing. -

genehmigte Dissertation

Promotionsausschuss:

Vorsitzender: Prof. Dr. rer. nat. Wolfgang H. Müller
Berichter: Prof. Dr.-Ing. Dietmar Göhlich
Berichter: Prof. Dr.-Ing. Lucienne Blessing

Tag der wissenschaftlichen Aussprache: 28.11.2011

Berlin 2012

D83



Summary

The fracture splitting process enables the selective splitting of a component by fracture. Usually this is done in order to mount the splitted parts to another component. Often bolts are the fastener of choice in order to keep the fractured parts together. Such a bolted joint with fractured surfaces can be found for instance in modern connecting rods. The shape of fractured surfaces is distinctly different from the shape of plain surfaces which are commonly used for bolted joints. Nowadays, with respect to connecting rods, this difference was regarded as an aid for assembly of the fractured parts. It was not taken into account that the mechanical properties of the joint surface could have changed. Consequently, the fracture splitting process and materials for fracture splitting are aims of intensive research and optimization - the mechanical behavior of a joint with fractured surfaces was not. A series of connecting rod failures due to failure of the bolted joint revealed this lack of knowledge.

The research described in this document focuses on the determination of two mechanical properties that are crucial for the design of a bolted joint with fractured surfaces: shear load transfer and relaxation. For this fundamental research a special kind of specimen was created based on fracture splitted connecting rods.

For the measurement of the relaxation losses eight test series with different parameters have been run. The results have been compared with the experience from literature concerning relaxation of bolted joints. No noteworthy deviations have been found.

The determination of the transferrable shear load was the aim of six related test series. It turned out that the amount of transferrable shear load is between 0.8 and 1.9 times the amount of installed preload and is showing a non-linear behavior. This behavior is the result of two different failure modes that occur in a joint with fractured surfaces in parallel: failure due to slipping and failure due to shearing. A new correlation factor that describes this behavior was defined: the effective friction coefficient. Additionally, the experimental results have been compared with results from a numerical analysis. Both show a strong correlation.

The combination of the results of a fractured surface analysis using a laser scanner, the experimental findings and the numerical results was needed to build up a mechanical model of a joint with fractured surfaces. This model was successfully used to describe all distinctive features of a joint with fractured surfaces, including the non-linearity of the effective friction coefficient.

Content

Table of Figures	VIII
Symbols	XVII
1 Introduction	1
1.1 Goals	2
1.2 Research Questions	3
1.3 Structure of this dissertation.....	4
2 State of the Art	5
2.1 Force Connections	5
2.1.1 Coulomb’s Law	6
2.1.2 Roughness and Adhesion	13
2.1.3 Conclusions	17
2.2 Form connections	17
2.2.1 Influencing factors.....	18
2.2.2 Pressure and Stress	19
2.3 Connections with Mixed Force transfer	20
2.4 Bolted Joints	21
2.4.1 Joint diagram	22
2.4.2 Embedding.....	24
2.4.3 Relaxation of Bolted Joints	25
2.4.4 Effect of Temperature on Relaxation	27
2.4.5 Conclusions	29
2.5 Connecting Rods	29
2.5.1 Function and Geometry of Connecting Rods	29
2.5.2 Materials and Production Processes of Connecting Rods	32
2.5.3 Development of Cracked Connecting Rods	34
2.6 Parameters of Surface Roughness	37
2.7 Conclusions	40
3 Cracked Connecting Rods	44
3.1 Self Loosening of Bolts.....	44
3.2 Topographical Investigations of Fractured Surfaces.....	45

3.2.1	Character of a Fractured Surface	45
3.2.2	Fitting Accuracy of a Pair of Fractured Surfaces.....	47
3.2.3	Structure of Fractured Surfaces	50
3.3	Sources of Possible Threats in Fractured Surfaces	51
3.4	Conclusions.....	52
4	Research Approach.....	54
4.1	Research Questions and Hypotheses	54
4.1.1	Characteristic Parameters of Fractured Surfaces	54
4.1.2	Relaxation in Bolted Joints with Fractured Surfaces	54
4.1.3	Shear Force Transfer in Bolted Joints with Fractured Surfaces ..	55
4.2	Research Methods.....	56
4.3	Specimens	57
4.3.1	Connecting Rods.....	57
4.3.2	Con-Rod Bolting Specimen	58
4.4	Experimental Investigations	59
4.4.1	Experimental Design and Procedures	59
4.4.2	Data Analysis	61
5	Fractured Surfaces	66
5.1	Aims of the Fractured Surface Analysis	66
5.2	Separation Test	66
5.3	Analysis of Laser Scanner Data.....	68
5.3.1	Single Surface Survey.....	68
5.3.2	Matching Fractured Surface Pairs.....	77
5.3.3	Parameter Correlation	84
5.4	Surface Inspections	85
5.5	Conclusions.....	88
6	Con-rod Bolting Specimen Tests	90
6.1	Relaxation Tests.....	90
6.1.1	Relaxation Test Series.....	91
6.1.2	Inspections after Relaxation Tests	93
6.1.3	Relaxation Test Results.....	95
6.2	Transferrable Shear Load Tests	102
6.2.1	Shear Load Test Series.....	103

Content

6.2.2	Surface Inspections after Shear Load Tests.....	105
6.2.3	Shear Load Test Results	106
6.3	Comparison with FEM Calculations	114
6.3.1	FEM Preprocessing	115
6.3.2	Influence of Element Size	118
6.3.3	Influence of Imperfections	120
6.3.4	Influence of Clamping Load.....	121
6.3.5	Comparison of FEM and Experiments.....	125
6.4	Conclusions	125
7	Mechanical Model	129
7.1	Preliminary Considerations	129
7.2	Model Building	129
7.3	Limits of Transferrable Shear Force	132
7.3.1	Local Limit due to Shearing.....	133
7.3.2	Local Limit due to Slipping.....	134
7.3.3	Effective Local Limit of Transferrable Shear Force	134
7.4	Load Distribution in a Joint with Fractured Surfaces	137
7.5	Distinctive Features of Fractured Surfaces	142
7.6	Conclusions	144
8	Connecting Rod Tests	145
8.1	Relaxation Tests	145
8.1.1	Con-Rod Test Series.....	145
8.1.2	Con-Rod Test Results.....	146
8.2	Conclusions	151
9	Conclusions	152
9.1	Fractured Surfaces.....	152
9.2	Preload Losses.....	153
9.3	Transferrable Shear Loads	154
9.4	Mechanical Model.....	156
9.5	Additional Results	156
9.5.1	Fractured Surfaces	156
9.5.2	Preload Losses	157
9.5.3	Shear Load Transfer	158

9.5.4	Simplified FEM Model	159
9.6	Contributions	160
9.7	Outlook	160
9.7.1	Open Questions	160
9.7.2	New Applications for Fractured Surfaces	161
Appendix	163
I. Literature	164
II. Technical Setup	170
II.1	Manufacture of Con-Rod Bolting Specimen	170
II.2	Test Equipment	172
II.3	Ultrasonic Devices	174
II.4	Experimental Test Setup	176
II.4.1	Separation Test	176
II.4.2	Surface Topology Scan	177
II.4.3	Laser Scanner Data Analysis	180
II.4.4	Shear Load Test	183
II.4.5	Relaxation Test	184
II.5	Specimen Setup	185
II.5.1	Bolt Preparation	185
II.5.2	Elongation Measurement Process	186
III. Detailed Test Results	189
III.1	Relaxation Test Results with CBS	189
III.2	Shear Load Transfer Results with CBS	196
III.3	Relaxation Test Results with Con-rods	198
III.4	Simplified FEM-Model by Alraheb	202

Table of Figures

Figure 1-1: Fracture splitted connecting rod of a modern diesel engine.....	1
Figure 2-1: A body on an inclined plane with friction (left) and the derived mechanical model (right)	7
Figure 2-2: A system of two cogging surfaces with friction, a global normal force (F_N^*) and a global shear force (F_Q^*)	8
Figure 2-3: Free cut of an element of Figure 2-2	8
Figure 2-4: Model of a stochastic surface from Greenwood and Williamson with the asperite radius r_A and the contact distance h_c (based on (Popov, 2009))	10
Figure 2-5: Data from Coulombs original experiment (oak against oak lubricated with talc): static friction force as a function of the natural logarithm of elapsed time (based on (Popov, 2009))	12
Figure2-6: Static friction coefficient as a function of temperature for experiments with copper against copper and against two kinds of steel (Köhler, 2005).....	13
Figure 2-7: Lennard-Jones potential curve (schematic illustration) with areas of attraction (negative potential energy) and repulsion (positive potential energy) (based on (Popov, 2009))	14
Figure 2-8: Schematic diagrams of force vs. elongation with markings for an assembly force F_M and the resulting elongations for a bolt (left) and for the clamped parts (right).....	22
Figure2-9: Basic joint diagram (schematic) – derived from the diagrams of bolt and clamped parts.....	23
Figure 2-10: Enhanced joint diagram (schematic) including assembly load F_M , influence of application factor α_A , the derived preload F_V and the load loss by relaxation and embedment F_Z (based on (VDI2230, 2003)).....	24
Figure 2-11: Examples for improper bore sizes (left: bore to small; right: bore to large).....	26

Figure 2-12: Relaxation of bolts of different materials after 1000h for different temperatures (C: non-alloy steel, B7: CrMo steel, B16: CrMoV steel, 304: 18Cr8Ni steel, 316: 16Cr13Ni2Mo steel) (taken from (Sachs, et al., 1973)).....	27
Figure 2-13: Ratio of remaining clamping load and initial preload for yield-controlled tightened bolted joints after 300h relaxation for different temperatures (taken from (Granacher, et al., 1994)).....	28
Figure 2-14: Position and function of a con-rod in a four stroke combustion engine	30
Figure 2-15: Straight split con-rod (left) and angular split con-rod (right) with the most important length specifications (taken from (Köhler, et al., 2006)).....	31
Figure 2-16: Comparison of the process steps for con-rod production (based on (Blauel, et al., 2000))	33
Figure 2-17: Principle of fracture splitting con-rods with a wedge (taken from (Ohrnberger, et al., 1992))	35
Figure 2-18: Con-rods with breakouts (see markings) (taken from (Blauel, et al., 2000)).....	36
Figure 2-19: Texture of a surface containing unevenness of different scales (taken from (ISO4287, 2010))	38
Figure 2-20: Transmission characteristic of the roughness profile (interval 1) and wave profile (interval 2) (based on (ISO4287, 2010))	38
Figure 3-1: Track of a large particle (3mm x 1.2mm) on the fractured surface of a con-rod.....	46
Figure 3-2: A small (left) and a large (right) crack on a fractured surface of a con-rod.....	47
Figure 3-3: Material retractions in a large (left) and a small (right) area	47
Figure 3-4: Separation force of a total of 87 con-rods almost evenly distributed between three con-rod batches (left) and images of laser notches from con-rod batches 255 (upper right) and 263 (lower right)	48

Table of Figures

Figure 3-5: Cut, grinded and polished con-rod prepared for the examination of the contact line of the fractured surfaces using a microscope.....	49
Figure 3-6: Examples of contact lines from close fit (left) to no fit in combination with a large cavity (right)	49
Figure 3-7: Origin of the CT specimen (left) and the transformation process of the 3-dimensional CT image to a set of 2-dimensional layers for the data analysis (from second left to the right).....	50
Figure 3-8: Model of the structure of a fractured surface	51
Figure 4-1: connecting rods used for experimental investigations	57
Figure 4-2: Initial position of a con-rod bolting specimen within a con-rod (high lightened as FEM model)	59
Figure 5-1: Results of the separation test	67
Figure 5-2: Diagrams of typical surface samples of the yellow batch (left), green batch (center) and red batch (right) with color indication for the surface elevation level (red color = high level, green = medium level, blue = low level).....	69
Figure 5-3: Definition of the coordinate system	69
Figure 5-4: Common definitions of roughness R_Z and averaged roughness R_C ...	70
Figure 5-5: Roughness R_Z , the corresponding standard deviation (represented by colored bar thickness) and scatter range (empty bars) averaged per laser notch batch.....	71
Figure 5-6: Averaged roughness, the corresponding standard deviation (represented by colored bar thickness) and scatter range (empty bars) averaged per laser notch batch	73
Figure 5-7: Definition of inclination angle α_i	74
Figure 5-8: Point-to-point inclination angle, the corresponding standard deviation (represented by colored bar thickness) and scatter range (empty bars) averaged per laser notch batch	75

Figure 5-9: Sliding average inclination angle, the corresponding standard deviation (represented by bar thickness) and the scatter range (empty bars) of all three laser notch batches..... 76

Figure 5-10: Example of surface contact survey (areas not in contact are marked red) with a threshold of 0.05mm and a corresponding matching rate of 94.3% 78

Figure 5-11: Matching rate as a function of the threshold for all three laser notch batches (bar thickness represents average value +/- standard deviation) 79

Figure 5-12: Comparison of the material distribution of two fractured surfaces and the distance ΔX of their balance point lines (profile height “0” marks the median of the distribution of the measurement points of surface B) 80

Figure 5-13: Vertical distance of all three batches..... 82

Figure 5-14: average cavity volume (standard deviation = bar thickness) per laser notch 83

Figure 5-15: Vertical distance in dependence of matching rate at a threshold of 0.05mm with markings for an area containing large cavities, an area with an increasing amount of numerical errors as well as an area containing pure numerical errors 85

Figure 5-16: Sample of the yellow laser batch (left) and SEM pictures of two typical laser notches with a depth of about 0.2mm (top right) and 0.4mm (bottom right)..... 86

Figure 5-17: Sample of the green laser batch (left) and SEM picture of a typical laser notch with a depth of about 0.6mm (right) 86

Figure 5-18: Sample of the red laser batch (left) and SEM picture of a typical laser notch with a depth of about 0.8mm (right) 86

Figure 5-19: A sample with an imprint of an emplaced particle (marked with a circle) 88

Figure 6-1: Photo of specimen R10A after relaxation test with mismatched assembly (right) and contact analysis of the laser scan data of the same specimen before the test with potential areas of deformation for a matching rate of 14% of the overall area (left - mirrored) 94

Table of Figures

Figure 6-2: Overall results of the relaxation tests with con-rod bolting specimens at 150°C (dark bar color) and 22°C (light bar color)	95
Figure 6-3: Relaxation losses at 150°C of the reference test series Relax_Ref (n=45) and the test series with planished joint surface Relax_Plan (n=6).....	96
Figure 6-4: Relaxation losses at 150°C of test series Relax_Ref (n=15 per batch), Relax_T1 (n=10 per batch) and Relax_Dyn (n=10 per batch) with itemization of laser notch batches	97
Figure 6-5: Relaxation losses at 150°C of reference test series Relax_Ref (n=45) and test series Relax_MA (n=10) with systematic mismatched assembly	98
Figure 6-6: Relaxation losses at 150°C of reference test series Relax_Ref (n=45) and the test series Relax_1P (n=10) with 1 embedded particle and Relax_3P (n=5) with 3 embedded particles in the fractured surface .	99
Figure 6-7: Relaxation losses at 150°C of reference test series Relax_Ref (n=45) and test series Relax_Dyn (n=30) after 5×10^6 load cycles at 9kN tumescent load.....	101
Figure 6-8: Relaxation losses of reference test series Relax_Ref (n=45), test series Relax_T1 and Relax_T2. Relax_T1 and Relax_T2 involved the same 30 specimens, which were measured 4 times at intervals of 168 hrs at different temperatures.	102
Figure 6-9: A comparison of specimens of test series 10kN (10kN preload - top) and 40kN (bottom) with samples from red laser batch (smooth surface topology - left) and yellow laser batch (distinct surface topology - right).....	105
Figure 6-10: Schematic sketch of test set-up for shear load tests	106
Figure 6-11: Diagram of shear load and hydraulic tie-bar displacement	107
Figure 6-12: Con-rod bolting specimen after shear load test	108
Figure 6-13: Transferrable shear load as a function of the installed preload, including scatter range, of each test series	109
Figure 6-14: Effective friction coefficient as a function of the installed preload	111

Figure 6-15: Elastic shear limit of all specimens as a function of the matching rate with a linear trend line 113

Figure 6-16: Transferrable shear load, including scatter range, of test series Yield_cold (~41kN preload) and 40kN (40kN preload)..... 113

Figure 6-17: Transferrable shear load, including scatter range, of test series Yield_cold (~41kN preload) and Yield-warm (~41kN preload)..... 114

Figure 6-18: Illustrations of the FEM models of (a) a con-rod bolting specimen (CBS) and (b) a con-rod (taken from (Lyszczan, et al., 2010)) 115

Figure 6-19: FEM pre-processing of the con-rod bolting specimen (CBS) – generation of a pair of artificial fractured surfaces: import of CAD model to FEM software, merging of the two parts and mesh generation (left), mesh splitting into two meshes (center), contact definition (right) (taken from (Lyszczan, et al., 2010)) 116

Figure 6-20: artificial fractured surface for FEM calculations (taken from (Lyszczan, et al., 2010))..... 117

Figure 6-21: Simulation of the bolting process of a con-rod bolting specimen including preloading by defining inner forces in the bolt shaft (left) and shear loading by node displacement of defined surface areas ant the CBS (right) (taken from (Lyszczan, et al., 2010)) 118

Figure 6-22: Influence of element size on transferrable shear load (with 40kN preload) with the stress distribution at the end of the test runs 0.70 / 2 (upper) and 0.375 / 2 (lower) (taken from (Lyszczan, et al., 2010)) 119

Figure 6-23: Generation of imperfections by random deactivation of surface elements (taken from (Lyszczan, et al., 2010))..... 120

Figure 6-24: Influence of imperfections on transferrable shear load (with 40kN preload and element size 0.7/2) (taken from (Lyszczan, et al., 2010))... 121

Figure 6-25: Impact of preload (= clamping load) on transferrable shear load (element size 0.7/2 and no imperfections) (taken from (Lyszczan, et al., 2010))..... 122

Figure 6-26: Transferred shear load as a function of the applied preload (black full curve) and the curve of the correlation function (taken from (Lyszczan, et al., 2010))..... 123

Table of Figures

Figure 6-27: Relation between the preload and the effective friction coefficient of con-rod bolting specimen resulting from FEM calculations and experimental investigations.....	124
Figure 7-1: Detail of a joint with fractured surfaces obtained by grinding the facing surface of the big eye of a con-rod (taken from (Lyszczan, et al., 2007))	130
Figure 7-2: Sketch of a mechanical model of a joint with fractured surfaces loaded with a normal force and transferring a shear force via labeled contact areas	131
Figure 7-3: Detail of a contact area taken from Figure 7-2 (with respect to Figure 2-3)	132
Figure 7-4: Characteristic of the shear limit and the slip limit of a surface element of a joint with fractured surfaces in dependence of the local inclination angle (with $\mu_{\text{stat}}=0.1$, $F_N=40\text{N}$, $\sigma_{\text{perm}}=900\text{N/mm}^2$ and $A=0.118\text{mm}^2$)	135
Figure 7-5: Characteristic of the shear limit and the slip limit of a surface element of a joint with fractured surfaces in dependence of the local inclination angle and the static friction coefficient (with $F_N=40\text{N}$, $\sigma_{\text{perm}}=900\text{N/mm}^2$ and $A=0.118\text{mm}^2$).....	137
Figure 7-6: Example of joint with fractured surfaces loaded with normal force and transferring a shear load which is distributed among four labeled surface elements	138
Figure 7-7: The stepwise increase of the global shear load (left) and its distribution among the four surface elements (right) shown in Figure 7-6 including the failure limits	138
Figure 7-8: Comparison of the results of the FEM calculation, the experiments and the simple numerical simulation with the model of a joint consisting of 10 surface elements.....	141
Figure 8-1: Overview of the results of the relaxation tests with connecting rods at 150°C (dark bars) and at 22°C (light bars) as well as test results from CBS tests (transparent bars) for comparison.....	147
Figure 8-2: Relaxation losses at 150°C of con-rod bolting specimen reference test series Relax_Ref (n=45) and con-rod reference test series Con_Ref (n=15).....	148

Figure 8-3: Relaxation losses at 150°C of con-rod reference test series Con_Ref (n=15) and con-rod test series Con_BS (n=15) with bearing shells mounted	149
Figure 8-4: Relaxation losses of con-rod bolting specimen test series Relax_T1 (n=30) and con-rod test series Con_T (n=15) at 22°C and at 150°C.	150
Figure II-1: Standard con-rod	170
Figure II-2: Shaft cut off the con-rod.....	170
Figure II-3: Segmentation of the clamped parts	171
Figure II-4: Smoothen side faces	171
Figure II-5: Tension testing machine	172
Figure II-6: Hydropulser Instron 8801	172
Figure II-7: Shear loading device	173
Figure II-8: Drying kiln	173
Figure II-9: Tube furnace.....	174
Figure II-10: Norbar USM III.....	174
Figure II-11: Proprietary device for ultrasonic controlled bolt tightening with ½ inch sockets for the connection to the bolt and to the torque tool	176
Figure II-12: Test setup for measurement of disassembly force.....	177
Figure II-13: LART test bed (1) with control unit (2) and con-rod specimens (3) equipped with Scansonic TH-03D laser scanner (4) and data recorder (5)	178
Figure II-14: Retaining fixture for CBS	179
Figure II-15: Retaining fixture for con-rod body (left) and con-rod cap (right) .	180
Figure II-16: Surface detail of a profile scan before (left) and after (right) smoothening.....	181

Table of Figures

Figure II-17: Vertical orientation of a surface scan before alignment process (P1 and black dashed line) and target orientation (P2 and red dashed line).	182
Figure II-18: Section of the data grit of a surface scan before (left) and after (right) revision by interpolation.....	183
Figure II-19: Shear loading device for CBS inside the tube furnace at the hydropulser (left) and sketched detail of the specimen fixture (right)...	183
Figure II-20: Tension stress and torsion stress during a yield-controlled assembly of a bolted joint and some related important elongations – relaxation step 1	187
Figure II-21: Tension stress and torsion stress during and after a yield-controlled assembly of a bolted joint and some related elongations – relaxation step 2	188
Figure III-1: Detailed summary of test results of the relaxation tests with CBS	189
Figure III-2: Detailed summary of test results of the shear load tests regarding the elastic limit. In each test 5 specimens per batch were involved.....	196
Figure III-3: Detailed summary of test results of the shear load tests regarding the shear limit. In each test 5 specimens per batch were involved.	197
Figure III-4: Detailed summary of test results of the relaxation tests with con-rods	198

Symbols

Latin symbols

A_{contact}	area transferring pressure load in a welded junction	F_R	friction force
A_{pressure}	contact area transferring pressure load only	F_{Res}	resulting force of F_N and F_Q
A_{real}	true contact area on microscopic level	F_{sep}	required force for separation of con-rod cap and body
A_{shear}	area transferring shear load in a welded junction only	F_T	transferrable shear force
A_{tension}	area transferring tension load in a welded junction only	F_V	preload of a bolted joint
b_{sc}	breadth / width at introduction level of nominal load F_{nom}	F_Z	loss of bolt load due to embedding and relaxation
c_{99}	confidence interval with 99% confidence	g	gravitational acceleration of earth
d_{AVD}	(virtual) average vertical distance of a pair of fractured surfaces	h_c	average contact distance on microscopic level
d_p	elongation of clamped parts in a bolted joint	h_{sc}	true contact height of a form connection on macroscopic level
d_s	elongation of bolt	i, j	counter variables
d_{TVD}	threshold for (virtual) vertical distance for cavity localization	k_1	load distribution factor
E	Young modulus	K_A	load application factor
E^*	effective Young modulus	$k_{\varphi\beta}$	load transfer factor
$F_{\text{adh, elastic}}$	adhesive force in an elastic contact	L_0	unloaded length of a bolt
$F_{\text{adh, solid}}$	adhesive force in a solid contact	L_{EPL}	elastic bolt elongation at required load level for shear load test
F_G	gravitational force	L_{max}	maximum elastic bolt elongation
F_M	assembly force of a bolted joint	L_{max^*}	maximum bolt elongation
F_N	(local) normal force	L_{plastic}	plastic elongation of a bolt after disassembly
F_N^*	global normal force	L_{point}	elastic bolt elongation at measurement point
F_{nom}	nominal load of a joint / connection	L_{point^*}	bolt elongation at measurement point
F_Q	(local) shear force	l_{sc}	true contact length of a form connection on macroscopic level
F_Q^*	global shear force	m	mass of a body

Symbols

M_{BT}	initial breakaway torque of con-rod bolt	$t_{duration}$	duration of a test run
$P_{contact}$	present pressure load	T_{max}	maximum mechanical tension
P_{perm}	permissible pressure load	t_{start}	date and time of the initial bolt loading
R	radius of a sphere	t_{point}	date and time of a measurement point
r_A	radius of an asperite	z	number of mating surfaces in a form connection
R_C	averaged roughness	Z_{batch}	average loss due to relaxation of all specimens of a laser batch
R_{loss}	ratio of preload loss due to relaxation	Z_i	maximum local distance from peak (bottom) to peak (top) of surface roughness
R_Z	(maximum) roughness	Z_{max}	maximum global distance from peak (bottom) to peak (top) of surface roughness
s	standard deviation	Z_{series}	average loss due to relaxation of all specimen of a test series
S_{batch}	individual standard deviation of each specimen per laser batch		
S_{series}	individual standard deviation of each specimen per test series		
s_ε	standard deviation of effect ε		

Greek symbols

α_A	application factor for bolt assembly	$\mu_{effective}$	effective friction coefficient
α_I	deviation angle between two data points	μ_{geom}	friction coefficient resulting from geometric angle
α_{point}	point-to-point inclination angle	μ_{global}	global friction coefficient
α_{slide}	sliding average inclination angle	μ_{stat}	static friction coefficient
γ	surface energy	ν	Poisson's ratio
ε	effect of laser batch on average value or standard deviation	σ_{hard}	penetration hardness
κ	tension strength coefficient	σ_m	tensile strength
λ_c	profile filter between roughness and waviness	σ_{perm}	permissible van-Mises load
λ_f	profile filter between waviness and longer wave lengths	τ_m	shear strength
λ_s	profile filter between roughness and shorter wave lengths	τ_{perm}	permissible shear load
		τ_{shear}	present shear load
		φ, φ_{geom}	geometric angle

1 Introduction

The development of the next generation of a product is usually closely related to cost reduction (Pahl, et al., 1999). One way to decrease costs is to simplify the manufacturing process of subassemblies or single parts. Usually a change of the production process also requires adaptations in the product design. Sometimes additional research is necessary to handle these adaptations.

At the beginning of this century the German automotive industry widely introduced a new production process for connecting rods (see Figure 1-1) – fracture splitting (Blauel, et al., 2000). Until then the main parts of a con-rod, cap and body, were manufactured separately. In order to assemble cap and body the connecting surfaces of both parts had to be machined and grinded carefully to allow exact alignment. Furthermore, special bolts – so called fitting bolts – had to be used in order to ensure exact positioning and shear load transfer (Ohrnberger, et al., 1992). The new production process requires that each con-rod is made out of a single moulding blank. Cap and body are formed by cracking the roughly pre-machined con-rod and then both parts are bolted together. The specific topology of the fractured surfaces enables an easy matching of con-rod cap and body. Consequently, intensive machining, grinding and the use of fitting bolts were no longer necessary. Consequently, the costs for the manufacture of a con-rod made with the new production process were cut by about 30% (Fatemi, et al., 2005).

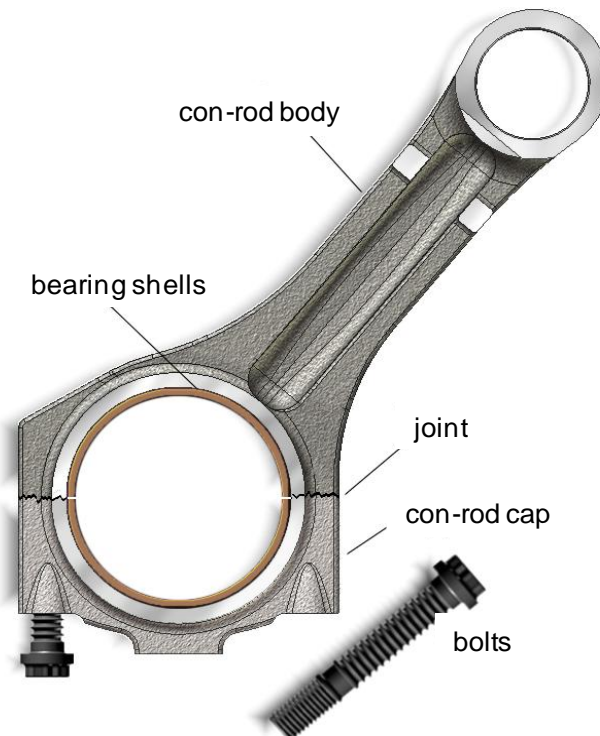


Figure 1-1: Fracture splitted connecting rod of a modern diesel engine

A joint with fractured surfaces varies distinctly from a joint with plain surfaces. Especially two parameters may have changed and thus became of high importance in the design process. These parameters are the relaxation in the joint and the mechanism of shear load transfer.

Formulas as well as analytical (Urlaub, 1995) and numerical tools (Müller, et al., 1997) for an exact calculation of the relaxation losses and the transferrable shear load exist only for bolted joints with plain connecting surfaces. These tools are not suitable for the calculation of bolted joints with fractured surfaces. There are no substantiated measurement data available that allow either analytical or numerical calculations of these joints. Until now calculations of joints with fractured surfaces base on estimations derived from extrapolation joints with rough (but plain) surfaces. The mechanical properties of joint with fractured surfaces are not taken into consideration because they are unknown. As a result, all actual calculations of joints with fractured surfaces have a low reliability.

The use of unreliable boundary conditions for con-rod calculations has lead to preload losses of an unexpected magnitude. As a result bolting failures appeared (Lyszczan, et al., 2007). To avoid that, higher safety factors have been installed. A higher safety factor results in bigger and heavier parts which results in less efficiency, higher fuel consumption and higher costs. Bolting failures can lead to damaged con-rods and bolts or even enable self loosening of the con-rod bolts which leads nearly instantly to the destruction of the entire engine.

1.1 Goals

According to the outlined challenges the main goal is the determination of the two parameters - relaxation losses and the transferrable shear load - in order to ensure an efficient and reliable computation of a bolted joint with fractured surfaces.

To assure the achievement of this main goal a number of sub goals are defined. Each sub goal focuses on one key point of this research: an applicable description of the surface topology, the determination of relaxation loss, the determination of transferred shear load and the description of the transfer mechanism. Relaxation and shear load transfer occur in the engine at moderately increased temperature, which is an additional key point. The following sub goals can be formulated:

- Description of fractured surfaces with a set of characteristic parameters
- Determination of characteristic losses by relaxation as well as the influence of moderately increased temperature
- Determination of transferrable shear load and the influence of moderately increased temperature
- Development of a mechanical model to describe the mechanism of shear load transfer in fractured surface

To achieve each sub goal the related topics are transformed into research questions which are answered using literature as well as experimental and analytical research.

1.2 Research Questions

In order to enable a focused research the sub goals are transformed into the following specific research questions:

- (1) What are suitable parameters to describe different fractured surfaces?
- (2) What is the impact of fractured surfaces on the relaxation of bolted joints?
- (3) What is the relation between surface topology and the amount of relaxation losses?
- (4) What is the effect of moderately increased temperature on the amount of relaxation losses?
- (5) What is the impact of the clamping force on the transferrable shear load in a bolted joint with fractured surfaces?
- (6) What is the relation between surface topology and transferrable shear load?
- (7) What is the effect of moderately increased temperature on the maximum transferrable shear load?
- (8) What kind of mechanism enables the load transfer?

The scope is first on basic research using a special kind of specimens called con-rod bolting specimens¹ in order to be able to draw more generic conclusions about bolted joints with fractured surfaces. In addition it will be verified whether the conclusions apply to a tangible product namely to con-rods.

¹ These simplified specimens are described in section 4.3.2.

1.3 Structure of this dissertation

Chapter 1 introduces the topic, the main goal and the research questions.

In Chapter 2 the current state of the art concerning friction and shape based force transfer as well as mixed force transfer concepts as found in literature are described. Furthermore short introductions to bolted joints with a special focus on relaxation and con-rods are presented.

Chapter 3 provides results of prior research of fractured con-rods carried out by the author of this dissertation. These results provide a basis for the investigations described in this document.

In Chapter 4 the research hypotheses are formulated and the research methods are described.

Chapter 5 focuses on the inspections of the fractured surfaces. Research hypothesis (1) is verified in this chapter.

In Chapter 6 the experimental investigations of the con-rod bolting specimens are presented. Furthermore the results of a FEM analysis and a comparison with experimental results of the shear load tests with the con-rod bolting specimens are described. Research hypotheses (2), (3), (4), (5), (6) and (7) are verified in this chapter.

Chapter 7 presents the development of a mechanical model to describe the mechanism of shear load transfer in a connecting with fractured surfaces. Research hypothesis (8) is verified in this chapter.

Chapter 8 focuses on the results of experiments with con-rods to verify the experimental findings concerning relaxation in section 6.1.

In Chapter 9 conclusions combining all investigations are presented. Furthermore, a summary concerning the contributions and an outlook for further investigations are provided.

The appendices contain detailed information on setup, processes and results of the conducted experiments.

2 State of the Art

Experimental research is a long-winded and resource intensive exercise. To keep the effort for a research project as low as possible it is very useful to avoid re-research activities in fields where scientific results are already available. To handle the research questions raised in Section 1.2 as effectively as possible, a literature research was conducted.

Different kinds of force transfer are surveyed in order to prepare the response of the research questions (5), (6), (7) and (8) concerning the characteristics and the mechanism of shear load transfer in connections with fractured surfaces. The collection of recent knowledge about friction based force transfer in force connections, shape based force transfer in form connections and mixed force transfer in mixed connections is summarized in Sections 2.1, 2.2 and 2.3 respectively.

The experience of relaxation in bolted joints which is needed to deal with the research questions (2), (3) and (4) is described in Section 2.4.

There are no particular research questions concerning con-rods. Nevertheless, basic knowledge about con-rods is required in order to achieve the main goal of this research project – the efficient and reliable computation of con-rods. This knowledge is provided in Section 2.5.

Information and recent definitions concerning surface parameters which will be useful to answer research question (1) will be provided in Section 2.6.

A conclusion concerning the state of the art with respect to the research questions is provided in Section 2.7.

2.1 Force Connections

Friction based force transfer is realized by application of normal forces onto working surfaces of the involved components. Normal forces are caused by an external energy supply. In many applications this external energy is conserved as elastic deformation energy of parts or components within the force flow. In other applications external energy may be provided as a magnetic or an electromagnetic energy or as a reaction force to hydrodynamic or aerodynamic forces ((Bickford, 1995), (Pahl, et al., 1999)).

Independent of the source of external energy the correlation between normal force (F_N) and friction force (F_R) in a static state is in a first approximation as follows:

$$F_R = \mu_{\text{stat}} \cdot F_N \quad (2-1)$$

Correlation factor μ_{stat} is called static friction coefficient. This proportionality was first discovered by Guillaume Amontons but is often called Coulomb's law² (Dowson, 1979). In a connection with friction based force transfer, shear load is transferred up to the magnitude of the friction force.

Friction always calls for contact of surfaces of the involved components. Depending on the degree of the fitting accuracy, surface adhesive forces appear in addition to friction forces (Popov, 2009). Adhesive forces "locally weld" the surfaces together. As a result, the transferable shear load is increased by the shear force that is necessary to destroy the adhesive connection.

Generally the degree of the fitting accuracy of the surface is a function of macroscopic and microscopic surface topology as well as the elasticity of the involved parts. Macroscopic surface topology equals the surface shape. This shape may be classified into rather even, flat surfaces and rather uneven surface shapes. Microscopic surface topology is described by the surface roughness.

In the following sections Coulomb's law and the influences of roughness and adhesion are discussed.

2.1.1 Coulomb's Law

Static friction is a very complex phenomenon which includes many different physical and chemical interactions. Despite this fact a very simple law of friction, Coulomb's law, is valid for most engineering applications. Coulomb's law deals with the proportionality of friction force and normal force (see equation 2-1) and shows that friction force is independent of the size of the contact area, the surface roughness and – in case of dynamic friction – the sliding speed.

The proportionality constant is called static friction coefficient μ_{stat} . It can be obtained by measuring the angle of inclination a tapered plane needs to be adjusted to so that a mass just starts to slide down that plane (see Figure 2-1).

² Coulomb discovered the proportionality of dynamic friction force and normal force and found out that there is nearly no difference between static friction coefficient and dynamic friction coefficient. He also stated that the friction coefficient is independent from contact area and from surface roughness which is true in a first approximation (Müser, 2003).

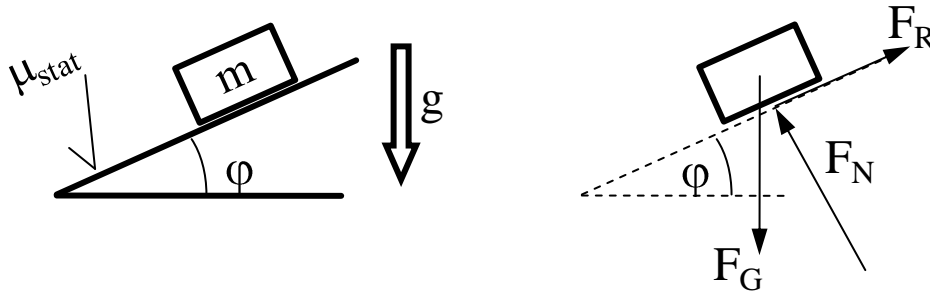


Figure 2-1: A body on an inclined plane with friction (left) and the derived mechanical model (right)

The mass m and the gravitational acceleration g generate the gravitational force F_G of the mass onto the plane. With increasing angle of inclination φ the magnitude of the local normal force F_N and of the local friction force F_R change according to following formulas:

$$\text{x-axis (direction of } F_R\text{): } F_R = F_G \cdot \sin(\varphi) \quad (2-2)$$

$$\text{y-axis (direction of } F_N\text{): } F_N = F_G \cdot \cos(\varphi) \quad (2-3)$$

Together with equation (2-1) the correlation of friction coefficient μ_{stat} and inclination angle φ can be calculated to:

$$\tan(\varphi) = \mu_{\text{stat}} \quad (2-4)$$

The tangent of the inclination angle φ is equal to the friction coefficient μ_{stat} ; the inclination angle φ is called friction angle.

2.1.1.1 Global friction coefficient

According to (Popov, 2009) the simple definition of friction coefficient by use of friction angle can be taken to describe friction on different scales. In a system of two cogging surfaces with friction, loaded with a global normal force F_N^* and transferring a global shear force F_Q^* , the toothed shape can be translated into a macroscopic friction source (see Figure 2-2).

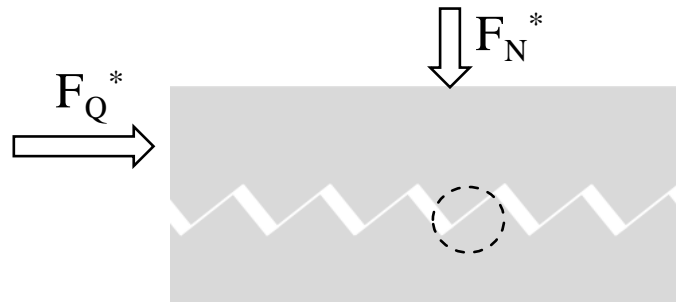


Figure 2-2: A system of two cogging surfaces with friction, a global normal force (F_N^*) and a global shear force (F_Q^*)

A single element of Figure 2-2 is shown as a detail in Figure 2-3. This element is used to describe the mechanical model of the global friction coefficient.

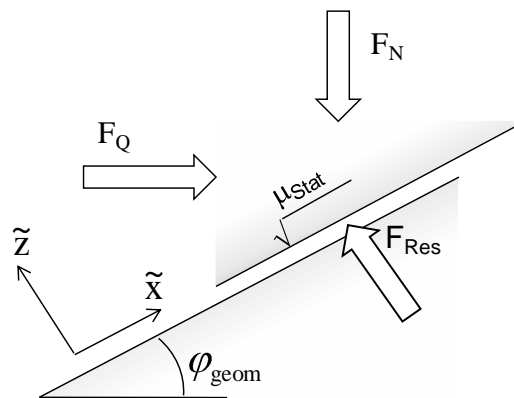


Figure 2-3: Free cut of an element of Figure 2-2

In Figure 2-3 a free cut of an element of the described system is shown. F_Q is the local shear force, F_N the externally fed local normal force³ while F_{Res} is the sum of all local reaction forces of F_Q and F_N . The angle φ_{geom} is the local inclination angle of the involved two surfaces. Assuming the local inclination angle is valid for all contact areas and the static friction coefficient is a global value, the number of teeth shown in Figure 2-3 does only increase the overall contact area. As a result, the global forces can be split into local forces attached to single elements. This has

³ For the reason of simplicity it is assumed that the global normal force is much greater than the weight so the influence of weight is neglected.

no effect on the ratio of F_N^* and F_Q^* and, hence, no effect on the transferrable shear load. The balance of forces in each local direction can be calculated to (Popov, 2009):

$$\text{Direction } x\tilde{\text{:}} \quad F_N \cdot \sin \varphi_{\text{geom}} + F_{\text{Res}} \cdot \mu_{\text{Stat}} = F_Q \cdot \cos \varphi_{\text{geom}} \quad (2-5)$$

$$\text{Direction } z\tilde{\text{:}} \quad F_N \cdot \cos \varphi_{\text{geom}} + F_Q \cdot \sin \varphi_{\text{geom}} = F_{\text{Res}} \quad (2-6)$$

The geometric angle can be interpreted as a friction angle. With $\tan(\varphi_{\text{geom}}) = \mu_{\text{geom}}$ a superposition of geometric and friction angle to a global friction coefficient can be calculated (Popov, 2009):

$$\mu_{\text{global}} = \frac{F_Q}{F_N} = \frac{F_Q^*}{F_N^*} = \frac{\mu_{\text{Stat}} + \mu_{\text{geom}}}{1 - \mu_{\text{Stat}} \mu_{\text{geom}}} \quad (2-7)$$

This way the microscopic friction coefficient μ_{stat} and the influence of cogging are merged into a new macroscopic friction coefficient μ_{global} . The macroscopic proportionality of transferrable global shear force F_Q^* and global normal force F_N^* in this system depends only on the overall global friction coefficient.

2.1.1.2 Basic mechanical approaches to friction

From his experiments Coulomb concluded that the static friction coefficient does neither depend on the normal force nor on the (microscopic) surface roughness. In addition, the kinetic friction coefficient⁴ does not depend on the sliding speed. All these independences are true for a first approximation. The primary reason for these phenomena is the difference between macroscopic and microscopic contact area.

There are two kinds of physical models to describe friction: those models that base on the apparent macroscopic contact area and those models that base on the real microscopic contact area. A popular model of the second kind was contributed by Greenwood and Williamson (Greenwood, et al., 1966). This model is a contact model of elastic surfaces, which excludes any chemical or physical forces like for example adhesion. In their model the microscopic surface shape equals a conglomerate of stochastically distributed hills and valleys with different heights and

⁴ The kinetic friction coefficient is used for surfaces in relative motion.

depths formed by small half circles called asperites which all share the same radius r_A (see Figure 2-4).

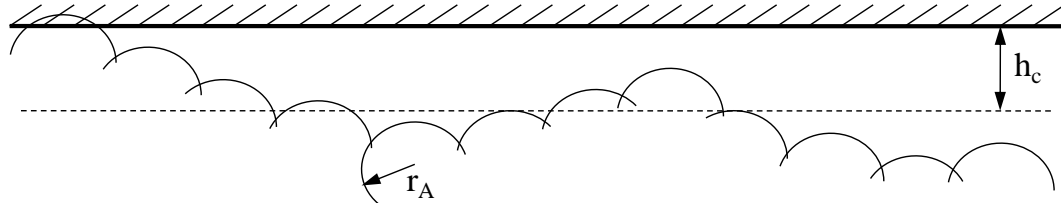


Figure 2-4: Model of a stochastic surface from Greenwood and Williamson with the asperite radius r_A and the contact distance h_c (based on (Popov, 2009))

In case of a macroscopic contact between two bodies, only a certain number of peaks of each surface are in contact. Regarding Figure 2-4 only asperites which are higher than the average contact distance h_c are in contact. This means that the real contact area is much smaller than the apparent macroscopic contact area. In a contact of metallic materials the true contact area is a quotient of normal force by material dependent permissible penetration hardness⁵:

$$A_{\text{real}} = \frac{F_N}{\sigma_{\text{hard}}} \quad (2-8)$$

Furthermore, the mentioned independence of the friction coefficient of contact area and normal force bases upon this effect. The number of asperites in contact does only depend on the normal force. With increasing macroscopic contact area the density of asperite contacts decreases - only the highest microscopic peaks are in contact. Consequently, an increase of the macroscopic contact area results in a slightly larger distance of the true average surface distance although this increase is macroscopically not perceptible. With increasing normal force the true average surface distance decreases. At the same time the number of asperites in contact increases exponentially. Consequently, the overall contact area increases but the average contact area per asperite remains nearly constant – and so does the friction coefficient.

For metallic materials the functionality of friction was described by Bowden and Tabor (Bowden, et al., 2001) as follows. Within the true contact area atoms of the

⁵ The penetration hardness of a metal is about a triple of the materials tensile strength (Tabor, 1951).

two contact partner get that close that atomic interactions take place⁶. Bowden and Tabor considered these interactions being a creation of welded junctions between the contact partners. Consequently, the friction force is equal to the shear force τ_m that is necessary to cut these junctions. When applying a normal force it was assumed that one half of the welded junctions are stressed by pressure and the other half is stressed by tension. Consequently, the true contact area is divided into a contact area of pressure A_{pressure} and a contact area of tension A_{tension} . Both contact areas have the same size and their sum is equal to the overall real contact area. The friction force can be described the following way (Popov, 2009):

$$F_R \approx \tau_m (A_{\text{pressure}} + A_{\text{tension}}) \quad (2-9)$$

Considering the true contact area in metal connections as well as the influence of the tension reducing the permissible contact pressure by a factor κ ⁷ the following formula can be derived (Popov, 2009):

$$F_N \approx \sigma_{\text{hard}} \cdot A_{\text{pressure}} - \sigma_m \cdot \kappa \cdot A_{\text{tension}} \quad (2-10)$$

$$\Rightarrow F_N \approx \sigma_m (3 \cdot A_{\text{pressure}} - \kappa \cdot A_{\text{tension}}) \quad (2-11)$$

Applying equation (2-9) and (2-11) to equation (2-1), transposing to friction coefficient and replacing τ_m by $\sqrt{3} \sigma_m$ the following coherency appears:

$$\mu_{\text{stat}} \approx \frac{1}{\sqrt{3}} \left(\frac{A_{\text{pressure}} + A_{\text{tension}}}{3 \cdot A_{\text{pressure}} - \kappa \cdot A_{\text{tension}}} \right) \quad (2-12)$$

Usually remains of lubricants can be found on the surface of metals that prevent atomic interactions. Consequently, the buildup of welding junctions is suppressed. Therefore only pressure occurs within the true contact area. Under these conditions the static friction coefficient can be calculated based on (2-12) to $\mu_{\text{stat}} = 1/(3 \cdot \sqrt{3}) \approx 0.19$ which is a value typical for the dry contact of metals.

⁶ These interactions are called adhesion. Adhesion will be discussed in section 2.1.2.

⁷ The magnitude of κ is about 1 to 2 and depends on material properties. Most metals have a weaker strength against tension than against pressure.

2.1.1.3 Influencing factors

The true contact area is much smaller than the apparent macroscopic contact area. Consequently, in non-brittle materials creep occurs, having a considerably impact on the friction coefficient. The amount of the impact is controlled by two factors - contact time and temperature.

Coulomb discovered that the static friction coefficient increases instantly with elapsed time independent of the contacting materials. The increase of friction force – and, hence, the increase of friction coefficient - was found to be proportional to time in a logarithmic manner.

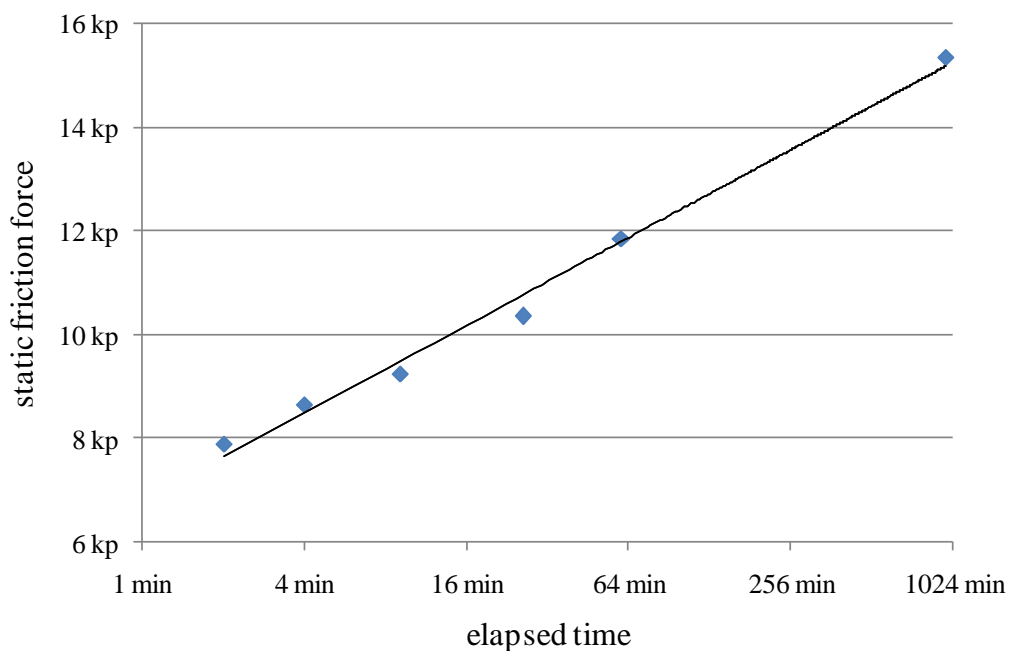


Figure 2-5: Data from Coulombs original experiment (oak against oak lubricated with talc): static friction force as a function of the natural logarithm of elapsed time (based on (Popov, 2009))

Figure 2-5 shows the data from one of Coulombs original experiments (Popov, 2009). The logarithmic proportionality of friction and contact time is obvious. The reason for this phenomenon is that the real contact area increases by the time due to creep of the material. The magnitude of creep decreases with an increase of the true contact area because its driving force – the contact pressure – is reduced. Creep is 1-dimensional parameter while area is a 2-dimensional parameter. Consequently, the interaction of both results in a logarithmic behavior. With growing true contact area the static friction force increases. This equals an increase of the static friction coefficient.

The effect of temperature on the friction coefficient is caused by two phenomena. First, creep of material at high temperature is much larger than at room temperature due to reduced Young modulus and other material properties. At temperatures above 200°C this effect becomes exceptionally strong.

Second, a higher temperature leads to the destruction of remains of lubricants on metal surfaces. This enables the formation of welded junctions which are able to transfer tension. With formula (2-12) and an estimation of $\kappa \approx 1.5$, a typical value for the static friction coefficient of warm metals of $\mu_{\text{stat}} = 2/(1.5 \cdot \sqrt{3}) \approx 0.77$ can be derived which closely meets expected friction values (see Figure2-6).

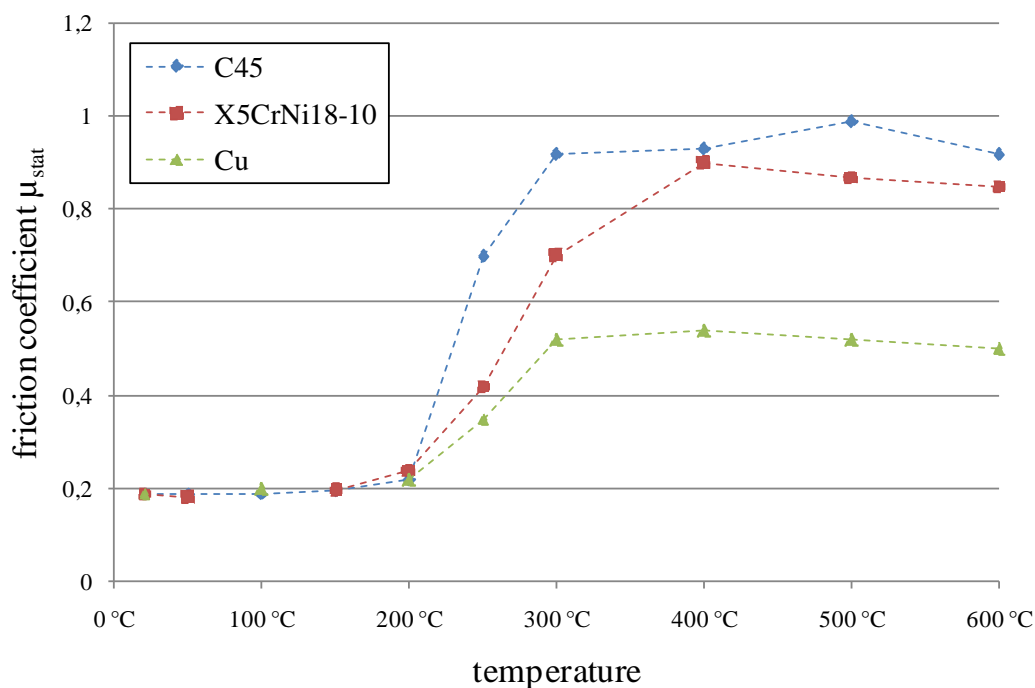


Figure2-6: Static friction coefficient as a function of temperature for experiments with copper against copper and against two kinds of steel (Köhler, 2005)

2.1.2 Roughness and Adhesion

The basic law of friction investigated by Coulomb is regarded as universally valid. It can be explained by rather simple models focusing purely on mechanical contact. However, as mentioned in Section 2.1.1.2 all contacts of materials are accompanied by adhesion. Adhesive forces, estimates of their magnitude and the influence of roughness onto these forces are the subject of this section.

2.1.2.1 Basic models of adhesion

Two electrically neutral atoms attract each other when placed at a distance equal or slightly larger than the interatomic distance. This attraction is called van-der-Waals interaction and belongs to the family of the weak nuclear forces. This force has a repulsive character at short distances (smaller than a typical interatomic distance), an attractive character at medium distances and has no effect on longer distances. It can be approximated by the Lennard-Jones potential shown in Figure 2-7 (Popov, 2009).

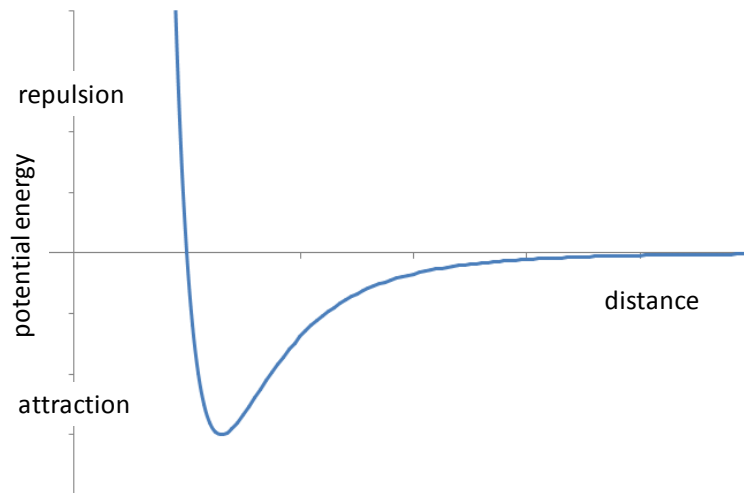


Figure 2-7: Lennard-Jones potential curve (schematic illustration) with areas of attraction (negative potential energy) and repulsion (positive potential energy) (based on (Popov, 2009))

In 1932 Bradley presented a solution for the calculation of adhesive forces for the contact of a solid sphere against a solid plane (Bradley, 1932):

$$F_{\text{adh,solid}} = -4\pi\gamma R \quad (2-13)$$

In this equation γ is the surface energy⁸ and R is the radius of the sphere. In good approximation this radius is equal to that distance in the Lennard-Jones potential where the potential energy changes from attraction to repulsion. Nearly 40 years

⁸ The surface energy is defined as half of the amount of energy that is necessary to generate two surfaces from one by separation. For metals the surface energy usually has a magnitude of 1 J/m² to 3 J/m². For iron the exact value is 2.4 J/m² (Persson, 2000).

later in 1971 Johnson, Kendall and Roberts (Johnson, et al., 1971) presented a model with a slightly different solution for the contact of two elastic bodies:

$$F_{adh,elastic} = -3\pi\gamma R \quad (2-14)$$

In strict sense the JKR model is only valid for large, soft spheres. In their investigations concerning different adhesion models in 1997 Johnson and Greenwood (Johnson, et al., 1997) stated that the JKR mode still generates very good results when used outside its defined area of validity. Consequently, this model is the most suitable one for the approximation of the adhesive force in a contact of two metal parts.

2.1.2.2 Influence of roughness

In a contact of metal parts an adhesive force is usually not detectable. More precisely an adhesive force usually cannot be measured when two metal parts are separated. The reason for the absence of an adhesive force could be either the presence of thick surface films or the surface roughness. Surface films can prevent a strong interaction of solid bodies. Furthermore, surface films themselves may have only a weak connection to the solid bodies (Geike, 2007). The influence of roughness on the amount of the adhesive force was aim of several experimental and theoretical investigations. It was discovered that even a low level of surface roughness prevents the build-up of a reasonable adhesive force (Fuller, et al., 1975), (Persson, 2000), (Persson, 2002).

The effect of surface roughness on the occurrence of an adhesive force can be explained with the following example. With formula (2-14) the adhesive force of a roughly grinded iron cube with an edge length of 100 mm (resulting in a weight force of about $F_N = 100 \text{ N}$) lying on a steel plate can be calculated to $F_{adh} = 200 \text{ N}^9$ resulting in a force necessary to lift the cube to about 300 N. This contradicts all known experience. The real adhesive force in such a system is much smaller; actually within most calculations adhesive forces can be neglected. The reason for this phenomenon is the influence of roughness.

⁹ With formula (2-8) and a penetration hardness of about 1000 N/mm^2 the real contact area can be calculated to 0.1 mm^2 . With a typical contact radius for the asperites of 0.01 mm (Popov, 2009) a number of about 1000 contacts can be derived. The overall adhesive force is calculated by the number of asperite contacts times equation (2-14) using the contact radius as sphere radius R .

Combining the surface model of Greenwood and Williamson and the JKR model it can be shown¹⁰ that the occurrence of a distinct amount of adhesive force depends on the RMS value of the roughness distribution which can be approximated by the mean roughness index R_a . A reasonable amount of adhesive force shall be expected when the mean roughness index is located below a material dependent threshold (E^* is the effective young modulus¹¹) (based on (Popov, 2009)):

$$\sqrt{\frac{3\pi^2\gamma^2R}{16E^{*2}}} > R_a \quad (2-15)$$

To illustrate the meaning of this formula, the example with the iron cube shall be used again. With the values from the calculation example, a mean roughness index of about $0.002 \mu\text{m}$ is required to enable the occurrence of a noticeable amount of adhesion force at the iron cube according to formula (2-15). Only highly polished surfaces have such roughness indexes which again meets common experiences.

The magnitude of γ – and with it the magnitude of the adhesive force - strongly depends on the size of the area that is created by an instant separation. Whenever two surfaces are peeled off, the magnitude of γ will be much lower than when two surfaces are instantly separated. Steel parts often have a relatively high stiffness which supports instant separations. This should support the occurrence of a distinct amount of adhesive force between such parts. However, the high stiffness of steel made parts allows only small elastic deformations to form the true contact area. Moreover the comparably distinct roughness of metallic surfaces decreases the available contact area. As a result the overall contact area is rather small and so is the adhesive force (Popov, 2009).

The adhesive force in steel parts can be substantially increased by slight surface pollutions with soft materials such as lubricants. As long as these pollutants form only a very thin surface film they help to gap the surface roughness in case of a contact of two steel made parts. In these cases the occurrence of a distinct adhesive force can usually be observed.

¹⁰ A calculation example can be found in (Popov, 2009)

¹¹ The effective Young modulus is to be calculated with $E^* = E \cdot (1 - \nu^2)^{-1}$ with $\nu \approx 0,3$ for metals (Geike, 2007)

2.1.3 Conclusions

For most applications the force transfer in a force connection can be specified by the ratio of transferrable shear force by available normal force and a friction coefficient. This friction coefficient depends on material combination, surface roughness, surface pollution, contact time and temperature.

When friction shall be considered along different scales, a global friction coefficient can be calculated based on the average inclination angle of the surface topology in each scale level. This global friction coefficient contains the influences of all friction coefficients of lower scales.

In a contact of two parts, the real contact area is formed by the peaks of the surface roughness called asperites. Consequently, the real microscopic contact area is much smaller than the apparent macroscopic contact area. In a contact of metal parts, the asperites are linked by welding junctions based on interatomic reactions. In such connections the friction force is equal to the shear force that is necessary to cut these junctions. Surface pollution decreases the number of welding junctions and lowers the friction coefficient.

Adhesion is an interatomic force that appears at the contacting asperites and occurs as a force normal to the connection areas. Its measureable appearance is strongly influenced by the degree of surface roughness. Slight surface pollution is likely to support the amount of adhesive force while thicker surface films prevent the necessary interactions of the contact partners.

2.2 Form connections

In form connections force is transferred via tangent surfaces put into contact by the transferred forces itself. The transferred forces generate surface pressure and shear stresses via the contact areas within the involved parts. Accordingly form connections are generally designed for a permissible surface pressure p_{perm} as well as a permissible shear stress τ_{perm} of (Haberhauer, et al., 2007):

$$\frac{F_T}{A_{contact}} = p_{contact} \leq p_{perm} \quad (2-16)$$

$$\frac{F_T}{A_{shear}} = \tau_{shear} \leq \tau_{perm} \quad (2-17)$$

For most applications the permissible shear stress is not a limiting value as long as the permissible surface pressure is not exceeded. In these formulas F_T is the transferrable shear force, $A_{contact}$ the effective area for normal load transfer and A_{shear}

the effective area for shear load transfer. These three variables are to be determined by the calculation of a set of influencing factors.

Different factors influence the amount of transferrable force and contact area in form connections. The amount of transferrable force is influenced by its magnitude as well as its spatiotemporal distribution. The contact area depends on the size of the effective macroscopic contact area. For both parameters the influencing factors will be introduced and briefly described.

2.2.1 Influencing factors

The transferrable shear force F_T does often not appear as a constant static load but as a variety of loads with alternating and time dependent magnitudes, represented by the load spectrum¹². For easier analytical calculations the load spectrum is often transformed into an effective load which is a constant load with a damage impact equivalent to the load spectrum. It is a product of the nominal load F_{nom} and an application factor K_A . This factor can either be taken from tables based on experience from different applications or calculated according to the cumulated damage of expected or measured load amplitudes.¹³

Macroscopic surface divergences caused by manufacture generate an uneven load distribution along the contact area. In shaft-hub-connections this imbalance is increased by the difference in torsional stiffness of shaft and hub and is additionally influenced by the momentum flow¹⁴. These imbalances generate a higher local stress within the parts than computations predict, as these refer to nominal stress only. A load distribution factor k_l is used in calculations to consider this phenomenon.

Often more than one pair of mating surfaces is involved in the process of force transfer. Macroscopic divergences generated during manufacture and assembly process cause an uneven load distribution between the contact surface pairs. As a result the overall amount of the transferrable force increases only disproportional

¹² There are several approaches to define and calculate a load spectrum. The most common approach is the Palmgren-Miner approach. Further information can be found for instance in (Haibach, 2006).

¹³ A calculation of an application factor based on different Palmgren-Miner approaches is shown in (Forschungsvereinigung Antriebstechnik, 2004).

¹⁴ The longer the distance between the entrance and exit area of the force flow within a connection the better the utilization level of the design and the more even the load distribution will be.

in comparison to the overall size of all contact areas. In calculations this fact is addressed by the use of a load transfer factor $k_{\varphi\beta}$.

All introduced factors have to be taken into account when a form connection is designed. The calculation of the expected stresses considering all influencing factors will be presented in the next section.

2.2.2 Pressure and Stress

For the estimation of occurring surface pressure the following formula is used considering (2-16) and all mentioned influencing factors (Forschungsvereinigung Antriebstechnik, 2004):

$$p_{contact} = \frac{F_{nom} \cdot K_A}{l_{sc} \cdot h_{sc} \cdot z} \cdot k_l \cdot k_{\varphi\beta} \quad (2-18)$$

Compared to (2-16) the contact area has been replaced by the product of the true contact length l_{sc} , the true contact height h_{sc} and the load distribution factor k_l . Additionally the number of mating surfaces z and the corresponding load transfer factor $k_{\varphi\beta}$ has to be taken into account. The transferred force has been divided into a nominal force and an application factor.

When all or some participating mating surface pairs do not share a common size or shape, the product of the number of mating surfaces z and the contact area has to be replaced by a sum of all mating surface areas.

An estimation of the occurring shear stress considering all influencing factors is given with the following formula:

$$t_{shear} = \frac{F_{nom} \cdot K_A}{l_{sc} \cdot b_{sc} \cdot z} \cdot k_l \cdot k_{\varphi\beta} \quad (2-19)$$

In comparison to (2-17) this formula contains all changes that have been introduced with (2-18) with one exception. The contact height plays no role for the occurring shear stress but the parts' width b_{sc} at the nominal load introduction level.

2.3 Connections with Mixed Force transfer

In some connections two different working principles are used in parallel to transfer forces and loads. The parallel use of different working principles is intended to either increase the effectiveness of the joint, decrease production costs or increase the safety of the force transfer.

An example for the increase of effectiveness by the use of two working principles is the glued shrink fit connection which is a combination of an adhesive bond and a force connection. The adhesive located in the contact area suppresses the relative movement that could occur under load to a certain extent. Consequently, the probability of failure due to fretting is decreased (Niemann, et al., 2005).

An example for the decrease of production costs is the straight-knurled press fit connection which is a combination of a form connection and a force connection. A hard straight-knurled shaft is pressed into a soft hub with a simple bore. At the knurl tips the bore is extended and partly hub material is removed. The costs for further machining of the hub bore to enable a pure form connection can be saved¹⁵.

The plain taper key connection is another example for a combination of form connection and force connection. In this case the combination of the working principles aims for increased safety of the force transfer. After an initial slip the force connection prevents further relative movement of shaft and hub increasing the strength of the connection against abrupt loadings (Niemann, et al., 2005).

The force transfer in these connections is ambiguous - hence a direct analytical calculation considering all working principles at once is not possible. Still there are two ways to conduct estimation based values for the design of such connections. One way is to determine the predominant working principle and use its formula for the calculations. The other working principle is used to increase the safety of the final design (Niemann, et al., 2005). The other way is to experimentally investigate the performance of such connections within their specific applications.

Connections with mixed force transfer offer advantages compared to connections based on a single working principle. For example the glued shrink fit connection offers either the option of distinctly lesser surface pressure or an increased strength at the same load level in comparison to standard shrink fit connections

¹⁵ The straight-knurled press fit connection is still aim of investigations concerning its performance and durability (Just, 2008).

(Niemann, et al., 2005). Generally connections with mixed force transfer enable either lighter designs at comparable loads or higher performance with comparable design parameters. Usually the price for these advantages is a more complex design of the single parts and/or a more expensive manufacturing and assembly process.

2.4 Bolted Joints

Whenever two parts have to be assembled with a certain clamping force often the bolt is the fastener of choice. The relatively easy and low-cost assembly recommends its use in a wide range of applications from simple tools to complex structures. Although the bolt itself is a rather simple fastener the behavior of a bolted joint is very complex, especially when the joint consists of two or more bolts.

A bolted joint usually consists of at least four parts: bolt, nut and clamped parts. Its purpose is to transfer shear loads (perpendicular to the axis of the bolts) or axial loads (parallel to the axis of the bolts) or a combination of both between the clamped parts by the use of a certain clamping force. The function of a bolt is to create and to maintain this clamping force with support of the nut (Bickford, 1995).

In dependence of the load direction the bolted joint either works as a form connection or a force connection fulfilling a different function. Axial loads are transferred via surface pressure within the contact areas of the joint members and either as tensile stress or pressure stress within the material of each part – the bolt works as a form connection. The function of the clamping load is to enable a load distribution between the bolt and the clamped parts. This is done by preloading the bolted joint as a serial connection of springs and then by loading the joint as a parallel connection of springs. Shear loads are transferred by friction between the clamped parts. The bolt has to provide the necessary normal force and hence the bolted joint works as a force connection. This necessary force is the installed clamping load (Haberhauer, et al., 2007).

To ensure the function of a bolted joint the correct magnitude and a proof of stability of the clamping force between the joint members have to be calculated – including the influence of operating conditions and other factors. For the calculation of a bolted joint with a single bolt guidelines are available¹⁶. Additionally

¹⁶ A straight forward calculation guideline for detailed general analytical calculation is provided here (VDI2230, 2003). Some general and many specific US calculation guidelines and additional information concerning bolted joints can be found in this book (Bickford, 1995).

analytic approaches for some basic multiple bolted joints are presented in (VDI2230, 2003) although numeric calculations should be the first choice for designing these complex joints (Wiegand, et al., 1988).

A basic tool to visualize the interaction of forces and elongations of the bolt and the clamped parts is the joint diagram. With the use of this tool external and internal influences of the bolted joint can be shown. These influences are the specific bolt tightening process, embedding and relaxation as well as the working load of the joint (VDI2230, 2003).

2.4.1 Joint diagram

The joint diagram has been developed to visualize the loads within a bolted connection. The characteristics of load deflection of the bolt and the clamped parts are displayed. Additionally the changes of both parameters due to internal and external influences are shown. The buildup of the joint diagram and the influencing factors is equal to the chronologic procedure of the assembly of the joint and its following use.

Subsequent to the assembly phase the bolted joint can be simplified into a technical system of two springs (bolt and clamped parts) in a parallel connection loaded with a force called assembly force. The magnitude of the assembly force is equally distributed between bolt and clamped parts (Wiegand, et al., 1988). The impact of the assembly force on the elongation of bolt and clamped parts is shown in Figure 2-8.

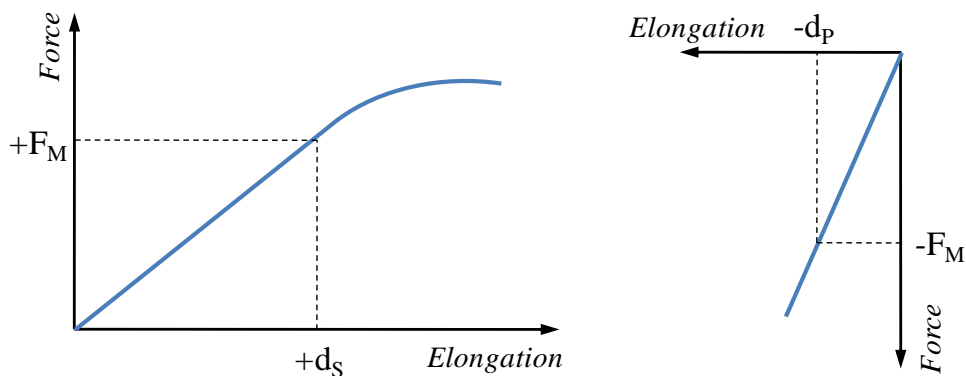


Figure 2-8: Schematic diagrams of force vs. elongation with markings for an assembly force F_M and the resulting elongations for a bolt (left) and for the clamped parts (right)

Due to the assembly force F_M^{17} - which is not identical to the residual clamping force at the end of the assembly process - the bolt is stretched by the amount d_S while the clamped parts are compressed by the amount d_P . Usually both amounts are not of the same magnitude which is a result of the different resiliencies of bolt and clamped parts.

Bolt and clamped parts form an interacting technical system. Hence it is advantageous to represent them in a single diagram. For this purpose the graph of the clamped parts is merged into the diagram of the bolt within two steps. First the graph is reflected along the elongation axis. In a second step the graph is moved along this axis until the points of intersection of assembly force and elongation of both graphs intersect. The result can be seen in Figure2-9 and is called basic joint diagram.

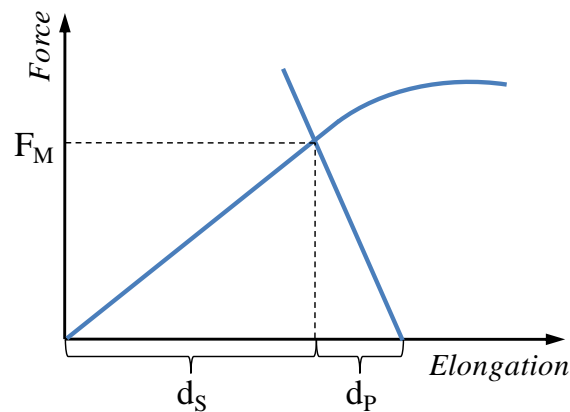


Figure2-9: Basic joint diagram (schematic) – derived from the diagrams of bolt and clamped parts

To install a specific preload to a bolted joint during assembly it is necessary to control the actual bolt load. Usually this cannot be done by direct load measurements. Instead other characteristic values are taken, e.g. applied torque, turned angle of nut or bolt head or bolt elongation. The specific preload is calculated from these characteristic values and additional parameters, like friction coefficient, Young modulus or material specific sonic speed. These additional parameters often have to be estimated. As a result the final assembly load of a certain bolted joint will differ from the ideal value.

¹⁷ The denomination is chosen according to the nomenclature of (VDI2230, 2003).

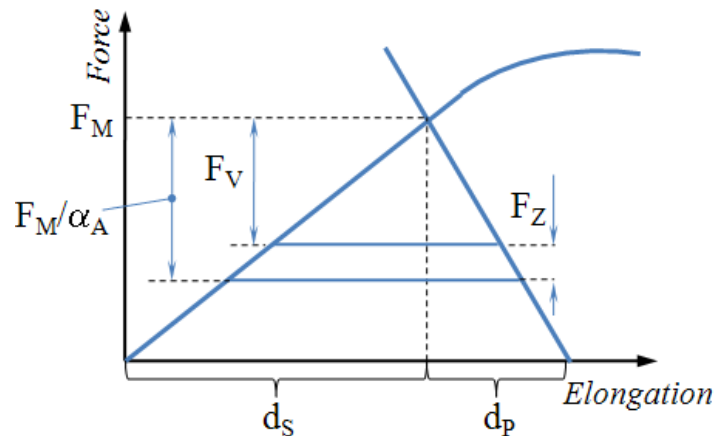


Figure 2-10: Enhanced joint diagram (schematic) including assembly load F_M , influence of application factor α_A , the derived preload F_V and the load loss by relaxation and embedment F_Z (based on (VDI2230, 2003))

The expected range of achievable preload is described by the application factor α_A ¹⁸. Besides the application factor relaxation loss and embedding have an impact on the preload and with it the clamping force (see Figure 2-10). In order to ensure the function of the bolted joint the amount of loss must be considered in the bolt calculation. Several factors have an increasing effect on embedding and relaxation. In the following section these factors will be described in detail.

2.4.2 Embedding

During assembly the surface roughness of the bolt head, the contact areas of the joint partners, the engaged thread and the nut is reduced. Due to the difference of microscopic and macroscopic contact area described in section 2.1.1.2 material creep appears at the surfaces between all contact partners in the bolted joint. This results in a loss of preload which is called embedding. During the assembly phase this loss is compensated by the continuous bolt engagement. Embedding reaches a saturation limit usually after about 24 hours. Embedding can be estimated in dependence of the roughness of each participating part¹⁹ or must be determined in tests. A typical value for the embedding loss of a bolt M8-8.8 with a clamping

¹⁸ A list of application factors for different methods of preload application and measurement can be found in (VDI2230, 2003).

¹⁹ see (VDI2230, 2003) table 5.4/1

length of 70mm (resilience of the bolt $7.5 \mu\text{m/kN}$) and two clamped parts with smooth surfaces is about $10\mu\text{m}$ or about 5% of the initial preload.

2.4.3 Relaxation of Bolted Joints

Furthermore in bolted joints which are engaged close to the yield strength limit or which are operated at moderately increased temperatures additional losses occur. These losses are the result of slow plastic deformations and material creep within the material of bolt, joint parts and nut. The amount of this creep depends on pressure, material (and material inhomogeneity), temperature and contact time and results in a time dependent conversion of elastic extension into plastic extension (Jähnliche, et al., 1950), (Pfützner, 1965), (Schmidt, et al., 1972). Though the preload is stored as elastic extension of the bolt this conversion represents a preload loss (Granacher, et al., 1994). After assembly this conversion is no longer compensated by the bolt engagement and hence leads to a permanent decrease of the preload over time. This kind of preload loss is called relaxation. Unlike embedding the amount of relaxation loss cannot be calculated and thus can only be determined by experiments (Strelow, 1983), (Wiegand, et al., 1988), (Beelich, et al., 1968). The relaxation loss at 20°C for a bolt M8 with a clamping length of about 70mm ranges from 5% to 12% of the initial preload (Granacher, et al., 1994), (Köhler, et al., 1991).

In the relaxation mechanism contact pressure is the driving force. It generates stress within the material that leads to plastic deformations. The amount of necessary pressure to start these deformations depends on the properties of the stressed material. The higher the materials yield stress the more pressure is needed.

There are a number of factors that support the mechanism of relaxation (Bickford, 1995):

- **Poor thread engagement:**
Both threads of a bolted joint share the same nominal value, but are located diametrically at the allowed tolerance range in a way that the effective bolt thread diameter is smaller than the effective nut thread diameter. In this situation, the effective contact area is comparably small. This results in a higher surface pressure in this area which has an increasing effect on relaxation.
- **Soft materials:**
Relaxation loss is likely to appear or is increased when the yield strength of one or more parts of a bolted joint is distinctly lower in comparison to that of other parts. This may occur in intended combinations of hard and soft materials, e.g. steel and aluminum, as well as in unintended combinations, such as steel with a poor heat treatment in combination with a well

treated steel.

- **Bending of the bolt:**
The occurrence of bending load leads to an increase of the surface pressure within those parts of the thread that are loaded with additional bending tension. A bending load of the bolt either results from external loads (bending based working load with u-shaped bending or shear based working load with s-shaped bending) or from a geometrical deviation (bad design or poor assembly leading to non perpendicular nut and bolt head causing s-shaped bending).
- **Improper bore sizes:**
Embedment and relaxation are increased when the contact area of the bolt head or the nut is much smaller than intended (see Figure 2-11). This happens when the bore is either too small or too large. In both cases the actual surface pressure exceeds the intended surface pressure which leads to an unintended additional relaxation loss.

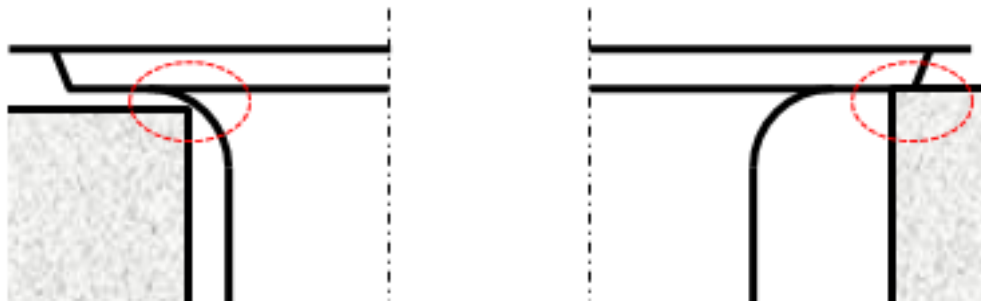


Figure 2-11: Examples for improper bore sizes (left: bore too small; right: bore too large)

In multi-bolt joints the change of the clamping load is not only due to relaxation, but also to elastic interaction between the bolts. These interactions are likely to happen, especially when the joint members are distinctly stiffer than the bolts. The interactions appear as a decrease in clamping load of the already engaged bolts during the assembly of a further bolt. The additional clamping load delivered by assembling a further bolt, supports the total clamping pressure of all other bolts. This leads to a partial relieve of the already engaged bolts (Bickford, 1995).

When the embedment and relaxation behavior of a bolted joint is to be investigated all the named factors have to be considered in the setup of the experiment.

Besides these mechanical influences, temperature plays a major role on the occurrence and amount of relaxation. The following section will deal with this fact in detail.

2.4.4 Effect of Temperature on Relaxation

The impact of temperature onto the properties of materials, e.g. the magnitude of yield stress and Young modulus, is well known (Keil, et al., 1972). These material properties play a major role in the mechanisms of embedment and relaxation. With surrounding temperatures of an internal combustion engine of about 150°C, temperature will have a significant effect on the relaxation of the bolted joints of a con-rod. This temperature will be referred to as operating temperature (of the con-rod).

In a bolted joint the functionally vital clamping load is provided by the elongation of the bolt and the pressure of the clamped parts. Due to the reduction of magnitudes of yield stress and young modulus with increasing temperature the permissible stress decreases²⁰. As a result relaxation appears (VDEh, 1989).

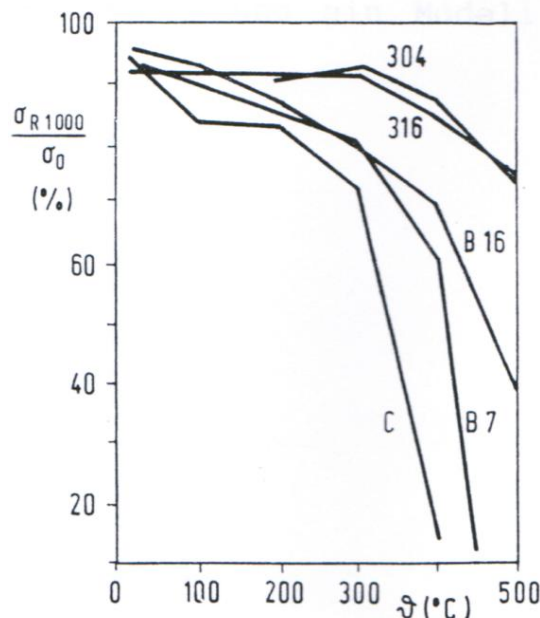


Figure 2-12: Relaxation of bolts of different materials after 1000h for different temperatures (C: non-alloy steel, B7: CrMo steel, B16: CrMoV steel, 304: 18Cr8Ni steel, 316: 16Cr13Ni2Mo steel) (taken from (Sachs, et al., 1973))

The relaxation of bolted joints at moderately increased temperature was subject of several studies. In most studies relaxation was analyzed for temperatures of 300°C

²⁰ The level of permissible stress depends on material and temperature and is usually distinctly lower than the yield strength.

or higher, due to the large impact of creep at this temperature level. The tests showed that, depending on the material, the relaxation loss ranges from 10% up to 60% of the initial preload at a temperature of 300°C (Strelow, 1983), (Köhler, et al., 1991), (Sachs, et al., 1973), (Beelich, 1970). Figure 2-12 shows an excerpt of the results of (Sachs, et al., 1973).

Additionally, these results suggest that relaxation is already highly affected at temperatures below 300°C. This was taken up by (Granacher, et al., 1994), who investigated the relaxation of bolted joints at a temperature range of 20°C to 300°C. The tests with yield-controlled tightened bolted joints show relaxation losses of 12% up to 20% of the initial preload at 160°C. These results are shown in Figure 2-13.

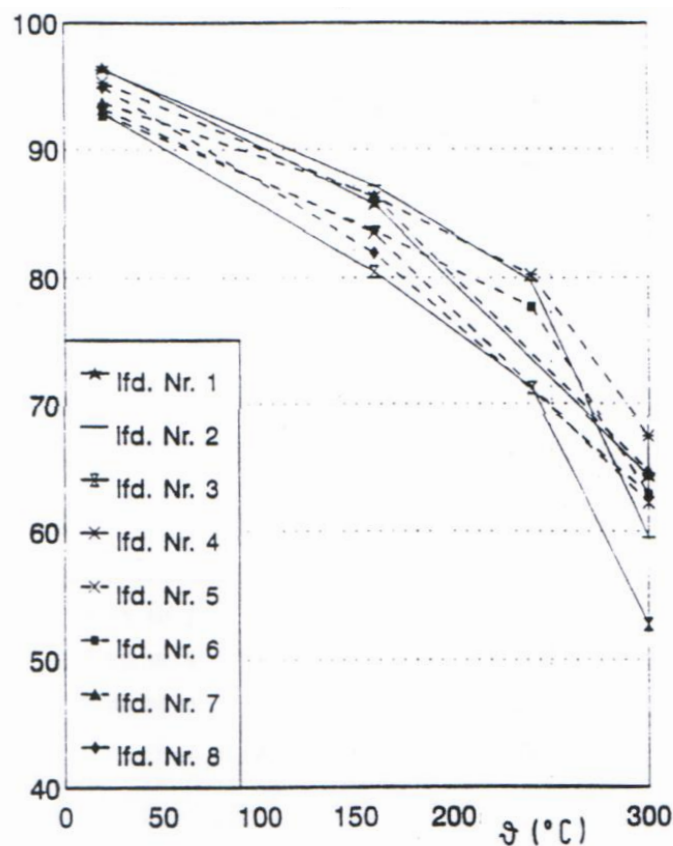


Figure 2-13: Ratio of remaining clamping load and initial preload for yield-controlled tightened bolted joints after 300h relaxation for different temperatures (taken from (Granacher, et al., 1994))

Furthermore, thermal expansion of a bolted joint during the phase of temperature increase is often a very dynamic process with different expansion speeds for the involved parts. Some parts are more exposed to a temperature source than others, and expand faster. As a result, different thermal elongations are added to the mechanical elongations of the parts involved. In case the thermal elongation of parts

under pressure is higher than of parts under tension, the overall load is increased and leads to additional relaxation loss or even plastic deformation. In case the thermal elongation is distributed the other way around, the overall load is decreased. This results in a decrease of the clamping load and may end up in a failure of the bolted joint (Wiegand, et al., 1988).

2.4.5 Conclusions

Forces, stresses and elongations of a bolted joint can be calculated analytically with the help of current guidelines like (VDI2230, 2003) as long as the joint only contains one bolt. For the calculation of multiple bolts, numerical calculation methods like FEM are required. A useful tool to visualize forces and elongations in a bolted joint is the joint diagram.

The loss of preload in a bolted joint over time is classified into two types. Both are a consequence of material creep in the bolted joint. Creep at the surface of parts does always occur and is called embedding. High stresses additionally lead to creep inside the material, which is called relaxation. Typical relaxation losses have a magnitude of up to 10% of the initial preload. Moderately increased temperatures (up to 150°C) increase relaxation losses up to 20% of the initial preload. In addition, deviations of geometry and material properties can increase relaxation. All these factors have to be taken into account when analyzing and predicting the behavior of bolted joints.

2.5 Connecting Rods

This section deals with the actual state of knowledge about con-rods. First the function and the geometry of con-rods are described. Then typical materials and production processes are introduced. Finally, the state of the art of cracked connecting rods is presented.

2.5.1 Function and Geometry of Connecting Rods

Connecting rods (con-rods) are used in combustions engines to transmit the translational movement of the piston and the oscillating force of inertia of the driving mechanism onto the rotating crankshaft (Köhler, et al., 2006).

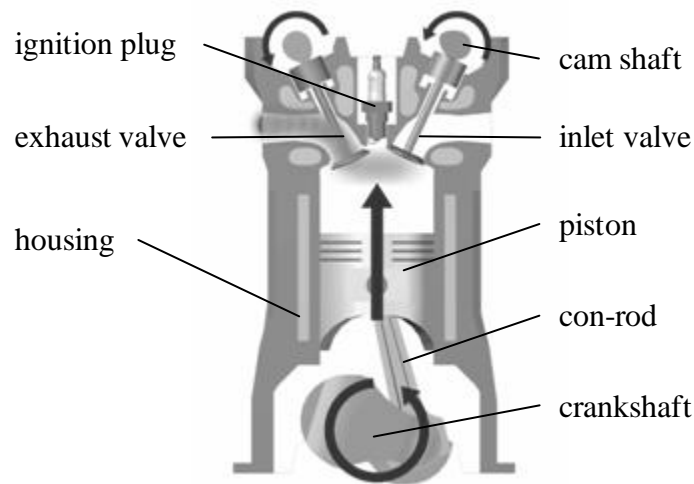


Figure 2-14: Position and function of a con-rod in a four stroke combustion engine

In Figure 2-14 the position of a con-rod in a four stroke combustion engine as well as its transmitting function between piston and crankshaft is shown. Usually the crankshaft is casted or forged as a single part. As a result the con-rod needs to consist of at least two parts to get assembled to the crankshaft (Köhler, et al., 2006).

The function of the con-rod determines the requirements regarding shape and dimensioning shown in Figure 2-15 (Köhler, et al., 2006). The shape of a con-rod is determined by the stresses due to the combustion pressure and the oscillation force of inertia. Hence a con-rod needs to be stiff enough to resist the bending stresses that result from the transmission of translational movement of the piston into rotational movement of the crankshaft. To meet this requirement the con-rod shank usually has an I-beam shape normal to the crankshaft axis²¹.

Furthermore, it needs to provide enough contact area in order to prevent plastic deformation of the bearings at the connection to the piston (small con-rod eye) and to the crankshaft (big con-rod eye). The bushing for the piston pin is fixed by means of a press fit in the small con-rod eye. As mentioned above, the big con-rod eye is split to enable the assembly of the con-rod to the crankshaft. As a result the bearing located in the big eye for the connection with the crankshaft is a bipartite bearing. The bipartite bearings are slightly bigger than the big eye and fixed by a

²¹ In high performance engines (e.g. racing cars) the con-rod shank is H-shaped. This shape has advantages regarding to weight and stiffness but is more costly in production (Urlaub, 1995).

clamping force provided by the con-rod bolts. Therefore, the con-rod bolts have two functions, connecting con-rod cap and con-rod body, as well as fixing the bipartite plain bearing. The parting line of the big con-rod eye is usually located horizontally (see Figure 2-15 left). In case of a large crankshaft diameter the parting line is turned 40° counter clockwise²² (see Figure 2-15 right). Finally, the con-rod needs to be as light as possible to keep the load of the oscillating force at a low level.

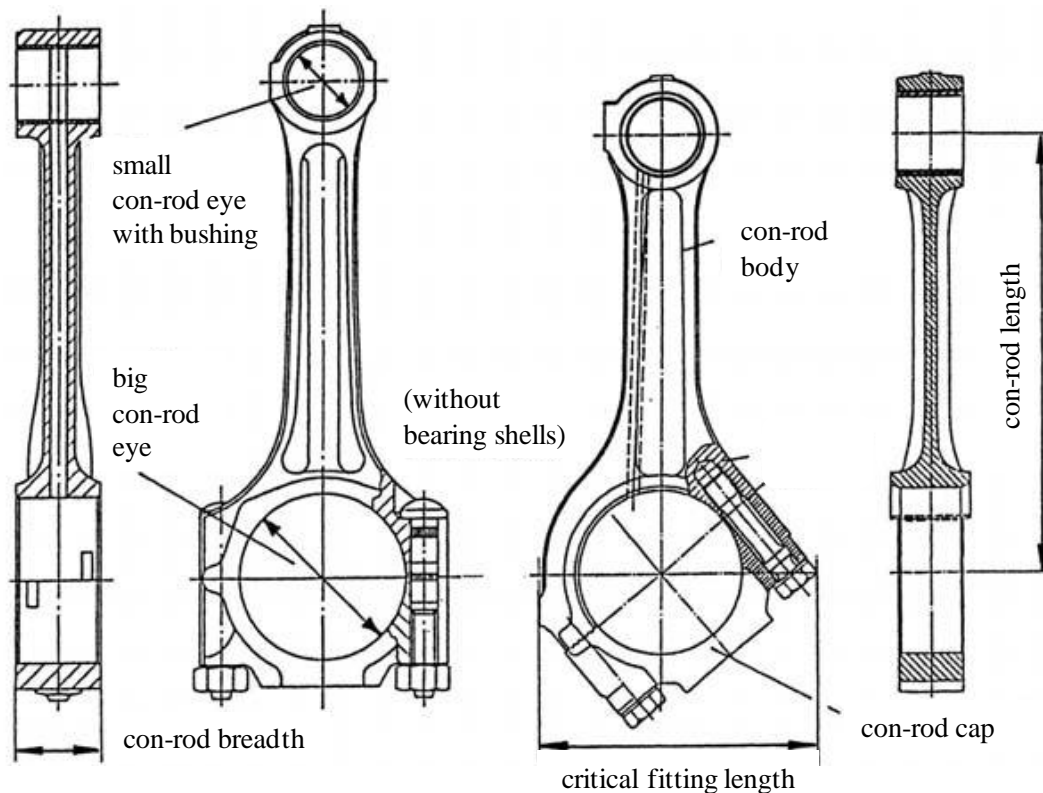


Figure 2-15: Straight split con-rod (left) and angular split con-rod (right) with the most important length specifications (taken from (Köhler, et al., 2006))

²² The con-rod must be passed through the cylinder to be mounted to the crankshaft. When the big con-rod eye has a large diameter there is no space for two bolts besides the big eye within the cylinder. As a result, the position of the bolts is adjusted by turning the parting line.

2.5.2 Materials and Production Processes of Connecting Rods

Today the manufacture of the raw part of a con-rod is realized by one of three basic shaping processes: casting, sintering and forging²³. Each primary shaping process is connected to a different kind of con-rod material.

Typical casting materials for con-rods are spheroidal graphite cast iron (for example EN-GJS-700-2) and black heart malleable cast iron (e.g. EN-GJMB-700-02). Casted con-rods can usually be found in large diesel engines for trucks or ships (Schäfer, et al., 2010).

Typical metal powders for sintering are Sint F30 and Sint F31 (Schäfer, et al., 2010). The forging is a fairly expensive production step in the sintering process. For that reason several research projects have been carried out to develop new technologies to either avoid this production step or cut down the overall costs (Reppen, 1998), (Hoffmann, et al., 2002), (Afazal, et al., 2004).

The choice of material used for forged con-rods depends on the final manufacturing process of the con-rod, see below. For the conventional manufacturing process the con-rods were made of micro alloy steel like 27MnVS6 BY or C40mod BY (Schäfer, et al., 2010). For the novel manufacturing process the con-rods are made of C70 S6 BY or 36MnVS4. High performance con-rods are made of 34CrNiMo6 V which needs additional heat treatment after the forging process (Kuratomi, et al., 1995),(Wegener, 1998). After the raw part is produced, additional machining is necessary to bring the con-rod into its final shape with the required dimensions and functions. Here one can distinguish between conventional machining and the new process based on fracture splitting, as illustrated in Figure 2-16.

²³ Sintered con-rods are common in the US, while forged con-rods are predominantly produced in Europe and Japan.

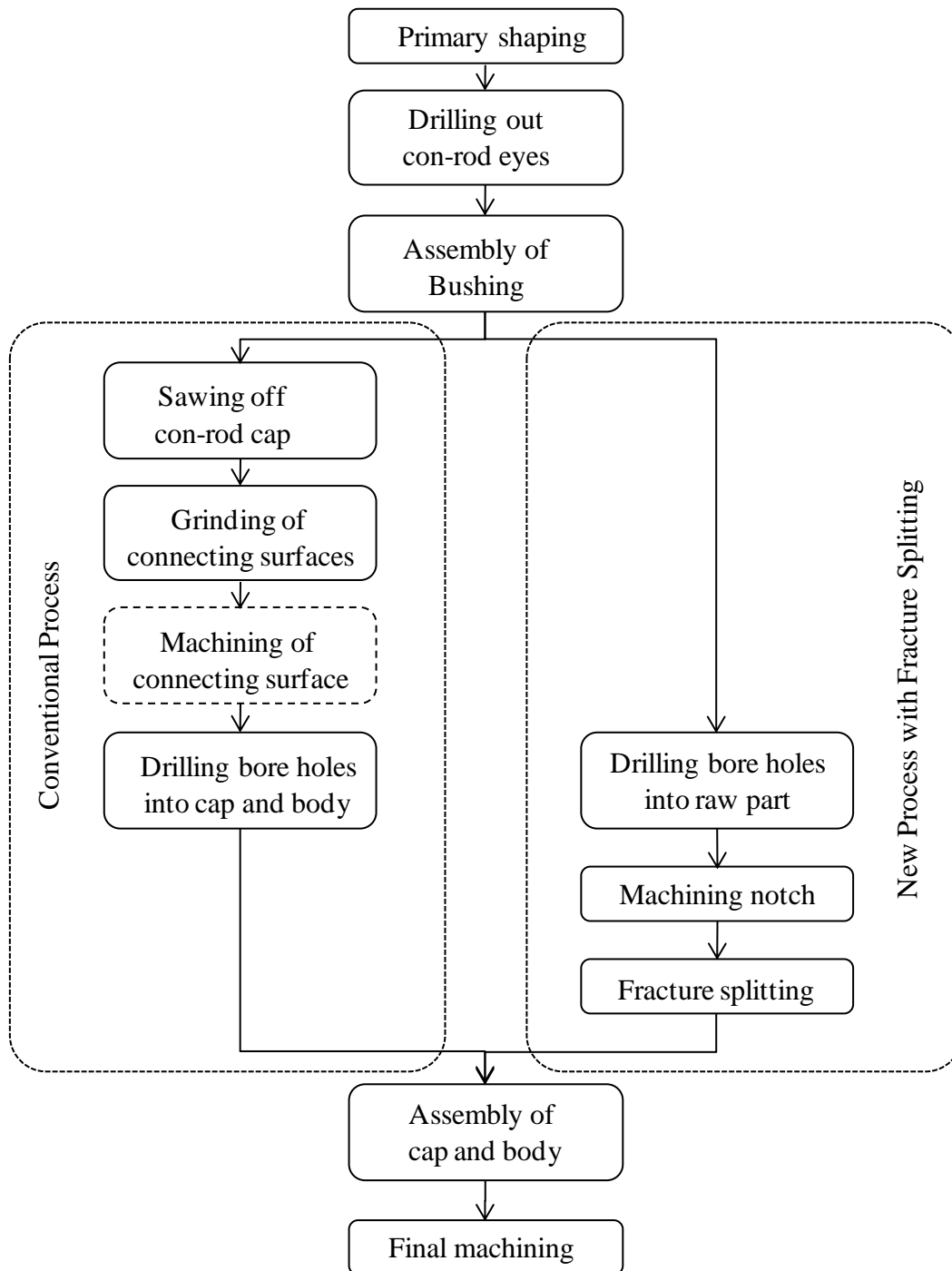


Figure 2-16: Comparison of the process steps for con-rod production
(based on (Blauel, et al., 2000))

The conventional manufacturing process starts with drilling out both con-rod eyes followed by the assembly of the bushing into the small con-rod eye. After that the con-rod cap is sawn off the con-rod body and the occurring connection surfaces

are grinded. When the positioning of con-rod cap and body is realized by pins or a serration the correspondent machining process takes place. In case of the use of fitting bolts this manufacturing step can be skipped. Then bore holes for the con-rod bolts are drilled and con-rod cap and body are bolted. In the next step the bore of the big con-rod eye and all adjacent surfaces have to be machined until the final dimensions have been reached (Ohrnberger, et al., 1992), (Urlaub, 1995).

In this conventional process the machining procedure after the sawing of con-rod cap and body is very costly. To cut down these costs a new manufacturing process was (re-)invented²⁴ in the late 1980's and developed to the maturity phase around the turn of the century – the so called fracture splitting process (Blauel, et al., 2000). This new process starts with drilling out both con-rod eyes followed by the assembly of the bushing into the small con-rod eye. Then the bore holes for the bolts are drilled. After that a new production step is added – the notch manufacturing. The notch is necessary for the subsequently performed selective fracture splitting of con-rod cap and body. Though cap and body break off basically in a brittle manner, the fractured surfaces of cap and body fit perfectly. As a result, the connecting surfaces do not need additional machining. The last step is machining the con-rod to the final dimensions (Blauel, et al., 2000), (Lyszczan, 2005).

2.5.3 Development of Cracked Connecting Rods

The development of cracked con-rods started in the late 1980's with the patent application of devices for the cracking process like shown in Figure 2-17 (Fetouh, 1986), (Brovold, 1988).

²⁴ Fracture splitting was a production process used in the late 19th century for manufacturing large drive wheels used in water mills and other historic facilities containing large transmission shafts (Hoenow, et al., 2008)

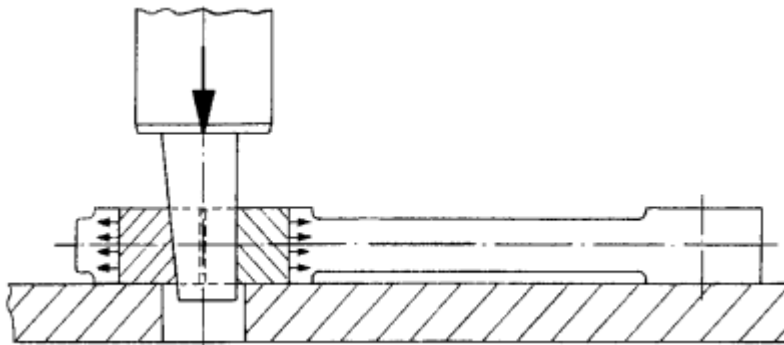


Figure 2-17: Principle of fracture splitting con-rods with a wedge
(taken from (Ohrnberger, et al., 1992))

Due to the high ductility of the materials used for forged steels at that time only con-rods made of brittle materials like cast steel and powder metal were used for this process. In the early 1990's the process of fracture splitting already reached production maturity for casted and sintered con-rods. The most important process parameters have been identified and their impact onto the fracture splitting process has been studied (Ohrnberger, et al., 1992):

- **Brittleness of the material:**
The more brittle the material, the less unwanted plastic deformations of the con-rod during the fracture splitting process.
- **Temperature of the material:**
The lower the temperature, the more brittle the material and the better the ability to be fracture split without plastic deformations.
- **Fracture speed:**
For each kind of material a specific fracture speeds must be applied in order to gain good fracture splitting results without plastic deformations.
- **Direction of initial fracture force:**
The direction of the initial fracture force should be oriented normal to the direction of the desired crack growth to use velocity-embrittlement effects.
- **Shape of the notch:**
The shape of the notch influences the tracking stability of the crack growth; the more instable the crack growth, the higher the possibility of the occurrence of particle break-outs.

(Ohrnberger, et al., 1992) also summarizes studies investigating the applicability of different kinds of cast steel and sintered steel on the fracture splitting process..

Up to this point the focus of research concerning fracture splitting was primarily on the process. On the material side, studies mainly aimed at surveying the suitability of existing materials.. Due to the level of maturity of the fracture splitting process, in the beginning of the 1990's performance and productivity became

more important. The limitations of cast steel regarding maximum strength and the comparably high costs of sintered steel lead to research for new materials that are usable in the fracture splitting process. A very promising way to gain both more performance and more productivity was the development of new micro alloyed forgeable steels like C70S6BY and 49MnVS3 (Olaniran, et al., 1993), (Kuratomi, et al., 1995).

By the turn of the millennium the fracture splitting process using forgeable steels were established and widely introduced in the production of automotives. Furthermore, the mechanisms of the fracture splitting process were known:

- The con-rods break one-sided, even under abrupt loading. Due to the fast crack growth, the fracture energy only depends on the initial impulse of the wedge (see Figure 2-17). As a result, the first crack is formed by pure normal load. When this side of the big con-rod eye is broken, dynamic recovery impulses appear. As a result, the wedge is able to load the con-rod with additional energy and the con-rod cap breaks off at the other side due to bending load (Blauel, et al., 2000).
- The crack grows from the notch to the outside of the con-rod. In that way the crack must grow around the bolt hole. As a result the crack splits up into two growing cracks that travel around the bolt hole. During this phase every small deflection of the cap or the con-rod body has an impact on the direction of the crack growth. This impact usually takes place during the breaking process of the second con-rod flange under bending load. The impact leads to additional torsion loading which results in a helical growth of both cracks around the bolt hole, thus no longer sharing the same horizontal level anymore. They unite again by forming small vertical crack paths. Consequently, steps or particle breakouts appear (see Figure 2-18) (Blauel, et al., 2000).

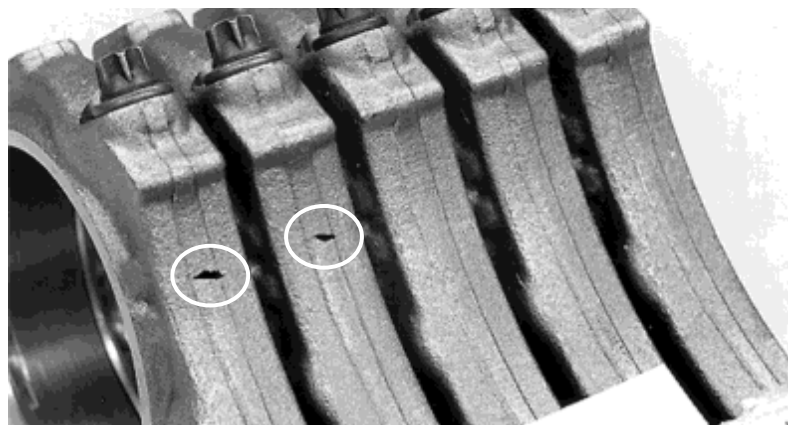


Figure 2-18: Con-rods with breakouts (see markings) (taken from (Blauel, et al., 2000))

Further investigations of cracked connecting rods aimed either at enhancing the production process (Knoll, et al., 2001), (Guigis, et al., 2002), (Kubota, et al., 2005) or at the development of new materials (Hoffmann, et al., 2002), (Afazal, et al., 2004), (Kato, et al., 2007). The mechanical behavior of bolted joints with fractured surfaces has not been investigated yet.

2.6 Parameters of Surface Roughness

The surface roughness and related parameters were described in several national, regional and international standards e.g. DIN 4762²⁵. During a worldwide revision of standards of the appearance of products in 1995, the geometric product specification – short GPS– was defined²⁶. This meta-standard consists of a number of standards which define and describe the dimensions, spatial orientation, tolerances, surface texture and other spatial parameters of a product.

For the description of the surface texture of a product the following standards exist:

- ISO 3274 – Version 1998:
In this standard profiles and the general layout of stylus instruments are defined. Especially the definition of profiles is of interest for the research described in this dissertation (ISO3274, 1998).
- ISO 4287 – Version 2010:
This standard contains definitions and parameters to describe the surface texture measured by a stylus instrument (ISO4287, 2010).
- ISO 4288 – Version 1998:
This standard establishes rules for the comparison of measurement data and tolerance limits, as well as surface parameters defined in ISO 4287. Furthermore, the critical wavelength for the measurement of parameters defined in ISO 4287 performed with stylus instruments as described in ISO 3274 is defined (ISO4288, 1998).
- ISO 11562 – Version 1998:
In this standard the process of phase accurate filtering of the measurement data of surface profiles is defined, specially the separation of long-wave and short-wave fractions (ISO11562, 1998).

²⁵ (DIN4762, 1984) – this standard had been withdrawn

²⁶ see (ISO/TR14638, 1995) for details

The texture of a surface is defined as a superposition of unevenness with different wave lengths as shown in Figure 2-19.

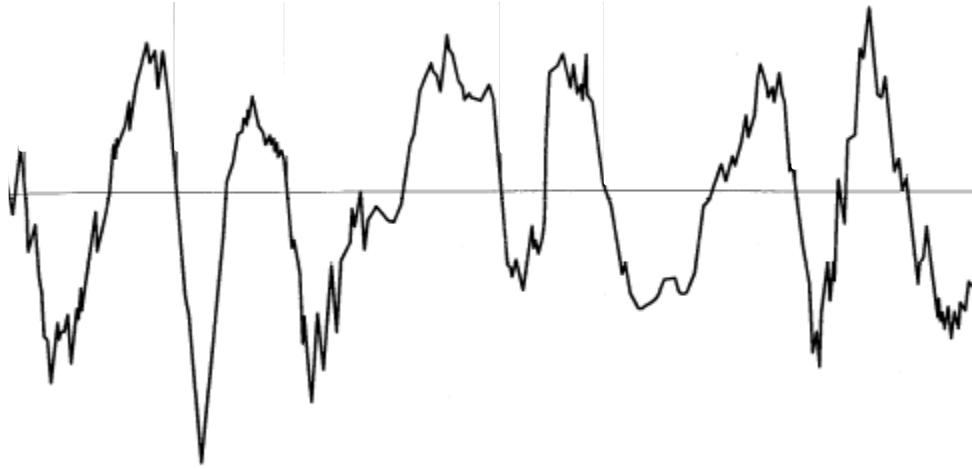


Figure 2-19: Texture of a surface containing unevenness of different scales (taken from (ISO4287, 2010))

The aim of the surface texture related standards in GPS is to disentangle the different wavelengths through filtering, to enable a proper description of the surface at different scales or, rather, wavelength intervals (see Figure 2-20).

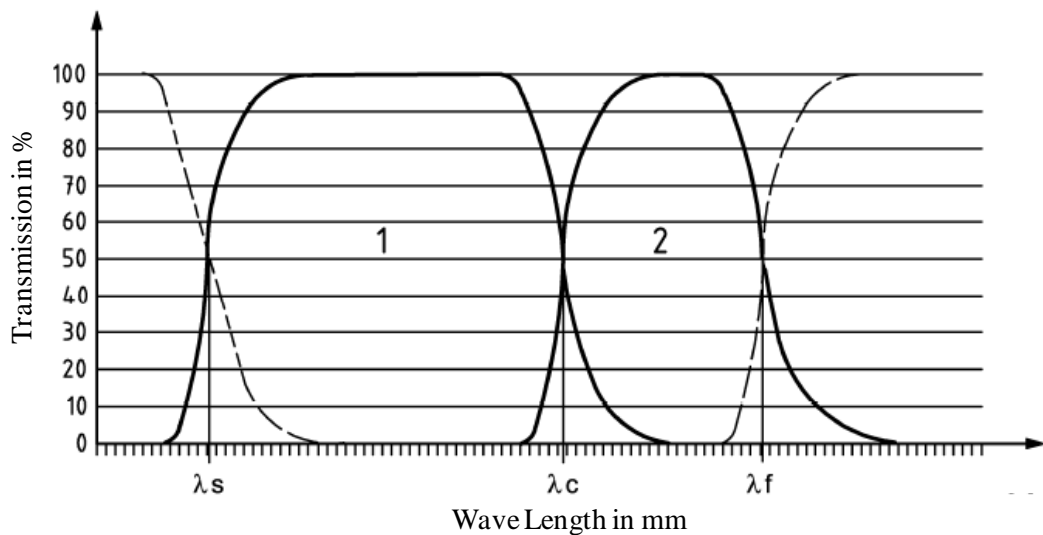


Figure 2-20: Transmission characteristic of the roughness profile (interval 1) and wave profile (interval 2) (based on (ISO4287, 2010))

In (ISO4278, 2010) the real profile is separated into four intervals of different wave lengths called profile filters²⁷:

- λ_s – profile filter:
Filter that defines the intersection between roughness and an interval with shorter wave lengths (such as noise). The primary profile is obtained by using the λ_s filter with the real surface profile.
- λ_c – profile filter:
Filter that defines the intersection of roughness and waviness. The roughness profile is obtained by using the λ_c filter with the primary profile.
- λ_f – profile filter:
Filter that defines the intersection of waviness and an interval with longer wave lengths. The waviness profile is obtained by using the λ_f filter with the roughness profile.

Based on the three types of profile levels (primary, roughness and waviness) a set of geometric parameters is defined in (ISO4287, 2010). These parameters are, for example, the location of the center line of each profile level, the length of measurement distances, local and global maxima and minima²⁸ (peaks and valleys) of the measured profile, and gradients of measurement data. These parameters are the foundation for the calculation of surface parameters: the amplitude parameters, the distance parameters and the characteristic graphs.

The class of amplitude parameters contains surface parameters such as greatest local peak, greatest global peak (roughness R_z) and average peak height (average roughness R_a). The distance parameters are the average groove width of the profile elements and the peak counter. The characteristic graphs are: material fraction of the profile, material fraction curve²⁹, relative material fraction, and amplitude density curve.

All parameters are calculated based on measurement data obtained by a surface profile scan with a scanning device³⁰. The necessary measurement length of the

²⁷ see (ISO11562, 1998) for further information concerning filtering

²⁸ A local peak is defined as the area of a profile between a positive and a negative profile gradient. A global peak is the distance between the deepest and the highest points of a measured profile.

²⁹ also known as Abbot-Firestone-Curve

³⁰ see (ISO3274, 1998)

scanning procedure depends on the expected roughness or waviness size. For the determination of roughness parameters the measurement length is defined in (ISO4288, 1998). The measurement length for the determination of waviness parameters is not established in a standard.

There is neither a topology parameter nor measurement procedure available for the description of very rough surfaces with a limited measurement length.

2.7 Conclusions

In this section, the knowledge obtained from the literature is used to address the research questions formulated in Section 1.2, in order to identify knowledge gaps and the need for additional research.

Research question (1):

What are suitable parameters to describe different fractured surfaces?

In ISO 4287 different levels of surface texture are defined along with a set of surface parameters. The roughness parameters are measured depending on a characteristic length which, in turn, depends on the maximum level of the expected surface roughness. Promising surface parameters are the maximum roughness R_{\max} , the average roughness R_a and the Abbot-Firestone-Curve.

The available measurement length of a fractured surface of a con-rod is much shorter than the necessary measurement length based on the characteristic length. Due to the dependency of the surface parameters on the characteristic length, there are no suitable surface parameters available for the characterization of the topology of fractured surfaces. A set of applicable parameters has to be determined.

Research question (2):

What is the impact of fractured surfaces on the relaxation of bolted joints?

The bolted joint with a single bolt and plain contact surfaces can be calculated very precisely in an analytical way. Being an important part of the bolt calculation, the process of preload loss is very well known. Preload loss takes place due to embedding and relaxation. Embedding is a process of preload loss by flattening of surface roughness of the contact surfaces of a bolted joint. The impact of embedding can be estimated in dependency of the surface roughness of all involved contact surfaces for a defined range of roughness. Often the preload loss due to embedding is less than 1% of the initial preload at room temperature (22°C). Relaxation is the process of creep within the material of the bolted joint due to high stresses or due to high temperature. If relaxation takes place, the exact amount of preload loss cannot be calculated and must be determined by experiments. Generally, the amount of preload loss due to relaxation has much more impact than the

preload loss due to embedding. Usually this amount has a magnitude of about 5% of the initial preload at room temperature (22°C).

There is no information about the characteristic surface roughness of fractured surfaces. Furthermore, a fractured surface cannot be treated and described like a surface with the common definition of roughness. For this reason the preload loss of a bolted joint with fractured surfaces cannot be estimated using current knowledge available and needs to be determined through experiments.

Research question (3):

What is the relation between surface topology and the amount of relaxation losses?

A suitable parameter to describe characteristic surface topology of a plain surface is the roughness R_z and the average Roughness R_c . In a bolted joint with common contact surfaces, relaxation losses increase linearly with increasing surface roughness.

The necessary surface parameters cannot be determined according to the related standard (ISO4287, 2010). As a result there are no parameters available that describe the characteristic surface topology of fractured surfaces. A relation between surface topology and relaxation loss of bolted joints with fractured surfaces cannot be estimated and needs to be determined experimentally.

Research question (4):

What is the effect of moderately increased temperature on the amount of relaxation losses?

A moderately increased temperature significantly decreases the stress level at which material creep starts. In a bolted joint with plain contact surfaces, this results in increased preload losses due to relaxation. Investigations show that an ambient temperature of 150°C increases the amount of relaxation losses in a bolted joint up to 20% of the initial preload.

The preload loss due to relaxation at this temperature of a bolted joint with a *fractured* contact surface can hardly be estimated. This is mainly due to the unknown amount of creep within the fractured surface. The effect of a moderately increased temperature of 150°C on the amount of relaxation loss needs to be determined.

Research question (5):

What are suitable parameters to describe different fractured surfaces?

In a bolted joint the relation of clamping force and transferrable shear load of a pair of plain contact surfaces can be estimated using the friction coefficient μ . The

magnitude of the friction coefficient is independent of the magnitude of the clamping force. Therefore, an increasing clamping force results in a proportional increase in transferrable shear load.

In a bolted joint with fractured contact surfaces, the transferrable shear load is unknown. The impact of the clamping force in such a connection needs to be determined.

Research question (6):

What is the relation between surface topology and transferrable shear load?

The magnitude of the friction coefficient μ depends on the materials of the contact surfaces, the contact time, and the ambient temperature. The surface roughness of a pair of common plain surfaces with randomly distributed microscopic surface peaks and valleys has no impact on the magnitude of μ . Estimated values for the friction coefficient μ of some common material combinations are available. Furthermore, the friction coefficient of a certain scale includes all friction coefficients of smaller scales and thus becomes an effective friction coefficient. The friction coefficient needs to be determined by experiments.

The surface roughness of a pair of fractured surfaces is in all probability not comparable with the surface roughness of common plain surfaces. A relation between the surface topology and the friction coefficient cannot be excluded. Furthermore, no knowledge or estimates exist concerning the magnitude of a friction coefficient of fractured surfaces. As a result the friction coefficient in a connection with fractured surfaces needs to be determined.

Research question (7):

What is the effect of moderately increased temperature on the maximum transferable shear load?

A moderate increase of the ambient temperature to 150°C decreases the strength of standard bolt steel slightly. The friction coefficient is not influenced by an ambient temperature of about 150°C. This results in a slight decrease of the transferable shear load.

It can be expected that the transferrable shear load in a bolted joint with fractured surfaces is slightly decreased at a moderately increased temperature of 150°C in comparison to room temperature. This expectation needs to be proven experimentally.

Research question (8):

What is the relation between surface topology and transferrable shear load?

The shear load transfer in a bolted joint with fractured surfaces has not been subject to any investigations so far. It is expected that the shear load transfer is either friction based or shape based or a combination of both. A friction based force transfer in a common force connection can be calculated using Amontons law³¹. In case the contact surfaces are fitting accurately a non-negligible adhesive contact force may be added depending on the force directions. A shape based force transfer in a form connection is usually calculated with respect to the maximum permissible surface pressure or the maximum permissible shear stress³². For a connection with mixed force transfer there are two ways of calculation. One way is to determine which working principle is predominant and to base the calculation on this working principle, leaving the other working principle as a safety factor. The other way is to determine the transferable shear load experimentally.

In a bolted joint with fractured surfaces no working principle is predominant. Consequently, a closer experimental investigation is needed to describe the interaction of both working principles.

³¹ See section 2.1.1

³² See section 2.2

3 Cracked Connecting Rods

The past and recent research in the field of fracture splitted con-rods focused on the development of new and advanced production processes and materials. Fractured surfaces have been subject of investigations in materials science in terms of fracture behavior and appraisal of fracture growth within cyclic loaded components (Fuhrmann, 2003), (Gross, et al., 2007), (Weißbach, 2007). In the literature no mentioning is made of investigations into the influence of the fractured surface on the mechanical properties and characteristics of a con-rod.

A number of engine failures occurred shortly after the introduction of the fracture splitting process. The engine failures have been traced back to the self loosening of the con-rod bolts. The investigations to identify the source of this phenomenon have been executed by the author in the FVV project “Self loosening of Bolts” in the period of 2004 – 2007 (Lyszczan, et al., 2007). During these investigations basic knowledge was collected about fractured surfaces used as mating surfaces in a joint. This knowledge is the basis for the research as described in this dissertation.

3.1 Self Loosening of Bolts

As mentioned earlier, during the introduction of connecting-rod production using fracture splitting, the con-rod bolts were found to unscrew occasionally. Processes based on conventional machining produce flat surfaces that need careful alignment for mating, whereas fracture splitting creates mating surfaces which align perfectly. The FVV project “Self Loosening of Bolts” aimed to identify the causes of the unscrewing process in this environment by numerical and experimental studies (Lyszczan, et al., 2007).

The numerical studies were primarily based on a detailed half-symmetry model of a connecting-rod. This model was used for the calculation and visualization of internal stresses and deformations. On the one hand, these results were used for the preparation of the experiments. On the other hand, they were useful for identifying parameters which have an impact on the self-loosening process. Furthermore, a full structure model of a simple joint with one cylindrical bolt was used for numerical simulations of the self-loosening process.

The experimental studies included fatigue testing of connecting rods and topographic investigations of the fractured surfaces of con-rods. A series of parameters had been identified which were assumed to have an impact on the self-loosening process. These parameters were varied one by one and in small parameter groups to determine limiting values and identify possible dependencies between the parameters. A special test rig had been developed, which uses the eigenfrequency of the framework to load the specimen. The topographical investigations were used

to estimate and explain the influences of the fractured surface on the bolted connection.

The self-loosening process was driven by a combination of a massive loss of the clamping force of the bolted connection, the magnitude and direction of the external forces, and the geometric properties of the con-rod. As a cause for the massive loss of clamping force at operating temperature (about 70% loss at 150°C) large particles (about 2mm in diameter) were identified in the mating surfaces. These particles were remainders of the fracture splitting process, which had not been removed by the cleaning mechanism (air blast cleaning).

The following section provides detailed information about the results of the topographical investigations of the fractured surfaces, which are relevant for the research described in this dissertation.

3.2 Topographical Investigations of Fractured Surfaces

In a first step, a number of methods have been reviewed to describe the character of a fractured surface and to estimate the fitting accuracy of a pair of fractured surfaces (Lyszczan, et al., 2005). The aims of these investigations were to determine the most suitable measurement and analysis methods for these investigations, as well as to build up a model of a fractured surface to enable a deeper understanding of its possible influence on the mechanical properties of the con-rod and the con-rod bolting.

3.2.1 Character of a Fractured Surface

For the determination of the surface character, the fractured surfaces have been examined with a binocular loupe and with a scanning electron microscope (SEM). The examinations with the binocular loupe revealed that there were particles and particle tracks on the fractured surfaces, in the form of imprints (see Figure 3-1). Furthermore, indications of cracks of different sizes within the fractured surfaces were found (Lyszczan, et al., 2007).

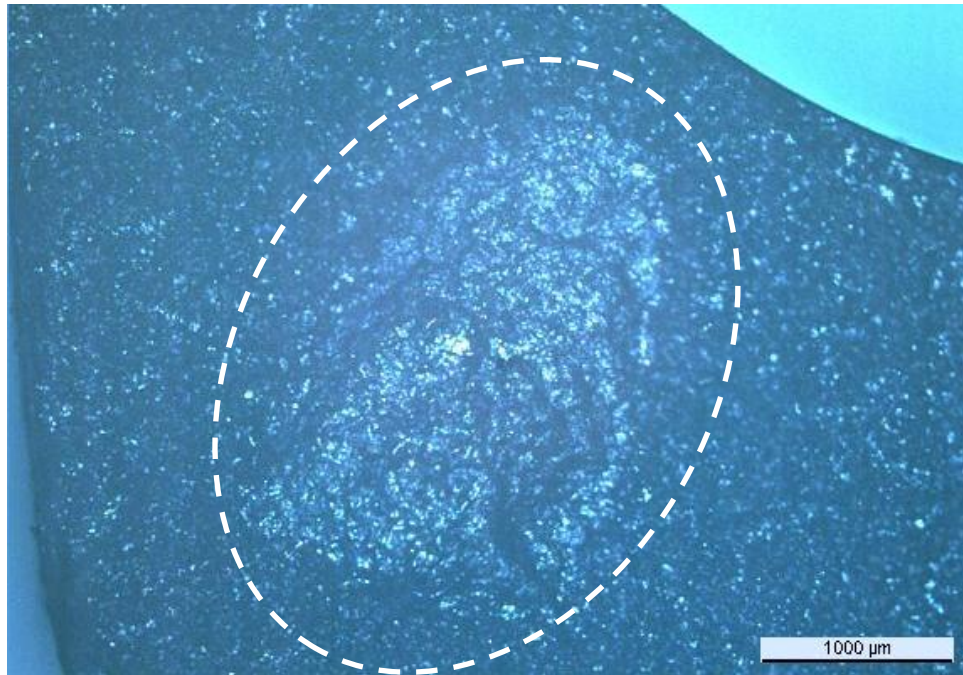


Figure 3-1: Track of a large particle (3mm x 1.2mm) on the fractured surface of a con-rod

A crack detection spray was used, which is commonly used to pinpoint cracks in component parts. However, this method only worked with larger cracks that were already easily detectable with the binocular loupe, and hence did not provide any additional insights (Lyszczan, et al., 2005).

The SEM was used to investigate the cracks within the fractured surface. A large numbers of cracks of different sizes were found, as shown in Figure 3-2, which are distributed all over the surface. Especially at steps on a fractured surface, as described in section 2.5.3 (Figure 2-18), these cracks seem to have significant impact on the creation of particles. Furthermore, retractions have been found on some fractured surfaces as shown in Figure 3-3. These retractions also have been identified as possible important sources of particles (Lyszczan, et al., 2007).

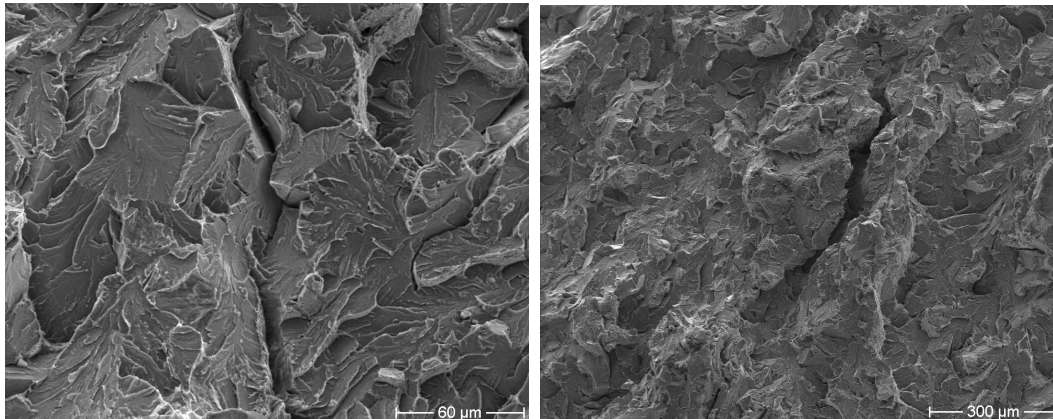


Figure 3-2: A small (left) and a large (right) crack on a fractured surface of a con-rod

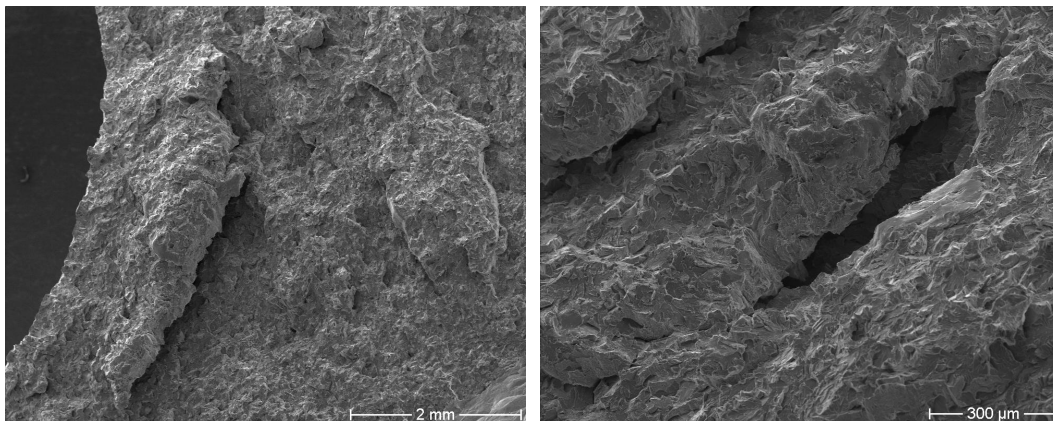


Figure 3-3: Material retractions in a large (left) and a small (right) area

3.2.2 Fitting Accuracy of a Pair of Fractured Surfaces

For the determination of the fitting accuracy of pairs of fractured surfaces several measurement devices have been used. The separation force that was necessary to separate con-rod cap and body was measured using a mechanical force measurement device. A profile meter and a laser scanner were used to predict the fitting accuracy by virtually comparing the surface profiles. The fitting accuracy of paired fractured surfaces was measured using a microscope and a computer tomography device. Each measurement was combined with an appropriate method of analysis to enable a proper estimation of the fitting accuracy of the examined pair of fractured surfaces.

The measurement of the separation force was performed by pulling the con-rod cap from the con-rod body in the direction normal to the fractured surface. The measurement was conducted with the con-rods of three con-rod batches, which were expected not to differ significantly. Surprisingly, the average separation force of one of these batches, batch 255, was significantly higher than the others (see Figure 3-4). The laser notches of the con-rods of batch 255 were distinctly smaller

than the laser notches of the other con-rod batches (see images in Figure 3-4). This difference was traced back to manufacturing irregularities, which could not be explained by the manufacturer: they should have been similar. A further finding was that on the fractured surface of con-rods with a separation force of “0N” tracks of particles could be found that are similar to the track shown in Figure 3-1. Besides a clearly higher average separation force, the con-rods of batch 255 had a more distinct surface topology than the surface topologies of the other con-rod batches (Lyszczan, et al., 2007).

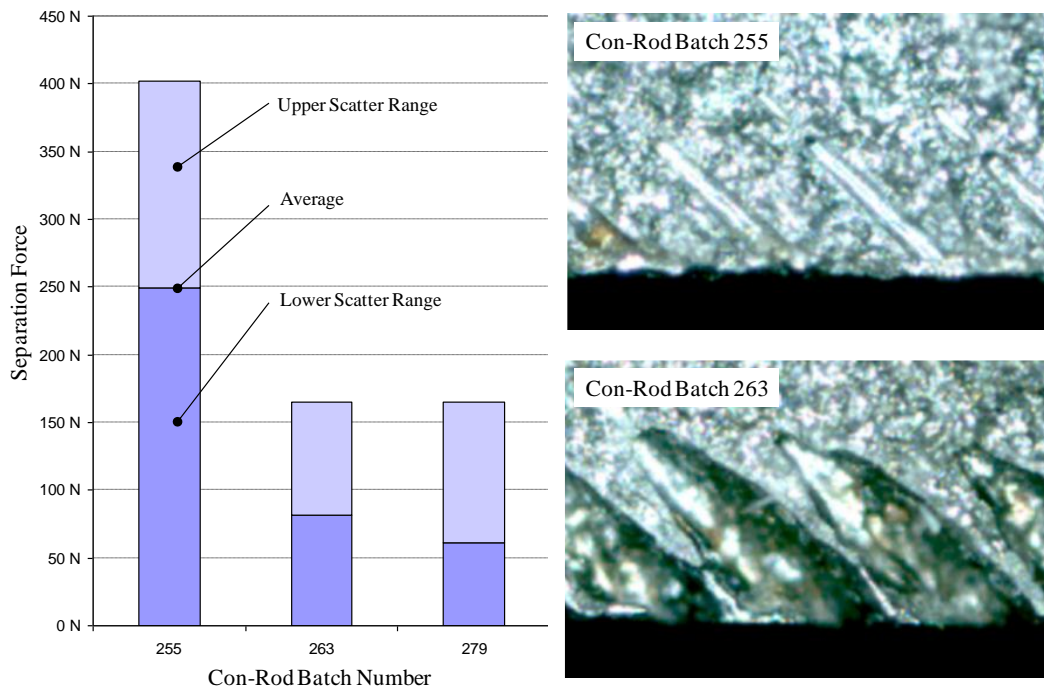


Figure 3-4: Separation force of a total of 87 con-rods almost evenly distributed between three con-rod batches (left) and images of laser notches from con-rod batches 255 (upper right) and 263 (lower right)

In first instance, a profile meter was used to collect the data of a fractured surface and of the imprint of the other fractured surface of the same pair to conduct compare the surfaces at some preselected positions, in order to identify the potential quality of the alignment of this pair of surfaces. It turned out that this method did not provide the expected results (Lyszczan, et al., 2005).

For this reason, another method was chosen: surface topology scanning using a laser scanner prototype from Scansonic Company. Proprietary software from Scansonic was used to display and compare the topology data of the laser scans of pairs of surfaces. This method seemed to be able to provide data of sufficient quality for the analysis of the fitting accuracy, but to fully exploit this method for

the intended detailed investigation described in this dissertation hardware and software required further development (Lyszczan, et al., 2005).

As a further method to assess the fitting accuracy of already paired fractured surfaces in a con-rod, rather than the separate surfaces investigated with the other methods, a digital microscope was used. This method required special preparations of the specimens. The bolted con-rods were cut at the body and the front and back face of the big eye grinded and polished as shown in Figure 3-5. This treatment enabled a close examination of the four visible contact lines of the fractured surfaces of con-rod cap and con-rod body.

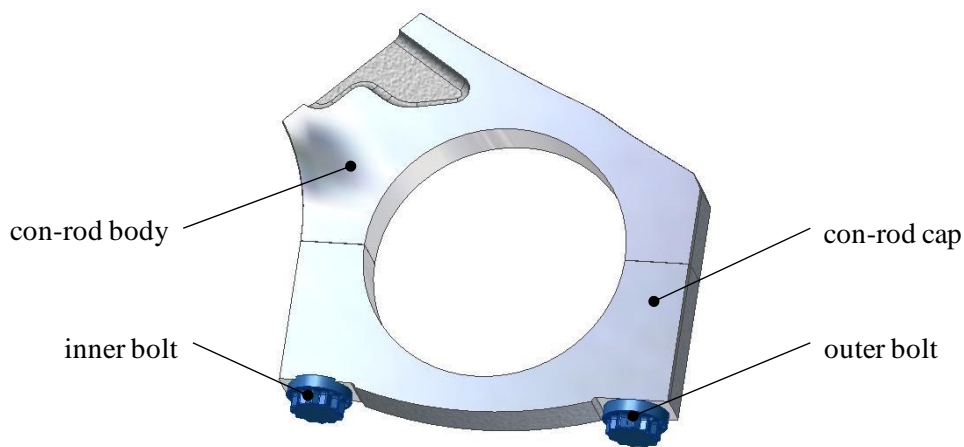


Figure 3-5: Cut, grinded and polished con-rod prepared for the examination of the contact line of the fractured surfaces using a microscope

The examination of the bolted and grinded con-rods showed that the fitting accuracy varies at each specimen from close fit (see left image in Figure 3-6) to very poor fit often in combination with large cavities (see right image in Figure 3-6).

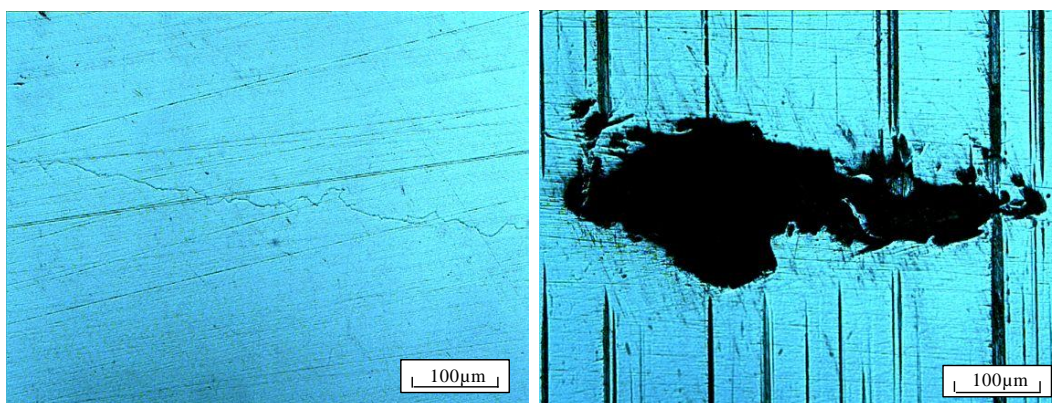


Figure 3-6: Examples of contact lines from close fit (left) to no fit in combination with a large cavity (right)

The analysis of all images shows that about 90% of all contact lines are in the state of close fit (see Figure 3-6 left). In general, the front and back connection lines at one side of a con-rod have a similar fit. However, the connection lines at the other side of the con-rod could have a different fit. Based on these results, it is assumed that the fit in the connection lines represent the fit of the contact area of that side of the examined specimens, and that, hence, it can be assumed that about 90% of the available surface area in a pair of fractured surfaces is in close contact (Lyszczan, et al., 2007).

Another method for assessing the fitting accuracy of paired fractured surfaces, which was tested, was computer tomography (CT). A pair of fractured surfaces was cut out of a con-rod and placed loosely together for the CT scan. The analysis involved the transformation of the 3-dimensional CT image, which consists of voxels with an edge length of 15 μ m, into a set of 2-dimensional layers as shown in Figure 3-7.

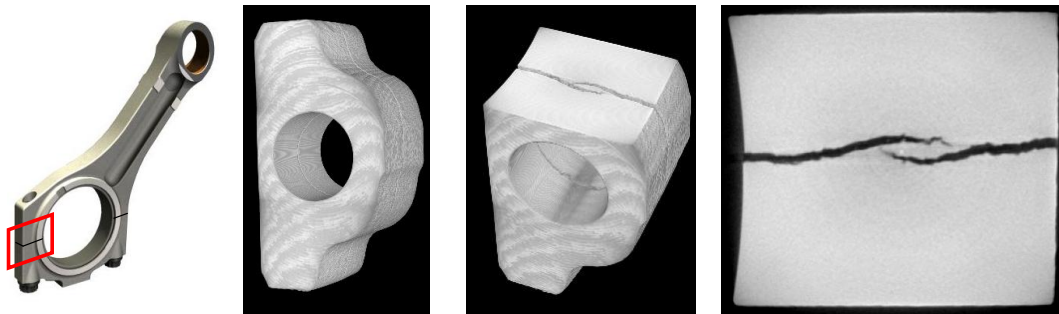


Figure 3-7: Origin of the CT specimen (left) and the transformation process of the 3-dimensional CT image to a set of 2-dimensional layers for the data analysis (from second left to the right)

The analysis of the CT data revealed that material retractions as shown in Figure 3-3 as well as in Figure 3-7 (rightmost figure), prevent the fractured surface pairing from full surface contact, when there is no external clamping force. Furthermore, Figure 3-7 (rightmost figure) indicates that it is only a small step from a material retraction to a loose particle (Lyszczan, et al., 2007). Despite the amount of detailed data, the method has several disadvantages with respect to the intended investigation. The specimen needs to be small (10 mm height) to obtain a suitable resolution. This prevents the use of a bolt for clamping. Other clamping methods would no longer represent reality.

3.2.3 Structure of Fractured Surfaces

The sum of the experiences collected by all fractured surface examinations and knowledge from literature concerning the manufacturing process (e.g. (Blauel, et al., 2000)) was used to build a model of a joint with fractured surfaces. Using this

model some specific surface phenomena can be described with, e.g. cracks, material retractions and the occurrence of particles. The model is shown in Figure 3-8.

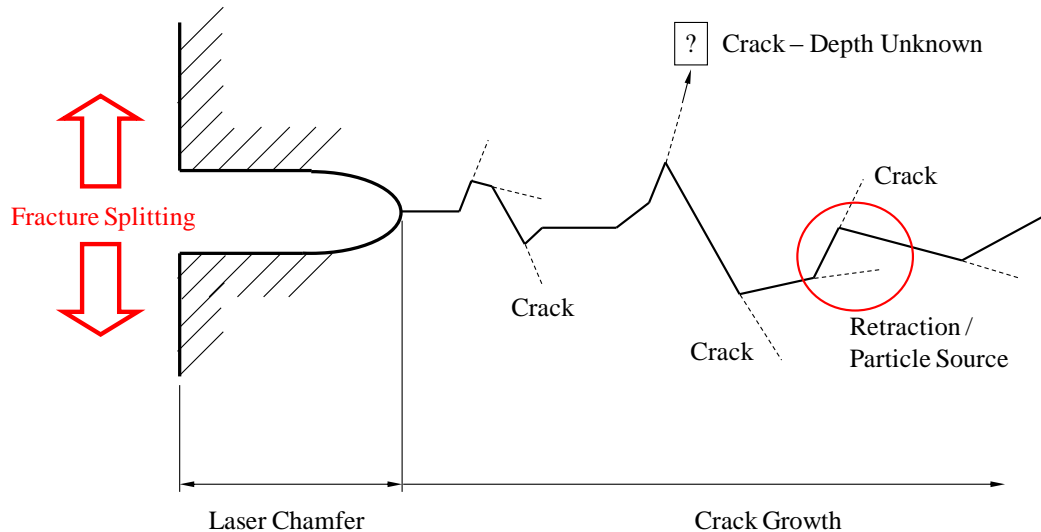


Figure 3-8: Model of the structure of a fractured surface

Due to inhomogeneity of the material the strength against crack growth varies locally. During the fracture splitting process this leads to an irregular crack path and to formation of several crack branches. When a branch of a crack is located too close to the main crack path, then material retractions appear or a particle is generated. The depth as well as the complexity of crack branches is still unknown, although they do play an important role in the emergence of retractions and particles. Although not observed, it can be expected that crack branches may produce further, so-called secondary branches. (Lyszczan, et al., 2007)

A source of the particles found within the fractured surface joints was found by combining the model of a joint with fractured surfaces and the results of the measurement of the separation forces (see Figure 3-4). Particles may not only be generated during the fracture splitting process, but every time a fractured surface is separated forcibly. During a forceful separation particles are ripped out, in particular where branch cracks have weakened the material.

3.3 Sources of Possible Threats in Fractured Surfaces

The research of (Lyszczan, et al., 2007) revealed a number of parameters that could have a negative effect on the mechanical behavior of bolted joints with fractured surfaces.

The surface inspections in 3.2.1 showed that particles from the manufacturing process may remain within the fractured surface. Some random tests indicated that these particles increase the relaxation loss of the bolted joint very distinct. The research additionally indicated that large embedded particles are likely to emerge especially at surfaces with a distinct topology³³.

Furthermore, the research indicated that in con-rods with a rather smooth topology of the fractured surface the possibility of a mismatched assembly of con-rod cap and body is higher than in con-rids with distinctive fractured surfaces. The kind of mismatched assembly ranged from a certain offset in any direction to a twisted positioning of cap and body. Independent of the kind of mismatched assembly, the size of the contact area decreases distinctly. This could result in increased relaxation losses.

Dynamic loading of the con-rod could also increase relaxation losses. The reason for this suspicion is the difference between fatigue strength and yield strength of the material. During static relaxation tests creep occurs when the yield strength is exceeded, locally generating relaxation losses³⁴. Due to these relaxation losses the preload, which supplies the creep, decreases. Therefore the harmful source of creep disappears with the time. Under dynamic load the general principles of relaxation are comparable to static relaxation with one important difference. In addition to the preload, the operating load amplitude gains importance due to its additional supply of the creep. The dynamic loading does usually not decrease with time so the harmful source for creep does not disappear. To stop this mechanism, the sum of local stresses must fall below the materials yield strength. This can only be achieved by compensation due to additional preload losses.

3.4 Conclusions

The results of the investigations conducted in the FVV project “Self Loosening of Bolts” showed that bolted joints with fractured surfaces are effected by fractured surfaces in terms of increased relaxation. In particular, the occurrence of particles within the joint was found to be a major cause of massive increase of relaxation losses, and hence to be a major threat to the functionality of the bolted joint. Fractured surfaces of the con-rods had more or less distinct surface topologies, but an effect of the topology on the mechanical behavior was not measured.

³³ A surface with a distinctive topology has a rough, cliffy and fissured character. A proper example for a fractured surface with a distinctive topology is shown in Figure 5-16.

³⁴ See Section 2.4.3 for details.

It was, furthermore, found that for con-rod designers, the lack of sound, evidence-based information about the mechanical properties of the fractured surfaces, namely the amount of shear load transmission and the amount of relaxation, is problematic. Especially the amount of transferrable shear load the designers used in their calculations was based on an imaginative and wide range of assumptions³⁵, while the amount of relaxation was estimated by some random tests.

Additionally, the working principle of shear load transfer in a joint with fractured surfaces is still unknown. Some fatigue experts suggest that micro cogging, as a pure shape based force transfer, could be a suitable working principle for this phenomenon. Others mention that a combination of friction based force transfer and an enhanced adhesive influence may be the key mechanism.

Finally, a number of influencing factors appeared in the investigations which seemed to have a strong impact on the mechanical behavior of the con-rod bolting. The occurrence of embedded particles is one of the most evident influencing factors. Furthermore, a mismatched assembly of con-rod cap and body seems to have a strong negative effect on the relaxation process and, with that, on the bolting quality. Another factor that seems to amplify relaxation losses is dynamic loading of the con-rod. This is accompanied by a critical distribution of loads and moments at the bolting of an angular splitted con-rod (Lyszczan, et al., 2007).

These results introduced a number of questions: Is the amount of transferrable shear loads influenced by the surface topology? Is the amount of relaxation loss influenced as well? If there is an influence, how can the different kinds of surface topology be described properly? What is the mechanism of shear load transfer? How do the other observed factors influence the functionality of a fracture splitted con-rod?

The research described in this dissertation aims to address these questions.

³⁵ The range of the static friction coefficient for fractured surfaces used in FEM calculations ranged from 0.1 (equal to a plain surface contact) to infinite (“rough contact” in FEM).

4 Research Approach

In this chapter the research hypotheses are formulated (Section 4.1) based on the formulated research questions. The research methods are presented in Section 4.2. The specimens used for the experiments are described in Section 4.3. The description of the experimental setup and the data analysis is the topic of Section 4.4.

4.1 Research Questions and Hypotheses

Based on the state of the art in research (Chapter 2), the preliminary investigations into fracture splitted connecting rods (Chapter 3), as well as the identified knowledge gaps (Chapters 2 and 3), research hypotheses can be set up to answer the research questions raised in Section 1.2.

4.1.1 Characteristic Parameters of Fractured Surfaces

- (1) What are suitable parameters to describe different fractured surfaces?

Parameters that are able to describe different fractured surfaces can be obtained by adjusting and combining standardized roughness parameters.

This hypothesis is discussed in Chapter 5.

4.1.2 Relaxation in Bolted Joints with Fractured Surfaces

- (2) What is the impact of fractured surfaces on the relaxation of bolted joints?

The fractured surface has a significant impact and cannot be ignored in the calculation of the bolted joint.

This hypothesis is discussed in Chapter 6.

- (3) What is the relation between surface topology and the amount of relaxation losses?

The more distinctive the surface topology, the larger is the amount of relaxation losses.

This hypothesis is discussed in Chapter 6.

- (4) What is the effect of moderately increased temperature on the amount of relaxation losses?

A moderate increase of the operating temperature (150°) results in an exponential loss due to relaxation.

This hypothesis is discussed in Chapter 6.

4.1.3 Shear Force Transfer in Bolted Joints with Fractured Surfaces

- (5) What is the impact of the clamping force on the transferrable shear load in a bolted joint with fractured surfaces?

The amount of transferrable shear load (F_Q) in a bolted joint with fractured surfaces is determined by the magnitude of the clamping force (F_N) in the following way: $F_Q = \mu_{\text{effective}} \cdot F_N$. (The effective friction coefficient is to be determined by experiments.)

This hypothesis is discussed in Chapter 6.

- (6) What is the relation between surface topology and transferrable shear load?

The more distinctive the surface topology, the larger is the effective friction coefficient. The larger the effective friction coefficient, the larger the transferrable shear load (see question 5). Hence: the more distinctive the surface topology, the larger the transferable shear load.

This hypothesis is discussed in Chapter 6.

- (7) What is the effect of moderately increased temperature on the maximum transferrable shear load?

A moderate increase of the operating temperature (150°C) decreases the amount of transferrable shear load slightly.

This hypothesis is discussed in Chapter 6.

- (8) What kind of mechanism enables the load transfer?

The mechanism of load transfer in a fractured surface joint is a combination of form based load transfer in some areas and force based load transfer in other areas.

This hypothesis is discussed in Chapter 7.

4.2 Research Methods

In Table 4-1 an overview of the research questions and the related experiments to verify the corresponding research hypotheses is shown. The columns in the matrix show the research questions. The rows list the specific tests and the different test blocks. The tests are listed in chronological order. The separation tests are described in Section 5.2, the surface scan tests in Section 5.3, the relaxation tests in Section 6.1, and the shear load tests in Section 6.2

	Surface Parameters	Relaxation & Fractured Surfaces	Relaxation & Surface Topology	Relaxation & Increased Temperature	Shear Load Transfer & Clamping Force	Shear Load Transfer & Surface Topology	Shear Load Transfer & Increased Temperature	Shear Load Transfer & it's Mechanism
Research Question	1	2	3	4	5	6	7	8
Separation Test	X							
Surface Scan	X	X				X		X
Relaxation Tests	Relax_Ref		X	X				
	Relax_Plain		X	X				
	Relax_MA		X					
	Relax_1P		X					
	Relax_3P		X					
	Relax_T1		X	X	X			
	Relax_T2				X			
	Relax_DYN				X			
Shear Load Tests	10kN				X	X		X
	20kN				X	X		X
	30kN				X	X		X
	40kN				X	X		X
	Yield_cold					X	X	X
	Yield_warm						X	X

Table 4-1: Overview of the research questions and the related experiments to verify the corresponding research hypotheses

4.3 Specimens

In this research project two different specimens were used. Both kinds are based on connecting rods with different laser notch depths. The first kinds of specimen are con-rods and the second kinds are special con-rod bolting specimens. These specimens were made out of some of the available con-rods. Both kinds of specimen are described in the following sections.

4.3.1 Connecting Rods

The specimens for this research project consist of 300 connecting rods for diesel engines delivered by a large automotive company. All specimens are made out of the same batch of C70 S6 BY forged steel. All con-rods were machined in one shift under the conditions of standard serial production and made ready for engine assembly. The con-rod bolts were fully tightened in a yield controlled bolting process. The bearing shells for the big con-rod eye were delivered separately from the con-rods.



Figure 4-1: connecting rods used for experimental investigations

In contrast to the preliminary study (see Chapter 3), in which the depths of the laser notches differed as a result of the normal manufacturing process, the con-rods for the experiments have deliberately been manufactured with notches with different depths. It was found that this depth had a distinct impact on the shape of the fractured surface (Lyszczan, et al., 2007).

For the making of the laser notches three different power settings have been used – full laser power, medium laser power (setting for serial production) and low laser power. In the following, the groups of specimens with different laser notches will be referred to as different laser notch batches. The laser notch batches are marked with different colors as follows:

full laser power	=	red batch
medium laser power	=	green batch
low laser power	=	yellow batch

The impact of the laser power setting onto the surface topology is described in chapter 5.

4.3.2 Con-Rod Bolting Specimen

Connecting rods are not suitable for basic research on relaxation and shear load transfer for three reasons. First, elastic interactions between the con-rod bolts (see section 2.4.3 Relaxation of Bolted Joints) hinder the exact application of preload of a single bolt. Second, the effect of relaxation is divided between both bolts so that an effect at a single bolt is not measurable. Third, in the shear load tests the amount of the overall transferred shear load of two fractured surfaces would be measured. Any closer resolution of the effect of a single bolted joint would not be possible.

Besides these facts, there is a practical reason for the use of con-rod bolting specimens. These specimens can be manufactured out of every kind of connecting rod. Consequently, the test design does not rely on a certain con-rod model and a certain con-rod manufacturer.

A con-rod bolting specimen is made out of a common connecting rod³⁶. It consists of those parts of the con-rod that are closely related to the bolted joint. These parts are the clamped area of the con-rod cap, the threaded area of the con-rod body, and the con-rod bolt. The FEM model of a con-rod bolting specimen to be cut off a con-rod is shown in Figure 4-2. From each con-rod two con-rod bolting specimens can be obtained. All specimens have the same size of fractured surface area and the same clamping length.

³⁶ The manufacture of a con-rod bolting specimen is described in Appendix II.1

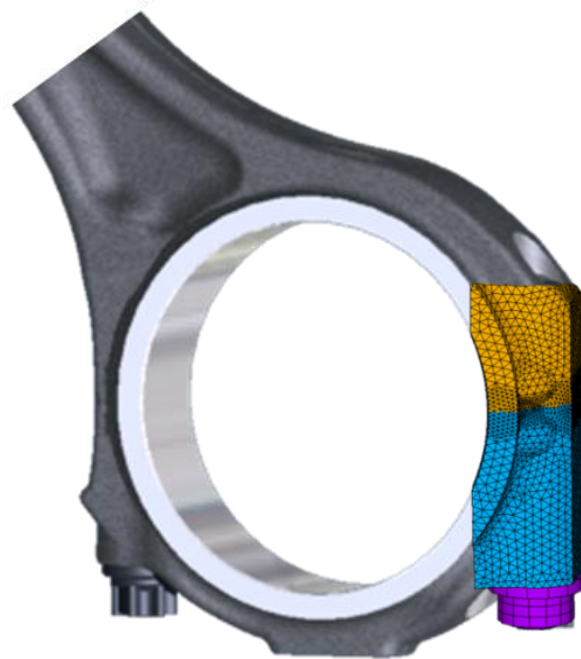


Figure 4-2: Initial position of a con-rod bolting specimen within a con-rod (high lightened as FEM model)

Hereafter, the con-rod bolting specimens are referred to as CBS (one specimen) or CBSs (multiple specimens).

4.4 Experimental Investigations

The following sections provide a summary of setup and procedures of the experimental investigations, as well as the data analysis procedures.

4.4.1 Experimental Design and Procedures

Four different kinds of test have been conducted. Disassembly tests with con-rods and surface topology scans of con-rods and CBSs have been performed to obtain parameters for proper description of the surface topology. Shear load tests with CBSs have been carried out to obtain information about the transferrable shear loads and its working principle. Finally, relaxation tests with con-rods and CBSs have been performed. All test setups and procedures are described briefly in the following sections. Detailed information is given in Appendix II.2 .

4.4.1.1 Separation Test

The separation tests have been performed at ambient temperature (22°C) using a bench vice, a crane, a mechanical tension measurement device of HBM company, and an electronic torque measurement device, Garant TT1. The procedure started with the disassembly of the bolts measuring the required maximum torque. Then the con-rod cap was pulled off by the crane, while the necessary pulling force was measured. (see Appendix II.4.1)

4.4.1.2 Surface Topology Scan

For the investigation of proper characteristic surface parameters the topology of all fractured surfaces has been measured. The measurement was executed at ambient temperature (22°C) using a surface scanner with a test bed for the necessary linear movements. For the surface scanning two Scansonic laser row scanners, type TH-03D and type TH-06D³⁷, were used. For the linear movement of the specimens the LART test bed was used. (see Appendix II.4.2)

4.4.1.3 Relaxation Test

The measurement of relaxation loss was performed at ambient temperature (22°C) as well as at operating temperature (150°C). In both cases the relaxation loss was measured using the ultrasonic bolt elongation measurement device Norbar USM III. The ultrasonic transducers used for the measurements have been glued directly to the bolts³⁸. For the relaxation tests at ambient temperature the specimens have been stored in an air-conditioned room to ensure a constant temperature level. For the operating temperature tests a drying kiln from Fritz Ruhland Company was used. (see Appendix II.4.5)

4.4.1.4 Shear Load Test

The transferrable shear load tests have been conducted as quasi static shear tests at ambient temperature (22°C) and at con-rod operating temperature (150°C). The tests have been performed with a hydro pulser, Instron 8801. The hydro pulser was equipped with a proprietary shear loading device for the con-rod bolting specimens and a tube furnace from Thermoprozess Company. (see Appendix II.4.4)

³⁷ The scanner type TH-06D is a scanner with three serially arranged laser lines. For the topology scans only the data from the center line have been used.

³⁸ For further information about ultrasonic measurement see chapter II.3

4.4.2 Data Analysis

In this section the type of recorded data and the data processing of the experimental tests and the surface scans are described, and measurement accuracy and other possible limitations are discussed.

4.4.2.1 Data of Separation Test

For the analysis of the separation test the following data have been recorded:

- Specimen ID Number
- Date and time of test
- Initial breakaway torque of the con-rod bolts - M_{BT}
- Maximum mechanical tension for separation of con-rod cap - T_{max}

The separation force F_{sep} was calculated using a calibration factor³⁹ and the gravitational acceleration:

$$F_{sep} = 0.1285 \left[\frac{kg}{\mu m} \right] \cdot T_{max} [\mu m] \cdot 9.806 \left[\frac{m}{sec^2} \right] \quad (4-1)$$

The accuracy of measurement of the tension measurement device is +/- 5 μ m. The initial breakaway torque was measured with an accuracy of +/- 0.2Nm.

The initial breakaway torque was found to be of no further importance. As a result, no further data processing was necessary. The specimen ID, the date and the time have been used for identification purposes only.

For the data analysis for each laser notch batch, the average separation force and the standard deviation have been calculated⁴⁰. The results are discussed in Section 5.2.

³⁹ The calibration factor for the used mechanical measurement device was provided by the manufacturer.

⁴⁰ See (Ross, 2006)

4.4.2.2 Data of Relaxation Tests

For the analysis of the relaxation tests a form was created to record the following data:

- Specimen ID Number
- Initial unloaded length - L_0
- Date and time of the initial loading - t_{start}
- Initial specimen temperature
- Maximum elongation – L_{max}^*
- Date and time of measurement - t_{meas}
- Specimen temperature at measurement time
- Elongation at measurement time – L_{meas}^*
- Plastic deformation after disassembly - $L_{plastic}$

The accuracy of the elongation measurement is about +/- 0.1 μ m. This includes possible imprecision of the measurement of the initial bolt length. The accuracy of the temperature measurement is about 0.2K.

The initial specimen temperature and the initial bolt length were used for the setup of the ultrasonic measurement device. This allowed instant temperature compensation during the subsequent measurements.

For the data processing, only the data from the final measurement time have been used⁴¹. The following factors were calculated for each specimen:

- Duration of the test - $t_{duration}$:
Difference between date and time of initial loading and date and time at final measurement time

$$t_{duration} = t_{meas(final)} - t_{start} \quad (4-2)$$

- Maximum elastic elongation - L_{max} :
Difference between maximum elongation and plastic deformation after disassembly

$$L_{max} = L_{max}^* - L_{plastic} \quad (4-3)$$

- Elastic elongation at final measurement time - $L_{elastic}$:
Difference between elongation at measurement time and plastic deformation after disassembly

$$L_{elastic} = L_{meas(final)}^* - L_{plastic} \quad (4-4)$$

⁴¹ For further information see section II.5.2

- Ratio of loss due to relaxation– R_{loss} :
Ratio of elastic elongation at final measurement time to maximum elastic elongation, in percentage of the initial preload F_V

$$R_{\text{loss}} = L_{\text{plastic}} / L_{\text{max}} = X\% F_V \quad (4-5)$$

For the statistical analysis of the measured data⁴² the following factors have been calculated:

- Average value of loss due to relaxation - Z_{batch} :
Average loss due to relaxation of all specimens of a laser notch batch per test series
- Standard deviation per batch - s_{batch} :
Standard deviation of each batch based on the average value of loss due to relaxation
- Overall average value of loss due to relaxation - Z_{series} :
Average loss due to relaxation of all specimens of all laser notch batches per test series
- Standard deviation per test series s_{series} :
Standard deviation of each test series based on the overall average value of loss due to relaxation
- Effects of laser batch on average value and standard deviation - ϵ :
Differences between Z_{batch} and between s_{batch} of each possible combination of the three laser batches
- Standard deviation of effect - s_{ϵ} :
Standard deviation of the effects of Z_{batch} and of s_{batch} for each possible combination of laser batches
- Confidence interval (99% confidence) – c_{99}

For the data analysis the effect and the corresponding confidence interval of the analyzed laser batches and/or test series have been compared. The results can be found in Section 6.1.

⁴² See (Ross, 2006)

4.4.2.3 Data of Shear Load Tests

For the analysis of the shear load tests the following data have been recorded:

- Specimen ID Number
- Initial unloaded length – L_0
- Elastic elongation at required preload level - L_{EPL}
- Date and time of the initial loading - t_{start}
- Initial specimen temperature
- Elongation after assembly – L_{max*}
- Specimen temperature after relaxation
- data (ASCII) from load cell and from movement of tie-bar synchronized at 11Hz with hydro pulser steering and control computer⁴³

The accuracy of the elongation measurement is about +/- 0.1 μ m. This includes possible imprecision of the measurement of the initial bolt length. The accuracy of the temperature measurement is about 0.2K. The accuracy of measurement of the load cell is about 0.25% of the indicated load. The accuracy of measurement of the tie-bar position is about 1 μ m.

The initial specimen temperature and the initial bolt length were used for the setup of the ultrasonic measurement device. This allowed instant temperature compensation during the subsequent measurements.

The (final) elongation after assembly was used to determine the applied bolt preload of each specimen. The preload F_V was calculated using the elongation at required preload L_{EPL} , the elongation after assembly L_{max*} and the target preload F_V^* , using formula (4-6):

$$F_V = F_V^* \cdot \frac{L_{max*}}{L_{EPL}} \quad (4-6)$$

For the determination of the transferrable shear load, the raw data of the load cell and the tie-bar position have been analyzed using MS Excel 2008. The elongation at each point in time was calculated as the difference between the initial position and the actual position of the tie-bar.

⁴³ The data have been recorded with BlueHill software in shear tension test mode.

This elongation is a combination of the elongation of the specimen along the shear axis, the axial deformation of the specimen due to bending, and the elongation of the shear loading device. The different kinds of deformation have been checked for their effect on the overall elongation value. This check involved an uncracked specimen and revealed that the influence due to bending of the specimen and elongation of the loading device is linear up to a shear load of 40kN covering the entire tested shear load range.

The data analysis is described in section 6.2.3.

4.4.2.4 Scanner Data

For the analysis of the laser scanner data the following data have been recorded:

- Specimen ID Number
- Date and time of the scanning procedure
- Traverse movement speed
- Binary raw data files from the CCD sensor of the scanner containing the following information:
 - Header with pre-processing parameters according to the scanner software settings described in section 4.4.1.2
 - CCD sensor information for each sensor picture:
 - timestamp for each CCD sensor shot
 - data blocks consisting of position of the 6 brightest points of each CCD sensor row and the brightness values of each point
→480 rows = 480 data blocks
 - about 750 lines per data file describing the 750 pictures per surface scan (+/- 50 pictures per scan)

To enable the data processing with the help of Matlab R2008, the binary raw data files have been converted into ASCII files. All further steps of the analysis have been realized by writing a single m-file for Matlab.

The accuracy of the position of the profile data at the end of the processing process is about 50 μ m in all three spatial directions.

A detailed description of the analysis process can be found in Appendix II.4.3.

5 Fractured Surfaces

The goal of this chapter is the identification of parameters to characterize the surface topology of fractured surfaces. The aims are to verify the research hypothesis established in Section 4.1.1 and to support the analysis of the test results in Chapter 6.

First, the details of the aims are described (Section 5.1), followed by the results of the separation tests (Section 5.2). In Section 5.3 the analysis of the laser scanner data is presented, and in Section 5.4 the results of the surface inspections are described. In Section 5.5 the conclusions on the analysis of the fractured surfaces are presented.

5.1 Aims of the Fractured Surface Analysis

The surface analysis aims for the verification and particularization of research hypothesis (1) (Section 4.1.1):

Question: What are suitable parameters to describe different fractured surfaces?

Hypothesis: Parameters that are able to describe different fractured surfaces can be obtained by adjusting and combining standardized roughness parameters.

The visual surface inspections of the con-rod bolting specimens are also used for the analysis of the test results in Chapter 6. In detail the following tasks have been performed:

- Determine a set of parameters to describe different types of fractured surfaces through:
 - separation test of all con-rods
 - analysis of single surface scans
 - analysis of the matching quality of surface pairings
- Inspect the surfaces of the con-rod bolting specimens to support the analysis of the con-rod bolting specimen tests in Chapter 6

5.2 Separation Test

The aim of this test was to determine the force that is necessary to separate the con-rod cap from the body. Due to the experiences from (Lyszczan, et al., 2007), mentioned in Chapter 3, this separation force could be a suitable parameter to identify the degree of surface roughness.

For this test only one test series was specified. This test series involved all conrods from each of the three laser batches. The test results are summarized in Table 5-1 and displayed in Figure 5-1.

	Yellow	Green	Red
Average	574 N	730 N	402 N
RMS	287 N	135 N	248 N
Maximum	1094 N	994 N	809 N
Minimum	0 N	368 N	0 N

Table 5-1: Details of the results of the separation test for of the three laser batches yellow (min. laser power), green (medium laser power) and red (max. laser power) (100 specimens per batch)

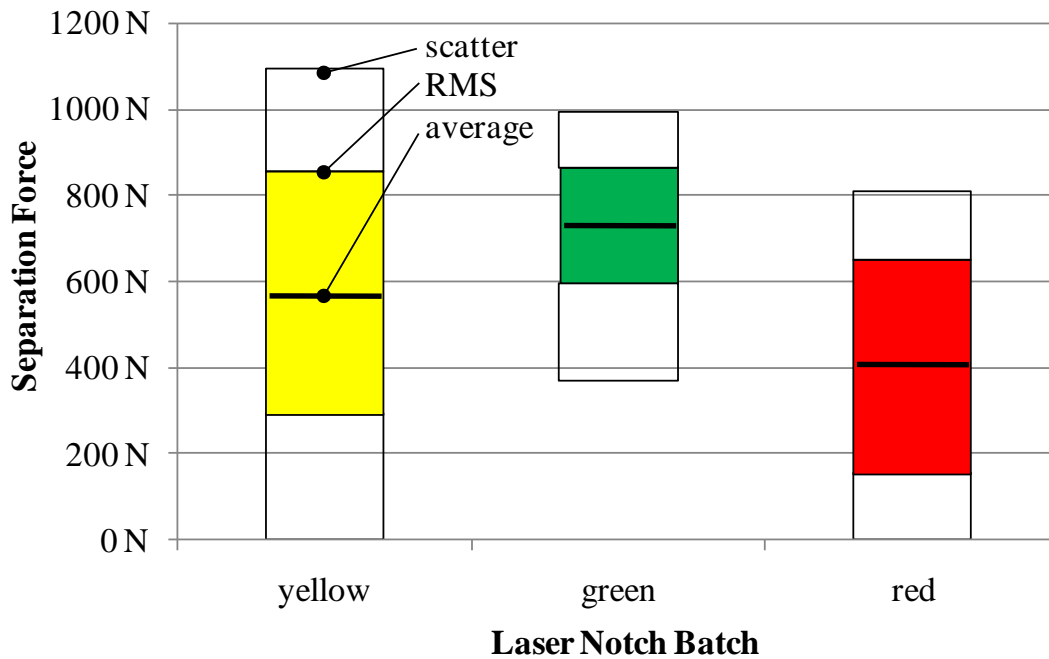


Figure 5-1: Results of the separation test

The distribution of separation force of the yellow batch, with the small laser notch, is very scattered. This batch contains the specimens with the highest separation force value as well as the lowest value. After the disassembly of the bolts three specimens could be parted without any additional force (separation force 0 N). These specimens contained imprints of large particles on their fractured sur-

faces⁴⁴. The average separation force of the yellow batch lies between those of the other two batches. This is only to a small extent due to the three zero values.

The specimens of the green batch, with the medium laser notch, show the smallest scatter band in combination with the highest average separation force. In this batch no specimen required a force less than 360N to separate.

The red laser batch, with the large laser notch, has the smallest maximum and the smallest average separation force in this test series. This batch contains five specimens with a separation force of 0N. Large particles were not found here.

The result of the separation test leads to the conclusion that, against expectation, there are no significant differences between the batches concerning the separation force. That is, the type of notch does not seem to have an effect on the separation force. The separation force is not a suitable parameter for the indication of the degree of surface roughness.

The tests showed that the occurrence of large particles reduces the separation forces to zero. In general, a considerable separation force is usually needed to disassemble an unbolted con-rod.

5.3 Analysis of Laser Scanner Data

This section is about the analysis of the laser scan data⁴⁵, collected as described in Section 4.4.1.2. The analysis was performed for the survey of single surfaces and for pairs of mating surfaces.

5.3.1 Single Surface Survey

Fractured surfaces were visualized by photographs as well as by means of so called profile diagrams resulting from the laser scan data. These diagrams clearly show the different degrees of surface fracture in the three laser batches. In Figure 5-2 three representative samples are shown, one of each batch.

⁴⁴ For further information see Section 5.4

⁴⁵ Find detailed information in (Fürst, 2010)

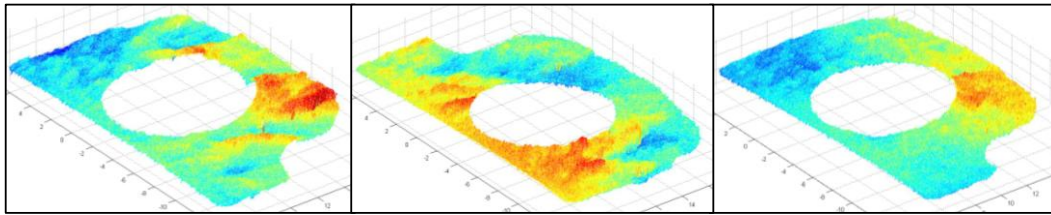


Figure 5-2: Diagrams of typical surface samples of the yellow batch (left), green batch (center) and red batch (right) with color indication for the surface elevation level (red color = high level, green = medium level, blue = low level)

The laser notch batches have distinct differences concerning the topology of their fractured surfaces (see Figure 5-2 and Section 5.4). The analysis of the diagrams of all 300 surfaces showed that the yellow and green laser batches have a distinct surface topology with quasi-isotropic orientation. Most elements in the surface texture are aligned normal to the crank shaft axis and in the direction of the shear load transfer. In the yellow batch this phenomenon is more distinct. The red laser batch, however, does not show a distinct surface topology, no common orientation of the individual surface elements was found.

To obtain a precise description, for each surface a set of potential characteristic parameters was calculated. These values are based on the definition of the coordinate system of the fractured surfaces and its orientation with respect to the con-rod geometry as shown in Figure 5-3.

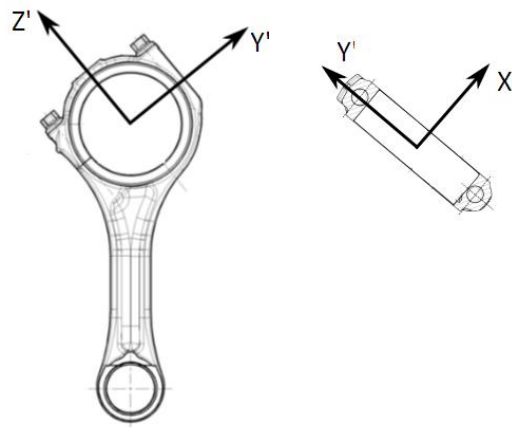


Figure 5-3: Definition of the coordinate system

The following potential characteristic parameters were calculated:

- roughness R_Z
- averaged roughness R_C
- point-to-point inclination angle α_{point}
- sliding average inclination angle α_{slide}

The parameters have been analyzed regarding their ability to identify the laser notch batch to which a certain specimen belongs. A characteristic parameter is a parameter with which a specimen with a certain surface topology can unambiguously be correlated to a certain laser notch batch.

5.3.1.1 Roughness R_Z

The roughness of the surface R_Z was calculated based on (ISO4287, 2010), which defines roughness as the distance between the global minimum and maximum of a surface along a characteristic length (see Z_{max} in Figure 5-4). In this standard, the value is adjusted for the angle of the surface by transforming the “0-level”, which can take any shape, into a flat reference surface, assuming that the shape of the surface does not play a role. This allows a comparison of different surfaces.

However, in the case of the cracked surfaces of a con-rod, the angle of the surface plays a major role in the transfer of shear load. Furthermore, the “0-level” of a fractured surface is equal to the ideal splitting layer of the con-rod. The exact position of this splitting layer can hardly be determined with the available data. For these reasons a “0-Level” transformation was not performed.

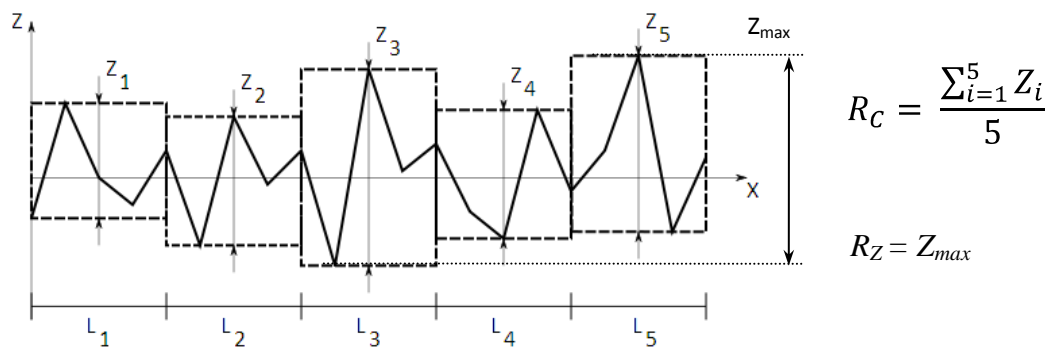


Figure 5-4: Roughness R_Z and averaged roughness R_C (see formulas at the right)

Besides these facts, the ISO standard assumes that the surface roughness is uniform outside the characteristic length scale. Measurements of the surface rough-

ness at different areas of a specimen should always return (almost) the same result. However, as Figure 5-2 shows, this is not the case in our specimens.

Additionally, for an anticipated surface roughness of about $10\mu\text{m}$ the measurement length is about 10mm ⁴⁶. Following this rule, for a fractured surface with visible level differences of 1mm , the measurement length should have a size of about 1m . However, the specimens used have an overall length of 20mm – partly interrupted by the bolt hole. Consequently, another parameter based on roughness R_z was needed. For reasons of simplicity, the roughness was defined as the distance of the global maximum and minimum of the whole specimen surface.

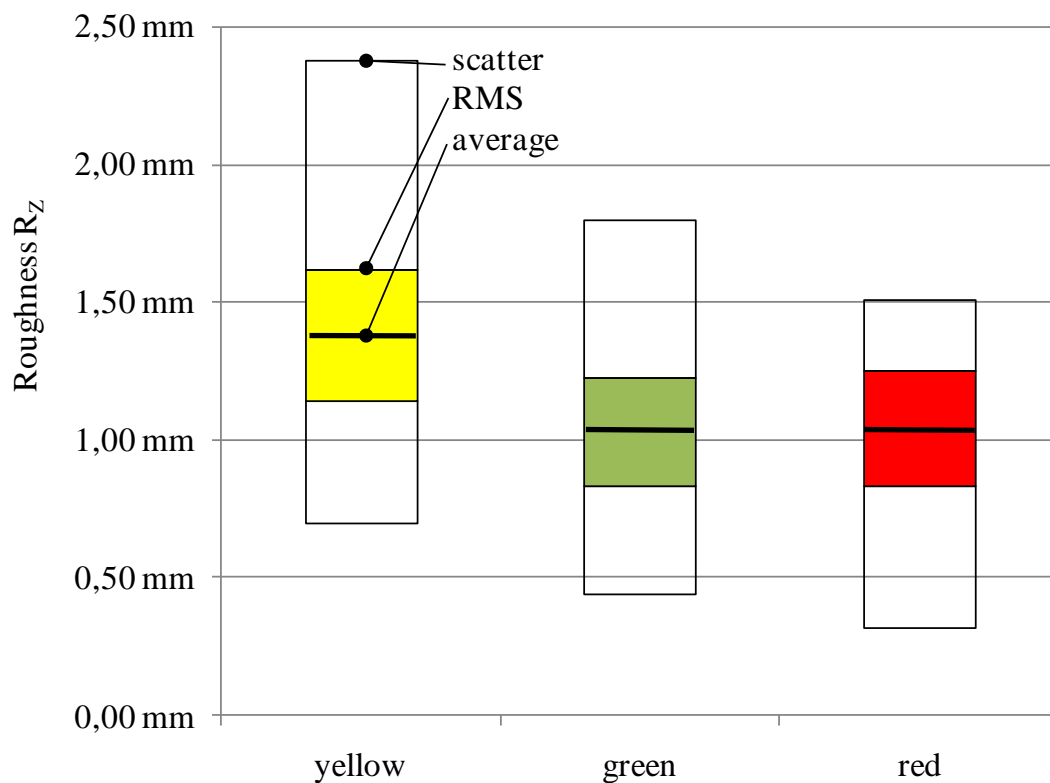


Figure 5-5: Roughness R_z , the corresponding standard deviation (represented by colored bar thickness) and scatter range (empty bars) averaged per laser notch batch

The result of the calculation of the roughness R_z presented in Figure 5-5 show that a differentiation between the green and red laser notch batches is not possible with this parameter. The average roughness of the yellow batch is about 1.38mm with a

⁴⁶ See (ISO4288, 1998), table 2

standard deviation of $s = 0.24\text{mm}$ (about 17%). The average roughness values of the green and red batches are 1.03mm and 1.04mm respectively. Both batches have a standard deviation of 0.2mm (about 20%).

In consequence, this parameter does not have the potential for a substantial differentiation between the laser notch batches.

5.3.1.2 Averaged Roughness R_C

The averaged roughness R_C was calculated based on (ISO4287, 2010). For the determination of R_C the measurement length is divided equally into five sections. For each section the difference of the local maximum and minimum is calculated. R_C is the average value of these five local peak-to-peak values (see Figure 5-4).

The determination of R_C suffers the same limitations as R_Z concerning the “0-level” transformation and the necessary measurement length. As a result this transformation was not performed. Furthermore, the calculation procedure was adjusted with respect to the necessary measurement length.

For the calculation, each data row along the x-axis was defined as a measurement path. Each measurement path was divided into five sections of equal length⁴⁷. In each section the difference between the local maximum and minimum height was determined. Subsequently, the average of these section height values was calculated. This procedure was performed with all data rows that contained more than 30 data points. Finally, all average row values have been averaged to the average roughness R_C .

In Figure 5-6 the result of the calculations is presented. The average roughness of the yellow batch is about 0.203mm with a standard deviation of $s = 0.018\text{mm}$ (about 8%). The average roughness values of the green and red batches are 0.169mm and 0.161mm respectively. Both batches have a standard deviation of 0.017mm (about 9%). The difference between all laser notch batches is not significant.

Because of the large scatter range of the single values, the average roughness does not allow a definite categorization but at least a rough indication.

⁴⁷ The measurement path contains at least 30 and maximum about 250 data points. The length of each section is varies in dependence of the number of available data points per measurement length.

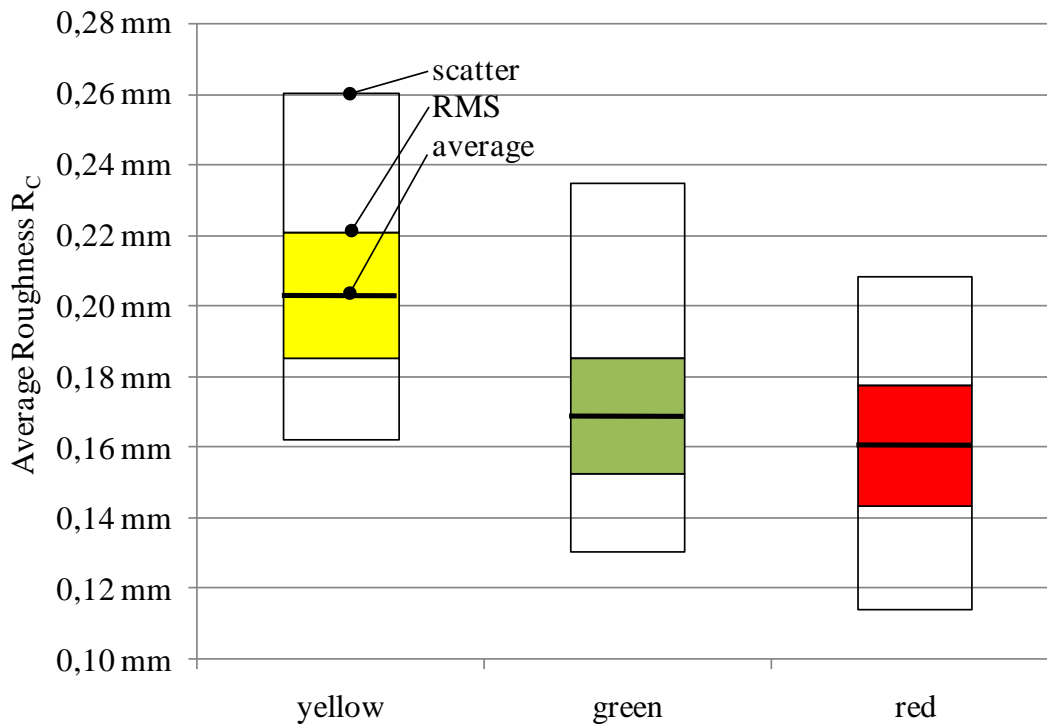


Figure 5-6: Averaged roughness, the corresponding standard deviation (represented by colored bar thickness) and scatter range (empty bars) averaged per laser notch batch

5.3.1.3 Point-to-Point Inclination Angle α_{point}

On a macroscopic scale the inclination angle between two adjacent measurement points of smooth surfaces is smaller than of surfaces with a distinct surface roughness. This would imply that the inclination angle is a suitable characteristic parameter.

However, this is only true up to a certain level of resolution. When the resolution is too high, the distance of two adjacent measurement points will be very small. The smaller the distance of these two points, the more the inclination angle is affected by the microscopic topology. This would prevent the use of the angle for the macroscopic surface description. When the resolution is too low, the distance of two adjacent measurement points will be very large. This results in small differences between the inclination angles of surfaces with different roughness. This too would prevent the use of the angle. Consequently, the determination of the most suitable resolution is of high importance for this parameter.

The calculation of the point-to-point inclination angle is performed by using all data rows along the x -axis. In each row, the inclination angle α_1 from data point to data point is determined for all n data points (see Figure 5-7).

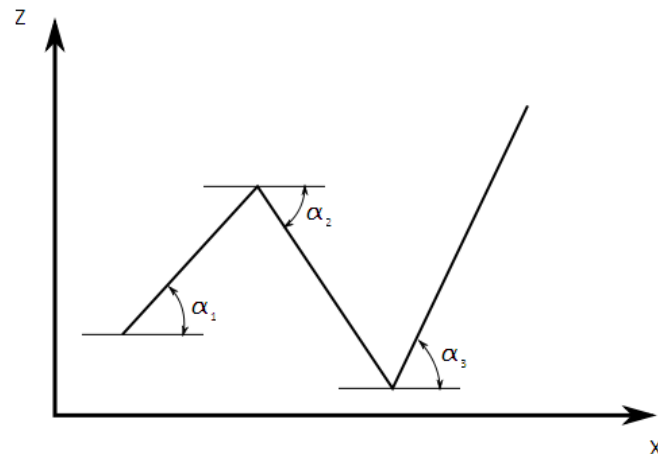


Figure 5-7: Definition of inclination angle α_i

For each row the average inclination angle is calculated. The point-to-point inclination angle α_{point} is the average value of all m averaged inclination angles of a fractured surface according to equation (4-1).

$$\alpha_{\text{point}} = \frac{\sum_{j=1}^m \frac{\sum_{i=1}^n |\alpha_i|}{n}}{m} \quad (4-1)$$

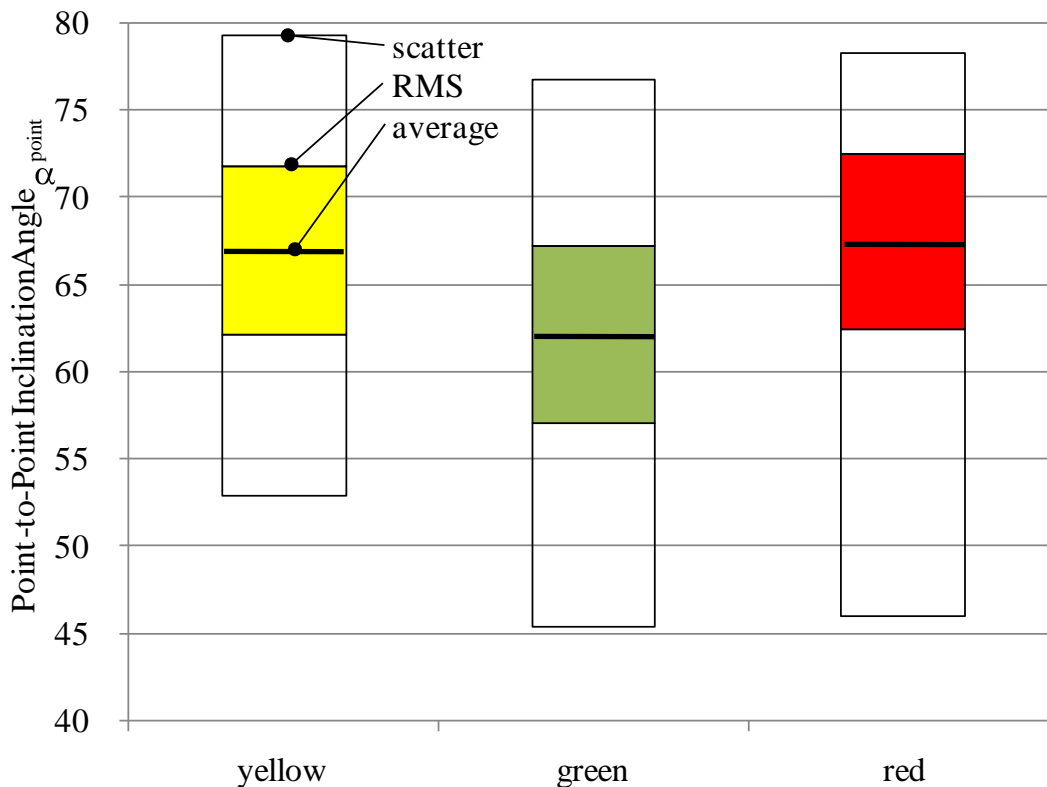


Figure 5-8: Point-to-point inclination angle, the corresponding standard deviation (represented by colored bar thickness) and scatter range (empty bars) averaged per laser notch batch

Figure 5-8 shows that the yellow and red laser notch batches have about the same average value for α_{point} of about 67° . The average value of α_{point} for the green laser notch batch is about 62° which is slightly lower. Furthermore, the scatter range of all three batches is very large. Obviously, the resolution of the data points used for this parameter is too high (as discussed on page 73). As a result, a reasonable differentiation is not possible with this parameter.

5.3.1.4 Sliding Average Inclination Angle α_{slide}

The sliding average inclination angle is an enhanced version of the point-to-point inclination angle. The result of Section 5.3.1.3 indicates that the resolution of the available measurement data is too high to use directly for the calculation of meaningful inclination angles. There are two ways to lower the resolution to an acceptable level. Either a number of measurement points could simply be deleted or a set of measurement points could be combined into a single point. The first procedure has the disadvantage that the information of the deleted points concerning the surface topology is lost. During the second procedure this information is re-

tained within the combination process. This seems to be the more promising solution.

Instead of focusing on the inclination angle of just two data points the sliding average inclination angle α_i^* was chosen to be based on areas of 5 x 5 data points. The calculation procedure for α_{slide} is equal to the calculation of α_{point} (see equation 4-1) with the only exception that α_i is substituted by α_i^* .

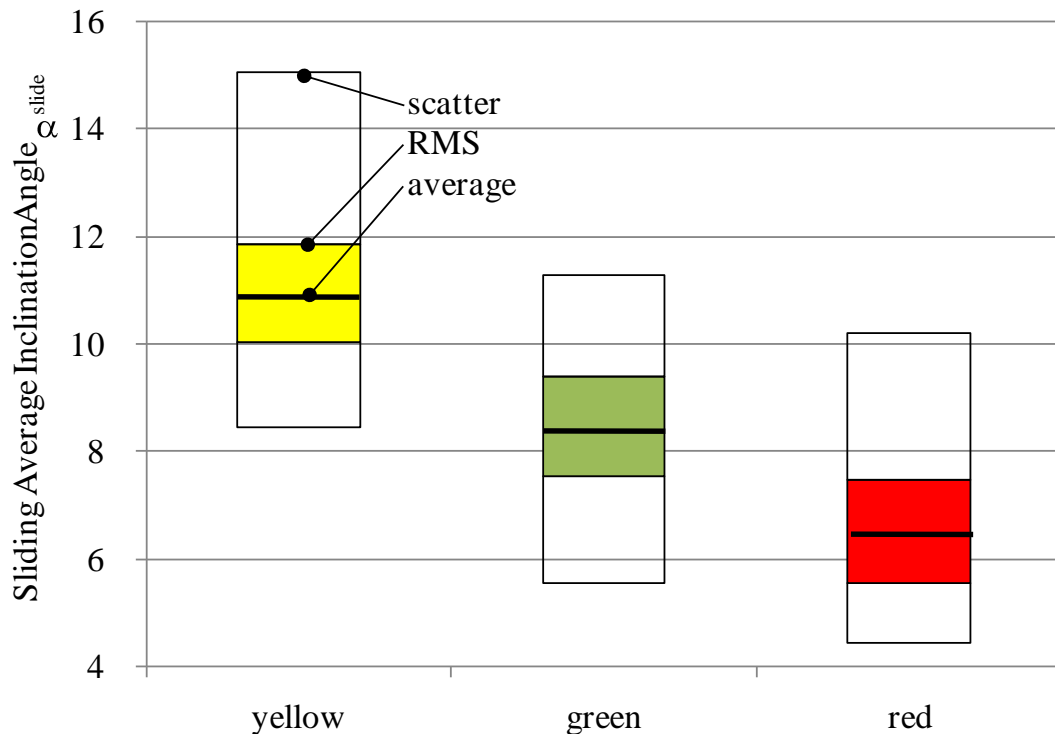


Figure 5-9: Sliding average inclination angle, the corresponding standard deviation (represented by bar thickness) and the scatter range (empty bars) of all three laser notch batches

The results of the calculation are shown in Figure 5-9. The average sliding inclination angle of the yellow batch is about 10.94° with a standard deviation of 0.91° (about 8%). The values of the green and red batch are 8.47° with a standard deviation of 0.94° (about 11%) and 6.52° with a standard deviation of 0.96° (about 15%) respectively. All differences between the laser notch batches are significant.

The differences of the laser notch batches are fairly distinct due to comparably low scatter. In summary, the sliding average inclination angle α_{slide} fulfills all requirements to become a characteristic parameter.

5.3.2 Matching Fractured Surface Pairs

To determine how well fractured surface pairs match, a series of parameters that should be able to describe the matching quality were tested:

- Matching rate
- Material distribution
- Vertical distance
- Profile balance point
- Cavity Volume

In the following sections these parameters and their ability to describe the matching quality are discussed.

5.3.2.1 Matching Rate

In a pair of fractured surfaces the matching rate indicates the amount of contact areas relative to the overall area. The calculation of this parameter is based on the distances of all pairs of measurement points of both surfaces in z direction according to the coordinate system defined in Figure 5-3. To specify whether there is contact or not, and taking into account measurement uncertainty, a threshold value ε_d was introduced. Contact is realized when the distance between two measurement points is below this threshold value. This value has been determined as follows.

The minimum value of the threshold depends on the measurement uncertainty in z direction of the laser scanning process and was determined to be about 0.05mm^{48} . The elastic deformation of the surface layer after the bolting process was found to be negligible⁴⁹.

The maximum value of the threshold is limited by the informative value of the matching rate. When the threshold value is too high, all surface pairs will seem to

⁴⁸ See (Fürst, 2010) for detailed information

⁴⁹ With a resilience of the clamped parts of about $1.67 \cdot 10^{-6} \text{ mm/N}$ (based on ANSYS calculations – see (Lyszczan, et al., 2010)) and an initial preload of about 51kN, an overall elastic deformation of the clamped parts of about 0.085mm can be expected. Considering the clamping length of 38 mm and estimating the thickness of the surface layer to be about 1mm, the expected elastic deformation of the surface layer is about 0.002mm which is far below the threshold value.

match perfectly. In this case the matching rate will no longer describe the matching quality.

A threshold range of 0.05mm to 0.1mm in steps of 0.01mm was analyzed. An example of the results for one sample with a threshold of 0.05mm is shown in Figure 5-10. The summary of all calculation results is shown in Figure 5-11.

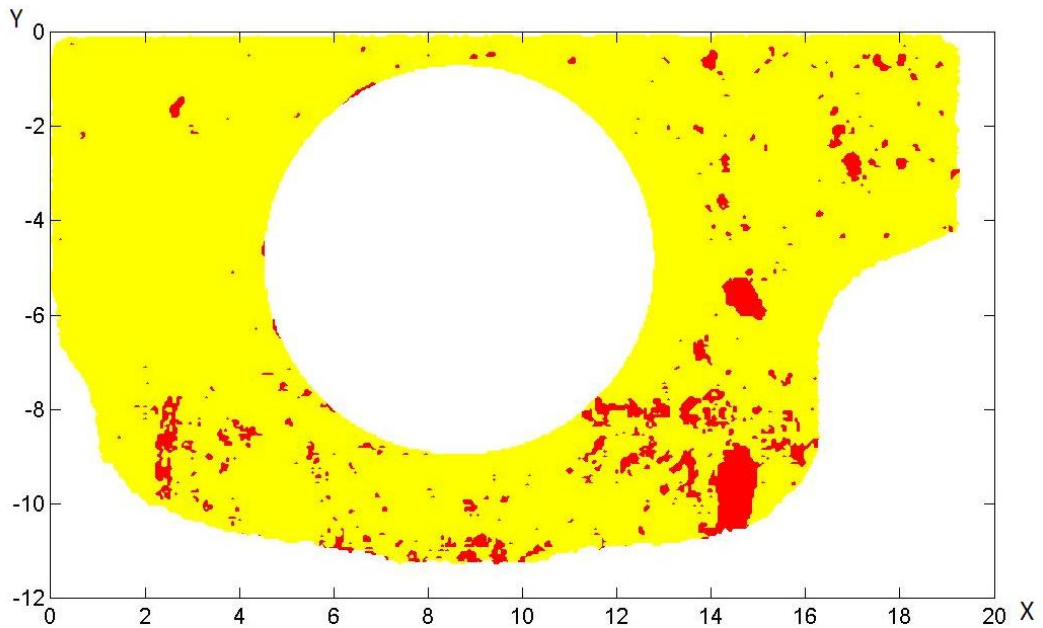


Figure 5-10: Example of surface contact survey (areas not in contact are marked red) with a threshold of 0.05mm and a corresponding matching rate of 94.3%

As expected the matching rate increases with increasing threshold range. Furthermore, the standard deviation decreases with increasing threshold. Due to the magnitude of the matching rate this is of no surprise. Smaller surface distances no longer play a role when the threshold increases.

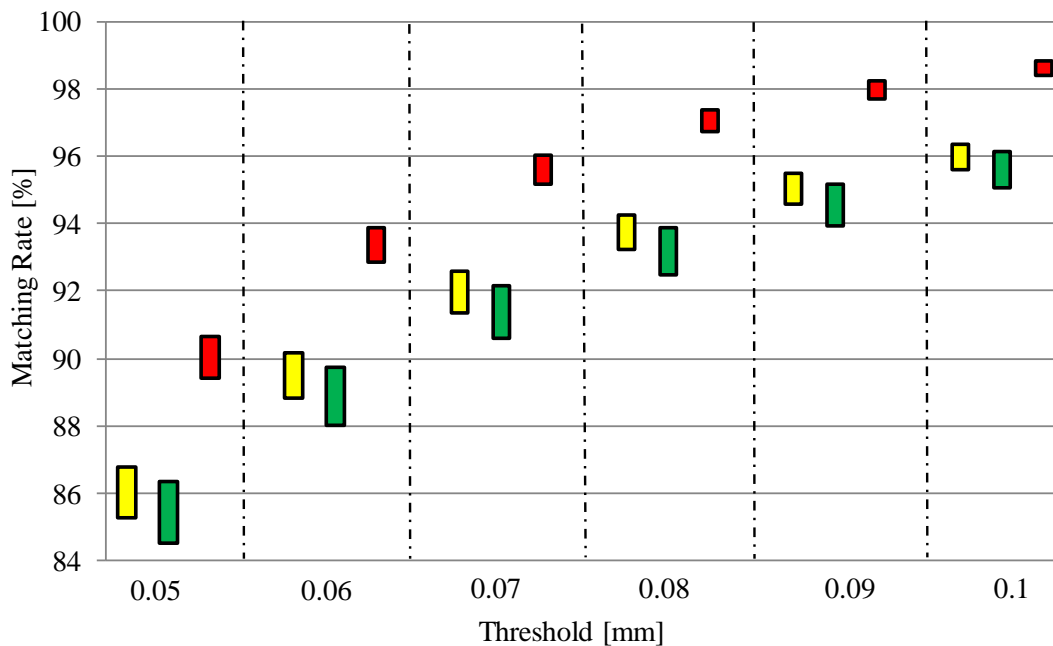


Figure 5-11: Matching rate as a function of the threshold for all three laser notch batches (bar thickness represents average value +/- standard deviation)

As shown in Figure 5-11, the average matching rates of the yellow and green batches are quite similar. For all threshold values, the standard deviation of the green batch is larger than that of the yellow batch. The difference in standard deviation increases with increasing threshold. In the examined threshold range from 0.05mm to 0.1mm the average matching rate of the red batch is significantly higher than the average matching rates of the other two batches. This difference only slightly decreases with increasing threshold range. The standard deviation of the red batch is significantly smaller in comparison to the other two batches.

Overall, the relative differences between the laser notch batches remain the same for all thresholds, but the absolute values of the matching rate differ. It was decided to choose the highest resolution, that is, the lowest threshold, which is 0.05mm. The average matching rate of all three batches for this threshold is 87.8%. This is very close to the matching rate of 90% estimated through visual inspections in a previous project (see Section 3.2.2).

5.3.2.2 Material Distribution

This parameter determines the quality of surface matching by comparing the frequencies of the profile depths on each surface pair. The frequency distribution describes the material distribution in z-direction according to the coordinate system shown in Figure 5-3. An example is shown in Figure 5-12.

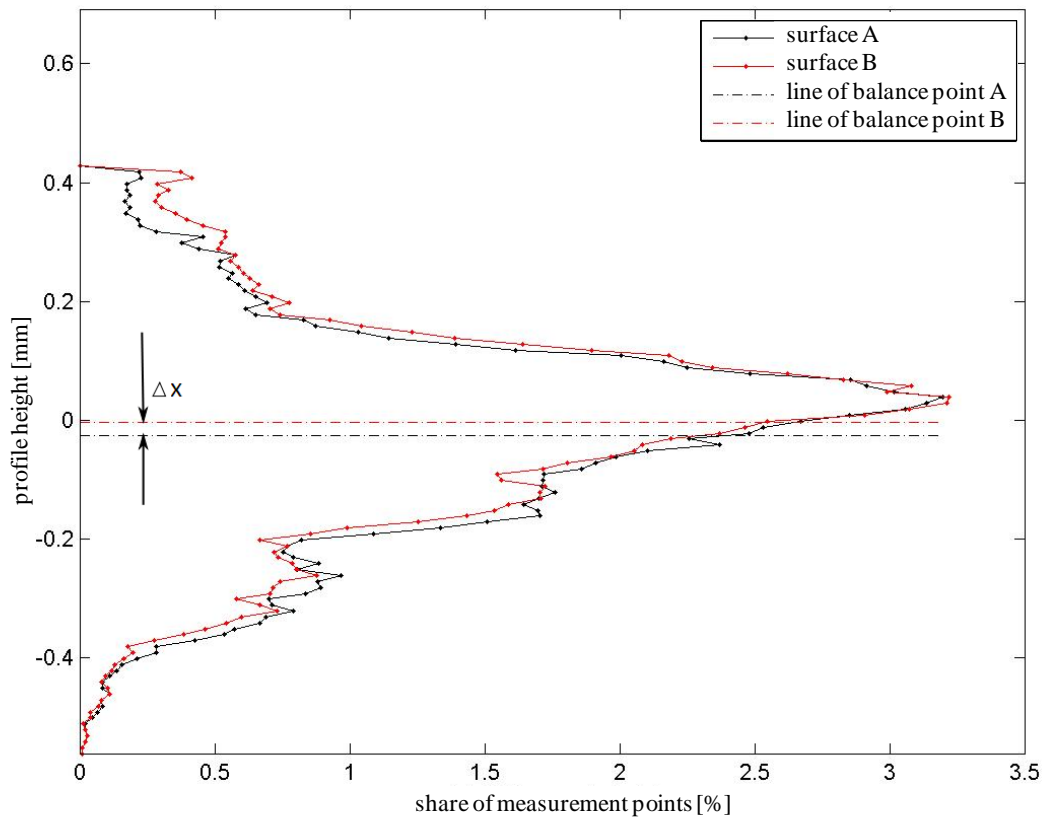


Figure 5-12: Comparison of the material distribution of two fractured surfaces and the distance ΔX of their balance point lines (profile height “0” marks the median of the distribution of the measurement points of surface B)

This figure shows the material distribution of a pairing of fractured surfaces (continuous lines) and the difference between their medians (dash-dotted lines). The graph of the material distribution represents the share of measurement points in each height level. The median of one surface is defined as the height level “0”, in this case the median of surface B. Due to slight deviations of the surface topologies, e.g. due to particle breakouts, material retractions, and cavities, at the end of the numerical alignment process⁵⁰ the median of the other surface, which is surface A in this case, is different to a certain extent. The magnitude of this difference is an indicator for the matching quality. The smaller the difference, the higher is the matching quality. However, focusing on this indicator it is not possible to differentiate between many small deviations or some larger deviations.

⁵⁰ For further details see Appendix II.4.3

This parameter has potential to describe the individual characteristic surface profile. However, the resulting graphs require further processing to allow comparison.

Although this parameter seemed to deliver promising results, it turned out that it fails to provide data for indicating the matching quality. The reason for this failure is that numerical alignment of the surface data is based on the best match assuming perfect matching and does not take into account true topology differences such as gaps (see Figure 5-10). That is, the balance point does not only reflect true topological differences (as intended), but also possible incorrect numerical alignment. Although incorrect alignment also affects the matching rate determined in Section 5.3.2.1, this is easy to detect. The effect on the balance point, however, is large and can hardly be detected.

It seems that a proper comparison requires the identification of sub parameters that unambiguously describe the graph of a material distribution of a single surface. The sub parameters should enable a clear differentiation between the surface topology of the batches and within the batches.

5.3.2.3 Vertical Distance

Whereas the matching rate (see Section 5.3.2.1) indicates areas with a vertical distance of above the threshold, it does not give the actual vertical distance. For this purpose the parameter vertical distance is introduced to represent the average distance in z-direction between two fractured surfaces. This distance primarily bases on the presence and the size of non-contact areas in relation to the overall area. The smaller the average distance the better the matching quality. A large distance indicates large break-outs (> 1mm depth). In this way, particle break-outs should be easy to detect. To calculate the parameter *vertical distance* the individual distances of all data point pairs along z-axis in a surface pair have been averaged.

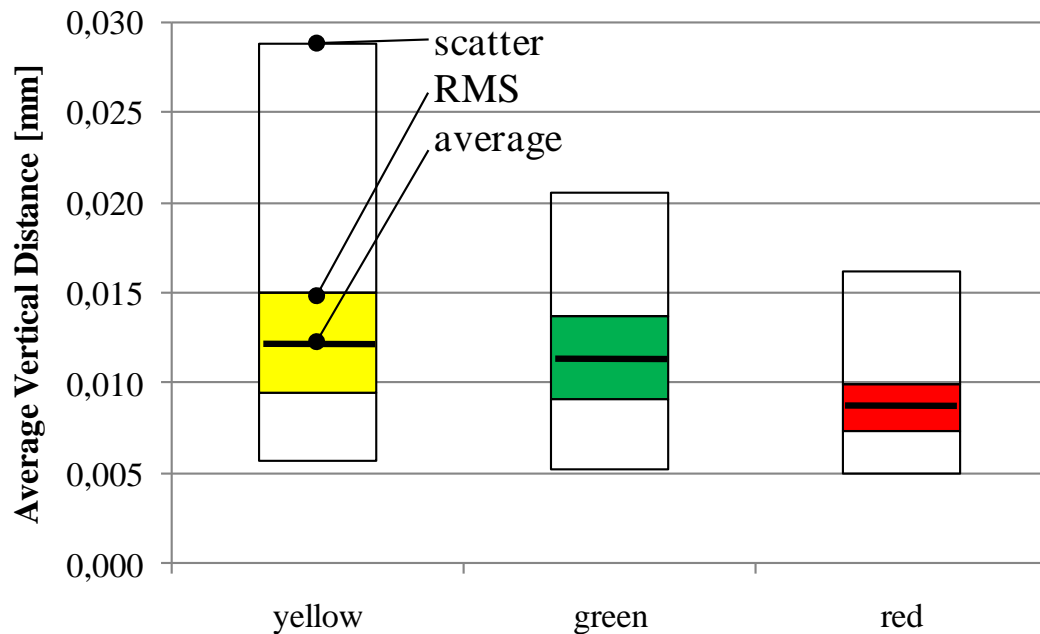


Figure 5-13: Vertical distance of all three batches

In Figure 5-13 the results of the calculation of all specimens is shown. Due to the lowest average vertical distance the matching quality of the red batches is better than the matching quality of the other batches with higher average vertical distances (compare Figure 5-10).

A large distance indicates the existence of one or more cavities within a fractured surface pair. The exact threshold, i.e. the minimum vertical distance, indicating a cavity is different from batch to batch because of the differences in the average vertical distances (see Figure 5-13). Based on an empirical analysis of the data this threshold d_{TVD} can be calculated based on the average vertical distance per batch d_{AVD} using the following formula:

$$d_{TVD} = 1.8 * d_{AVD} \quad (4-2)$$

An average vertical distance above this threshold points at the existence of large cavities. Another possibility is an incorrect alignment of the surface data. However, this would only occur in case of a large number of errors and can easily be detected in the images as shown in Figure 5-10.

5.3.2.4 Cavity Volume

The parameter cavity volume is a derivative of the matching rate and the vertical distance. It is calculated by multiplying the areas of the point pairings⁵¹ identified as not in contact (see matching rate) with the vertical distance of all data point pairings located within those areas. Figure 5-14 shows the cavity size as a function of the threshold ε_d of the matching rate.

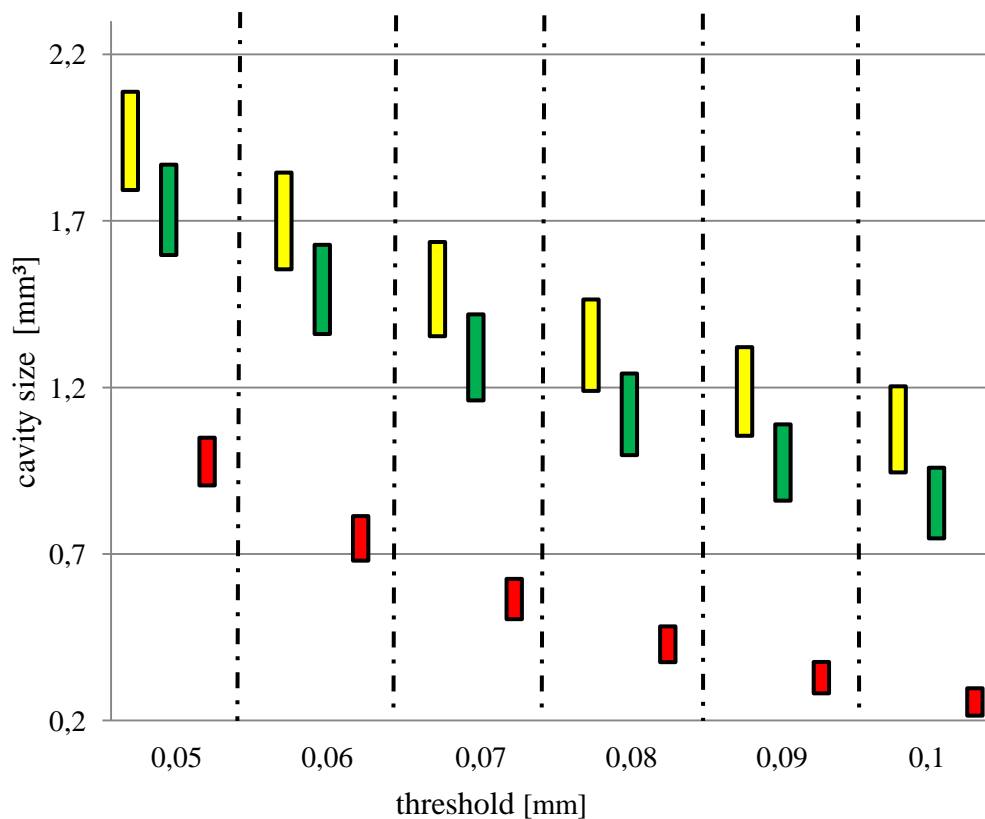


Figure 5-14: average cavity volume (standard deviation = bar thickness) per laser notch batch in dependence of threshold

In general the matching quality computed by this parameter is comparable to the matching quality calculated with the Vertical Distance.

⁵¹ The area of each point pairing is predefined based on the scanner data processing and measures 0.0025mm² (see Appendix 180II.4.3)

The average cavity volumes of the yellow and the green batches as well as the standard deviation of these two batches are equal. Those of the red batch are significantly smaller. The average cavity volume decreases in all batches with increasing threshold of the matching rate. The standard deviation of the yellow batch and of the green batch remains at a near constant level, while the standard deviation of the red batch decreases with increasing threshold. A constant standard deviation indicates a real difference between surface pairings with and without cavities. The decreasing standard deviation of the red batch indicates the existence of small cavities and comparably high signal-to-noise ratio of surface alignment.

5.3.3 Parameter Correlation

For the indication of the matching quality all parameters require a parameter depended threshold. Even the use of such a threshold does not enable a differentiation between a true bad matching quality, due to cavities, and a fictitious bad matching quality, due to numerical errors from data processing. To cope with this problem the parameters have been correlated with the aim of finding the best indicators to distinguish true cavities from numerical errors, and to develop an algorithm to support their identification from the scan data.

Based on the knowledge gained by the tests, it was found that the correlation of Matching Rate and Vertical Distance at a threshold of 0.05mm was the best indicator (see Figure 5-15). The correlation of Matching Rate and Vertical Distance indicates, as expected, that a decrease of the matching rate relates to an increase of the vertical distance. Small cavities and minor numerical errors cannot clearly be distinguished. Major numerical errors, however, can be identified as having a low matching rate and a relatively large vertical distance. The analysis of the scan data showed indeed, that from a matching rate of $< 80\%$ at a threshold of 0.05mm, a decreasing matching rate increasingly indicates a bad numerical surface alignment. A matching rate of less than 70% is caused by bad numerical alignment. Large cavities are more easily to identify: they are indicated by a high matching rate in combination with a large vertical distance. In Figure 5-15 all encircled specimens had large cavities and were the only ones with large cavities. Interestingly, these are all from the yellow batch with the small laser notch. The analyses based on the individual parameters (see previous sections), however, did not show a clear distinction between the green and yellow batches. In order to determine of a clear threshold further testing is needed.

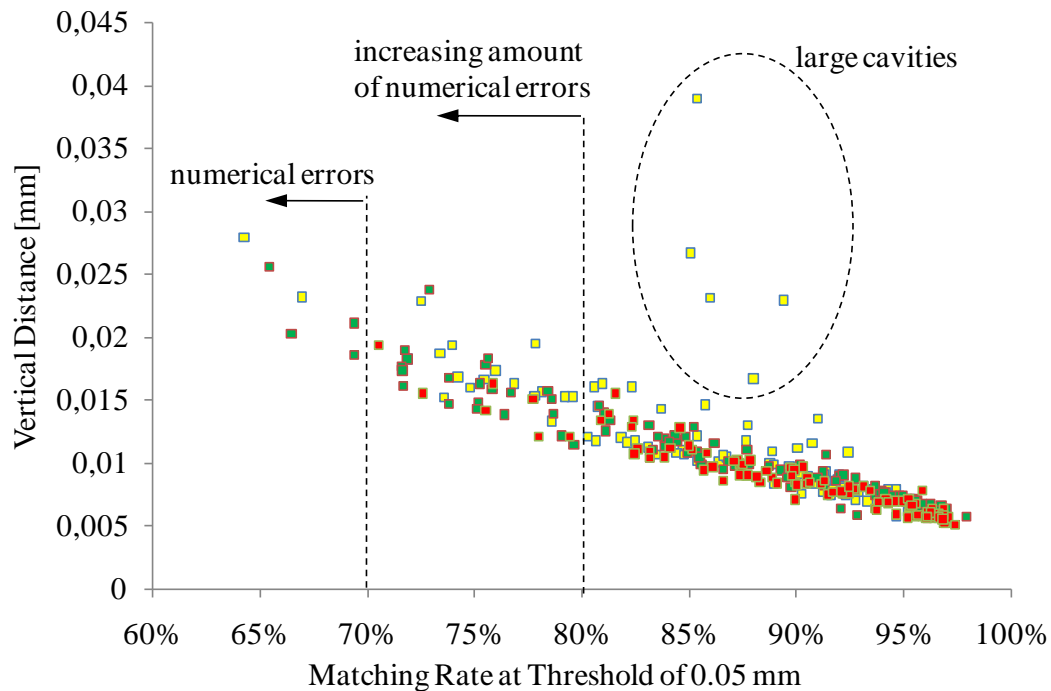


Figure 5-15: Vertical distance in dependence of matching rate at a threshold of 0.05mm with markings for an area containing large cavities, an area with an increasing amount of numerical errors as well as an area containing pure numerical errors

In summary, the parameter “Correlation of Matching Rate and Vertical Distance” enables a fast and fairly certain differentiation between invalid alignment data, i.e. numerical errors, and cavities. It therefore enables a reliable determination of the matching quality and gives a hint concerning the error rate of the numerical surface alignment.

5.4 Surface Inspections

During the separation test the fractured surfaces of each specimen have been inspected visually. This inspection aimed primarily at the detection of particles at the fractured surface. From each laser notch batch photos were taken in order to visualize the different surface topologies.

Four specimens per laser batch had not been manufactured completely. They were removed from production directly after the cracking process, that is, the big eye was not honed leaving their laser notches unaltered and available for analysis. These samples have been inspected with a SEM device. Figure 5-16, Figure 5-17 and Figure 5-18 show, for each batch, typical samples of the surface texture (left hand figure) and the laser notch (right hand figure).

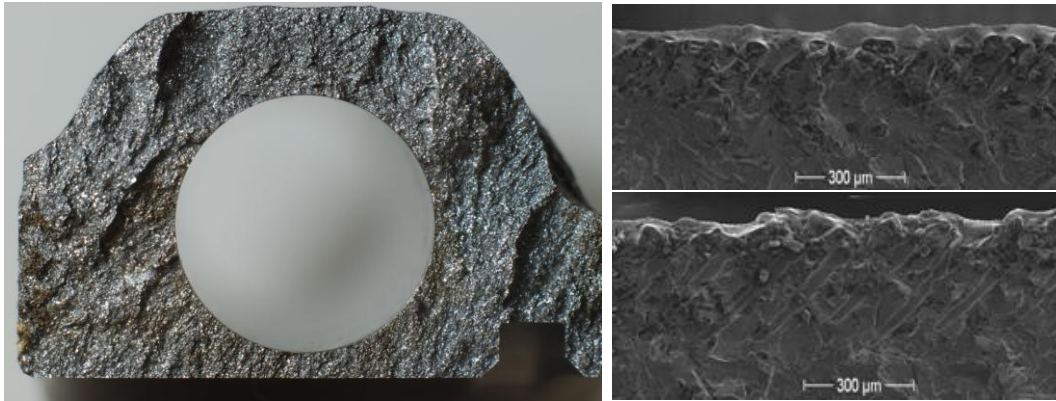


Figure 5-16: Sample of the yellow laser batch (left) and SEM pictures of two typical laser notches with a depth of about 0.2mm (top right) and 0.4mm(bottom right)

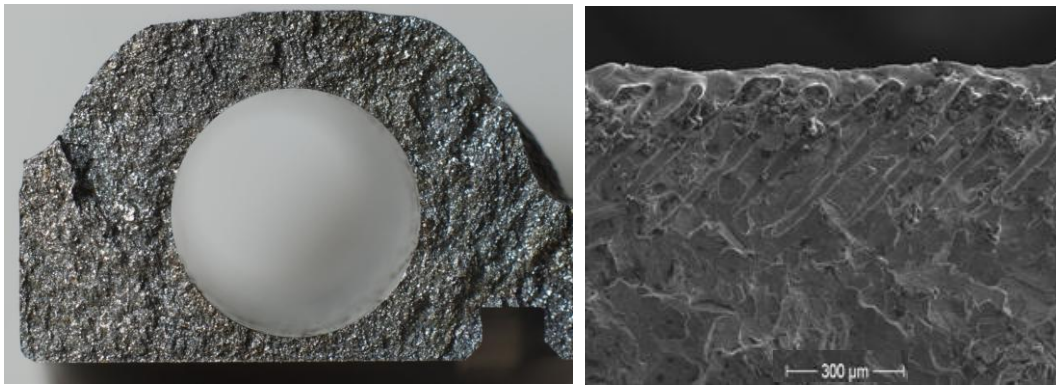


Figure 5-17: Sample of the green laser batch (left) and SEM picture of a typical laser notch with a depth of about 0.6mm (right)

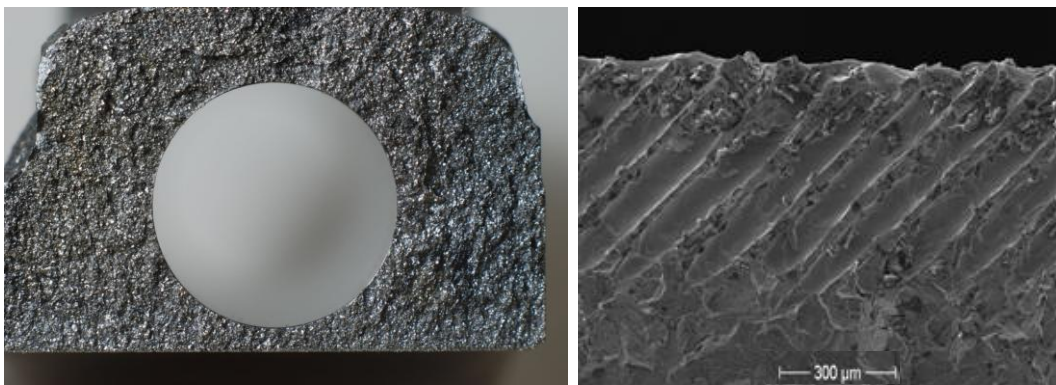


Figure 5-18: Sample of the red laser batch (left) and SEM picture of a typical laser notch with a depth of about 0.8mm (right)

The depth of the laser notch of the yellow batch (see Figure 5-16) varies between 0.2mm and 0.4 mm, both are depicted. The laser holes forming the notch vary strongly in depth and shape. As a result, all specimens of this batch have a very distinct topology. The outside of several specimen surfaces⁵² show a step with a height of up to 1.5mm. According to (Blauel, et al., 2000) (see Section 2.5.3) this is the result of unwanted torsion load that appeared during the fracture splitting process. Furthermore, on the surface of three specimens of the yellow batch, imprints of particles of a size of more than 1mm were found. These imprints are local plastic deformations of the surface that are located in the same area on both parts of a specimen (see Figure 5-19). The measured separation force of these specimens was “0N” (see Section 5.2).

In the green batch (see Figure 5-17) the depth of the laser notch was measured to be about 0.6mm without any noteworthy deviation. All laser holes that form the notch have a similar but not clearly definable shape. The specimens of this batch have a less distinct topology than the yellow batch. As in the yellow batch steps could be found on the surface of several specimens in a comparable number and size. Imprints of large particles were not found.

The depth of the laser notch of the red batch (see Figure 5-18) was measured to be about 0.8mm. All laser holes have a similar and distinct shape. All specimens have in common that the surface topology is rather smooth without any larger elevations. The only specimens with larger deviations are those specimens with a step on the surface. The height of these steps, however, does not exceed 1mm. The number of specimens with steps is comparable to those of the other laser notch batches. During the separation tests five specimens could be separated without any measurable force. Unlike those specimens of the yellow batch these specimens show no imprints of emplaced particles. Instead, these five specimens have a very plane topology compared to all other specimens irrespective of the batch.

Besides these specific characteristics, the specimens of all laser notch batches have one thing in common. In each laser notch batch, a small number of specimens was either contaminated by small visible particles of a size less than 0.5mm or showed imprints of particles of that size. These particles did not influence the result of the separation test. Furthermore, confined areas of the fractured surface of nearly all specimens were polluted by substances and remainders of the manufacturing process. These substances have not been removed before the tests to

⁵² The outside of a sample surface is the area of the fractured surface located behind the bolt bore viewed in the direction of the crankshaft / laser notch

keep the characteristic of the surfaces as realistic as possible. Because nearly all specimens were affected the effect on the measurement could not be identified.

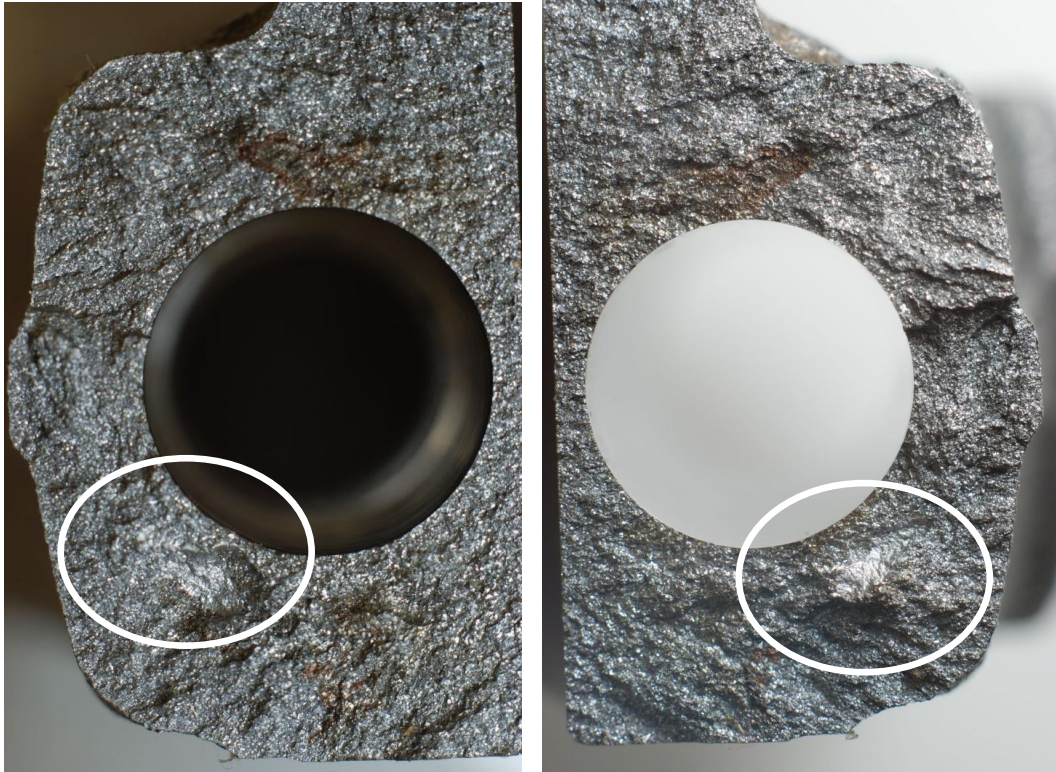


Figure 5-19: A sample with an imprint of an emplaced particle (marked with a circle)

5.5 Conclusions

In this chapter the results of the analyses of the fractured surfaces have been presented and a set of parameters has been determined in order to verify research hypothesis (1) proposed in Section 4.1.1.

The following results have been achieved:

Hypotheses (1):

Parameters that are able to describe different fractured surfaces can be obtained by adjusting and combining standardized roughness parameters.

To verify this hypothesis, separation tests as well as an analysis of the laser scanner data of single surfaces and of surface pairings have been performed.

The parameter Sliding Average Inclination Angle was found to describe the characteristic surface topology of a fractured surface with acceptable results. Fur-

thermore, the combination of the parameters Matching Rate and Vertical Distance provided good indication of the matching quality of a pair of fractured surfaces and enabled the differentiation between large cavities and numerical errors resulting from data processing. The results confirmed the hypothesis.

Additionally, the following findings were obtained:

The roughness parameters Average Roughness and Maximum Roughness defined in (ISO4287, 2010) need to be adjusted to the special boundary conditions of fractured surfaces. However, the proposed, modified roughness parameters failed to describe the characteristic surface topology of the fractured surfaces. The same applies to the proposed parameter Point-to-Point Inclination Angle. Further research is necessary to identify proper parameters for describing the roughness.

The average matching rate of a fractured surface pairing is about 88%. This value confirms our earlier estimations of a matching rate of about 90% (Lyszczan, et al., 2007).

The influence of the depth of the laser notch on the topology of the fractured surface was confirmed. Short laser holes result in a very distinct surface topology while long laser holes result in a rather smooth surface topology. Short laser holes can cause large cavities.

The occurrence of large particles can be verified by imprints within the fractured surface of both parts of a pairing. These imprints are local plastic deformations of the surface topology.

If no force is needed to separate two fractured surfaces and the surfaces have a very distinct topology, it is highly likely that the fractured surface contained large particles. However, when the surfaces are smooth a separation force of “0N” hardly ever points at a large particle.

6 Con-rod Bolting Specimen Tests

In this chapter the test series and the test results of the con-rod bolting specimens are described. These tests have been carried out in order to verify the research hypotheses established in Sections 4.1.2 and 4.1.3.

First, the tests for the determination of the relaxation losses are described followed by a report about the tests to determine the transferrable shear loads. Subsequently, results of a numerical analysis of the transferrable shear loads are presented and compared with the results of the experimental shear load transfer tests. Finally, the research hypotheses are verified.

6.1 Relaxation Tests

The relaxation tests aim for the verification of the research hypotheses (2), (3) and (4) described in Section 4.1.2:

Question: What is the impact of fractured surfaces on the relaxation of bolted joints?

Hypothesis: The fractured surface has a significant impact and cannot be ignored in the calculation of the bolted joint.

Question: What is the relation between surface topology and the amount of relaxation losses?

Hypothesis: The more distinctive the surface topology, the larger is the amount of relaxation losses.

Question: What is the effect of moderately increased temperature on the amount of relaxation losses?

Hypothesis: A moderate increase of temperature results in an exponential loss due to relaxation.

In detail the following tasks were performed:

- Specification of the impact of fractured surfaces on the relaxation of bolted joints in order to verify hypothesis (2)
- Determination of the relation between surface topology and amount of relaxation losses in order to verify hypothesis (3)
- Identification of the possible indirect impact of surface topology on relaxation in fractured surfaces due to the potential problems mentioned in Section 3.4:

- Mismatched assembly of con-rod cap and body at rather smooth surface topologies (red laser notch batch)
- Embedment of particles into the surface in the case of rough surfaces (yellow laser notch batch).
- Determination of the expected impact of dynamic loads of mechanical origin on the relaxation losses (see Section 3.3)
- Specification of the effect of temperature on the amount of losses in order to verify hypothesis (4)

6.1.1 Relaxation Test Series

Eight test series were investigated. In each test series all specimens were tested at the same time in the same set up. An exception is the dynamic mechanical load test, for which a serial testing procedure was necessary due to the limited amount of test beds available. To ensure accurate bolt elongation measurements in each test series, the bolt preparation, bolt assembly, and bolt post-processing followed the procedure described in Appendix II.5.

Below, for each test series the label and the specific test aims are summarized (see also Table 6-1). In addition, the number of specimens, their laser batch classification, as well as a set of the specific test parameters is presented.

The following test series have been carried out:

Relax_Ref:	reference test series identify relation between surface topology and amount of losses 15 specimens per laser batch (Σ 45 specimens) stored for 168h in a drying kiln at 150°C
Relax_Plan:	specify amount of losses with plain surface joint 6 specimens of red laser batch previously fractured surfaces planished by spark erosion average roughness of the planished surface $R_z \sim 1.6$ stored for 168h in a drying kiln at 150°C
Relax_MA:	specify amount of losses due to mismatched assembly 6 specimens of red laser batch assembled with a mismatch of 0.2mm along crankshaft axle stored for 168h in a drying kiln at 150°C
Relax_1P:	specify amount of losses due to a small amount of particles 10 specimens of yellow laser batch during assembly 1 particle (weight 7mg) placed within joint stored for 168h in a drying kiln at 150°C

- Relax_3P:** specify amount of losses due to a large amount of particles
5 specimens of yellow laser batch
during assembly 3 particles (overall weight ~37mg) placed
within joint
stored for 168h in a drying kiln at 150°C
- Relax_T1:** specify effect of temperature on the amount of losses
10 specimens per laser batch (Σ 30 specimens)
stored for 168h in conditioned room at 22°C
immediately after , stored for 168h in a drying kiln at 150°C
subsequently same specimens used for test series Relax_T2
- Relax_T2:** specify effect of temperature on the amount of losses
10 specimens per laser batch (Σ 30 specimens) from
test series Relax_T1
stored for 168h in conditioned room at 22°C
immediately after, stored for 168h in a drying kiln at 150°C
- Relax_Dyn:** specify amount of losses due to mechanical, cyclic loading
10 specimens per laser batch (Σ 30 specimens)
tumescant load (4.5kN static load + 4.5kN dynamic load)
 $5 \cdot 10^6$ load cycles at 60Hz in hydropulser with a tube furnace
at 150°C
subsequently stored for 168h in a drying kiln at 150°C

In Table 6-1 provides a short overview of the test series.

Test Series		Specimen per Laser Batch			Temperature & Duration		Remarks	
Name	Mode	Yellow	Green	Red	22°C	150°C		
Relax_Ref	Static	15	15	15		168h		
Relax_T1		10	10	10	168h	168h		
Relax_Plan				10			168h	planished surface
Relax_MA				6			168h	Mismatched assembly
1Part		10					168h	1 particle 7mg
3Part		5					168h	3 particles Σ 37mg
Relax_T2	dynamic	10*	10*	10*	168h	168h	* Relax_T1specimens	
Relax_DYN		10	10	10		168h	tumescant load	

Table 6-1: Test series for relaxation tests with con-rod bolting specimen

6.1.2 Inspections after Relaxation Tests

At the end of each relaxation test series all specimens were disassembled in order to measure the plastic bolt elongation and to visually inspect the fractured surfaces.

For most of the test series the inspections did not provide additional information. Noticeable deformation or plasticization of the surface topology could not be observed in test series Relax_Ref, Relax_Plan, Relax_T1, Relax_T2 and Relax_Dyn..

The specimens of test series Relax_1P and Relax_3P showed the typical imprints of particles on the fractured surface. This was expected due to the placement of particles in the joint at the beginning of these test series. The imprints looked very similar to those of the particles found during the disassembly of the con-rods as discussed in Section 5.2 (see also Figure 5-19).

In test series Relax_MA the influence of a mismatched assembly on the relaxation loss was examined. Plastic deformations were observed all over the surfaces, as expected. The combined deformed areas of each specimen were rather small. Based on the material properties of the con-rod material⁵³ and an initial preload of 51kN⁵⁴ the expected macroscopic contact area was calculated to be about 14% of the overall surface area. Although the deformed area was not measured, the visual inspections suggest that the calculations and real deformations have about the same magnitude.

To confirm this estimate, the event of a mismatched assembly was simulated numerically with the use of the laser scanner data collected before the relaxation test. This simulation started from the final state of the matching rate analysis described in Section 5.3.2. At this point both surfaces were separated by 0.05mm. Then, one of the surfaces was displaced by 0.2mm in the same direction as in the real test. After that, both surfaces were moved together again in steps of 0.001mm until the sum of contact area and penetration area reached a value of 14% of the overall surface area. Areas where penetration takes place are supposed to show distinct signs of plastic deformation. Besides, these penetration areas should be located at

⁵³ Based on a tensile strength of about 900N/mm² (information from bulletin of the con-rod manufacturer) the penetration hardness is about 2400N/mm².

⁵⁴ Based on the bolting procedure instructions of the con-rod manufacturer, the initial installed preload is about 51kN – 52kN.

the same locations as the deformed areas of the real specimen (the simulation was based on data of the real specimen).

Figure 6-1 shows the result of the scanner data analysis and the photo of a specific specimen. The blank areas of the real specimen represent the areas with deformation due to the mismatched assembly process. These areas should correspond with the penetration areas and potentially with the contact areas. Due to low quality of the photograph a comparison is difficult. However, the small overall area of contact of the data analysis and the deformed areas seem to be of the same magnitude. A scan of the surface with a laser scanner would have allowed a detailed comparison but could not be realized for practical reasons.

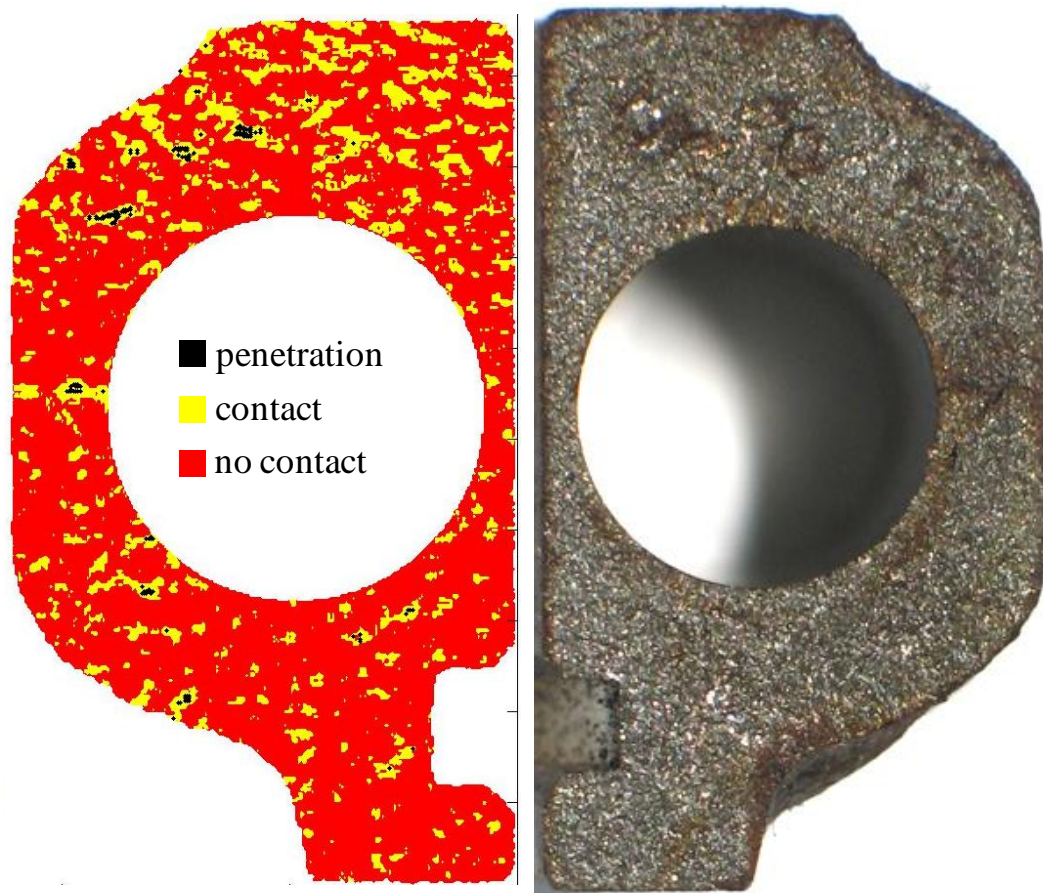


Figure 6-1: Photo of specimen R10A after relaxation test with mismatched assembly (right) and contact analysis of the laser scan data of the same specimen before the test with potential areas of deformation for a matching rate of 14% of the overall area (left - mirrored)

6.1.3 Relaxation Test Results

Figure 6-2 shows the loss of elastic elongation as percentage of the maximum elastic elongation for each test series. Each bar represents the average relaxation loss of all specimens of all three laser notch batches of a whole test series⁵⁵. The dual colored bars of the test series Relax_T1 and Relax_T2 represent the average relaxation losses of the tests at 22°C (light colored bar) and at 150°C (dark colored bar). Note that the specimens used in test series Relax_T2 were those used in test series Relax_T1. Furthermore, the values in each test series covered a wide range. Which of the differences between the test series are significant is discussed in the subsequent sections.

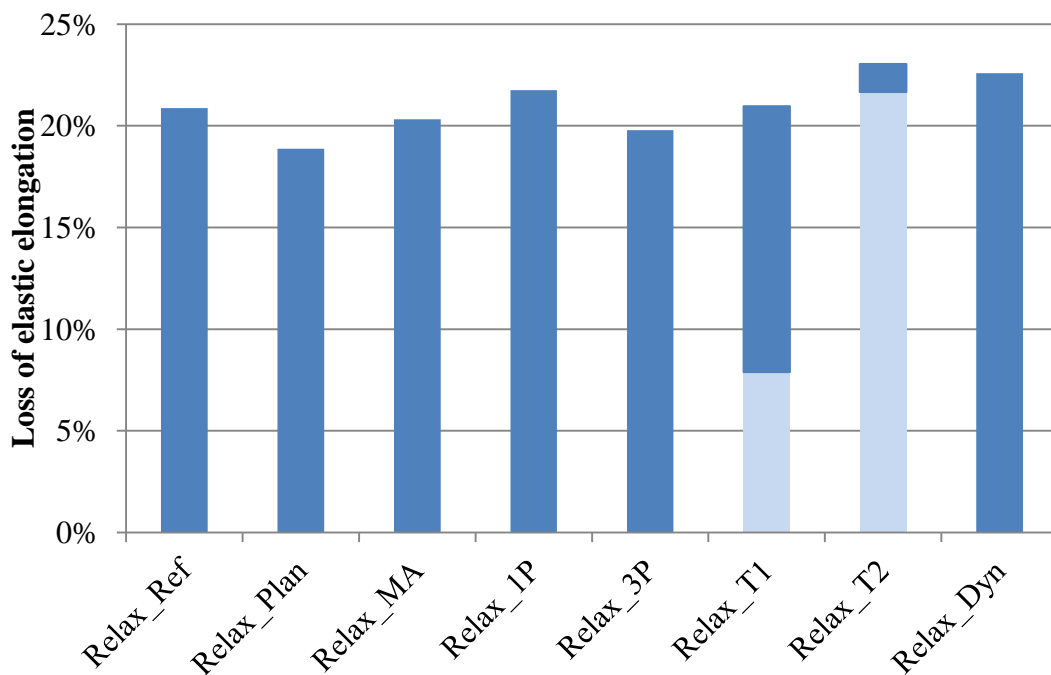


Figure 6-2: Overall elongation loss of elastic elongation of the relaxation tests with con-rod bolting specimens at 150°C (dark bar color) and 22°C (light bar color)

Values for average relaxation loss, RMS value and boundaries of the scatter area are provided in Table 6-2. Note that each of the test series had different combinations of laser batches.

⁵⁵ For details see Appendix III.1.

	Relax_Ref	Relax_Plan	Relax_MA	Relax_IP	Relax_3P	Relax_T1	Relax_T2	Relax_Dyn
Average	20,87%	18,88%	20,32%	21,75%	19,78%	20,97%	23,04%	22,59%
RMS	2,01%	1,11%	0,73%	1,99%	0,85%	2,08%	3,25%	2,35%
Maximum	24,77%	20,28%	21,25%	26,32%	20,96%	25,67%	29,66%	29,38%
Minimum	16,52%	17,05%	19,11%	18,81%	18,78%	16,30%	15,86%	18,20%
Specimens	45	10	6	10	5	30	30	30
Tests at 22°C						Mean	7,88%	21,65%
						RMS	1,22%	2,07%
						Max	10,74%	25,49%
						Min	3,50%	14,38%

Table 6-2: Relaxation loss data from tests with con-rod bolting specimens at 150°C (mind exceptions) as percentage of maximum elastic elongation of each specimen

6.1.3.1 Impact of fractured surfaces onto relaxation

To specify the impact of fractured surfaces on the relaxation of bolted joints the test series Relax_Ref and Relax_Plan were compared (see Figure 6-3). The loss of elastic elongation in the reference test series Relax_Ref is about 20.9% L_{max} , the maximum elastic elongation of each bolt at the end of the tightening process. In test series Relax_Plan with the planished surfaces, the relaxation loss is about 18.8% L_{max} .

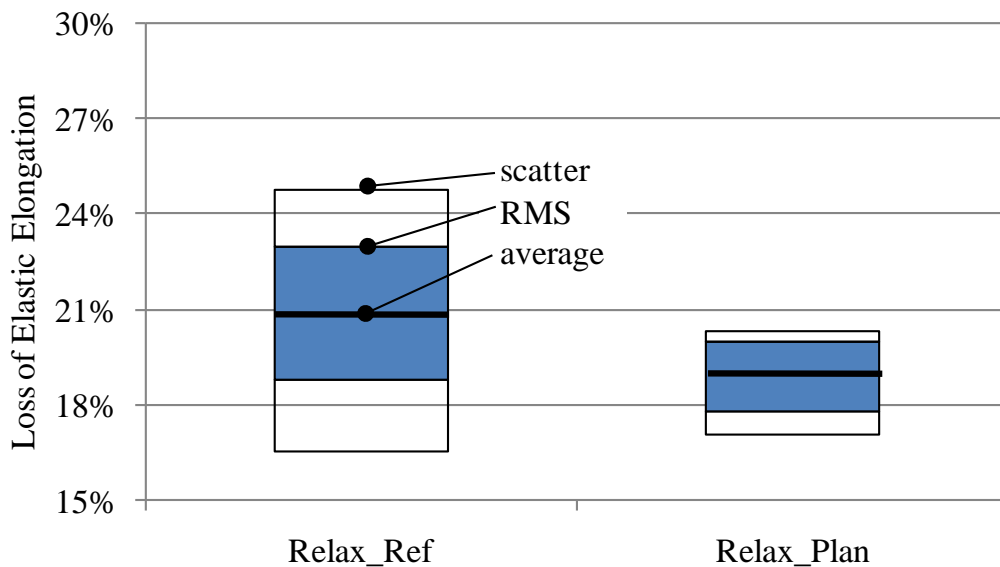


Figure 6-3: Relaxation losses at 150°C of the reference test series Relax_Ref (n=45) and the test series with planished joint surface Relax_Plan (n=6)

Although the figure may show a certain tendency, the differences were found to be statistically indifferent. A higher number of specimens is required in order to confirm or reject the effect of fractured surfaces on relaxation losses.

According to (VDI2230, 2003) rough surfaces should generate higher relaxation losses than smooth ones. In (VDI2230, 2003) the joining surfaces are rough and have a random topology. In a pair of fractured surfaces, both surfaces share a very similar topology so that the overall surface roughness used in (VDI2230, 2003) does not describe the contact status properly. Consequently, the common rule that rough surfaces generally lead to higher losses is not suitable for joints with fractured surfaces.

6.1.3.2 Relation between surface topology and amount of losses

In test series Relax_Ref, Relax_T1 and Relax_DYN specimens from all three laser notch batches were used. The different laser notch batches have different surface topologies (see Section 5.4). In none of the test series a significant difference between the laser notch batches could be identified (see Figure 6-4).

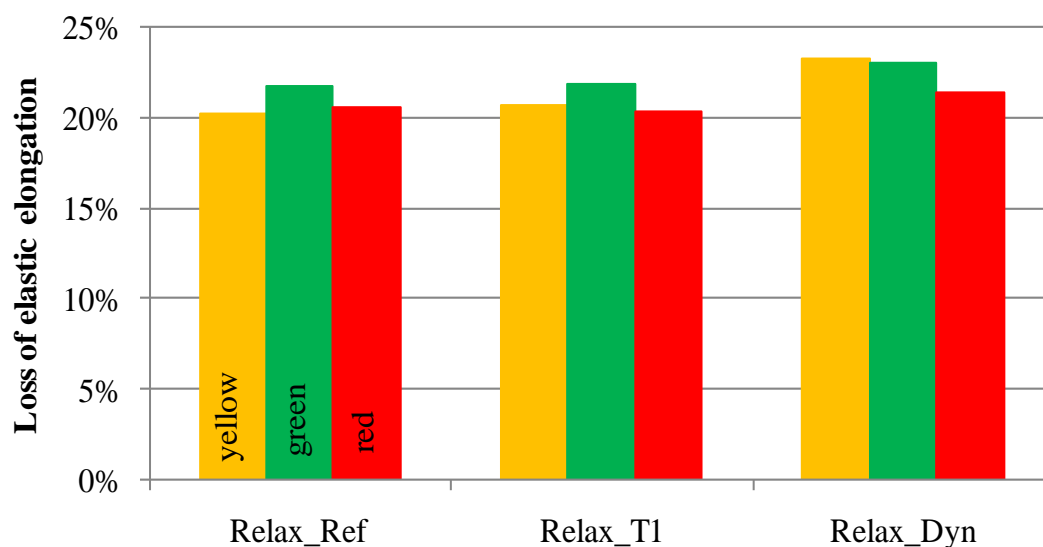


Figure 6-4: Relaxation losses at 150°C of test series Relax_Ref (n=15 per batch), Relax_T1 (n=10 per batch) and Relax_Dyn (n=10 per batch) with itemization of laser notch batches

This result leads to the conclusion that the amount of relaxation loss is independent of the surface topology. This is the case for all batches. That is, the matching rate is more important than the actual macroscopic topology. The reason for this behavior can be found in those material properties which play a major role during the fracture splitting process. The process of fracture is located in the brittle-ductile transition area at the border of a pure brittle fracture behavior. Only about

8% of the fracture process has a ductile character: The overall fracture behavior is brittle. As a result, the shapes of a pair of fractured surfaces at a macroscopic level are very similar independent of the laser batch. The matching rate of about 87% of fractured surface pairs discussed in Section 5.3.2 underlines this conclusion. At a microscopic level, however, differences can be found. These cause the range of values within a batch.

6.1.3.3 Impact of mismatched assembly onto relaxation losses

Fractured surfaces with a rather smooth surface topology have a noticeably increased risk of mismatched assembly in comparison to fractured surfaces with a rough surface topology where the surfaces more easily “find” the fitting position. The test series Relax_MA aimed at the identification of the impact of such mismatched assembly (see Figure 6-5) and involved only specimens of the red laser notch batch with its rather smooth surface topology. The average relaxation losses were measured to be around 20.3% L_{\max} and do not significantly differ from the relaxation losses of the reference test series, which involved specimens of all laser batches.

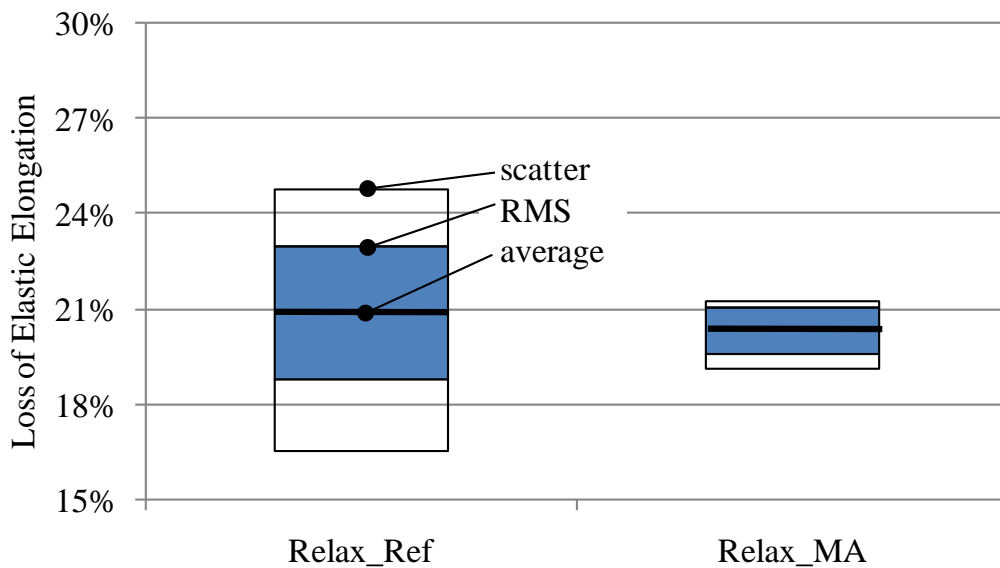


Figure 6-5: Relaxation losses at 150°C of reference test series Relax_Ref (n=45) and test series Relax_MA (n=10) with systematic mismatched assembly

This implies that a mismatched assembly of a joint with smoothly fractured surfaces does not result in additional relaxation losses. The smooth surface topology enables a considerable amount of contact area relatively independent of whether the two surfaces are in the same relative position as intended. As a result, the smoothly fractured surface may be treated like a unified rough surface where the individual topology plays only a minor role.

The results of the visual surface inspection after the relaxation test and the result of a displacement simulation with the laser scanner data, described in Section 6.1.2, underline this assumption. Another indicator is the result of the numerical analysis of the shear load transfer of a surface pair with stochastically modified fractured surfaces which will be discussed in Section 6.3.3.

6.1.3.4 Impact of embedded particles onto relaxation losses

In fractured surfaces with a very distinct topology there is a notably increased risk of particle embedding during manufacturing (see Section 3.2.1). The impact of such embedded particles has been studied in test series Relax_1P and Relax_3P. Figure 6-6 shows the impact compared to the reference test series.

In test series Relax_1P with a single emplaced particle with a weight of 7g the average relaxation loss was found to be 21.8% L_{max} . This is slightly more than the losses in the reference test series, but both series show a large distribution. In test series Relax_3P three particles with an overall weight of 36g were placed into each specimen. The average relaxation loss was 19.8% L_{max} , which is slightly less than the losses in the reference test series, but the distribution is far less than that both Relax_Ref and Relax_1P. However, test series Relax_3P contained only 5 specimens. The relaxation losses of all test series do not differ significantly from each other.

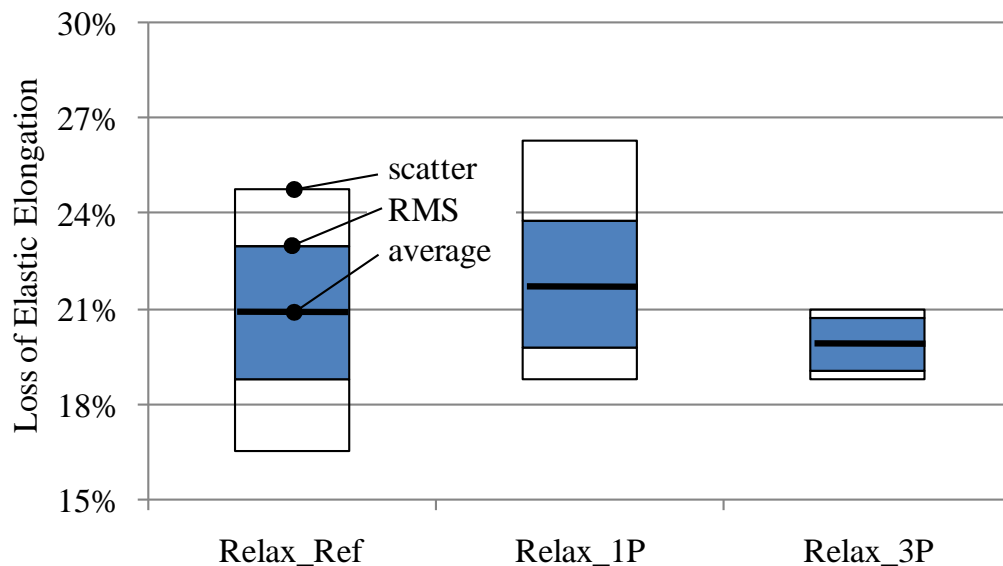


Figure 6-6: Relaxation losses at 150°C of reference test series Relax_Ref (n=45) and the test series Relax_1P (n=10) with 1 embedded particle and Relax_3P (n=5) with 3 embedded particles in the fractured surface

The tested particles were not found to have an impact on the relaxation loss. This result is contradictory to the findings in (Lyszczan, et al., 2007). A possible expla-

nation for this contradiction is the use of different particles of different origins within the research projects. The particles used in both research projects were not taken directly from the manufacturing process, but were replicated from con-rod material. The replication process was different in the two research projects.

In (Lyszczan, et al., 2007) the particles were obtained by planing a con-rod body. The produced particles were thick and compact and looked very similar to the two real particles found within the delivered con-rods. During the assembly process these particles were deformed plastically, but not in the exact shape of the surface topology. Due to their shape the particles were still a notable obstacle within the joint after the assembly process and still continued to deform up to the moment the test was stopped at the predetermined time of one week. This resulted among others (see Section 3.1) in extraordinary preload losses especially under operating temperature.

In this research project the planing machine was no longer available, so the particles had to be generated by sawing into a con-rod body. The obtained particles were comparatively thin, long, curly shape, which did not look like the shape of real particles. During the assembly process these particles were squeezed completely into the gaps between the fractured surface pairs. Due to this, it is assumed that the particles had no impact on the relaxation process.

6.1.3.5 Increase of relaxation losses through mechanical loads

In test series Relax_Dyn the specimens were dynamically loaded for 5×10^6 load cycles. The average relaxation loss was 22.6% L_{\max} . This test series shows a difference of about 2% L_{\max} compared to the reference test series (see Figure 6-7).

Against expectations (see Section 3.3) a significant difference between the impact of static and dynamic loading on the loss of elastic elongation could not be measured.

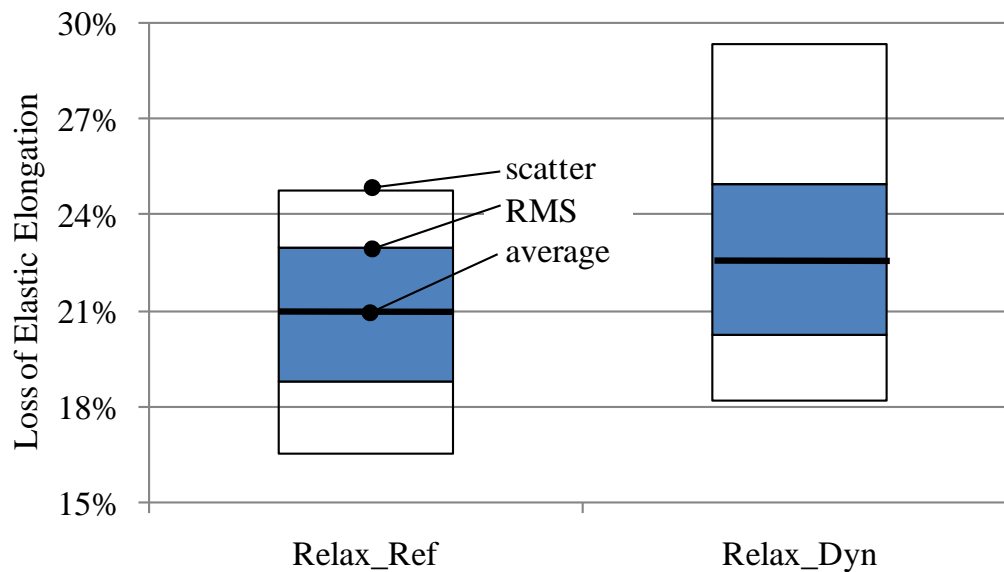


Figure 6-7: Relaxation losses at 150°C of reference test series Relax_Ref (n=45) and test series Relax_Dyn (n=30) after 5x10⁶ load cycles at 9kN tumescent load

6.1.3.6 Effect of temperature on relaxation losses

The aim of test series Relax_T1 was to specify the effect of temperature on the amount of relaxation losses. The results are shown in Figure 6-8. The average relaxation loss at 22°C after 168h was found to be 7.9% L_{max} . Subsequently, the specimens were stored in a kiln at 150°C for the same duration, resulting in a final average relaxation loss of 21.0% L_{max} . In test series Relax_T2 the specimens of Relax_T1 were stored for another 168h at 22°C. This only resulted in an increase of the average relaxation loss from 21.0% L_{max} to 21.7% L_{max} . Subsequently, the specimens were again stored in the kiln for 168h at 150°C. The final average relaxation loss was 23.0%.

It can be concluded that due to the highly significant relaxation loss measured in test series Relax_T1 after the storage in the kiln at 150°C temperature plays a major role in relaxation. This result meets the expectations⁵⁶. The difference of the final average relaxation of test series Relax_T1 and Relax_T2 and reference test series Relax_Ref is not significant. The slight increase of relaxation between the final states of Relax_T1 and Relax_T2 at 150°C is as expected. This leads to two conclusions. First, even moderately increased temperature has an eminent impact

⁵⁶ See section 2.4.4.

on the magnitude of relaxation. This finding is supported by the results of the literature mentioned in Section 2.4.4.

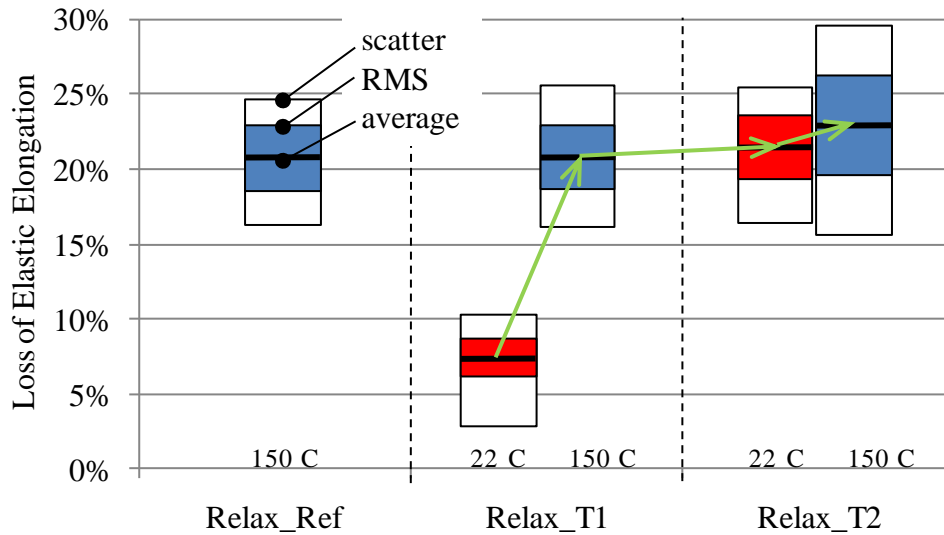


Figure 6-8: Relaxation losses of reference test series Relax_Ref (n=45), test series Relax_T1 and Relax_T2. Relax_T1 and Relax_T2 involved the same 30 specimens, which were measured 4 times at intervals of 168 hrs at different temperatures.

Second, any order of a mix of cool and warm relaxation has no additional impact on the final magnitude of relaxation loss. The measured amount of relaxation loss is slightly higher than the relaxation losses for standard bolted joints introduced in Section 2.4.4. The slight difference is of no statistical significance, so it can be assumed that the same increase of relaxation at moderately increased temperatures will occur in bolted joints with plane surfaces and with fractured surfaces.

6.2 Transferrable Shear Load Tests

The tests for the determination of the transferrable shear load aim for the verification of the research hypotheses (5), (6) and (7) situated in Section 4.1.3.

Question: What is the impact of the clamping force on the transferrable shear load in a bolted joint with fractured surfaces?

Hypothesis: The amount of transferrable shear load (F_Q) in a bolted joint with fractured surfaces is determined by the magnitude of the clamping force (F_N) in the following way: $F_Q = \mu_{\text{effective}} \cdot F_N$. (The effective friction coefficient is to be determined by experiments.)

Question: What is the relation between surface topology and transferrable shear load?

Hypothesis: The more distinctive the surface topology, the larger is the effective friction coefficient. The larger the effective friction coefficient, the larger the transferrable shear load (see question 5). Hence: the more distinctive the surface topology, the larger the transferable shear load.

Question: What is the effect of moderately increased temperature on the maximum transferrable shear load?

Hypothesis: A moderate increase of temperature decreases the amount of transferrable shear load slightly.

In detail the following tasks have been performed:

- Specification of the impact of clamping force on transferrable shear loads in fractured surfaces according to hypothesis (5)
- Determination of the relation between surface topology and amount of transferrable shear force to verify hypothesis (6)
- Identification of the impact of contact time on transferrable shear load according to influencing factors of friction mentioned in Section 2.1.1.3
- Specification of the effect of moderately increased temperature on the amount of transferrable shear force to verify hypotheses (7)

6.2.1 Shear Load Test Series

For the measurement of the transferrable shear load six test series were prepared. Test parameters are the installed preload, the ambient temperature during test run, and the state of relaxation. In Table 6-1 a summary about the shear load test series is provided.

The preload levels of the first four test series have been chosen according to the results of the FEM calculations described in Section 6.3.4. This allows a direct comparison between experimental und numerical data. These test series are labeled according to their nominal preload⁵⁷ 10kN, 20kN, 30kN and 40kN. The shear load test was performed immediately after the bolting process of each con-rod bolting specimen. This way the impact of relaxation was minimized⁵⁸. The

⁵⁷ The preload of each bolted joint was measured individually and was found to differ up to 1.95% from the nominal value.

⁵⁸ Despite the short time between bolting and test a relaxation loss of up to 2% of the installed preload can be expected.

temperature during the bolting process and the test was kept constant at 22°C. The aim of these test series was the specification of the influences of preload and surface topology on the transferrable shear load.

The last two test series were loaded with a preload of 51kN according to the assembly specification of the con-rod manufacturer. Additionally, the specimens were subjected to 168h of relaxation under operation temperature condition (150°C). Due to this relaxation, the average preload of the specimens had a magnitude of 41kN⁵⁹ at the beginning of the shear load test. This relaxation loss is in line with the findings described in Section 6.1.3. The test series in which the shear load test was performed under operating temperature conditions was labeled Yield_warm. The test series Yield_cold involved shear load tests performed at 22°C. These test series aim at determining the influence of temperature on the transferrable shear load.

The results of test series 40kN has also been compared with the two test series Yield_cold and Yield_warm to identify the effect of contact time on the transferable shear load. The test series 40kN specimens were tested immediately after bolting and in the other two series 168h after bolting.

Test Series		Specimen per Laser Batch			Test Temperature		Contact Time per Specimen	Remarks
Name	nominal Preload	Yellow	Green	Red	22°C	150°C		
10kN	10kN	5	5	5	X		2 min.	
20kN	20kN	5	5	5	X		2 min.	
30kN	30kN	5	5	5	X		2 min.	
40kN	40kN	5	5	5	X		2 min.	
Yield_cold	41kN	5	5	5	X		168 h	Relaxation 168h at 150°C
Yield_warm	41kN	5	5	5		X	168 h	Relaxation 168h at 150°C

Table 6-3: Test series for shear load tests with con-rod bolting specimen

⁵⁹ The individual preload of each specimen after relaxation differed up to 8% from this nominal value.

6.2.2 Surface Inspections after Shear Load Tests

Most of the specimens of the shear load tests did not fail completely, that is, the bolt did not shear off and the specimens remained in a bolted state. In the remaining specimens the bolts sheared at the end of the test. Those specimens broke down into single parts. After the execution of the shear load tests the surviving specimens were disassembled and the fractured surfaces inspected visually. The following are the main findings concerning the surface deformations shown in Figure 6-9 as light areas on the surface.

First, it turned out that all fractured surfaces had been deformed plastically in different degrees. The higher the preload of the bolt, the more area of the fractured surface was deformed plastically. This is most obvious when comparing specimens of 10kN preload with specimens of 40kN preload.

Second, the appearance of the damage is quite different between the laser notch batches. The deformed areas at the specimens of the yellow laser notch batch were rather large in dimension but small in number. The deformed areas at the specimens of the red laser notch batch were rather small in dimension but large in number. At each preload level the overall size of the deformed areas was similar irrespective of laser notch batches. With increasing preload the overall size of the deformed area increases, but the characteristic distribution related to the particular laser notch batches remained.

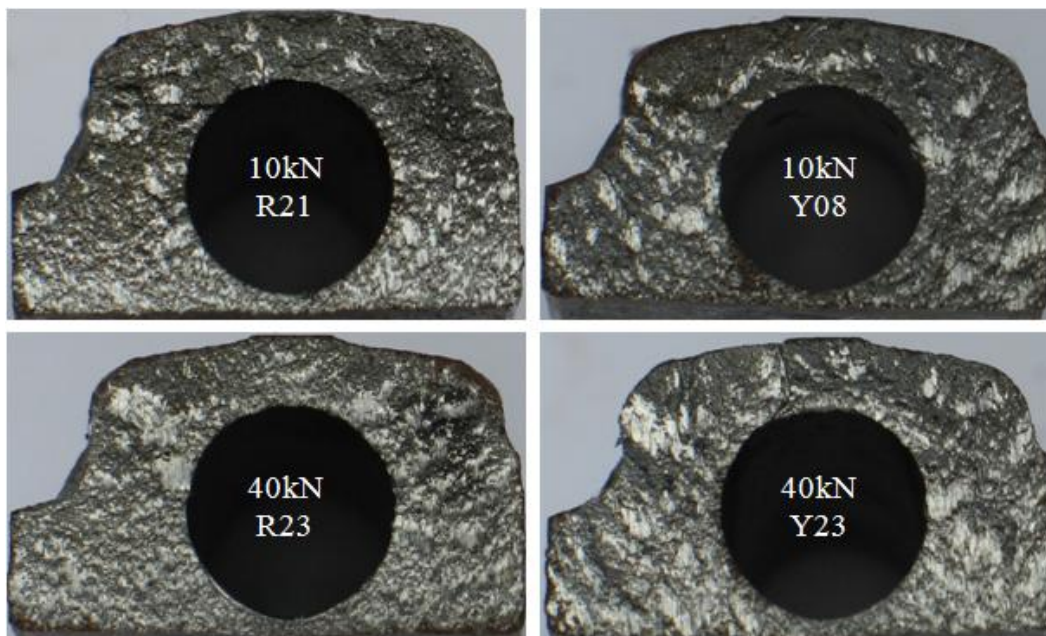


Figure 6-9: A comparison of specimens of test series 10kN (10kN preload - top) and 40kN (bottom) with samples from red laser batch (smooth surface topology - left) and yellow laser batch (distinct surface topology - right)

Finally, the defromed areas rise about 5° normal to the direction of shear force independently from the laser notch batch and the preload.

6.2.3 Shear Load Test Results

For the shear load tests the specimens are placed in a shear loading device in the hydropulser as shown in Figure 6-10 (see also Figure II-19 in the appendix). Each specimen is placed in the device in such a manner that the fractured surface is facing parallel to the direction of the load. The threaded part of the con-rod bolting specimen is placed in the passive part of the device while the other part of the specimen is the part on which the tie-bar of the device pulls. The contact area of specimen and shear load device was designed in such a way that the stiffness in the area of the fractured surface joint is not influenced by parts of the shear loading device.⁶⁰

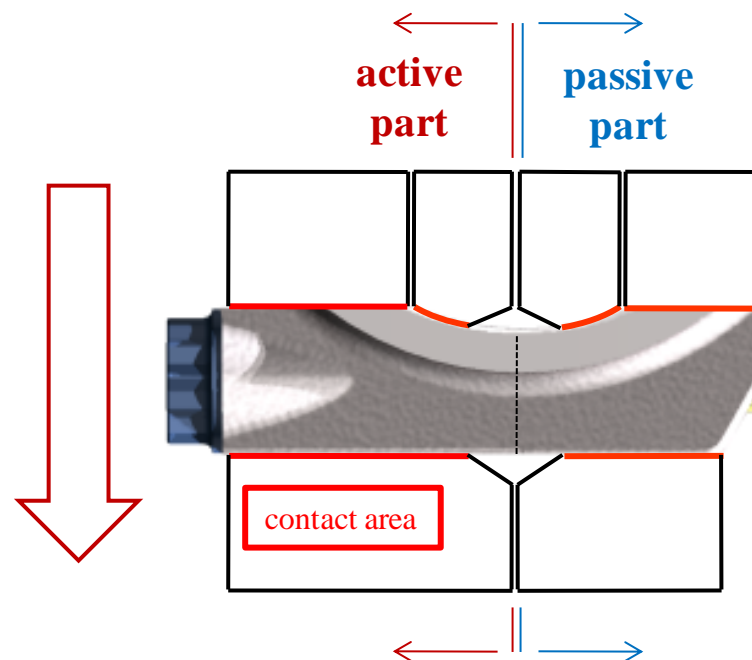


Figure 6-10: Schematic sketch of test set-up for shear load tests

During each shear load test the overall load at the device and the overall transversal movement of the tie-bar were recorded and plotted into a diagram as shown in Figure 6-11. The measured values of shear load and corresponding transversal

⁶⁰ The lack of influence of the device parts on the stiffness of the specimen was verified using FEM calculations. For further information see (Lyszczan, et al., 2010).

movement are shown as a continuous line. The diagram also shows a sliding average of the measured values (dashed line), its gradient (dotted line) and a trend line of the gradient in terms of a sixth grade polynom approximation (dash-dotted line).

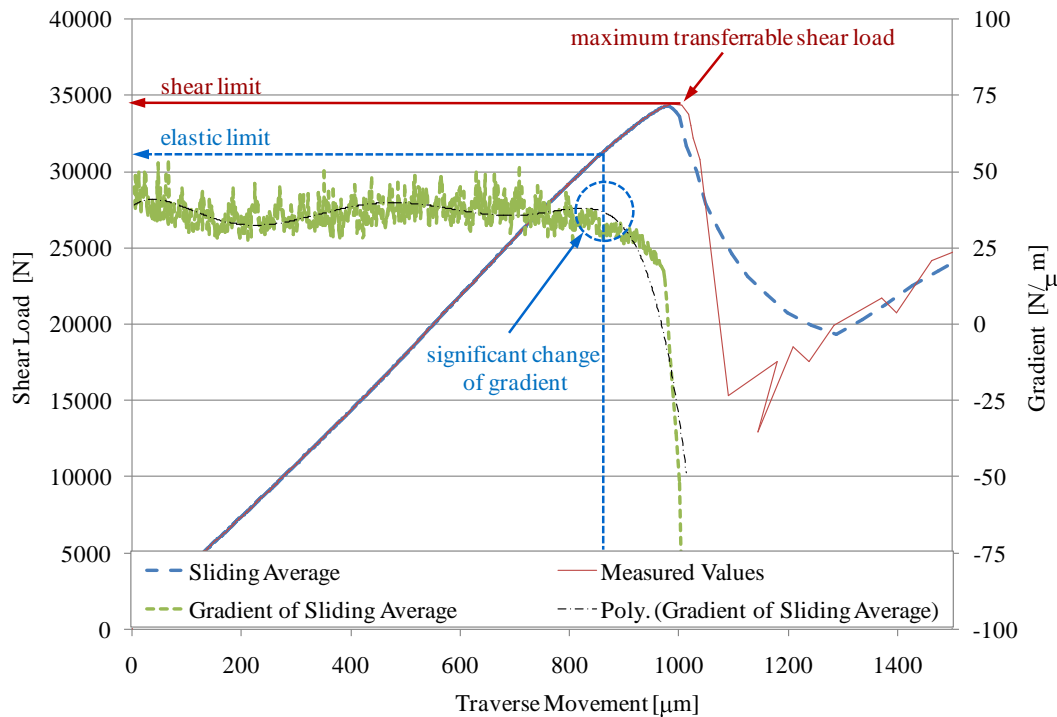


Figure 6-11: Diagram of shear load and hydraulic tie-bar displacement

The shear load in Figure 6-11 is equal to the measured force value at the load cell of the hydropulser. Due to the stiffness of the shear load device and the exact positioning of the specimen within the device, this measured force value is identical to the actual shear load in the fractured surface of the specimen. The bolt does not play a role because its diameter is about 1.2mm smaller than the hole. The transverse movement represents the sum of the elastic elongation of the overall device, the bending of the specimen and the cross traverse movement of the fractured surface of the specimen. Due to the high stiffness of the shear load device, its influence on the transverse movement can be neglected. The bending of the specimen was determined by tests with full body specimen of the same geometry, which showed a nearly constant gradient under shear load bending. Therefore the measured transverse movement is the combination of this bending behavior and the actual movement of the specimen.

It was expected that the curve of the shear load transfer is equal to a stress-strain-curve of a simple metal specimen. The curve of load and movement should be linear up to a certain extent. Then the inclination of the curve should decrease, the shear load should reach a maximum value, and then the curve should drop nearly

instantly. The maximum shear load value is defined as the maximum transferrable shear load or the shear limit. The threshold between the linear section and the decreasing section of the curve is defined to be the elastic limit. It is assumed, that at this point plastic deformations start to occur within the fractured surface to a greater extent.

For the analysis the shear limit was easy to identify. To locate the elastic limit the measured data had to be processed. The unsteadiness of the measured values necessitates the calculation of a sliding average containing 20 values to smoothen the signal. Then the gradient of this sliding average was calculated. This gradient still had a rather poor signal-to-noise ratio so it was necessary to approximate its run with a polynomial of 6th degree. The range of values of this polynomial was monitored from test start to the point of the shear limit. The first 70% of this section was used to determine the typical scatter band of the gradient of the linear section of the curve. The point where this threshold was exceeded in the remaining 30% of this section was defined to be the elastic limit.



Figure 6-12: Con-rod bolting specimen after shear load test

At the end of a shear load test the specimens displace along the fractured surface as shown in Figure 6-12. Sometimes the introduced shear load is only partly transformed into plastic deformation of the fractured surface. In these cases the remaining shear load results in a bolt failure.

In Figure 6-13 an outline of the results of the shear load tests is shown. In this diagram each rhomb represents the average elastic limit of the transferred shear load of all specimens of all three laser notch batches in that test series. The bars represent the scatter range of the values of the specimens in each test series⁶¹. The cross and the small circle represent the averaged elastic limit of the test series with yield controlled tightening of the bolts and 168h relaxation storage at 150°C followed by the shear load test at 22°C and 150°C respectively.

⁶¹ For detailed information see Appendix III.2.

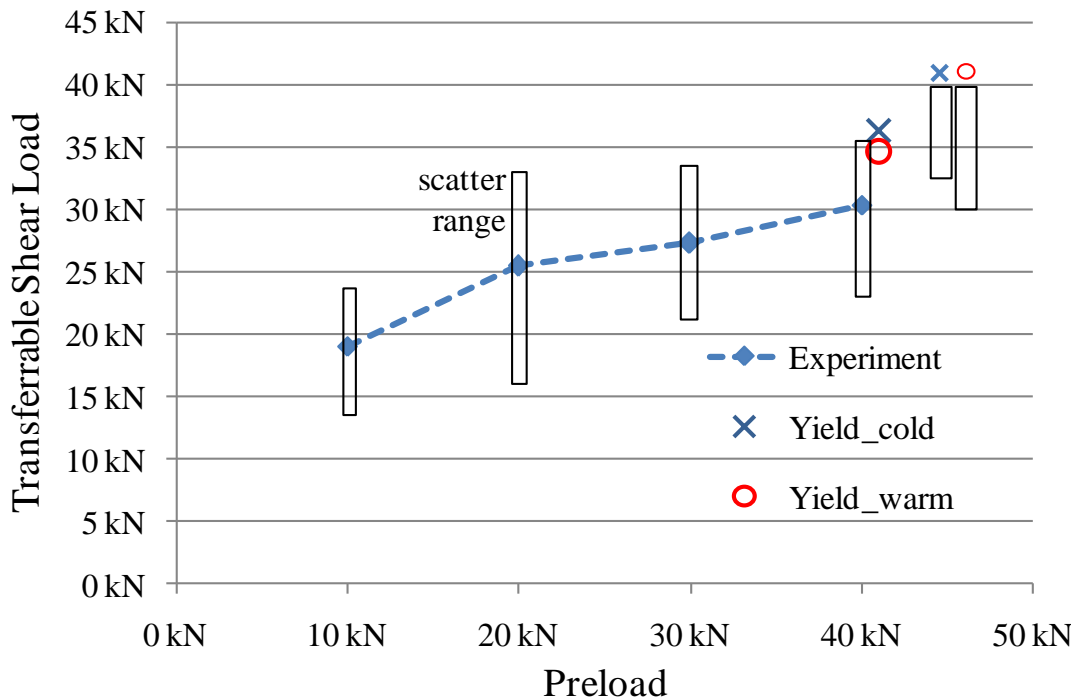


Figure 6-13: Average transferrable shear load and scatter range as a function of the installed preload of each test series

The average value, RMS value and limits of the scatter range of the elastic limit are provided in Table 6-4. A corresponding data set of the shear limit is shown in Table 6-5. All values were derived from the data of all laser notch batches that have been used for each test setup

	10kN	20kN	30kN	40kN	Yield_cold	Yield_warm
Preload	10.000 N	20.000 N	30.000 N	40.000 N	41.000 N	41.000N
Average	19.004 N	25.452 N	27.260 N	30.149 N	36.417 N	34.663 N
RMS	2.587 N	4.297 N	3.845 N	3.159 N	2.197 N	2.548 N
Maximum	23.793 N	33.199 N	33.031 N	35.507 N	39.029 N	39.190 N
Minimum	14.372 N	15.368 N	21.315 N	23.123 N	32.635 N	30.867 N

Table 6-4: Outline of the most important data of the shear load tests with con-rod bolting specimens with respect to the elastic limit

	10 kN	20 kN	30 kN	40 kN	Yield_cold	Yield_warm
Preload	10.000 N	20.000 N	30.000 N	40.000 N	41.000 N	41.000 N
Average	21.404 N	29.461 N	30.537 N	33.266 N	39.489 N	37.456 N
RMS	2.034 N	4.118 N	3.494 N	2.316 N	1.946 N	2.061 N
Maximum	25.874 N	37.367 N	36.800 N	38.402 N	43.765 N	42.446 N
Minimum	17.519 N	15.943 N	22.800 N	26.474 N	35.492 N	33.146 N

Table 6-5: Outline of the most important data of the shear load tests with con-rod bolting specimens with respect to the shear limit

For the following analysis of the test results only the values for the elastic limit are used. This is due to the fact that at this load level it is assumed that plastic deformation does not occur or only to a very limited extent. It can never be excluded that strongly protruding elements are plastically deformed.

6.2.3.1 Impact of clamping load on transferrable shear loads

The aim of test series 10kN, 20kN, 30kN and 40kN was to identify the impact of clamping load on the transferrable shear load. During the tests there was no axial load applied at the specimens except for a very small amount of parasitic axial load from the shear loader in order to lock the specimen. That is why the installed preload is considered equal to the clamping load. Based on the definition of the global friction coefficient described in Section 2.1.1.1, the ratio of preload and transferrable shear load is defined as the effective friction coefficient μ_{eff} .

As Figure 6-13 shows, a preload of 10kN allows, on average, the transfer of a shear load of 19.0kN. The effective friction coefficient μ_{eff} is in this case 1.9 (see Figure 6-14). A rise of preload by 10kN to 20kN increases the average transferrable shear load to 25.5kN, i.e. μ_{eff} is 1.28. A further step-up of the preload by 10kN to 30kN increases the average transferrable shear load to 27.3kN, which represents a μ_{eff} of 0.91. With 40kN preload an average shear load of 30.1kN can be transferred, giving a μ_{eff} of 0.75.

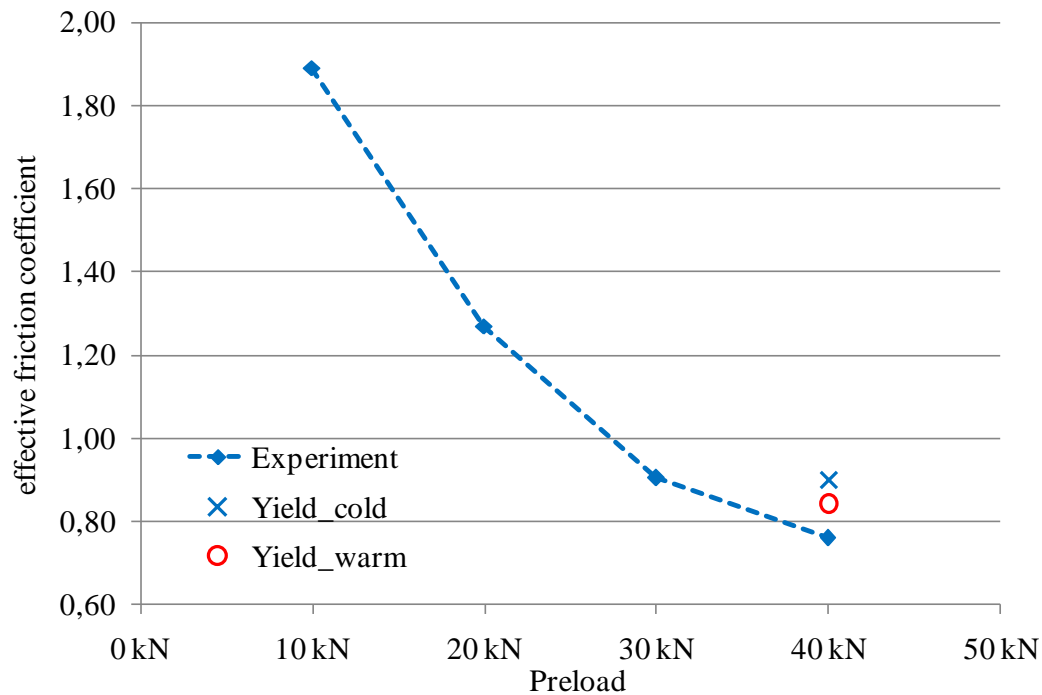


Figure 6-14: Effective friction coefficient as a function of the installed preload

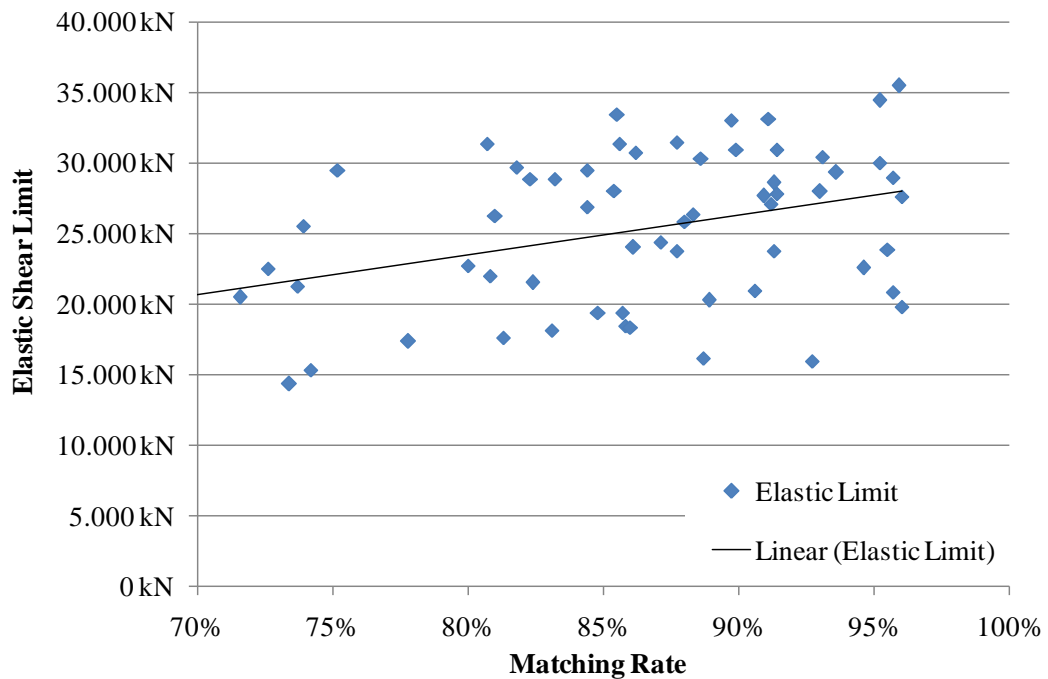
Within the range of preload considered in this research project the effective friction coefficient has a magnitude of 0.8 ~ 2. This is about one order of magnitude above the level of the static friction coefficient for inter-metallic contacts at room temperature $\mu_{\text{stat}} \approx 0.19$. Consequently, the transferred shear load in a joint with fractured surfaces is significantly higher than the transferred shear load in a joint with plain surfaces, i.e. the fractured surface topology increases the transferrable shear load significantly.

The transferrable shear load increases with increasing preload, and the effective friction coefficient decreases with increasing preload. This effect is statistically indifferent and accompanied by large scatter of the test values (see Figure 6-13). Nevertheless, a clear tendency is visible. This effect is not covered by the theory of the global friction coefficient (see Section 2.1.1.1). The global friction coefficient is independent of the normal force, i.e. the global friction coefficient is independent of the preload. An explanation for these results requires a mechanical model of a fractured surface joint which will be discussed in Chapter 7.

6.2.3.2 Relation between surface topology and transferrable shear load

The aim of this test series was to determine the relation of surface topology and transferrable shear load. In all six test series specimens from all three laser notch batches were used. For each preload level no differences between the laser notch batches could be identified.⁶²

Specimens with a very distinct surface topology transfer just as much shear load as specimens with rather smooth surface topology. The different types of surface topology have no impact on the amount of transferrable shear load. The most important parameter for the amount of transferred shear load is the overall size of the contact area. The overall contact area may consist of a small number of large areas, as well as of a large number of small areas. This conclusion is strongly supported by the results of the surface inspections after the shear load tests described in Section 6.2.2. Furthermore the tendency of a higher elastic shear limit with increasing matching rate is shown in Figure 6-15.



⁶² See Appendix III.2 for details.

Figure 6-15: Elastic shear limit of all specimens as a function of the matching rate with a linear trend line

6.2.3.3 Impact of contact time on transferrable shear load

The determination of the impact of contact time on the amount of transferrable shear load was the goal of test series Yield_cold in comparison to test series 40kN (see Figure 6-16). The average clamping load in test series Yield_cold was about 41kN after 168h storage at 150°C. The shear load test was conducted when the specimens had cooled down to 22°C. The average transferrable shear load in test series Yield_cold was about 36.4kN. This is 6.3kN more than in reference test series 40kN.

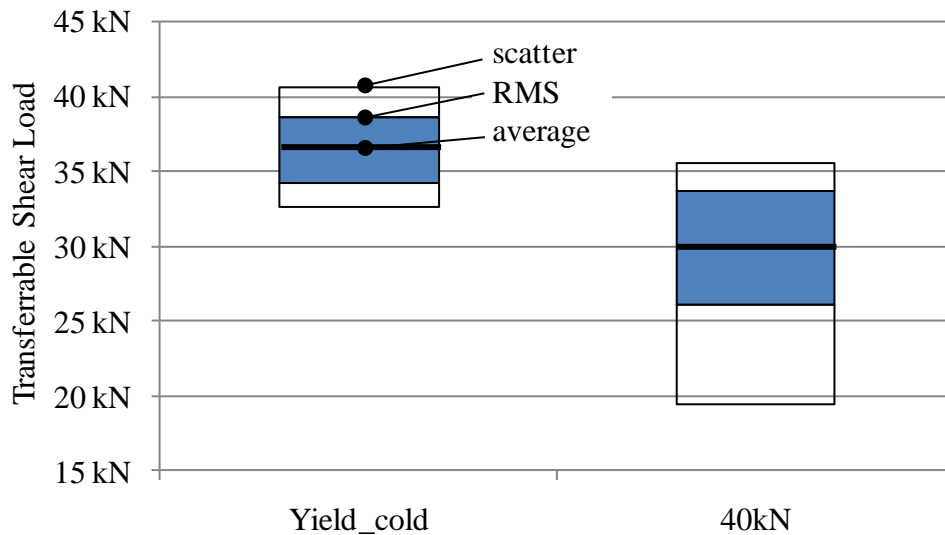


Figure 6-16: Transferrable shear load, including scatter range, of test series Yield_cold (~41kN preload) and 40kN (40kN preload)

The measured difference is statistically not significant but indicates a distinct tendency towards an increased load transfer with increased contact time. This effect bases on the reasonable increase of the static friction coefficient over time as described in Section 2.1.1.3. The slight difference in clamping load of about 1kN between both test series has nearly no influence in this matter.

6.2.3.4 Effect of temperature on transferrable shear load

The measurement of the effect of increased temperature on the amount of transferrable shear load was the aim of test series Yield_warm (see Figure 6-17). After 168h storage at 150°C the shear load test was conducted at 150°C. The average transferrable shear load is 34.7kN. This is 1.7kN shear load less than in test series Yield_cold which is the reference test series in this case.

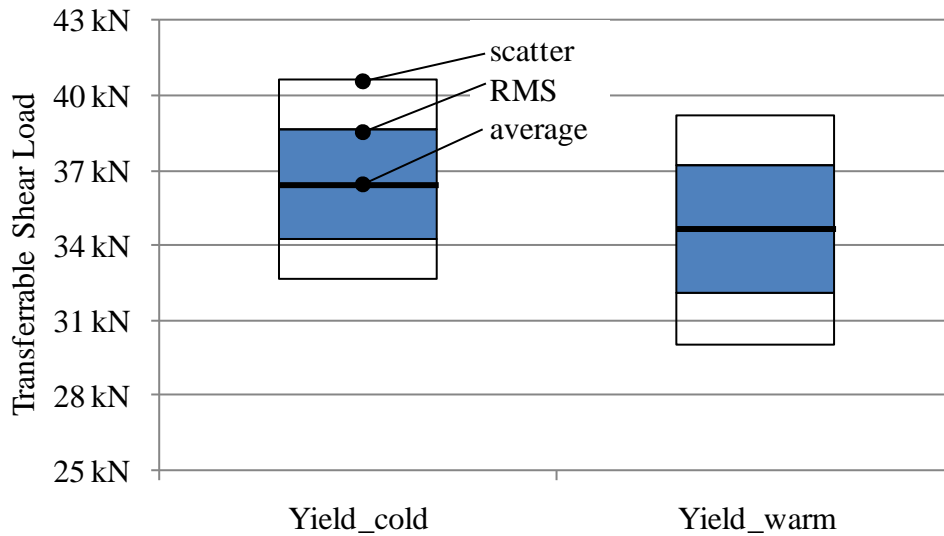


Figure 6-17: Transferrable shear load, including scatter range, of test series Yield_cold (~41kN preload) and Yield-warm (~41kN preload)

The difference in transferrable shear load is statistically not significant. Nevertheless there is a tendency towards lower transferrable shear load under a moderately increased temperature of 150°C. The reason for this behavior is basically located in the decrease of temperature depended material parameters like yield strength and Young modulus. The same mechanism enables the increase of relaxation losses under the condition of increased temperature.

6.3 Comparison with FEM Calculations

Prior to the experimental tests a numerical analysis of con-rod bolting specimens (CBS) and con-rods was conducted as shown in Figure 6-18. These investigations have been performed by Dr.-Ing. Osama Alraheb, TU Berlin. All of the following information concerning numerical procedures and results was taken from this research (Lyszczan, et al., 2010).

In this section, first the preprocessing is described with all necessary steps for the build-up of a CBS model with an artificially created fractured surface joint. Then the results of the numerical analysis are described and compared with the experimental findings.

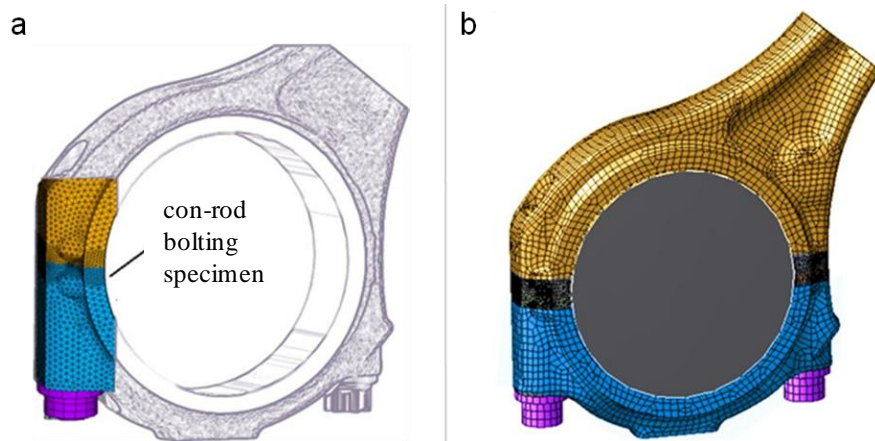


Figure 6-18: Illustrations of the FEM models of (a) a con-rod bolting specimen (CBS) and (b) a con-rod (taken from (Lyszczan, et al., 2010))

The focus of the numerical analysis was to calculate transferrable shear loads for a variation of the parameters that were found to be most important in (Lyszczan, et al., 2007). These parameters are:

- the element size used in the FEM model, especially for the fractured surface,
- the influence of the matching rate which was implemented as imperfections,
- the effect of different preloads.

Direct simulation of relaxation losses was not aim of the numerical research.

6.3.1 FEM Preprocessing

The FEM preprocessing involved the setup of the FEM model based on a CAD model of a con-rod, the virtual preloading of the bolts, and the preparation of the shear load introduction into the simulated specimen.

The CAD model of the con-rod type used for this research project was made available in the form of a STEP file by the manufacturer. Based on this CAD model the con-rod as well as the con-rod bolting specimen were prepared for the import into the FEM software ANSYS V12. Complex mesh structures have been avoided by removing small radii and the threads from the CAD models. The flat contact surfaces of the bolted joint were not modified.

After the import of the modified CAD model into ANSYS the con-rod cap and body were both merged into a single body. The same procedure was performed with the two parts of the CBS which are the partial cap and the partial body (see

Figure 6-18(a)). The next steps for the mesh generation are shown in Figure 6-19 for the CBS.

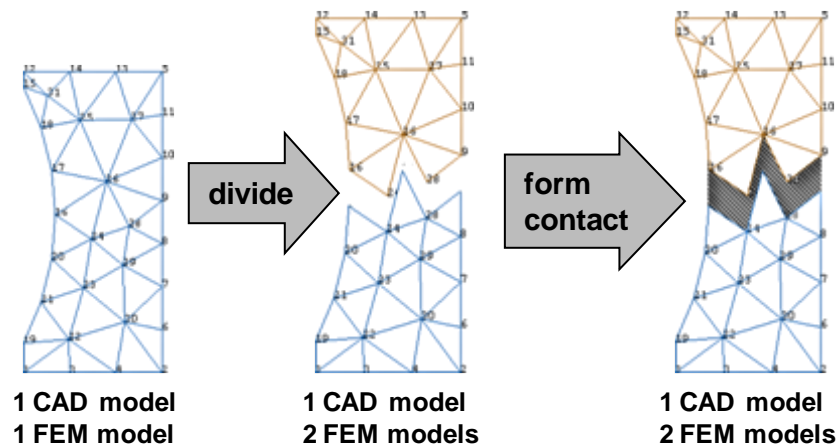


Figure 6-19: FEM pre-processing of the con-rod bolting specimen (CBS) – generation of a pair of artificial fractured surfaces: import of CAD model to FEM software, merging of the two parts and mesh generation (left), mesh splitting into two meshes (center), contact definition (right) (taken from (Lyszczan, et al., 2010))

The first step of the meshing procedure was the generation of a mesh of tetrahedrons with center nodes. The advantage of such a mesh is that the element surfaces are not located within a common layer. The elements had an edge length of 0.70 mm. Finally, the mesh was refined in the area where the fractured surface should be located by applying a factor of two, generating an element size of $0.70/2 (= 0.35 \text{ mm})$.

In the second step the mesh was split at the position of the fractured surface. During this splitting the number of nodes and elements at the junction plane was doubled. Finally, this splitting process produced two FEM models, one for the (partial) cap and one for the (partial) body. Both models have a fractured surface that forms a perfectly fitting joint.

In the third step, the contact between the two new models was defined. For this research project a non-linear, friction-assigned contact with elastic-plastic material behavior was defined.

Finally, the bolt was meshed and the contact to the adjacent parts defined. Because the thread had been removed the bolt was “glued” to the con-rod body. The final FEM model including a detailed view of an artificial fractured surface is shown in Figure 6-20.

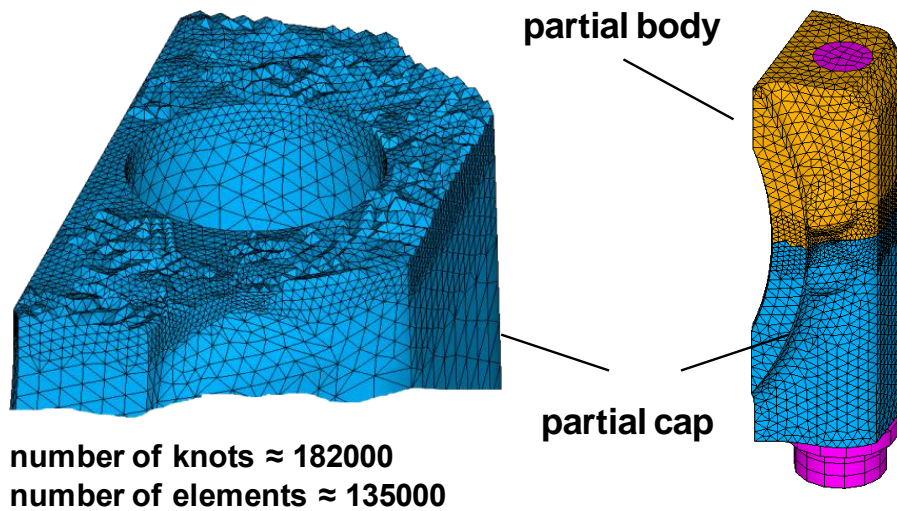


Figure 6-20: artificial fractured surface for FEM calculations
(taken from (Lyszczan, et al., 2010))

For some of the parameter studies the models had to be partially adjusted. These adjustments affected either the mesh refinement procedure (more refinement slopes for smaller mesh elements at the splitting layer) or the elements of the artificial fractured surface (deactivation of some random elements).

After the model preparation and the mesh generation the simulated specimen was loaded by preloading the bolt and then stressed with the shear load. The bolt preload was realized by introducing a defined inner force into the bolt shaft. The shear loading was performed by defining load areas at the specimen model. The locations of these areas were adjusted to represent the true contact location and areas of the real shear loading device to ensure comparable results. The shear stress was realized by displacing nodes. The whole loading process is shown in Figure 6-21.

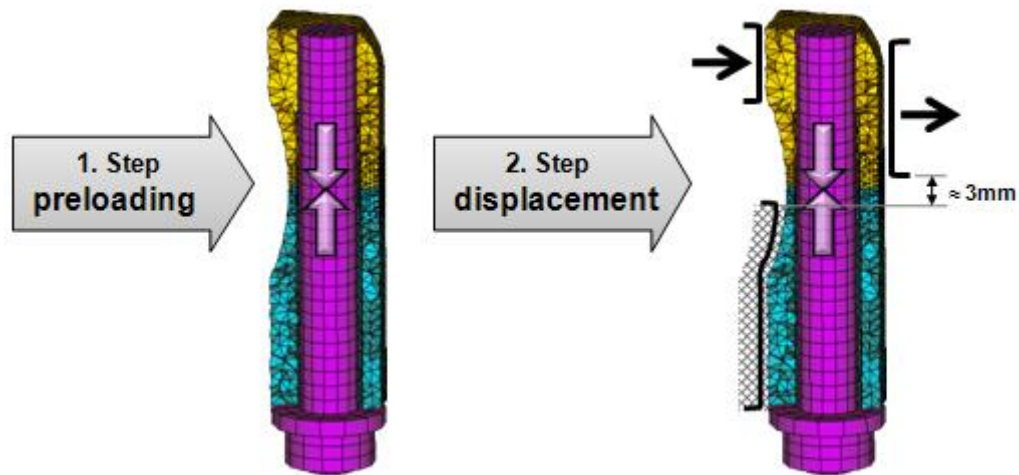


Figure 6-21: Simulation of the bolting process of a con-rod bolting specimen including preloading by defining inner forces in the bolt shaft (left) and shear loading by node displacement of defined surface areas and the CBS (right) (taken from (Lyszczan, et al., 2010))

The whole process including the adjustments was programmed with the ANSYS script language APDL to assure a consistent modeling procedure throughout the whole research project.

6.3.2 Influence of Element Size

The analysis of the structural behavior of fractured surfaces with differently shaped topologies is the aim of this numerical test series.

A total of four tests were run. Each test run had a different refinement level of the splitted mesh at the artificially created fractured surface layer (see Figure 6-19), that is, the size of the elements of the fractured surface was different. The basic element length varied from 1.5mm down to 0.375mm. At the fractured surface the element length was halved as described in the previous section (preprocessing step one). As a result the artificially created fractured surfaces of all four FEM models in this test series were completely different.

For each test run the bolt preload was fixed to 40kN. The fractured surface pairs had a matching rate of 100%. No additional imperfections were modeled. The FEM models were stressed stepwise with shear load by increasing the node displacement. A test run stopped as soon as the loading of one of its element reaches tensile strength.

The result of this test series is shown in Figure 6-22.

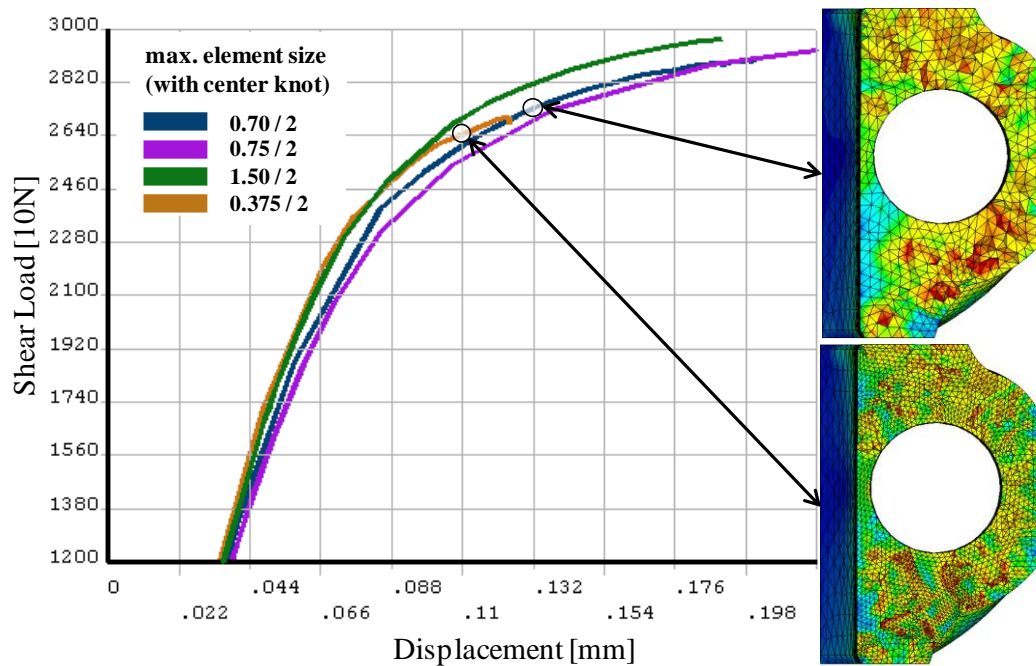


Figure 6-22: Influence of element size on transferrable shear load (with 40kN preload) with the stress distribution at the end of the test runs 0.70 / 2 (upper) and 0.375 / 2 (lower) (taken from (Lyszczan, et al., 2010))

The amount of the transferrable shear load is independent from the element size and has a magnitude of about 29kN.

The test with the smallest element size seems to be an exception to this trend: the calculation stopped at about 27kN. However, this is considered to be due to the before mentioned stop criterion. When surface elements are very small, local stresses have a larger impact than with bigger elements. The stress distribution at the end of this test run is shown at the bottom right in Figure 6-22. Obviously, there are still enough elements available that may carry more load before they also fail. It can be assumed that in a real test this element failure would not have been detected at this point and the test would have continued.

The determination of the impact of the surface topology on the transferrable shear load was another aim of the experimental investigations described in Section 6.2.3.2. The results of each laser batch showed no significant difference and no visible tendency regarding transferrable shear load. This is in line with the results of the numerical computations where the amount of the transferred shear load does not differ between the batches of each preload level.

The result of both research activities is that there is no measurable influence of the surface topology with respect to the element size on the amount of the transferrable shear load.

6.3.3 Influence of Imperfections

The goal of this numerical test series was to specify the impact of the size of imperfections onto the transferrable shear load.

For this test the fractured surface of the numerical model was modified. Imperfections were generated by deactivating a number of randomly chosen elements at the artificially created fractured surface (see Figure 6-23). By deactivating different numbers of elements, four different FEM models with increasing amount of imperfection were generated. A fifth model was a perfect model without imperfections. Furthermore, a sixth FEM model was created which had two non-matching fractured surfaces, simulating a mismatched assembly. In this model the position of the nodes of one of the fractured surfaces was changed randomly up to the magnitude of the element size. The stop criterion for the calculation was the same as in Section 6.3.2.

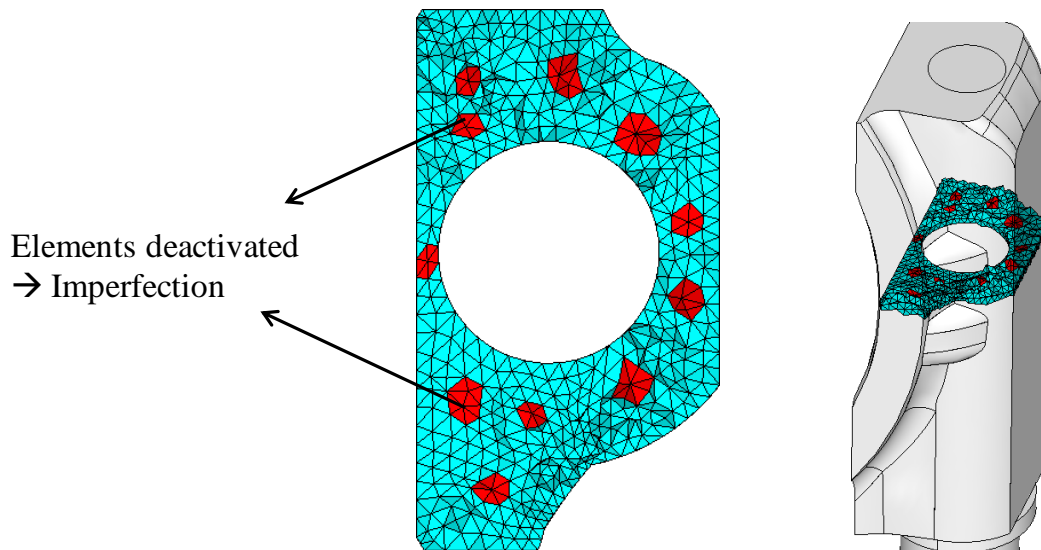


Figure 6-23: Generation of imperfections by random deactivation of surface elements (taken from (Lyszczan, et al., 2010))

Figure 6-24 shows the results of this test series. It can be seen that the more imperfections appear the less shear load can be transferred. For every 1% of imperfection about 0.5% less shear load is transferred.

This is in line with the experimental results of the test series 10kN, 20kN, 30kN and 40kN, which showed a relation between the matching rate and the transferrable shear load (see Figure 6-15). Hence, the experimental and numerical research results concerning the influence of the matching rate of fractured surfaces show comparable results. A notable influence of the matching rate on the amount of transferrable shear load was found.

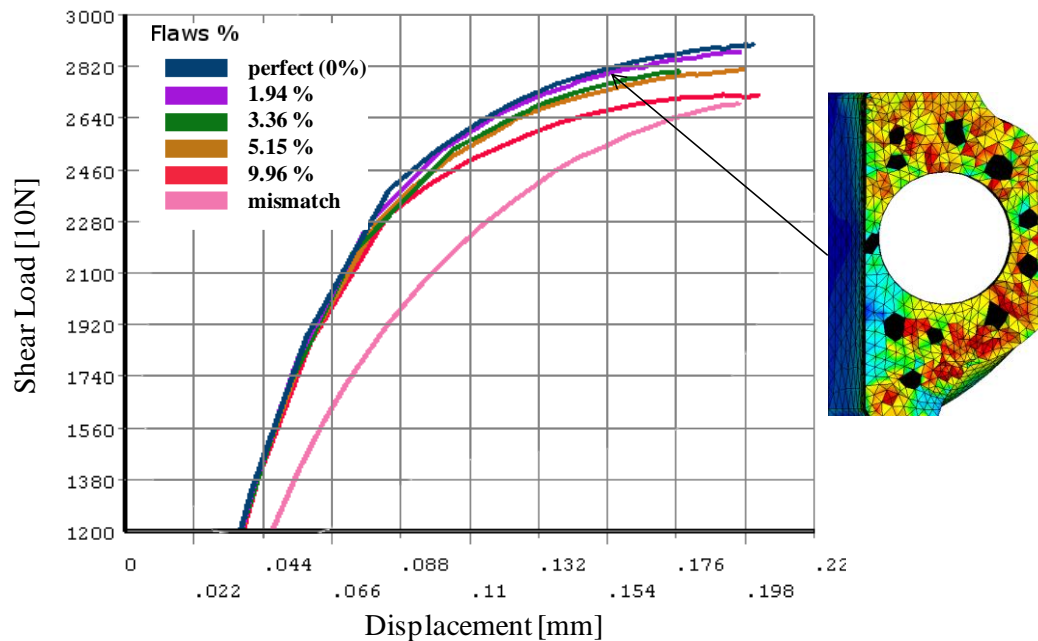


Figure 6-24: Influence of imperfections on transferrable shear load (with 40kN preload and element size 0.7/2) (taken from (Lyszczan, et al., 2010))

The least amount of shear load is transferred by the model with the two non-matching surfaces simulating a mismatched assembly. In this case about 5% less shear load is transferred. The difference in the amount of transferrable shear load between the mismatched assembly model and the model with about 10% imperfections is negligible.

The experimental test series with mismatched assemblies did not aim on determining the transferrable shear load but on the determination of relaxation losses (see Section 6.1.3.3). However, the latter can be used for an indirect comparison of the influence of mismatched assembly. In this relaxation test series a mismatched assembly was found to have a limited impact on the amount of relaxation losses and hence a limited amount of influence on the transferrable shear load is expected.

6.3.4 Influence of Clamping Load

This numerical test series aims at the determination of the effect of the clamping load level on the amount of transferrable shear load.

The clamping load was varied by setting the corresponding preload within the bolts. There was no additional axial load that could affect the bolted joint so the preload was equal to the clamping load. In this numerical test series only one FEM model was used where the bolt preload was adjusted.

The results are shown in Figure 6-25.

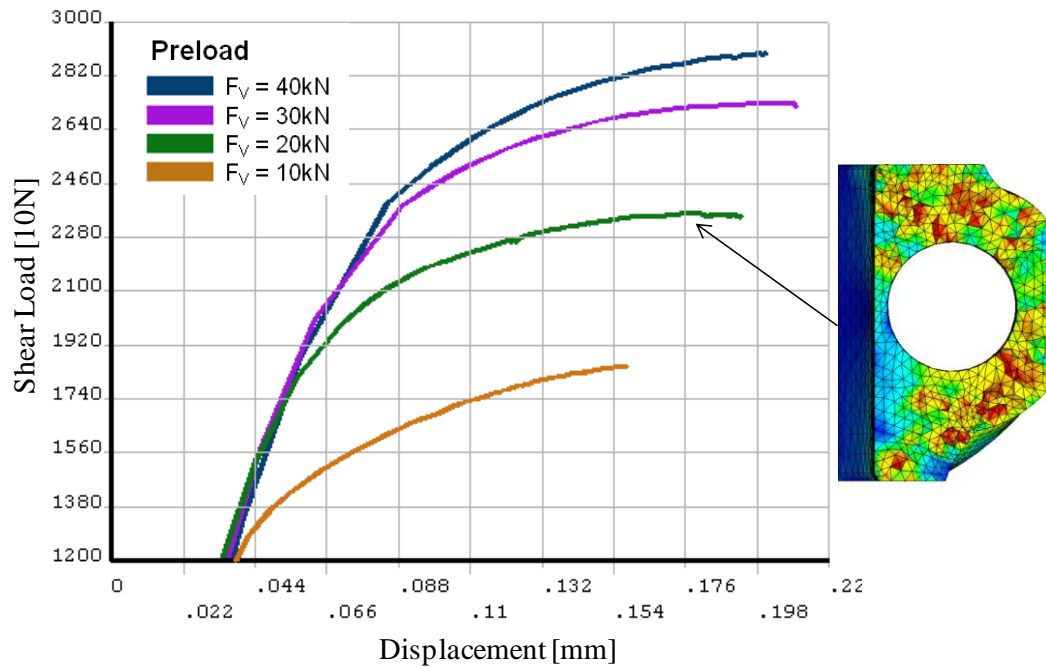


Figure 6-25: Impact of preload (= clamping load) on transferrable shear load (element size 0.7/2 and no imperfections) (taken from (Lyszczan, et al., 2010))

The more preload is applied, the more clamping load is available and the more shear load is transferred. The ratio of shear load to preload is decreasing with increasing preload. This tendency is shown in Figure 6-26.

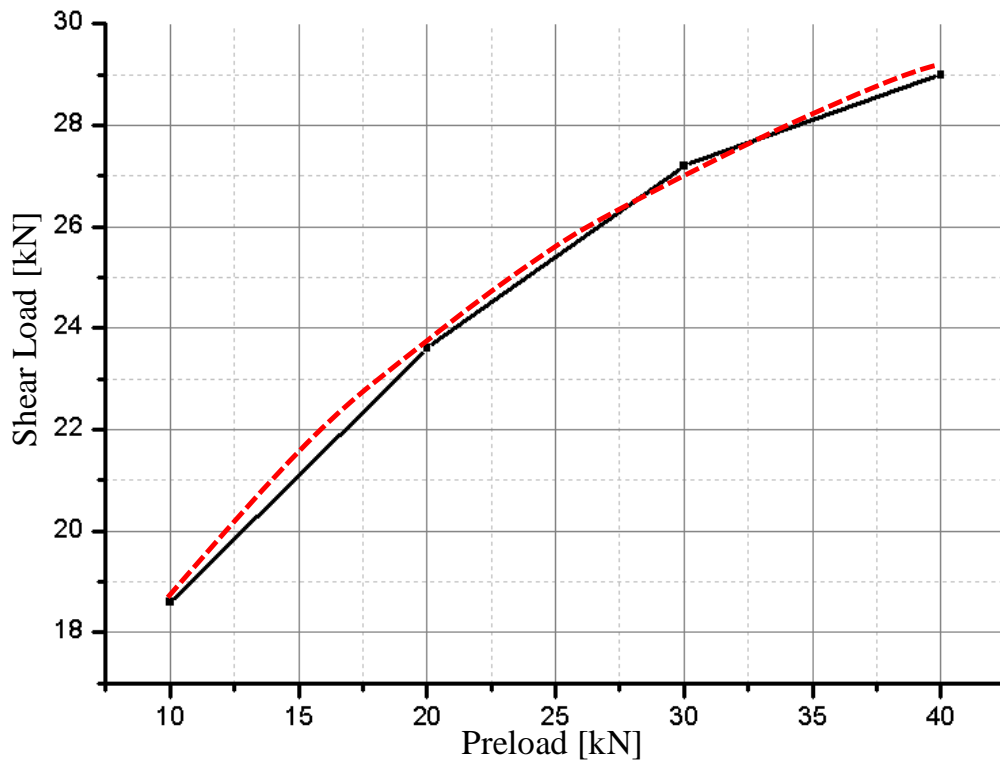


Figure 6-26: Transferred shear load as a function of the applied preload (black solid curve) and the dashed curve of the correlation function (taken from (Lyszczan, et al., 2010))

The transferred shear load (F_Q) as a function of the applied preload (F_V) can be described by the following formula obtained from the numerical data (red dashed line in Figure 6-26) with a reliability of 99.9% (Lyszczan, et al., 2010):

$$F_Q = A \cdot e^{\frac{F_V}{B}} + C \quad (5-1)$$

With the following constant parameters:

$$\begin{aligned} A &= -22.3\text{kN} \\ B &= 21.9\text{kN} \\ C &= 32.7\text{kN} \end{aligned}$$

With this function the theoretically maximal transferrable shear load can be calculated of about 33kN at an infinite preload. This limit cannot be reached in reality because of the limiting influence of the preload. The preload increases the overall loading of the surface elements, which is constrained by van-Mises' maximum shear strain energy criterion (van Mises, 1913).

The ratio of transferrable shear load to the applied preload is equal to the effective friction coefficient defined in Section 2.1.1.1. Figure 6-27 shows a comparison of the results of the numerical and experimental tests concerning the effective friction coefficient in dependence of the applied preload.

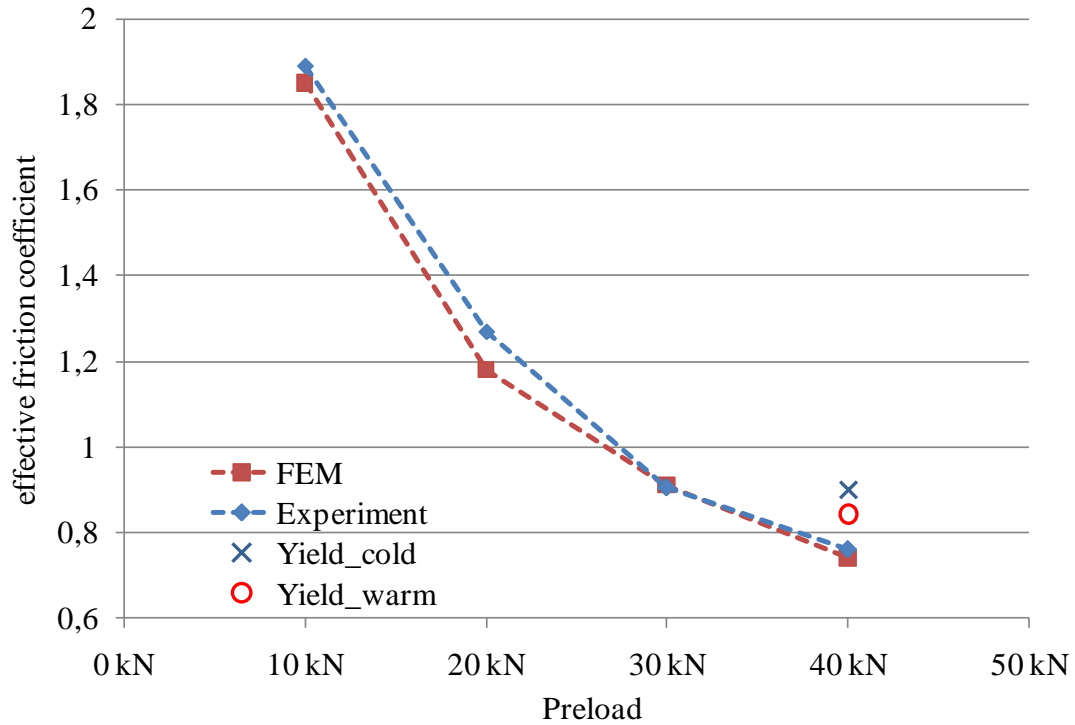


Figure 6-27: Relation between the preload and the effective friction coefficient of con-rod bolting specimen resulting from FEM calculations and experimental investigations

Figure 6-27 shows the results of the numerical computations and the results of the corresponding experimental test series, both sharing a strong correlation. The results of the experimental test series Yield_cold and Yield_warm with the increased static friction coefficient have not been reproduced as numerical computations. Both values have been added for the sake of completeness of the experimental results.

Applying the found effective friction coefficients in a calculation of the transferable shear load of a flat surface pair resulted in the same transferred shear load as found in the experiments and numerical calculations with artificially created fractured surfaces (see also Section 9.5.4).

6.3.5 Comparison of FEM and Experiments

A comparison of the results from the numerical and experimental investigations of con-rod bolting specimens is provided in Table 6-6.

	Experiment	FEM
Element Size / Surface Topology	No influence	No influence
Less Imperfections / Higher Matching Rate	Transferrable Shear Load slightly increased	Transferrable Shear Load slightly increased
Stochastic Contact/ Mismatched Assembly	(No influence)*	Minor influence
Increased Preload (Clamping Load)	Transferrable Shear Load increased	Transferrable Shear Load increased

Table 6-6: Comparison of comparable results of numerical and experimental investigations of the transferrable shear load of con-rod bolting specimens
*=-results from experimental investigations of relaxation loss

The experimental and the numerical results support each other. Especially the high level of correlation of the transferrable shear load in dependence of the applied preload confirms the reliability of the FEM computation of fractured surfaces.

6.4 Conclusions

In this chapter the results of the experimental investigations of relaxation losses and the transferrable shear load of con-rod bolting specimen have been presented, as well as numerical computations of FEM models of the specimens to allow a comparison with the experimental results. It was found that the numerical computations support the experimental findings in all relevant cases.

Concerning relaxation losses in con-rod bolting specimens the verification process of the related hypotheses formulated in Section 4.1.2 revealed the following results:

Hypothesis (2): What is the impact of fractured surfaces on the relaxation of bolted joints?

The fractured surface has a significant impact and cannot be ignored in the calculation of the bolted joint. The fractured surface has a significant impact and cannot be ignored in the calculation of the bolted joint.

To verify this hypothesis two test series with 45 specimens (15 per laser notch batch) and 6 specimens (only red laser notch batch with planished surfaces) have been compared regarding their preload losses at 150°C.

The relaxation loss of fractured surfaces is not significantly different from the relaxation loss of a plain surface (Section 6.1.3.1). The hypothesis has to be rejected.

Hypothesis (3):

The amount of the relaxation loss depends on the surface topology in a way that the more distinctive the surface topology⁶³, the larger is the amount of relaxation losses.

For this analysis the test results of four test series with a total of 105 specimens (35 per laser notch batch) were used.

The topology of the fractured surface does not have an influence on the amount of relaxation losses (Section 6.1.3.2). The hypothesis has to be rejected.

Hypothesis (4):

A moderate increase of the operating temperature (150°C) results in an exponential loss due to relaxation.

The results of two test series with a total of 30 specimens (10 per laser notch batch, each specimen used twice) are the source for this analysis.

The relaxation loss under operating temperature increased the relaxation losses by about 90% (Section 6.1.3.6). The hypothesis is confirmed.

The results of the verification process concerning the research hypotheses about the transferrable shear load formulated in Section 4.1.3 are the following:

Hypothesis (5):

The amount of transferrable shear load (F_Q) in a bolted joint with fractured surfaces is determined by the magnitude of the clamping force (F_N) in the following way: $F_Q = \mu_{\text{effective}} \cdot F_N$. (The effective friction coefficient is to be determined by experiments.).

⁶³ A surface with a distinctive topology has a rough, cliffy and fissured character. A proper example for a fractured surface with a distinctive topology is shown in Figure 5-16.

This hypothesis was verified using 4 experimental test series with 15 specimens each (5 specimens per laser notch batch) and 4 numerical test series with a single FEM model. The ratio of the transferrable shear load and the clamping load was approximated by the ratio of transferrable shear load to installed preload.

For a preload range between 10kN and 40kN this ratio, the effective friction coefficient, was determined experimentally (Section 6.2.3.1) and numerically (Section 6.3.4). Typical values are located within a range of $\mu_{\text{effective}} = 0.8 \dots 2$ in dependence of the applied preload. The use of these values in calculations with flat surface pairs resulted in the same transferrable shear load as the experiments with the fractured surfaces. The hypothesis is confirmed and a useful approximation obtained.

Hypothesis (6):

The effective friction coefficient, and with that the transferrable shear load, depend on the topology of the fractured surface in a way that the more distinctive the surface topology, the larger the transferrable shear load. Hence, the more distinctive the surface topology, the larger the transferrable shear load.

For this analysis the results of six test series with a total of 90 specimens (30 specimens per laser notch batch) have been taken into account.

The experimental results reveal that the topology of the fractured surface does not have an influence on the amount of transferrable shear load (Section 6.2.3.2). The hypothesis has to be rejected.

Hypothesis (7):

A moderate increase of temperature decreases the amount of transferrable shear load slightly.

The results of two test series with 30 specimens (15 specimens per laser notch batch) have been analyzed.

The experimental investigations reveal a 5% decrease of the transferrable shear load under operating temperature conditions (150°C) in comparison to ambient temperate conditions (22°C). This difference does not exceed the standard deviation of the average values (Section 6.2.3.4). Consequently, the hypothesis has to be rejected.

The experimental und numerical investigations revealed the following additional findings:

The amount of transferrable shear load depends on the matching rate of the fractured surface joint and on the size of the total contact area. The larger the fractured surface contact area, the more shear load is transferred.

The numerical calculations of a joint with fractured surfaces correspond largely to the experimental results. As a result, numerical calculations can be used for investigations of fractured surfaces with a low level of experimental support. This allows the analysis of parameters that are hard to manipulate by an experimental setup.

The effective friction coefficient, defined as quotient of transferrable shear load by applied preload, varies for different preloads. For that reason the effective friction coefficient is not identical with the global friction coefficient introduced in Section 2.1.1.1. The global friction coefficient only depends on the geometric angle and the static friction coefficient, which are fixed for each specimen.

When the shear load is higher than the individual load limit of a joint with a fractured surface, plastic deformation of the surface topology occur. The size of the damaged area only depends on the amount of transferred shear load, which in turn depends on the installed preload. The surface topology has no influence on the overall size of the deformed area.

7 Mechanical Model

The goal of this chapter is to build up a simple mechanical model of a joint with fractured surfaces. This model is intended to explain the distinctive features of a fractured surface joint, for instance the non-linear character of the effective friction coefficient, as well as the amount of shear force damage of the tested specimens given a certain clamping load. Based on this model research hypothesis (8) is to be verified.

Question: What kind of mechanism enables the load transfer?

Hypothesis: The mechanism of load transfer in a fractured surface joint is a combination of form based load transfer in some areas and force based load transfer in other areas.

In order to verify the hypothesis results of Chapters 2, 3, 5 and 6 were considered. First, information sources are identified (Section 7.1). Then the mechanical model is derived (Section 7.2). After that the failure modes are described with the mechanical model (Section 7.3). Then the load distribution of a fractured surface during shear loading is described (Section 7.4). The next section deals with the explanation of the distinctive features of fractured surfaces with the help of the mechanical model (Section 7.5). Finally, conclusions are drawn (Section 7.6).

7.1 Preliminary Considerations

Foundation for model building:

- calculation of form connections, Chapter 2
- calculation of force connections, especially the model of the global friction coefficient, Chapter 2
- typical shapes of fractured surfaces, especially from the FVV project “Self Loosening of Bolts”, Chapter 3
- laser scanner data, Chapter 5
- surfaces of tested specimens, Chapter 5
- FEM results, Chapter 6
- results and additional findings from Chapter 6

7.2 Model Building

The goal of the model building is to obtain a simple mechanical model which can be used to describe the failure modes and the distinct characteristics of a joint with fractured surfaces. A simple 2-D model should provide enough information to

reach that goal and is much less complex than the 3-D FEM model used in Section 6.3.

The starting point for the building of the model of a joint with fractured surfaces is the detailed image of a pair of fractured surfaces in a joint of a con-rod shown in Figure 7-1 which is representative of the collected images. The image of the contact line of both surfaces reveals a mixture of topology elements of different scales. In combination with the images of damaged surfaces from the tested specimens shown in Figure 6-9, it turns out that those surface elements of a certain scale that play a major role in shear force transfer while surface elements of other scales are not that important.

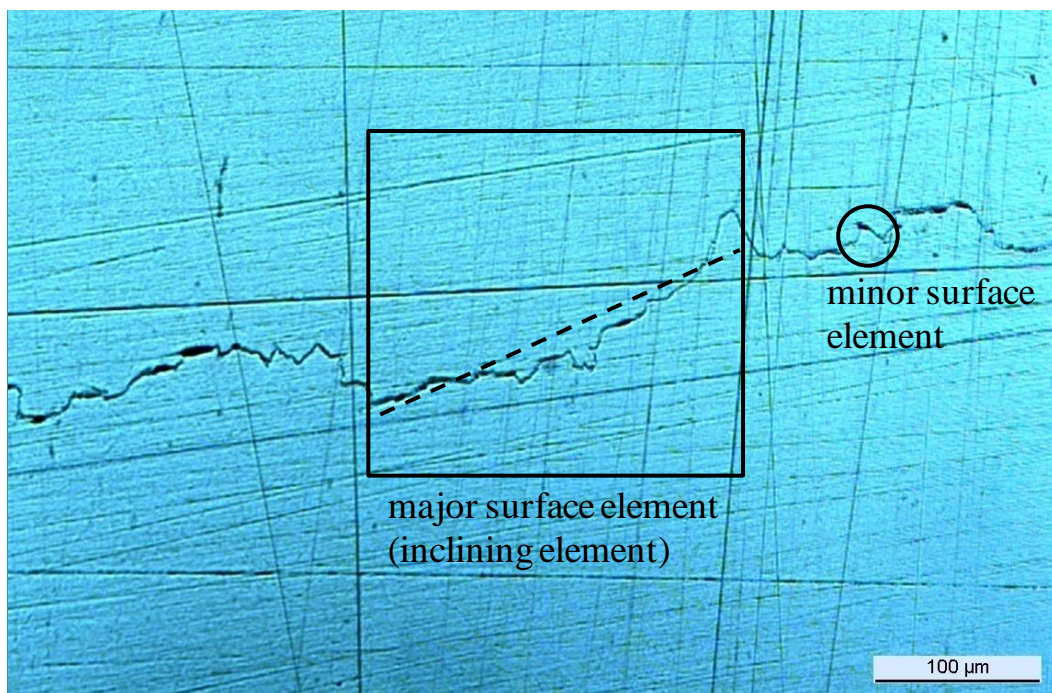


Figure 7-1: Detail of a joint with fractured surfaces obtained by grinding the facing surface of the big eye of a con-rod (taken from (Lyszczan, et al., 2007))

First, the geometric parameters are simplified by the following restrictions, primarily based on the images shown in Figure 6-9:

- The influence of surface shapes that are larger than 1mm is neglected, i.e. the slope of the overall surface topology from edge to edge or the overall inclination of the fractured surface (see Figure 7-1).
- The influence of small surface structures of a height less than 0.1mm is considered to be included in the local static friction coefficient according to the principle of the global friction coefficient in Section 2.1.1.1
- All remaining surface structures are included and considered important for the shear load transfer

- The shape of the model surface is considered to consist of triangular teeth with different inclination angles

In addition to the geometric parameters the mechanical parameters of the model require some simplifications and assumptions:

- Elastic deformations of the surface or surface elements are neglected
- The validity of the model is limited to pure elastic loading
- Yielding at stresses lower than the tensile strength is neglected

Figure 7-2 illustrates, using a simplified sketch, the mechanical model of a joint with fractured surfaces under normal load transferring a shear load. This figure shows that about one fourth of the surface elements have steep slopes, another quarter has medium slopes and the other half has rather flat slopes. Figure 7-2 shows the lowest resolution, i.e. the essence of the surface, but the model can be refined by differentiating more slopes.

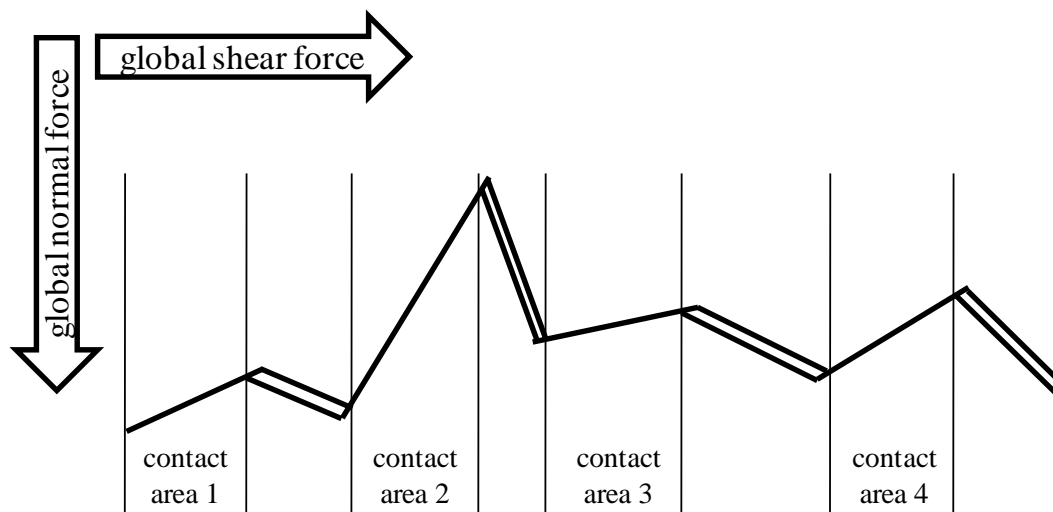


Figure 7-2: Sketch of a mechanical model of a joint with fractured surfaces loaded with a normal force and transferring a shear force via labeled contact areas

The calculation of this model is performed using the calculations of the global friction coefficient introduced in Section 2.1.1.1. At first the balance of forces at each contact area is calculated based on a detailed model of each contact area as shown in Figure 7-3.

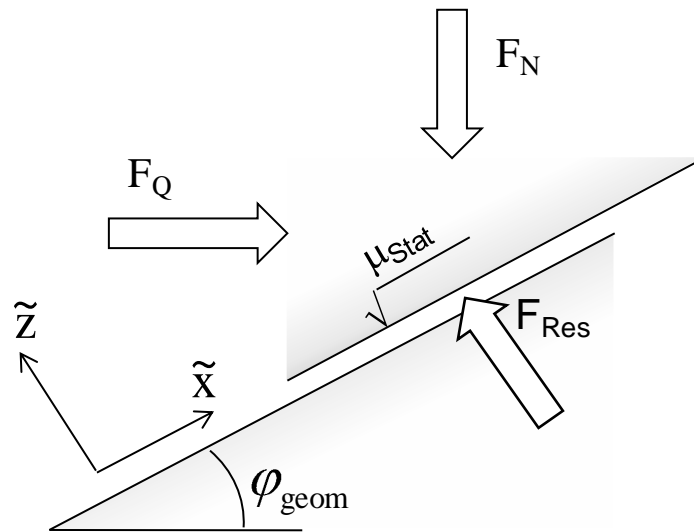


Figure 7-3: Detail of a contact area taken from Figure 7-2 (with respect to Figure 2-3)

The balance of forces shown in Figure 7-3 equals the balance of forces shown in Figure 2-3 in Section 2.1.1.1 with one important difference. Although the local normal forces of all contact areas are of an equal size, the geometric angles of each contact area as well as the static friction coefficients are specific for each contact area. As a result the transferrable shear force differs from contact area to contact area. Therefore, the following equations have to be set up individually for each contact area.

$$\text{Direction } z^{\sim} \quad F_N \cdot \cos \varphi_{geom} + F_Q \cdot \sin \varphi_{geom} = F_{Res} \quad (7-1)$$

$$\text{Direction } x^{\sim} \quad F_N \cdot \sin \varphi_{geom} + F_{Res} \cdot \mu_{Stat} = F_Q \cdot \cos \varphi_{geom} \quad (7-2)$$

$$\text{with} \quad F_{Res} = \sqrt{F_N^2 + F_Q^2} \quad (7-3)$$

With the help of these formulas the limit of the transferrable shear force can be calculated for different conditions of the geometric angle and the static friction coefficient.

7.3 Limits of Transferrable Shear Force

Plastic deformations are definitely a limit of the transferrable shear force as seen in Figure 6-9. These deformations occur at surface elements with large inclination angles φ_{geom} .

According to the basic mechanical model the transferrable shear force is limited by another critical value, slipping. This limit becomes important at rather small inclination angles φ_{geom} .

Both limits are described in the following sections and then merged into one failure model.

7.3.1 Local Limit due to Shearing

The limit of the transferrable shear force due to shearing is calculated on the basis of the balance of forces in z direction in Figure 7-3 represented by formula (7-1). The limit depends on the local normal force F_N , the local shear force F_Q , and the local inclination angle φ_{geom} . Both local forces are combined into the resulting force F_{Res} .

In case the overall load F_{Res} reaches a critical threshold in a local contact area of the fractured surface, plastic deformation occurs. As a result the joint starts to fail. This critical threshold is determined by the permissible shear stress τ_{perm} in combination with the sheared area A . The following restriction needs to be fulfilled in a joint with fractured surfaces to avoid a failure due to shearing:

$$F_N \cdot \cos \varphi_{\text{geom}} + F_Q \cdot \sin \varphi_{\text{geom}} = F_{\text{Res}} \leq \tau_{\text{perm}} \cdot A \quad (7-4)$$

With⁶⁴

$$\tau_{\text{perm}} = \frac{1}{\sqrt{3}} \cdot \sqrt{\sigma_{\text{perm}}^2 - \frac{F_N^2}{A^2}} \quad (7-5)$$

the limit of the transferrable shear force due to shearing can be calculated to:

$$\frac{\frac{1}{\sqrt{3}} \cdot \sqrt{\sigma_{\text{perm}}^2 \cdot A^2 - F_N^2} - F_N \cdot \cos \varphi_{\text{geom}}}{\sin \varphi_{\text{geom}}} \geq F_Q \quad (7-6)$$

⁶⁴ The formula for τ_{perm} is obtained from the formula of one-dimensional von-Mises stress:

$$\sigma_{\text{analog}} = \sqrt{(\sigma_{\tau/p}^2 + \sigma_b^2) + \frac{1}{3}\tau^2}$$

with the van-Mises stress (σ_{analog}) calculated by tension/pressure stress ($\sigma_{\tau/p}$), bending stress (σ_b) and shear stress (τ).

In formula (7-6) σ_{perm} is the permissible von-Mises stress of the material of the joint, A is the shear area, F_N is the local normal force, F_Q is the local shear force, and φ_{geom} is the local inclination angle. When F_Q exceeds this threshold the local contact element will fail by shearing.

The danger of a failure due to shearing is increased by an increase of the local inclination angle φ_{geom} , by an increase of the local normal force F_N , by a decrease of the sheared area A , or by a decrease of the permissible von-Mises stress.

7.3.2 Local Limit due to Slipping

Regarding a failure due to slipping, the transferrable shear force is limited by the global friction coefficient μ_{global} introduced in section 2.1.1.1. The global friction coefficient represents the ability or rather the potential of shear force transfer of a surface element with a certain inclination angle φ_{geom} and a certain static friction coefficient μ_{stat} , and depends on the local normal force F_N .

With $\tan(\varphi_{\text{geom}}) = \mu_{\text{geom}}$ the limit of the transferrable shear force due to slipping can be calculated based on formula (2-7):

$$F_Q \leq \frac{\mu_{\text{stat}} + \mu_{\text{geom}}}{1 - \mu_{\text{stat}}\mu_{\text{geom}}} \cdot F_N \quad (7-7)$$

In case the shear force exceeds this threshold the local contact will fail due to slipping. The calculation of the limit depends exclusively on friction, ignoring possible plastic deformations. Plastic deformation, however, is taken into account through the calculation of the shear limit.

The danger of a failure due to slipping is increased by a decrease of one or more of the following factors: inclination angle φ_{geom} , static friction coefficient μ_{stat} and local normal force F_N .

7.3.3 Effective Local Limit of Transferrable Shear Force

In the previous two sections two different failure modes have been described. Both failure modes limit the maximum amount of transferrable shear force of a local surface element. To decide which failure mode is active for a certain surface element, the magnitude of both limits need to be compared. Finally, the limit with the lower threshold will be decisive.

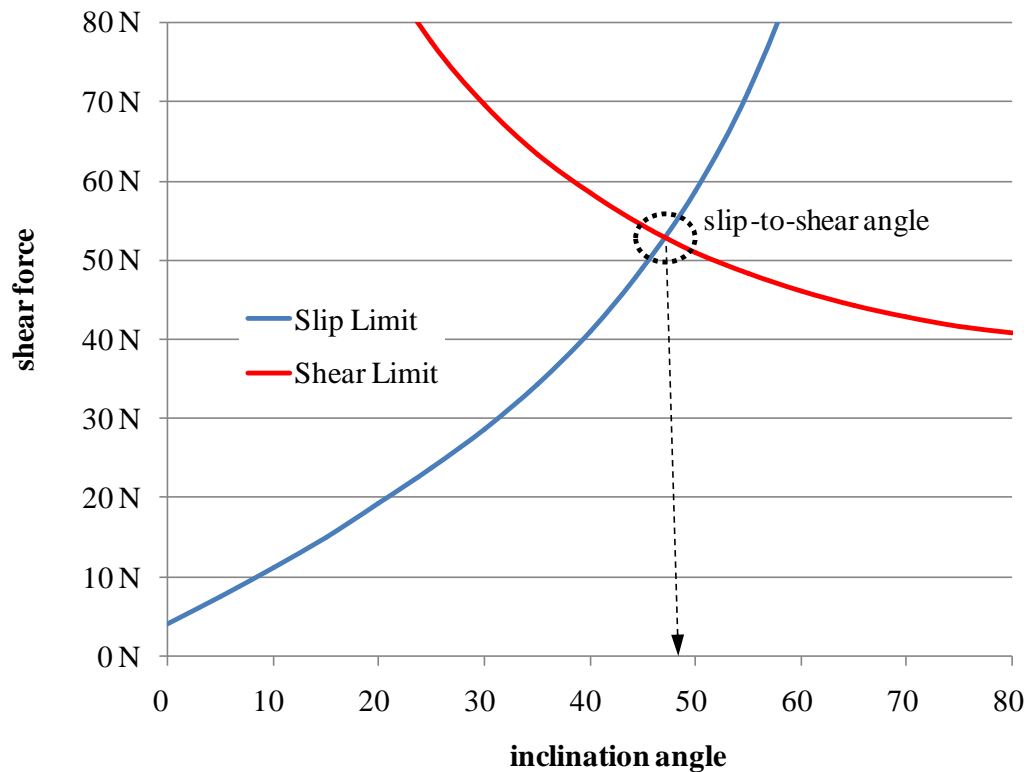


Figure 7-4: Characteristic of the shear limit and the slip limit of a surface element of a joint with fractured surfaces in dependence of the local inclination angle (with $\mu_{\text{stat}}=0.1$, $F_N=40\text{N}$, $\sigma_{\text{perm}}=900\text{N/mm}^2$ and $A=0.118\text{mm}^2$)

In Figure 7-4 the characteristics of both limits are shown as a function of the inclination angle φ_{geom} . The static friction coefficient μ_{stat} and the permissible von-Mises stress σ_{perm} have been set according to the specifications of the tested specimens given by the manufacturer. The local normal force F_N and the shear area A have been downsized according to the specimen data⁶⁵.

The characteristics of the failure limits of the example of a surface element shown in Figure 7-4 indicate that there is a slip-to-shear-angle of the failure mode at about 48°. A surface element fails due to slipping if it has an inclination angle up to 48°. In other words, the joint acts as a force connection. If the inclination angle

⁶⁵ The downsizing calculation bases on a global normal force of 40kN and a real contact area of 118mm² based on the overall area of 134mm² and an average contact ratio of 88% (see section 5.3.2.1). The downsizing calculation assumes a number of 1000 surface elements of even size and distribution.

is higher than 48° , then the surface element fails due to shearing. In other words, the joint acts as a form connection.

For each single element the exact position of the slip-to-shear angle also depends on the other mentioned parameters, i.e. static friction coefficient μ_{stat} and shear area A ⁶⁶. In a joint with fractured surfaces all contact elements share the same shear area⁶⁷. The strong correlation of FEM calculation results and experimental results shown in Figure 6-27 indicates that this assumption is close to reality. As a result, the failure mode of each surface element can be calculated in dependency of the local inclination angle and the static friction coefficient only. An example for this context is shown in Figure 7-5⁶⁸.

A fractured surface consists of many single surface elements with different static friction coefficients and different inclination angles. As a result the failure modes slip limit and shear limit occur a joint with fractured surfaces at different surface elements. The impact of this mixed global failure mode on the distribution of the global shear load among the single surface elements is described in the following section.

⁶⁶ The material is considered to be homogenous.

⁶⁷ A common element size also means an even distribution of the normal force F_N .

⁶⁸ The characteristics shown in Figure 7-4 are a subset of the characteristics shown in Figure 7-5 in terms of a slice cut out parallel to the inclination angle axis at friction coefficient 0.1.

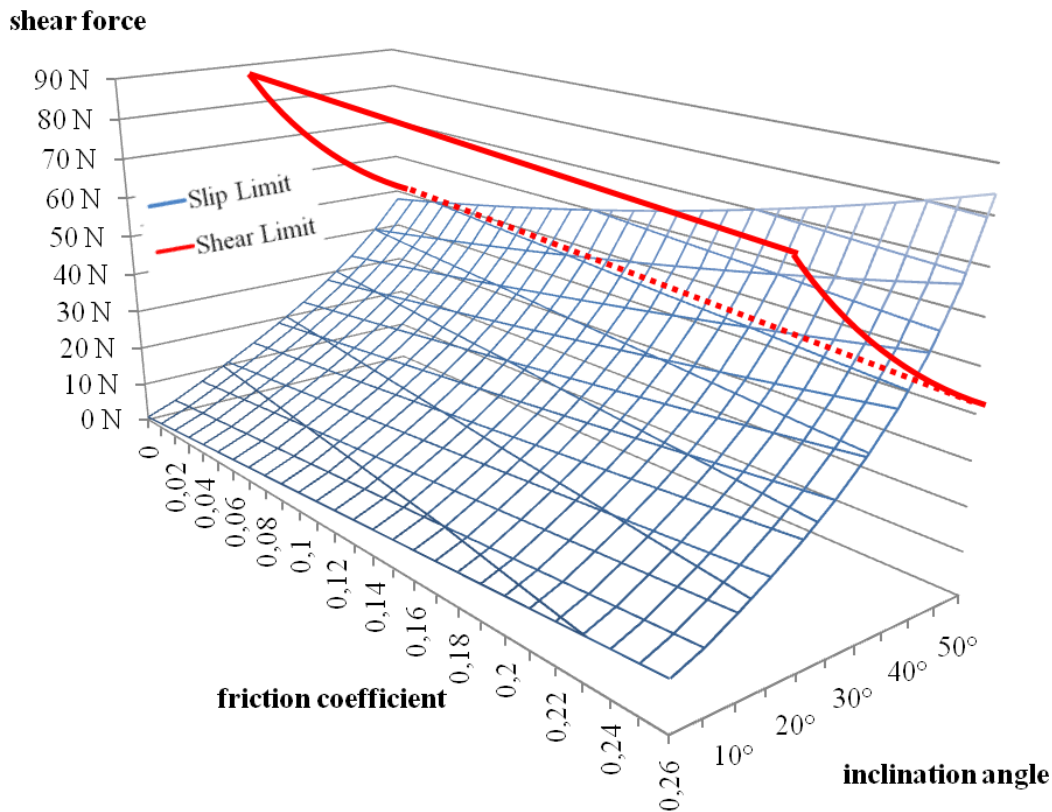


Figure 7-5: Characteristic of the shear limit and the slip limit of a surface element of a joint with fractured surfaces in dependence of the local inclination angle and the static friction coefficient (with $F_N=40\text{N}$, $\sigma_{\text{perm}}=900\text{N/mm}^2$ and $A=0.118\text{mm}^2$)

7.4 Load Distribution in a Joint with Fractured Surfaces

In a joint with fractured surfaces the global shear force is transferred by a distribution among the single surface elements. As a result each surface element transfers a local shear force up to its individual limit which is either the slip limit or the shear limit. Assuming that all surface elements have the same size and the global normal force is distributed evenly among all surface elements as a local normal force, the load distribution works the following way:

The global shear load is distributed evenly among all surface elements, i.e. each surface element carries the same shear load. This condition changes when the local shear force reaches the limit of a surface element. Usually the first elements fail due to slipping. These elements will then no longer transfer additional shear load. Instead, the transferred local shear force is frozen at the level of the local slip limit. When the global shear force raises beyond this point, the surplus of local shear load that these surface elements do not transfer anymore is distributed over

the remaining fully operative surface elements. The mechanism of load distribution is explained with the example shown in Figure 7-6 and Figure 7-7.

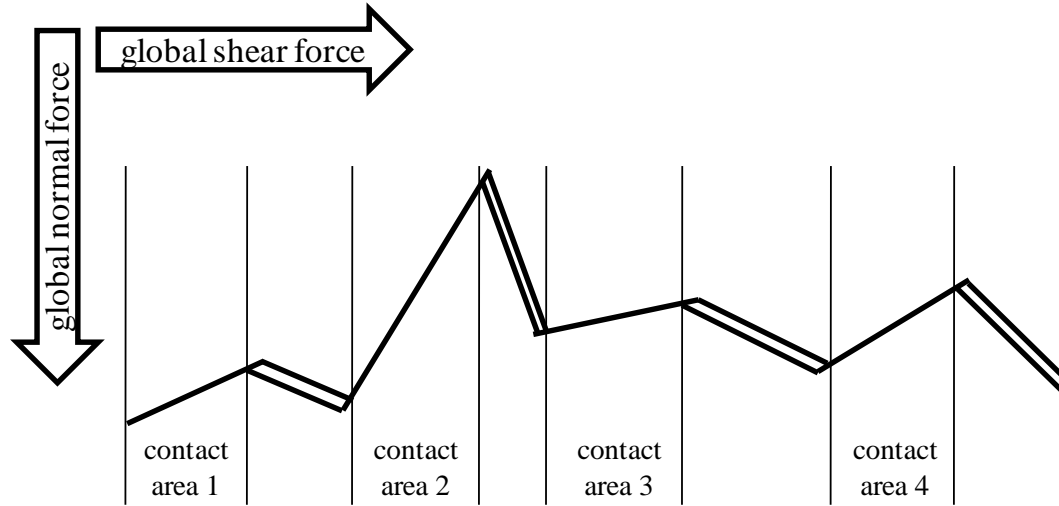


Figure 7-6: Example of joint with fractured surfaces loaded with normal force and transferring a shear load which is distributed among four labeled surface elements

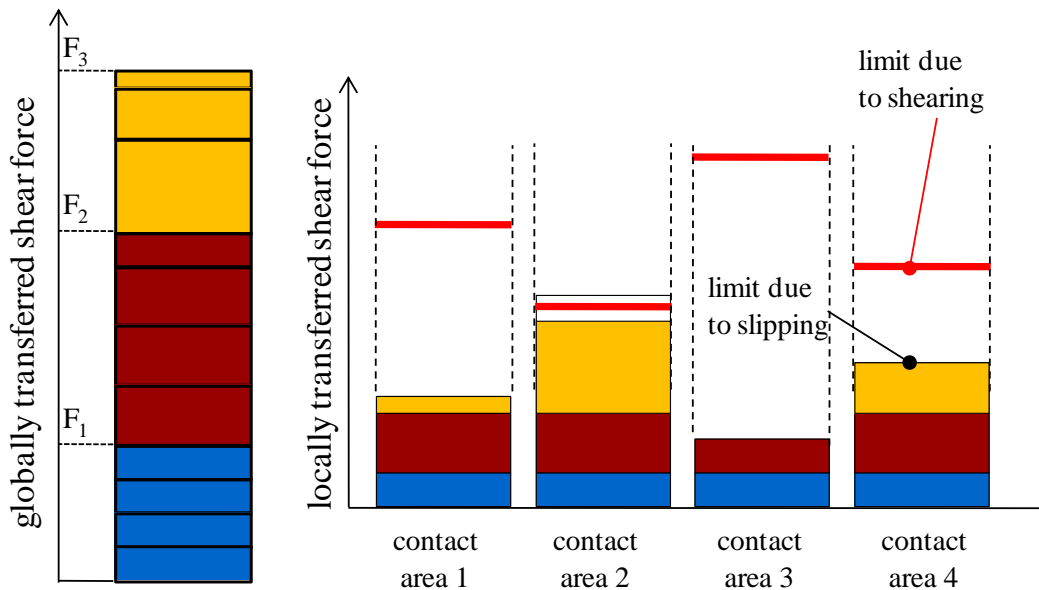


Figure 7-7: The stepwise increase of the global shear load (left) and its distribution among the four surface elements (right) shown in Figure 7-6 including the failure limits

The example shown in Figure 7-6 is the joint with fractured surfaces containing four surface elements discussed in Section 7.2. Each element transfers a fraction of the global shear load. The load distribution at each surface element during an

increase of the shear force is shown in Figure 7-7. In this example the global shear force shown in the left side of the figure is increased in three steps from zero to a maximum amount represented by F_3 . On the right hand side of the figure the local shear force of each surface element is displayed. The overall height of each bar represents the ability of shear load transfer based on the local static friction coefficient and the local inclination angle. In other words: the overall height of each bar is the limit due to slipping. The red line represents the limit due to shearing. Only at surface element 2 (contact area 2) the level of the shear limit is lower than the level of the slip limit because of the large inclination angle.

Consequently, surface elements 1, 3 and 4 will fail due to slipping and surface element 2 will fail due to shearing. Based on the limits of the basic mechanical model the overall joint will either fail when the first surface element fails due to plastic deformation (which is shearing) or all surface elements fail due to slipping (which is not the case in this example).

At load step F_1 the global shear force is distributed evenly among all surface elements. All surface elements transfer the same local shear force which sums up to the global shear force level F_1 .

When the global shear force is increased to level F_2 , the additional load is again distributed evenly among all surface elements. But this time surface element 3 reaches its slipping limit before F_2 is reached. Surface element 3 will not transfer more shear force than at its individual slip limit, i.e. the amount of shear force transferred by this element is frozen. The remaining amount of local shear force that is not transferred by element 3 is distributed evenly among the other three surface elements.

In the last step the global shear force is increased to level F_3 . Initially, the additional amount of shear force is distributed evenly among surface elements 1, 2 and 4. During the load increase, surface elements 1 and 4 reach their individual slip limit. First, surface element 1 reaches its slip limit. The surplus of local shear load is distributed among elements 2 and 4 until surface element 4 reaches its slip limit. At this point the remaining fraction of the global shear force is transferred by surface element 2 only.

After this loading stage there is only a very small potential for taking up additional load, represented by the “empty area” between the load level reached by surface element 2 and its individual failure limit which, in this case, is the shear limit. Consequently, the joint will fail when the global shear force is increased by at least this remaining amount.

This mechanism of load distribution in combination with the mixed failure mode can easily be verified by a small numerical experiment. In this experiment a joint

with fractured surfaces with 10 surface elements is simulated. The data of this joint are calculated based on the data of the con-rod bolting specimens⁶⁹. The goal of this simulation is to calculate the effective friction coefficient of this model and compare the result with the FEM calculations and the experimental results.

For this comparison the transferred shear force is calculated for a normal force (equal to the preload in the experiments) of 10kN, 20kN, 30kN and 40kN. An example of these calculations is shown in Table 7-1 where the elastic limit for a preload of 40kN is calculated.

element		limit		failiure
number	incl. Angle	slip	shear	
1	10°	1125 N	10024 N	1125 N
2	10°	1125 N	10024 N	1125 N
3	20°	1926 N	5617 N	1926 N
4	20°	1926 N	5617 N	1926 N
5	30°	2875 N	4432 N	2875 N
6	30°	2875 N	4432 N	2875 N
7	35°	3442 N	4190 N	3442 N
8	80°	53330 N	5062 N	5062 N
9	80°	53330 N	5062 N	5062 N
10	80°	53330 N	5062 N	5062 N
sum				30480 N

Table 7-1: Calculation of the shear force and the failure mode of a joint with fractured surfaces consisting of 10 surface elements

($\mu_{\text{stat}}=0.1$, $F_N^*=40000\text{N} \rightarrow F_N=4000\text{N}$, $A=11,8\text{mm}^2$)

In Table 7-1 for each surface element the limits for slipping and shearing are calculated in dependence of the local inclination angle using formulas (7-7) and (7-6) respectively. Due to the mixed failure mode each element will fail when the threshold of one limit is reached. In the displayed example elements 1 to 7 fail due to slipping and element 8 to 10 fail due to shearing. The maximum transferrable shear load of each element is added to the global transferrable shear load. In this case the global transferrable shear load is $F_Q^*=30480\text{N}$. The effective friction coefficient, defined as the ratio of the global transferrable shear load and the glob-

⁶⁹ Static friction coefficient is set to 0.1. For the calculation of the normal force and the shear area see footnote 65 (page 134) but for 10 elements.

al normal force, is calculated to $30480\text{N} / 40000\text{N} = 0.762$. This procedure is done for all remaining preload steps (normal force steps). The result is shown in Figure 7-8.

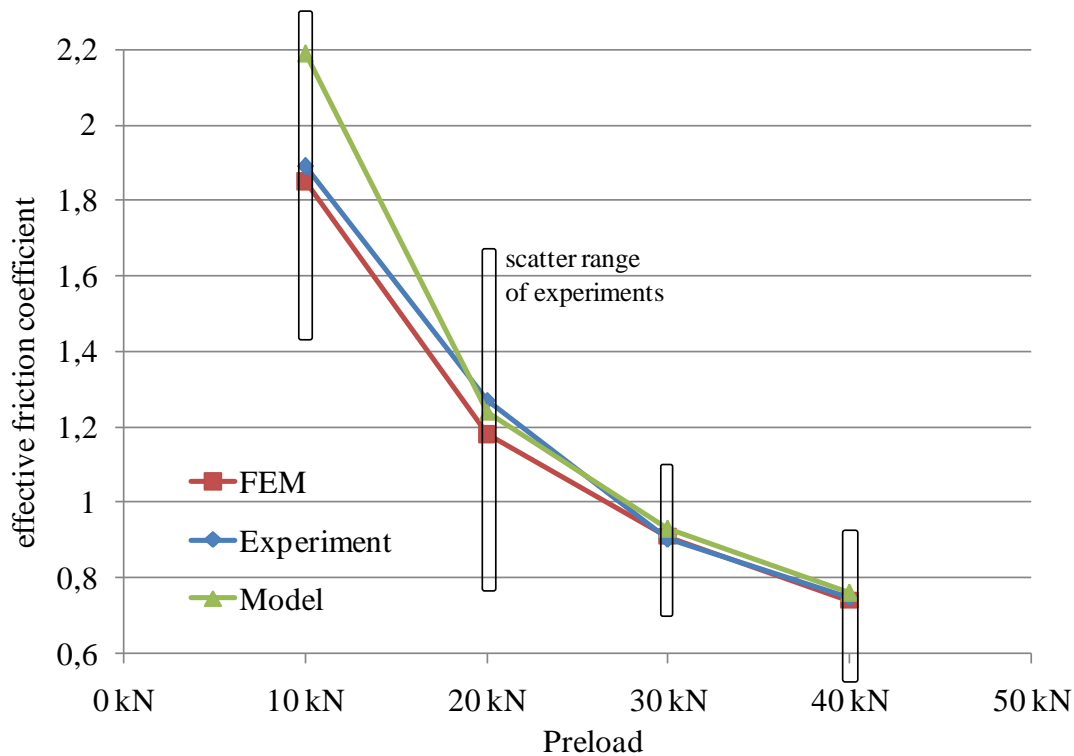


Figure 7-8: Comparison of the results of the FEM calculation, the experiments and the simple numerical simulation with the model of a joint consisting of 10 surface elements

Figure 7-8 shows that the results of the calculations of the effective friction coefficient using the mechanical model meet the numerical and experimental results to a large extent. In the preload range from 20kN to 40kN the results are identical. For the preload of 10kN the results of the mechanical model differ slightly but are still within the scatter range of the experiments. This deviation is a tribute to the very limited number of elements included in the calculated model. More elements would enable the possibility for a more realistic distribution and variation of element inclination angles and, hence, generate a better fit to the experimental and numerical results. The change of one or more element inclination angles would change the appearance of the curve more or less slightly and represents the naturally appearing differences of the real fractured surfaces. Moreover, these differences are the source of the rather large band of scatter of the experimental results.

7.5 Distinctive Features of Fractured Surfaces

In the previous sections a basic mechanical model for the shear load transfer, the failure modes and the load distribution for a joint with fractured surfaces has been developed. With this model the behavior of a joint with fractured surfaces can be explained, especially the following distinctive features:

- Non-linearity of the effective friction coefficient and its dependence of the applied normal force:
The effective friction coefficient has a non-linear characteristic as shown in Figure 6-14. This does not meet common expectations concerning a friction coefficient. The static as well as the global friction coefficient are, to a large extent, independent from the normal force. This independence of the static as well as the global friction coefficient is based on the prerequisite of pure elastic loading. In a joint with fractured surfaces this prerequisite is not fulfilled because a number of surface elements fail due to shearing, that is, plastic deformation. Consequently, the source for the non-linear characteristic of the effective friction coefficient is the mixed failure mode of the surface elements, especially the threshold of the slip-to-shear-angle (see Figure 7-4). With increased normal force the threshold of the slip-to-shear-angle decreases so that more surface elements fail due to shearing than at a lower level of normal force i.e. the shear limit decreases with increasing normal force. Consequently, with increasing normal force the global amount of transferred shear force is increasingly limited by plastic deformations. This leads to the non-linear characteristic of the ratio of global shear force and global normal force which is defined as the effective friction coefficient.
- Different amounts of surface damage at tested specimens at different normal forces (= preloads):
During the experimental investigation of shear load transfer it was found that specimens with higher bolt preload had a higher share of plastically deformed surface areas than specimens with a lower bolt preload (see Figure 6-9). The source for this phenomenon is directly connected to the source for the non-linearity of the effective friction coefficient. With increasing normal force the slip-to-shear-angle decreases. As a result more surface elements fail due to shearing, i.e. there is a higher share of plastic deformation of the surface area.
- Independence of the transferred shear force from surface topology:
A fractured surface with a rather smooth surface topology transfers just as much shear load as a fractured surface with a very distinct surface topology (see Figure 6-22 as well as Appendix III.2). It was expected that a dis-

tinct topology would enable higher shear loads to be transferred. This expectation was not confirmed, because it ignored the number of surface elements that transfer the shear force. At a surface with large surface elements, i.e. a distinct surface topology, each surface element transfers a rather large amount of shear force. However, due to the limited surface size only a small number of such surface elements will be available. At a surface with small surface elements, i.e. a rather smooth surface topology, each surface element transfers just a small amount of shear force but there will be a large number of elements. In the studied fractured surfaces extremely distinct or smooth surfaces do not occur. As a consequence, the surface topology does not have an impact on the amount of transferrable shear force.

- Large scatter range of the transferrable shear force at each normal force level (= preload level):

The experimental investigation of the transferrable shear force reveals a large scatter range as seen in Figure 6-13. The reason for this phenomenon is located in the force transfer by many individual surface elements. Each surface element has its individual inclination angle and hence its individual transfer limit. The distribution of elements with large inclination angles and elements with small inclination angles is random for each fractured surface. A fractured surface with many elements with a small inclination angle carries less shear force than a surface with many elements with high inclination angles. Obviously the area of the fractured surface of the conrod bolting specimens is too small to compensate an accumulation of elements with a larger or smaller inclination angle by stochastic means. Consequently, a large scatter range is to be expected.

- The remarkable correlation of FEM calculation and experimental results especially regarding the effective friction coefficient:

The results of the experimental investigations and the FEM calculations concerning shear load transfer show an extraordinary correlation (see Figure 6-27). The reason for this degree of correlation is the simplicity of the failure mode of a fractured surface. A fractured surface consists of a number of surface elements that fail individually due to slip or due to shear. These failure limits do only depend on some basic factors (normal force, element size = area, static friction coefficient, inclination angle) which are basic boundary conditions in a FEM calculation. The calculation of the element status – slipping or deformation – is one of the core functions of a FEM simulation. As a result the FEM predicts the transferrable shear load for a fractured surface very well and hence meets the experimental results remarkably.

7.6 Conclusions

Concerning the mechanical model of fractured surfaces the verification process of the related hypothesis formulated in section 4.1.2 revealed the following results:

Hypothesis (8):

The mechanism of load transfer in a fractured surface joint is a combination of areas with form based load transfer and areas with force based load transfer.

To verify this hypothesis, in this chapter a mechanical model for the calculation of the transferrable shear force of a joint with fractured surfaces was developed. In this model a fractured surface is sectioned into a finite number of surface elements. For each element the individual shear force limit is calculated. This limit depends on the expected failure mode which is either slipping or shearing. Which failure mode is active depends on the local inclination angle φ_{geom} , the local static friction coefficient μ_{stat} , the local normal force F_N , and the permissible von-Mises stress σ_{perm} . The hypothesis could be confirmed.

Although the mechanical model is only a 2-dimensional model and only valid for elastic deformations, it is able to properly describe the behavior of a fractured surface under shear load. All distinctive features of a fractured surface, such as the non-linearity of the effective friction coefficient, the different shares of surface damage at specimens tested with different bolt preloads, the independence of the transferrable shear force from the surface topology, as well as the large scatter range of the transferrable shear force can be explained. Additionally, the remarkable correlation of the experimental results and the FEM calculation concerning the transferrable shear force can be explained too.

8 Connecting Rod Tests

This chapter describes the test series involving real con-rods from automotive vehicles. These tests have been conducted in order to verify the test results gained from the relaxation test series with the con-rod bolting specimens described in Section 6.1.

8.1 Relaxation Tests

The aim of the relaxation tests is to verify the validity of the test results involving the con-rod bolting specimens (CBS). Furthermore, the influence of the bearing shells was to be determined.

The following tasks were performed:

- Determination of the amount of relaxation losses of the con-rods and comparison with the observed losses of CBS
- Identification of the impact of bearing shells on the amount of relaxation losses
- Determination of the influence of the fractured surface topology on the amount of losses and comparison with the topology influence in CBS
- Determination of the influence of moderately increased temperature on the amount of relaxation losses and comparison with the temperature influence in CBS

8.1.1 Con-Rod Test Series

Three test series have been designed to clarify potential differences in the relaxation behavior of connecting rods and of the con-rod bolting specimens. In each test series all specimens have been tested at the same time to avoid any influences of possible differences in ambient conditions. For accurate bolt elongation measurement all test series followed the procedure described in the Appendices II.5.1 and II.5.2 for bolt preparation, bolt assembly and bolt post-processing.

For each test series the specific objective is described below. Furthermore, specific test parameters and the corresponding CBS test series are listed. All test series have in common that 5 con-rods of each laser notch batch were used, which results in a total of 15 specimens (30 bolts) per test series.

Con_Ref: reference test series
 con-rods assembled without bearing shells
 stored for 168h in drying kiln at 150°C
 compared with CBS test series Relax_Ref

Con_BS: specify impact of bearing shells on relaxation losses
con-rods assembled with bearing shells
stored for 168h in drying kiln at 150°C
compared with CBS test series Relax_Ref

Con_T: specify effect of temperature on the amount of losses
con-rods assembled with bearing shells
stored for 168h in conditioned room at 22°C
subsequently stored for 168h in drying kiln at 150°C
compared with CBS test series Relax_T1

Table 8-1 gives an overview of all test series concerning con-rod relaxation.

Test Series		Specimen per Laser Batch			Test Temperature		Remarks
Name	Mode	Yellow	Green	Red	22°C	150°C	
Con_Ref	static	5	5	5		168h	without bearing shells
Con_BS		5	5	5		168h	with bearing shells
Con_T		5	5	5	168h	168h	with bearing shells

Table 8-1: Test series for relaxation tests with connecting rods (Add: compared with: Relax_Ref, Relax_T1)

8.1.2 Con-Rod Test Results

A summary of the results of the relaxation tests is shown in Figure 8-1. In this figure the loss of elastic elongation as percentage of the maximum elastic elongation is shown for each test series and for the corresponding CBS test Relax_Ref and Relax_T1. In Table 8-2 the values of the average relaxation loss, the RMS values, and the maximum and minimum values of each test series are given. Details are described in the subsequent sections.

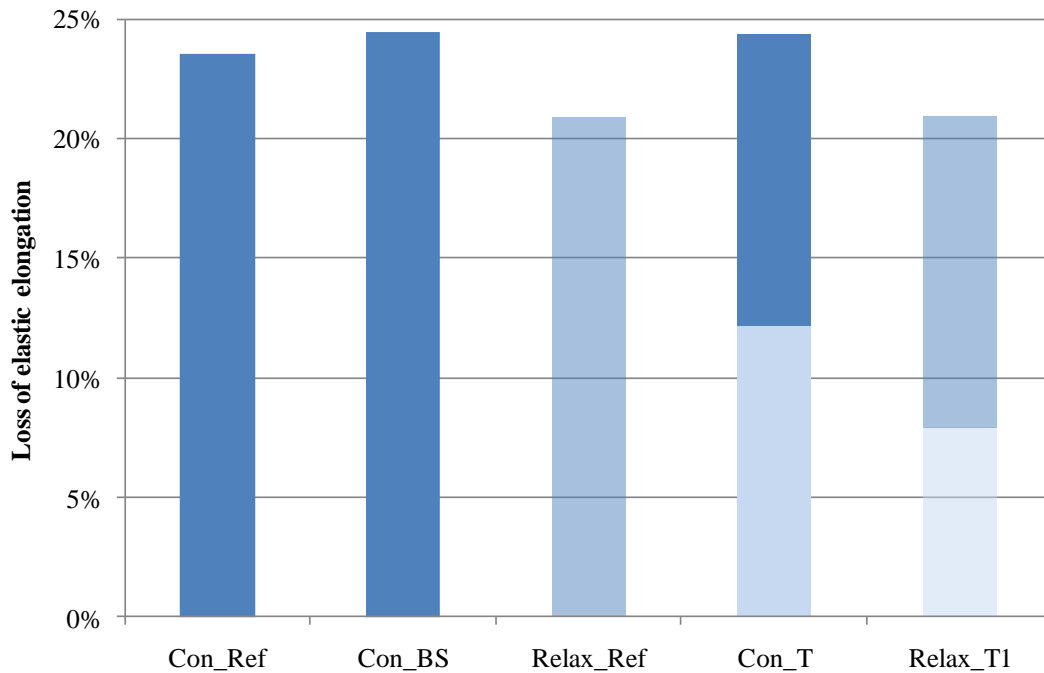


Figure 8-1: Overview of the results of the relaxation tests with connecting rods at 150°C (dark bars) and at 22°C (light bars) as well as test results from CBS tests (transparent bars) for comparison

	Con_Ref	Con_BS	Relax_Ref	Con_T	Relax_T1
Average	23,5%	24,4%	20,9%	24,4%	21,0%
RMS	1,0%	2,8%	2,0%	1,9%	2,1%
Maximum	26,7%	30,9%	24,8%	29,6%	25,7%
Minimum	21,9%	20,5%	16,5%	21,1%	16,3%
Tests at 22°C					
	Mean	12,2%	7,9%		
	RMS	1,7%	1,2%		
	Max	15,2%	10,7%		
	Min	9,0%	3,5%		

Table 8-2: Overview of the most important data of relaxation losses referring to maximum elastic elongation from relaxation tests with con-rods at 150°C and at 22°C as well as the data from CBS tests for comparison

8.1.2.1 Comparison of relaxation losses between CBS and con-rods

To identify differences between the magnitude of relaxation losses of CBS and connecting rods, the test series Con_Ref and Relax_Ref⁷⁰ were compared (see Figure 8-2). The loss of elastic elongation in the con-rod reference test series Con_Ref is 23.5% L_{\max} . In the CBS reference test series Relax_Ref the loss of elastic elongation is 20.9% L_{\max} , which is a difference of 2.6% L_{\max} .

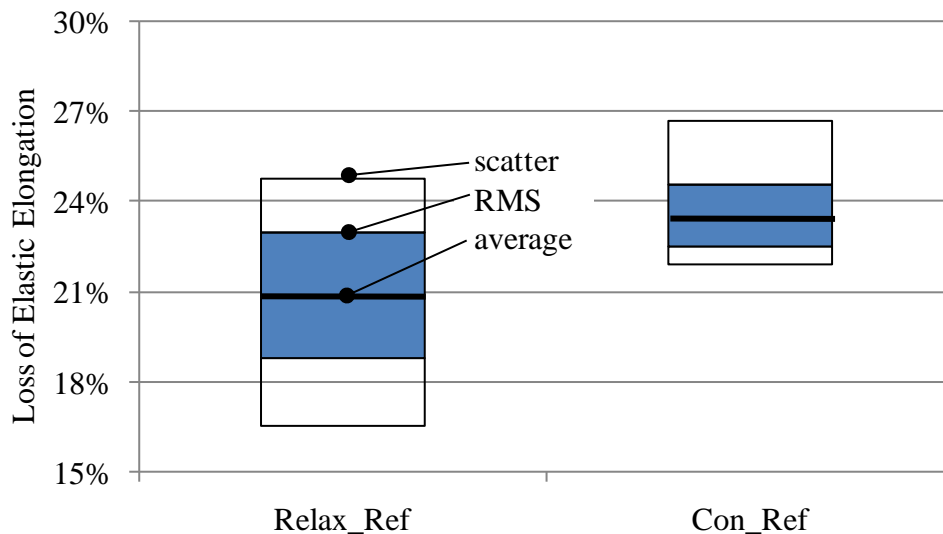


Figure 8-2: Relaxation losses at 150°C of con-rod bolting specimen reference test series Relax_Ref (n=45) and con-rod reference test series Con_Ref (n=15)

The results indicate that there is a noticeable difference in the magnitude of relaxation loss between the CBS and con-rods but also in the magnitude of the scatter band. Statistical deviations seem to be the major reason for both differences. These deviations could not be balanced due to the low number of specimens. Both, scatter and low number of specimens, turn the differences to be statistically not significant. It is very likely that the observed difference is an effect of the elastic interaction between the two bolts in the con-rod: the CBS only had one bolt⁷¹. This effect had already been encountered with bolted joints of con-rods during tests for the FVV project “Self Loosening of Bolts” (Lyszczan, et al., 2007).

⁷⁰ For details of Relax_Ref see Section 6.1.1

⁷¹ Further details regarding elastic interaction are provided in Section 2.4.3

8.1.2.2 Impact of bearing shells

For the specification of the impact of bearing shells on relaxation losses, the test series Con_BS is compared with test series Con_Ref (see Figure 8-3). The relaxation loss of test series Con_BS is 24.4% L_{max} with a RMS value of 2.8% L_{max} . In test series Con_Ref the relaxation loss is 23.5% L_{max} with a RMS value of 1.0% L_{max} .

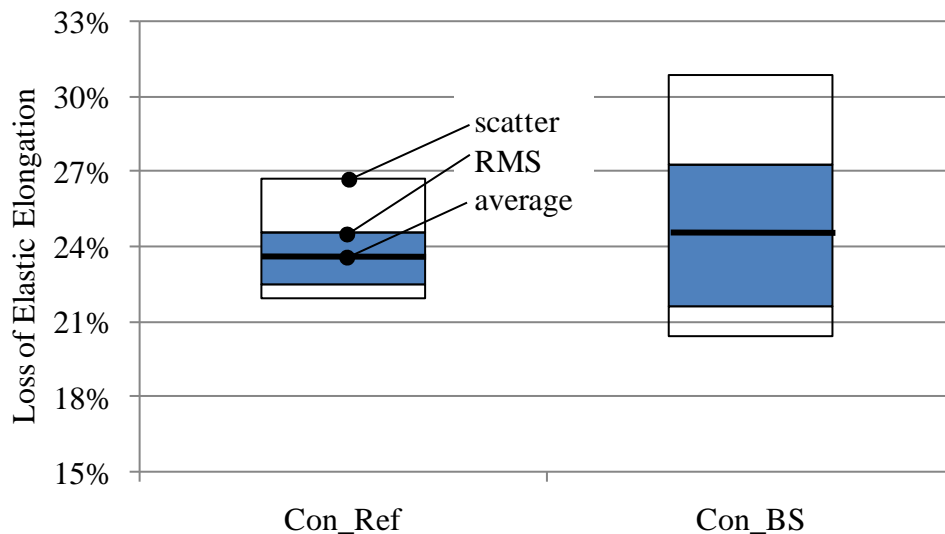


Figure 8-3: Relaxation losses at 150°C of con-rod reference test series Con_Ref (n=15) and con-rod test series Con_BS (n=15) with bearing shells mounted

The findings suggest that bearing shells have no impact on the average relaxation. Instead, the bearing shells seem to increase the scatter.

8.1.2.3 Influence of surface topology

In all con-rod test series specimens from all three laser notch batches have been used as was the case with the CBS tests. All test series have in common that there is no significant difference in the relaxation losses between the laser notch batches.

It can be concluded, that the surface topology has no impact on relaxation losses. This is in line with the results of the CBS test series⁷².

8.1.2.4 Effect of moderately increased temperature

The effect of temperature on the amount of relaxation loss was specified with test series Con_T in comparison with CBS test series Relax_T1 (see Figure 8-4). The average relaxation loss of Con_T after 168h at 22°C was found to be 12.2% L_{max} . After the subsequent storage of the con-rod for another 168h in a kiln at 150°C, the final average relaxation loss was 24.4% L_{max} . The average relaxation loss measured for the CBS (test series Relax_T1) was 7.9% after 168h at 22°C and 21.0% after another 168h at 150°C.

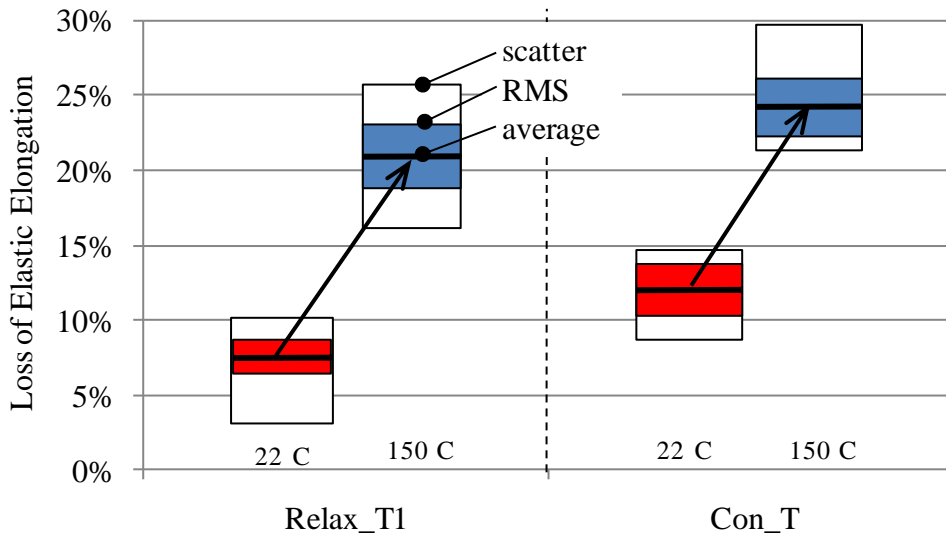


Figure 8-4: Relaxation losses of con-rod bolting specimen test series Relax_T1 (n=30) and con-rod test series Con_T (n=15) at 22°C and at 150°C.

The moderately increased temperature has a strong impact on the amount of relaxation losses in con-rods. This effect supports the results of the corresponding CBS test series⁷³. In both test series significant differences between cold and warm relaxation test results were observed. Furthermore, test series Con_T shows a difference of 4.3% L_{max} and 4.2% L_{max} in the average relaxation loss at 22°C

⁷² See Section 6.1.3.2 for further information

⁷³ See Section 6.1.3.6 for further details

and at 150°C respectively, in comparison to test series Relax_T1. Due to the scatter the difference at 22°C is statistically indifferent and at 150°C statistically not significant.

The test with the con-rods with bearing shells (test series Con_BS) at 150°C showed no difference of the final average relaxation loss compared to the test series Con_T. This implies that a prior relaxation at 22°C has no effect on the final relaxation loss. This is in line with the finding of the corresponding CBS test series in Section 6.1.3.6.

8.2 Conclusions

A comparison of the relaxation losses of con-rods and CBS did not reveal significant differences.

The bearing shells located within the big bore of the con-rod had no influence on the average amount of the relaxation loss. Nevertheless, bearing shells seem to increase the scatter of the relaxation losses.

The topology of the fractured surfaces was not found to have an impact on the amount of relaxation loss. This is in line with the results from the CBS tests.

The CBS tested in Chapter 6 seem to be a suitable replacement for the actual con-rod specimens.

9 Conclusions

According to the challenges outlined in Chapter 1 concerning the unknown mechanical behavior of fracture splitted connecting rods a number of research questions were formulated.

An analysis of the state of the art concerning force transfer, bolted joints, connecting rods and surface topology parameters was performed. The analysis was partly based on a literature study (Chapter 2) and partly on previous research of the author on fracture splitted connecting rods (Chapter 3). The goal was to identify the specific knowledge gaps regarding fractured surfaces and the mechanical behavior of fracture splitted connecting rods.

Based on this analysis research hypotheses related to the research questions were established (Chapter 4), which were verified in a number of test series. For the tests a special specimen, the con-rod bolting specimen (CBS), was developed to enable fundamental research into fractured surfaces. Three kinds of surface topologies were investigated from fairly smooth to distinct. The tests in Chapter 5 focused on these fractured surfaces. Chapter 6 describes the CBS tests concerning preload losses and transferrable shear loads. This resulted in Chapter 7 in a mechanical model for a joint with fractured surfaces. Chapter 8 involved test with actual con-rods in order to verify the applicability of results obtained with the CBS.

In the following sections the results of the verification of the hypotheses as well as additional findings are summarized.

9.1 Fractured Surfaces

The aim of the investigation of the fractured surfaces was to identify parameters which are able to describe different surface topologies.

Research Question (1):

What are suitable parameters to describe different fractured surfaces?

Hypothesis (1):

Parameters that are able to describe different fractured surfaces can be obtained by adjusting and combining standardized roughness parameters.

Results:

The hypothesis could not be confirmed: The standardized roughness parameters were not suitable. For that reason new parameters were created. The parameter *sliding average inclination angle* was found to be useful for a differentiation of specimens of different laser notch batches. Furthermore, the combination of the parameters *matching rate* and *vertical distance* was found to be a good indicator of the matching quality of a pair of fractured surfaces and enabled the differentiation between large cavities and numerical errors resulting from data processing.

9.2 Preload Losses

The investigations concerning the preload losses were conducted to identify influencing parameters and the respective magnitude of losses. The tested parameters are the impact of the fractured surface in general, the impact of the surface topology, and the effect of moderately increased temperatures.

Research Question (2):

What is the impact of fractured surfaces on the relaxation of bolted joints?

Hypothesis (2):

The fractured surface has a significant impact and cannot be ignored in the calculation of the bolted joint.

Result:

The hypothesis had to be rejected. The relaxation loss of pairs of fractured surfaces did not show any significant difference compared to the relaxation loss of pairs of plain surfaces.

Research Question (3):

What is the relation between surface topology and the amount of relaxation losses?

Hypothesis (3):

The more distinctive the surface topology, the larger is the amount of relaxation losses.

Result:

The hypothesis had to be rejected. The topology of the fractured surfaces was found to have no influence on the amount of relaxation losses. A possible explanation suggested by the available data is the high matching rate of the surfaces which results in a relatively large microscopic contact area.

Research Question (4)

What is the effect of moderately increased temperature on the amount of relaxation losses?

Hypothesis (4):

An increase of temperature to the operating temperature (150°C) results in an exponential loss due to relaxation.

Result:

The hypothesis could be confirmed. The average relaxation loss under operating temperature increased by about 90% compared to room temperature.

9.3 Transferrable Shear Loads

A number of test series has been conducted to identify parameters influencing the amount of transferrable shear load in bolted joints with fractured surfaces. Investigated influencing parameters were the clamping force of the bolted joint (equal to the bolt preload), the impact of the surface topology, and the effect of moderately increased temperature (150° operating temperature).

Research Question (5):

What is the impact of the clamping force on the transferrable shear load in a bolted joint with fractured surfaces?

Hypothesis (5):

The amount of transferrable shear load (F_Q) in a bolted joint with fractured surfaces is determined by the magnitude of the clamping force (F_N) in the following way: $F_Q = \mu_{\text{effective}} \cdot F_N$. (The effective friction coefficient is to be determined by experiments.)

Results:

The hypothesis could be confirmed. The ratio of the transferrable shear load and the clamping force (effective friction coefficient $\mu_{\text{effective}}$) was approximated by the ratio of transferrable shear load and installed preload. For a preload range between 10kN and 40kN this effective friction coefficient was determined experimentally and numerically. Typical values lie between $\mu_{\text{effective}} = 0.8 \dots 1.9$ depending on the applied preload. The use of these values in calculations with flat surface pairs resulted in the same transferrable shear load as the experiments with the fractured surfaces.

Research Question (6):

What is the relation between surface topology and transferrable shear load?

Hypothesis (6):

The more distinctive the surface topology, the larger is the effective friction coefficient. The larger the effective friction coefficient, the larger the transferrable shear load (see question 5). Hence, the more distinctive the surface topology, the larger the transferable shear load.

Result:

The hypothesis had to be rejected. No relation was found between the topology of the fractured surface and the transferrable shear load. This behavior can be explained with the developed mechanical model (see Chapter 7).

Research Question (7):

What is the effect of moderately increased temperature on the maximum transferable shear load?

Hypothesis (7):

An increase of temperature to the operating temperature (150°C) decreases the amount of transferrable shear load.

Result:

The hypothesis could not be confirmed. The experimental investigations show a slight decrease, but the difference between the transferrable shear load under operating temperature (150°C) and room temperature (22°C) is not statistically significant.

9.4 Mechanical Model

Based on the results of the investigations a mechanical model was developed.

Research Question (8):

What kind of mechanism enables the load transfer?

Hypothesis (8):

The mechanism of load transfer in a fractured surface joint is a combination of form based load transfer in some areas and force based load transfer in other areas.

Results:

A mechanical model for fractured surfaces was developed. In this model a fractured surface is sectioned into a finite number of surface elements. For each element the individual shear force limit is calculated. This limit depends on the expected failure mode which is either slipping or shearing, depending on whether the local element contributes to force based load transfer or form based load transfer respectively. The decision which failure mode is active depends on the local inclination angle φ_{geom} , the local static friction coefficient μ_{stat} , the local normal force F_N , and the permissible von-Mises stress σ_{perm} . This mechanical model is able to describe the behavior of a fractured surface under shear load. All behavioral features that were found to be typical for fractured surfaces can be explained, including the remarkable correlation of the experimental results and the FEM calculations.

9.5 Additional Results

Additional tests were performed to investigate topics that are closely related to the research hypotheses, but were not covered by the primary test series.

9.5.1 Fractured Surfaces

The investigations of the fractured surfaces resulted in some additional findings concerning the separation force, the influence of the laser notch, and the surface parameter *matching rate*.

Separation Force

The reason for the need to apply a considerable force to separate con-rod cap from the body was unknown. Adhesive forces or micro mechanical catching of surface

roughness were both claimed by industrial experts to be the main source. The test results and surface investigations suggest that adhesion is the source of this force. The surface scans revealed comparably large roughness values. However, these values only refer to individual surfaces. A pair of fractured surfaces each with a large roughness may still fit very well, in particular if the surfaces are mirrored images, which – at least theoretically – is the case in fractured surfaces. As the tests show, pairs of fractured surfaces fit very well, having an average matching rate of 87.8%. This can explain the existence of an adhesive force holding con-rod cap and body together.

Influence of Laser Notch

The influence of the depth of the laser notch on the topology of the fractured surface was confirmed. Short laser holes result in a very distinct surface topology while long laser holes result in a rather smooth surface topology. The occurrence of large particles shows up as tracks in the fractured surface of both parts of a pairing. These tracks are local plastic deformations of the surface topology. An indicator for the existence of large particles in the joint between the fractured surfaces is the ease of separation. A large particle can be expected when con-rod cap and con-rod body can be separated without any additional force.

Matching Rate

The matching rate of each specimen used in this research project was computed by analyzing the laser scanner data of fractured surface pairs. For the computation a threshold of 0.05mm was chosen⁷⁴. The average matching rate of all specimens was calculated to be 87.8%. The average matching rate of the specimens of the yellow (very distinct topology) and green laser notch batch (fairly distinct topology) is slightly below this global average, while the matching rate of the specimens of the red laser notch batch (fairly smooth topology) is slightly above this value. The differences are statistically not significant.

9.5.2 Preload Losses

The assumed influence of the surface topology on the risk of mismatched assembly of smooth fractured surfaces (red laser notch batch), as well as on the risk of particle embedment in fractured surfaces with a distinct surface topology (yellow laser notch batch), was analyzed. Furthermore, the influence of dynamic mechanical loading was investigated in a separate test series.

⁷⁴ For further information about the threshold see Section 5.3.2.1.

Mismatched Assembly

A test series with 10 con-rod bolting specimens (red laser notch batch only) was conducted to check the relaxation losses in case of mismatched assembly, involving a 0.2mm displacement along the crank shaft axle.

The result of the tests was that this type of mismatched assembly does not affect the relaxation losses (see Section 6.1.3.3). Apparently fractured surfaces with a smooth topology are, in this respect, comparable with smooth surfaces (low roughness value).

Embedded Particles

Two test series with 10 specimens and 5 specimens respectively, and a different amount of particle emplacement (1 particle with a weight of 7mg, and 3 particles with an overall weight of 36mg, respectively) were carried out to investigate the impact of particles on relaxation losses. The particles used in these test series were artificially produced.

The particles did not show any effect on the relaxation losses (see Section 6.1.3.4). This result was surprising because it is contrary to results of an earlier research project (Lyszczan, et al., 2007), where a large effect was observed. A likely reason for this difference is the shape of the particle caused by different ways of particle production.

Mechanical Loading

A test series with 30 specimens (10 specimens of each laser notch batch) was used to determine the impact of mechanical loading on the amount of relaxation losses. The specimens were loaded with a dynamic tumescent load of 9kN under operating temperature conditions (150°C).

This moderate dynamic mechanical loading did not increase the relaxation losses significantly (see Section 6.1.3.5).

9.5.3 Shear Load Transfer

The conducted shear load tests determination were also used to determine the impact of an increased static friction coefficient caused by a significantly increased contact time on the amount of transferrable shear load. Furthermore, the results of FEM calculations and tests regarding the transferrable shear load were compared.

Contact Time

The effect of increased contact time onto the amount of transferrable shear load was determined by two test series with a total of 30 specimens (10 specimens per laser notch batch).

The increase of contact time from some minutes to 168 hours resulted in an average increase of transferrable shear load of 20% (see Section 6.2.3.3) which is still statistically indifferent due to the large scatter. This increase of transferrable shear load is the result of the well known effect that the static friction coefficient μ_{stat} increases logarithmically over time. The static friction coefficient μ_{stat} is a part of the effective friction coefficient $\mu_{\text{effective}}$ which is a characteristic parameter for the shear load transfer in fractured surfaces.

FEM calculation

The results of the numerical calculation of a joint with fractured surfaces are nearly identical to that of the experimental. It can be concluded that the proposed modeling of the fractured surfaces and the related FEM calculations are suitable to complement the experiments and thereby reduce their number and allow to analyse parameters that are hard to manipulate in an experimental setup.

9.5.4 Simplified FEM Model

Alraheb (Lyszczan, et al., 2007) developed a simplified FEM model for the simulation of shear load transfer in con-rods with fractured surfaces based on the high conformity of the experimental data and numerical results with the initial more detailed FEM model. Instead of modeling a fractured surface joint, a joint with plain contact surfaces can be used. The characteristics of the fractured surfaces have been implemented using the effective friction coefficient rather than a static friction coefficient⁷⁵.

⁷⁵For further details see Appendix III.4

9.6 Contributions

The following contributions were made:

- Design and successful use of a special kind of specimen, the con-rod bolt-ing specimen (CBS), for the basic research of fractured surfaces
- Definition of an effective friction coefficient $\mu_{\text{effective}}$, which is non-linear due to the dual failure mode of fractured surfaces
- Increased knowledge concerning the use of fractured surfaces in bolted joints
 - Despite their individual high surface roughness, the surface pairs do match very well
 - With respect to relaxation losses fractured surfaces can be treated like plain surfaces
 - With respect to transferrable shear loads fractured surfaces transfer one magnitude higher loads than plain surfaces
 - FEM calculations can be used to directly calculate transferrable shear loads using plain surfaces but applying the empirically ob-tained $\mu_{\text{effective}}$ or by direct modeling of the surface topology
- Set up of a mechanical model to describe distinctive features of a joint with fractured surfaces
- Successful comparison of the results of tests with the CBS those with a real part, the connecting rod

9.7 Outlook

The research revealed several interesting directions for further research. On the one hand, a number of questions remain unanswered. On the other hand, new fields of application for fractured surfaces arise. Both points will be outlined in the next sections.

9.7.1 Open Questions

Although a joint with fractured surfaces has been made computable by means of the results of this research there are still some open questions:

The impact of particles on the amount of relaxation loss in fractured surfaces ana-lyzed in Section 6.1.3.4 was found to be negligible. This contradicts the findings in (Lyszczan, et al., 2007). It was already pointed out that there were distinct dif-ferences in the kind of particles used in the tests. But the basic question of the influence of particles remains:

- How do particles influence the amount of relaxation loss? What are the critical values concerning particle size, shape and number?

Besides the influence on the amount of relaxation loss, particles may also have an impact on the amount of transferrable shear load. No investigations are known that address this potential threat. This leads to the following question:

- How do particles influence the amount transferrable shear load? What are the critical values concerning particle size and number?

During the analysis of the results of the shear load tests in Section 6.2.3.1 large scatter was noticed. This large scatter is a handicap for the calculation of the transferrable shear load in fractured surfaces. To gain certainty concerning the transferrable shear load, large safety factors would need to be implemented, which has a negative effect on the optimization of shear load transfer. Consequently, an important question is:

- How to decrease the large scatter regarding the transferrable shear load in fractured surfaces?

The calculation of the matching rate with the data of the surface scans revealed large cavities within the fractured surfaces. During the investigations of relaxation loss and transferrable shear load these cavities seem to have no impact on the results. Nevertheless, for designers as well as for quality controllers the following question is still of relevance:

- What is the impact of large cavities on the behavior of fractured surfaces? Is there a critical threshold concerning cavity size?

The investigations into surface parameters to describe the characteristic surface topology of fractured surfaces revealed that standardized surface parameters are not suitable. New parameters were defined. However, the problems concerning the source of the separation force made clear that a parameter to describe the effective surface roughness between a pair of fractured surfaces is still missing:

- Which parameter(s) can describe the surfaces of a pair of fractured surfaces that allow predicting the behavior of such a joint?

9.7.2 New Applications for Fractured Surfaces

The results from this research project may be carried over to other applications which contain joints with fractured surfaces:

- Cracked crank shaft bearing housing:
Currently the bearing housing for a crankshaft is bolted to the motor casing via joints with plain surfaces. To save machining and assembly time as well as costs the bearing housing could be manufactured with the motor

casing as a single part. After raw machining of the bearing housing the housing caps could be cracked off and bolted again to the motor casing resulting in a fractured surface joint.

- **Cracked pump casing for gearings:**
Today the casing for the oil pump is manufactured as a part of its own. In the future the pump casing could be manufactured with the gear housing as an integrated part. After the casting process the pump casing could be cracked off the gear housing. Then the pump parts are assembled into the pump casing. Finally, the preassembled pump is bolted to the gear casing using the fractured surface as the joint surface.
- **Potential innovative shaft-hub-connections:**
In a power train the frontal press fit assembly is the shaft-hub-connection which typically needs some extra care. Often arrangements to increase the friction coefficient within the joints are necessary. To avoid this handicap fractured surfaces could be used to create an enhanced frontal press fit assembly. Hub and shaft could be manufactured as a single part by drop forging or casting. Then the hub is cracked off the shaft. During the assembly process the hub is mounted back to the shaft using a single centre bolt.

Appendix

I. Literature

Afazal, A. und Fatemi, A. 2004. A Comparative Study of Fatigue Behavior and Life Predictions of Forged Steel and PM Connecting Rods. *SAE Technical Paper Series* . 2004, 2004-01-1529.

Beelich, K.H. 1970. Gesichtspunkte zur Deutung des Relaxationsverhaltens und zur Auslegung temperaturbeanspruchter Schraubenverbindungen. *Draht-Welt*. 1970, 56.

Beelich, K.H. und Wiegand, H. 1968. Relaxation bei statischer Beanspruchung von Schraubenverbindungen. *Draht-Welt*. 1968, 54.

Bickford, J.H. 1995.*An Introduction to the Design and Behavior of Bolted Joints*. 3rd. New York : Marcel Dekker, 1995.

Blauel, J.G., Mayville, R.A. und Möser, M. 2000. Werkstoff und Mechanik beim Bruchtrennen von Automobilpleueln. *Materialwissenschaften und Werkstofftechnik*. 2000, 31.

Bowden, F.P. and Tabor, D. 2001.*The Friction and Lubrication of Solids*. Oxford : Clarendon Press, 2001.

Bradley, R.S. 1932. The Cohesive Force Between Solid Surfaces and the Surface Energy of Solids. *Philosophical Magazine*,. 1932, 13, p. 853.

Brovold, T.E. 1988.*System for Manufacturing Connecting Rods*. 4,754,906 USA, July 1988.

Childs, P.R.N. 2004.*Mechanical design*. 2nd. Burlington : Elsevier Butterworth-Heinemann, 2004.

DIN4762. 1984.*Surface Roughness - Terminology: Surface and its Parameters*. Berlin : Beuth Verlag, 1984.

DIN6892. 2009.*Drive Type Fastenings without Taper Action - Parallel Keys*. Berlin : Beuth, 2009.

Dowson, D. 1979.*History of Tribology*. London : Longman Group Limited, 1979.

Fatemi, A. und Shenoy, P. 2005. Connecting Rod Optimization for Weight and Cost Reduction. *SAE Technical Paper Series*. 2005, 2005-01-0987.

- Fetouh, M.A. 1986.***Method of Making a Split Bearing Assembly.* 4,569,109 USA, Februar 1986.
- Forschungsvereinigung Antriebstechnik. 2004.***FVA R 743: Tragfähigkeitsberechnung von Achsen und Wellen.* [FVA-Richtlinie] Frankfurt : s.n., 2004.
- Fuhrmann, E. 2003.***Einführung in die Werkstoffkunde und Werkstoffprüfung, Band 2.* Renningen : Expert Verlag, 2003.
- Fuller, K. N. G. und Tabor, D. 1975.** The Effect of Surface Roughness on the Adhesion of Elastic Solids. *Proceedings of the Royal Society of London.* 1975, Series A.
- Fürst, Th. 2010.***Methodische und numerische Passgenauigkeitsuntersuchungen von Bruchflächen.* Berlin : Technische Universität Berlin, 2010.
- Geike, T. 2007.***Theoretische Grundlagen eines schnellen Berechnungsverfahrens für den Kontakt rauer Oberflächen.* Berlin : s.n., 2007.
- Granacher, J., et al. 1994.***Relaxationsverhalten von hochfesten Schraubenverbindungen bei mäßig erhöhten Temperaturen (Relaxation).* Frankfurt/Main : FSV, 1994.
- Greenwood, J.A. and Williamson, J.B. 1966.** Contact of Nominally Flat Surfaces. *Proceedings of the Royal Society of London Series A.* 1966, 295.
- Gross, D. und Seelig, Th. 2007.***Bruchmechanik.* Berlin : Springer-Verlag, 2007.
- Guigis, S. und Bhattachatjee, S. 2002.** Process of Fracture Connecting Rods. *Internal Publication #WO 02/30603 A1.* 2002.
- Haberhauer, H. and Bodenstein, F. 2007.***Maschinenelemente.* 14th. Berlin : Springer Verlag, 2007.
- Haibach, E. 2006.***Betriebsfestigkeit: Verfahren und Daten zur Bauteilberechnung.* Berlin : Springer, 2006.
- Hoенow, G. und Meißner, T. 2008.***Konstruktionspraxis im Maschinenbau.* Leipzig : Fachbuchverlag Leipzig, 2008. ISBN 987-3-446-403130.
- Hoffmann, G., et al. 2002.** Fracture Splitting of Powder Forged Connecting Rods. *SAE Technical Paper Series.* 2002, 2002-01-0609.

Huschek, S. und Merzoug, D. P. 1995. *Zusammenhang zwischen Rauheit und Griffigkeit*. Bonn - Bad Godesberg : Bundesministerium für Verkehr, 1995. Forschung Strassenbau und Strassenverkehrstechnik 735.

ISO/TR14638. 1995. *GPS-Matrix Model*. Berlin : Beuth Verlag, 1995.

ISO11562. 1998. *Surface Texture - Metrological Characteristics of Phase Corrected Filters*. Berlin : Beuth Verlag, 1998.

ISO3274. 1998. *Surface Texture - Nominal Characteristics of Contact Instruments*. Berlin : Beuth Verlag, 1998.

ISO4287. 2010. *Surface Roughness - Terms, Definitions and Surface Texture Parameters*. Berlin : Beuth Verlag, 2010.

ISO4288. 1998. *Surface Texture - Rules and Procedures for the Assessment of Surface Texture*. Berlin : Beuth Verlag, 1998.

Jähnicke, W. und Thiel, G. 1950. Kriechen von Stahl unter statischer Beanspruchung bei Raumtemperatur. *Archiv Eisenhüttenwesen*. 1950, 21, S. 105 - 118.

Johnson, K.L. and Greenwood, J.A. 1997. An Adhesion Map for the Contact of Elastic Spheres. *Journal of Colloid and Interface Science*. 1997, Vol. 192, pp. 326-333.

Johnson, K.L., Kendall, K. and Roberts, A.D. 1971. Surface Energy and Contact of Elastic Solids. *Proceedings of the Royal Society of London Series A*. 1971, 324.

Just, T. 2008. Potentialstudie zum Einsatz von gerändeltes Pressverbindungen. TU Berlin : s.n., 2008.

Kato, S., et al. 2007. Development of Microalloyed Steel for Fracture Split Connecting Rod. *SAE Technical Paper Series*. 2007, 2007-01-1004.

Keil, E., Müller, O. und Walper, E. 1972. Zeitabhängigkeit der Festigkeits- und Verformbarkeitswerte von warmfesten Stählen im Temperaturbereich unter 400°C. *Archiv Eisenhüttenwesen*. 1972, 43.

Knoll, G. und A., Kalmann. 2001. Method and Device for Fracture Splitting a Machine Component with Bearing Eye. *Internal Publication # Wo 01/70440 A1*. 2001.

Köhler, E. und Flierl, R. 2006.*Verbrennungsmotoren.* Wiesbaden : Vieweg & Sohn Verlag, 2006.

Köhler, H., Roth, G. und Walper, E. 1991.*Hochfeste Verbindungselemente aus alternativen Werkstoffen ohne Schlußvergütung.* s.l. : Studiengesellschaft Stahlanwendung e.V., 1991.

Köhler, M. 2005.*Beitrag zur Bestimmung des Coulombschen Haftreibungskoeffizienten zwischen zwei metallischen Festkörpern.* Göttingen : Cuvillier Verlag, 2005.

Kubota, T., et al. 2005. Development of Fracture Splitting Method of Case Hardened Connecting Rods. *Yamaha Motor Technical Review.* 2005.

Kuratomi, H., et al. 1995. Development of a Lightweight Connecting Rod made of a Low-Carbon Martensite Steel. *JSAE Review.* 1995, 16.

Lyszczan, P. and Alraheb, O. 2007.*Investigation of effects on self-unscrewing bolts in cracked con-rods.* Frankfurt/Main : FVV, 2007.

Lyszczan, P. 2005.*Protokoll zur Besichtigung der Crackpleuefertigung.* Salzgitter : s.n., 2005.

Lyszczan, P. und Alraheb, O. 2010.*Experimental and numerical investigations in fractured surfaces of connecting rod connections.* Frankfurt / Main : FVV, 2010.

Lyszczan, P. und Brenner, M. 2005.*Untersuchungen von Messmethoden zur Bestimmung der Bruchgüte von Crackpleueln.* Berlin : TU Berlin, 2005.

Müller, G. und Groth, C. 1997.*FEM für Praktiker.* Renningen : Expert-Verlag, 1997.

Müser, M.H. 2003. Staistische Mechanik der Reibung und die Amontons'schen Gesetze. *Physik Journal 2.* 2003, 9, pp. 43-48.

Niemann, G., Winter, H. and Höhn, B.R. 2005.*Maschinenelemente.* 4th. Berlin : Springer Verlag, 2005. Vols. Band 1: Konstruktion und Berechnung von Verbindungen, Lagern, Wellen.

Ohrnberger, V. und Hähnel, M. 1992. Bruchtrennen von Pleueln erlangt Serienreife. *Werkstatt und Betrieb.* 1992, 125.

- Olaniran, M.A. und Stickels, Ch.A. 1993.** Separation of Forged Steel Connecting Rods and Caps by Fracture Splitting. *SAE Technical Paper Series*. 1993, 930033.
- Pahl, G. and Beitz, W. 1999.***Engineering Design: A Systematic Approach*. 2nd. Berlin : Springer, 1999.
- Persson, B. N. J. 2002.** Adhesion between elastic bodies with randomly rough surfaces. *Physical Review Letters*. 2002, 89 (24): 245502.
- Persson, B.N. 2000.***Sliding Friction: Physical Principles and Applications*. Berlin : Springer, 2000.
- Pfützenreuter, A. 1965.** Zur Frage des Kriechens und der Spannungsrelaxation an kaltverfestigten Spannbetonstählen. *Draht-Welt*. 1965, 51.
- Popov, V.L. 2009.***Kontaktmechanik und Reibung*. Berlin : Springer Verlag, 2009.
- Reppen, B. 1998.** Optimized Connecting Rods to Enable Higher Engine Performance and Cost Reduction. *SAE Technical Paper Series*. 1998, 980882.
- Ross, S.M. 2006.***Statistik für Ingenieure und Naturwissenschaftler*. Berlin : Springer-Verlag, 2006.
- Sachs, K. und Evans, D.G. 1973.***The Relaxation of Bolts at High Temperatures*. Wolverhampton (UK) : GNK Lab. Reprint No. 34, 1973.
- Schäfer, F. und von Basshuysen, R. 2010.** www.motorlexikon.de. [Online] Reimedia GmbH, 2010. [Zitat vom: 28. September 2010.] www.motorlexikon.de/?I=5530.
- Schmidt, W. und von den Steinen, A. 1972.** Besonderheiten des Kriechens von Stählen bei Raumtemperatur. *MAterialprüfung*. 1972, 14.
- Strelow, D. 1983.** Mechanische Eigenschaften hochfester Schrauben aus niedrig legierten Werkstoffen bei Raumtemperatur und bei 300°C. *VDI-Z 125*. 1983, 19.
- Tabor, D. 1951.***The Hardness of Metals*. Oxford : Oxford University Press, 1951.
- Urlaub, A. 1995.***Verbrennungsmotoren*. Berlin : Springer, 1995.
- van Mises, R. 1913.** Mechanik der festen Körper im plastisch-deformablen Zustand. *Nachr. Math. Phys.* 1913, Kl. 1, S. 582-592.

VDEh. 1989.*Ergebnisse deutscher Zeitstandversuche langer Dauer.* Düsseldorf : Verlag Stahleisen m.b.H., 1989.

VDI2230. 2003.*Systematische Berechnung von hochbeanspruchten Schraubenverbindungen.* Berlin : Beuth, 2003.

Wegener, K.-W. 1998. Werkstoffentwicklung für Schmiedeteile im Automobilbau. *ATZ Automobiltechnische Zeitschrift.* 1998, 100.

Weißbach, W. 2007.*Werkstoffkunde.* Wiesbaden : GWV Fachverlag, 2007.

Wiegand, H., Kloos, K.H. und Thomala, W. 1988.*Schraubenverbindungen.* 4. Auflage. Berlin : Springer-Verlag, 1988.

II. Technical Setup

This chapter deals with the description of the manufacture of the con-rod bolting specimen, the test equipment, especially the ultrasonic devices, the technical set-up of the experiments, and the specimen set up.

II.1 Manufacture of Con-Rod Bolting Specimen

The con-rod bolting specimens (CBS) are manufactured out of standard con-rods (see Figure II-1). Any kind of con-rod is suited for the production of a pair of CBS, in case its bolted joints include not more than 2 bolts.



Figure II-1: Standard con-rod

First, the shaft of the con-rod body is cut normal to the bolt axis (see Figure II-2). In case of an angular splitted con-rod (see right figure in Figure 2-15), the throat of the con-rod for the inner bolt is opened by the cut, but the bolt remains undamaged.



Figure II-2: Shaft cut off the con-rod

In the next step, the clamped parts are cut out (see Figure II-3). The cut is parallel to the bolt axis as well as parallel to the outer side face of the specimen.

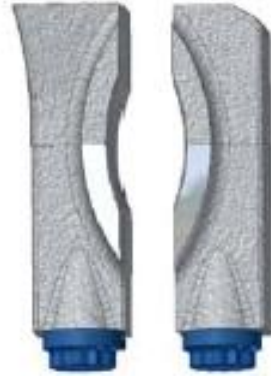


Figure II-3: Segmentation of the clamped parts

In the final step, the side faces are grinded (see Figure II-4).



Figure II-4: Smoothen side faces

II.2 Test Equipment

This section provides the technical data of the test beds and the test bed equipment used for the research described in this document.

Tension Testing Machine

The tension testing machine (see Figure II-5) was used for calibrating the bolts with glued-on ultrasonic sensors for the shear load transfer tests.



Figure II-5: Tension testing machine

- Hydraulic single axis tensile testing machine of Mohr & Federhaff (1965)
- Quasi-static loading only
- Maximum load:100kN

Hydropulser

The hydropulser was used for one relaxation test series (mechanical loading test) for dynamic loading (see Figure II-6). Furthermore, the hydropulser was used for the shear load tests in which it was operated as a quasi-static tension machine. In both cases, the device was operated in load controlled mode.



Figure II-6: Hydropulser Instron 8801

- Hydraulic single axis universal testing machine 8801 of Instron (2005)
- Dynamic loading up to 100Hz
- Maximum load: 100kN
- For con-rod bolting specimen (CBS) tests equipped with shear loading device
- For test under operating temperature (150°C) equipped with tube furnace

Shear Loading Device

The shear loading device was proprietary designed for the use with CBS (see Figure II-7). With the help of this device, the CBS were loaded with pure shear load. All other kinds of load, e.g. bending, torsion, axial tension or pressure, are excluded due to the specific design.



- Proprietary loading device for use with the hydropulser
- For applying static or dynamic shear load into a single con-rod bolting specimen
- Designed for use with tube furnace
- Maximum operating temperature of device: 200°C
- Maximum transferrable static load: 47kN
- Maximum transferrable dynamic load: 22kN

Figure II-7: Shear loading device

Drying Kiln

The drying kiln was used to relax the specimens, CBS, as well as con-rods, under operating temperature (150°C) for the relaxation tests, as well as for some shear load transfer tests (see Figure II-8).



- Drying kiln of Fritz Ruhland Company (1967)
- Maximum operating temperature: 200°C
- Analog temperature control
- Temperature stability: +/- 1°C
- Temperature measurement: rear side of kiln at about 1/3 of overall kiln height above the ground via resistance thermometer

Figure II-8: Drying kiln

Tube Furnace

The tube furnace (see Figure II-9) was used in combination with the hydropulser and the shear loading device for dynamic and quasi-static tests under operating temperature (150°C).



- Bipartite tube furnace of Thermoprozess Company (2008)
- Maximum Temperature: 450°C
- Digital temperature control
- Temperature stability: +/- 0.5°C
- Temperature measurement: directly at specimen via thermo couple

Figure II-9: Tube furnace

II.3 Ultrasonic Devices

This section is about the ultrasonic measurement device, the ultrasonic sensors and the proprietary ultrasonic devices used for measurement of bolt elongation in all of the tests.

Ultrasonic Measurement Device



- Ultrasonic device USM III of Norbar (2009)
- Especially designed for measurement of bolt elongation
- Measurement accuracy: 0.1ns (equal to about 0.2µm for a bolt size M8 of 60mm length)
- Max. operating temperature: 175°C
- Signal frequency: 1,25MHz to 10MHz (depending on connected sensor, stepwise adjustable)

Figure II-10: Norbar USM III

Ultrasonic Sensors

For the experimental tests glued-on sensors, also called transducers, in combination with proprietary connectors have been used. To verify the measurement accuracy of this combination, a hi-temp transducer from Norbar and a standard connector from Norbar were used prior to the tests.

- Glued-on transducers
 - Silver covered piezo ceramic discs,
 - Attached directly to bolt with glue
 - Eigenfrequency: about 5MHz
 - Diameter: 3mm
 - Height: 0.5mm
 - Operating temperatures up to 200°C (2/3rd of Curie temperature)

- Standard 1/4" transducer by Norbar
 - Magnetic transducer
 - Eigenfrequency: 5MHz
 - Diameter: 19.1mm
 - Height: 19.1mm
 - Operating temperature up to 175°C

- Standard connector by Norbar
 - Magnetic connector
 - For use with glued-on transducers
 - Diameter: 12mm

Proprietary Devices

The dimensions of the standard ultrasonic equipment, especially the diameter, were too large for the used specimens. Furthermore, some measurements required a device which was not available. Consequently, proprietary devices were designed and manufactured.

- Proprietary magnetic transducer connector
 - Optimized for use with bolts of size M8
 - Diameter: 6mm
 - Designed for operating temperatures up to 150°C

- Proprietary multi channel scanner
 - 12 channel scanner
 - Designed for use with transducer connectors
 - Enables fast ultrasonic measurement of up to 12 bolts serially
- Proprietary device for ultrasonic controlled tightening of con-rod bolts
 - Designed for use with glue-on transducers (see Figure II-11)
 - Connector for 1/2 inch sockets
 - Maximum applicable torque 120Nm

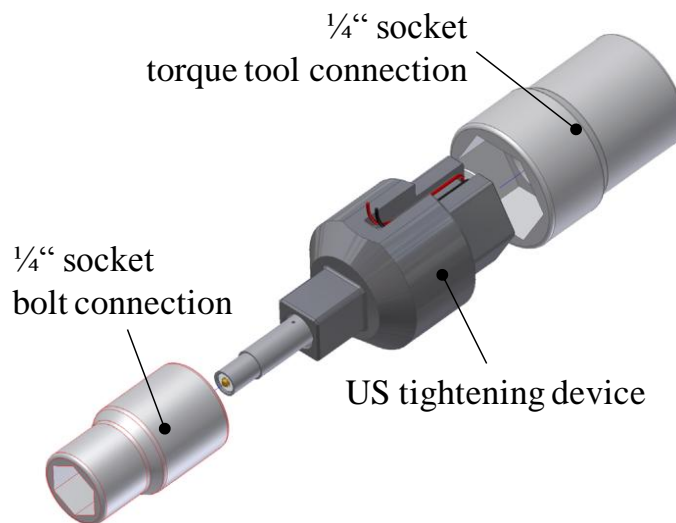


Figure II-11: Proprietary device for ultrasonic controlled bolt tightening with 1/2 inch sockets for the connection to the bolt and to the torque tool

II.4 Experimental Test Setup

This chapter deals with the technical set up of the experimental tests.

II.4.1 Separation Test

The separation tests were performed at room temperature (22°C) using a bench vice, a crane, a mechanical tension measurement device (HBS company) and an electronic torque measurement device Garant TT1. The test setup is shown in Figure II-12.

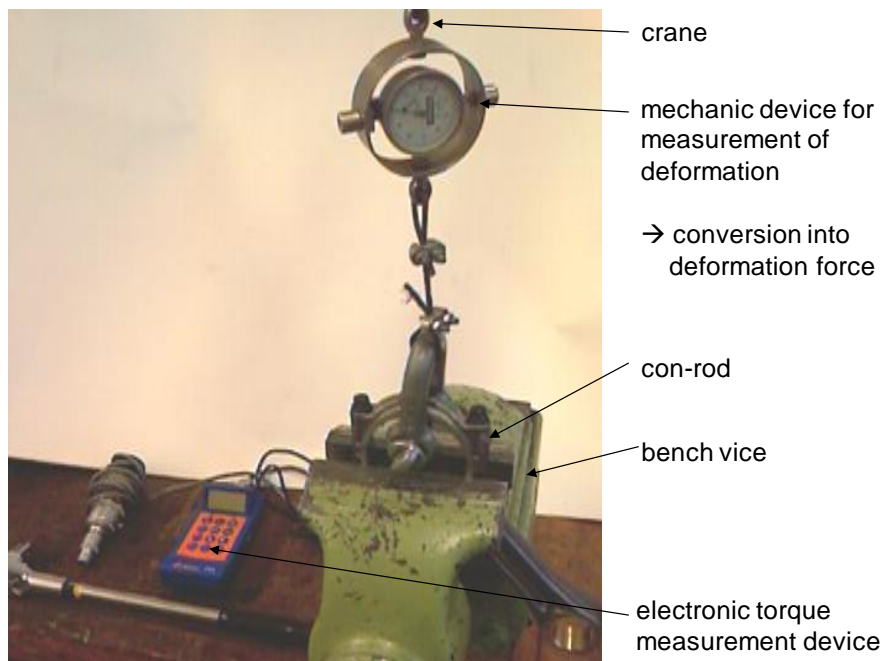


Figure II-12: Test setup for measurement of disassembly force

The con-rod body was fixed in the bench vice in such a manner that the con-rod bolts were oriented normally to the ground. The mechanical tension measurement device was mounted to the hook of the crane and connected with the con-rod cap via a cable and a bracket, allowing bending free axial tension loading of the con-rod cap. At test start the con-rod bolts were still fully engaged.

First, the bolts were disassembled and removed. During disassembly the initial breakaway torque was measured with an electronic torque measurement device. Secondly the tension was slowly and continuously increased by activating the crane until the con-rod cap was ripped off the con-rod body. The trailing pointer of the mechanical deformation measurement device shows the maximum measured deformation. This deformation was then converted into a force with a calibration table.

II.4.2 Surface Topology Scan

For the investigation of proper characteristic surface parameters the topology of the fractured surfaces was measured. The measurement was executed at room temperature (22°C) using a surface scanner with a test bed for traverse movements. For the surface scanning two Scansonic laser row scanners of type TH-03D

and TH-06D⁷⁶ were used. For the movement of the specimen the LART test bed of the neighbor institute of Prof. Dr.-Ing. Henning Meyer was used. In Figure II-13 a typical test setup is shown.

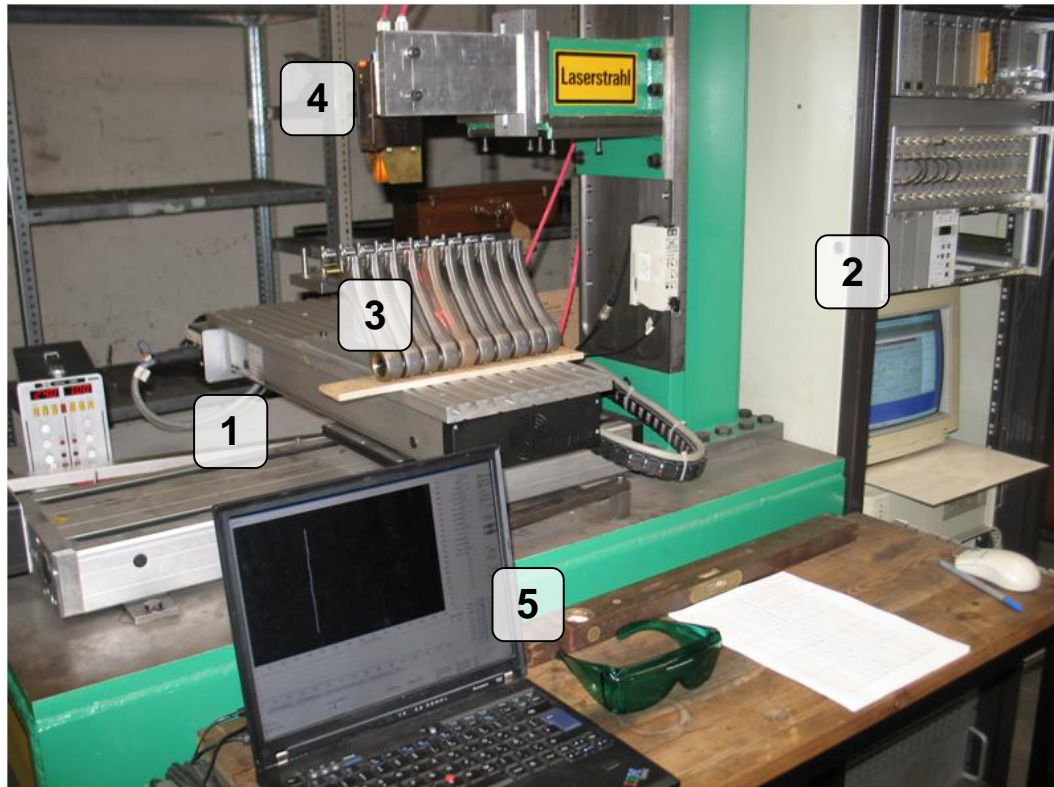


Figure II-13: LART test bed (1) with control unit (2) and con-rod specimens (3) equipped with Scansonic TH-03D laser scanner (4) and data recorder (5)

The LART test bed consists of a base plate and an adapter bar for measurement devices. On the base plate a bench with two linear drives is located (1) which allow a bench movement inside an area of 300mm x 500mm with a precision of 5 μ m in both directions. The adapter for the laser scanner is located about 200mm above the bench. The linear drives are operated via operation software from the control panel (2). For the surface scans the specimens are placed on the bench (3). The laser scanner is mounted on the adapter bar (4). The laser line has a thickness of about 50 μ m. The scanner is equipped with a video camera with a resolution of 640 x 480 pixels. The images are directly sent to the data recorder (5) and prepro-

⁷⁶ The scanner type TH-06D is a scanner with three serially arranged laser lines. For the topology scans only the data from the center line have been used.

cessed via the proprietary software SCIView of Scansonic. This preprocessing includes high-pass filtering with respect to the laser line brightness and a rough filtering of visual errors (removal of multiple peaks per data point). Then the data are stored for post-processing⁷⁷. The maximum processible picture rate of about 30 pictures per second determines the overall scanning process velocity that is required for a full scan of a single surface with about 40% overlap between two scanned surface lines. The calculated movement speed of 0.9 mm/sec⁷⁸ for the scanning procedure was entered into the LART control unit.

For each type of specimen (con-rod body, con-rod cap and CBS) another retaining fixture was used to ensure proper positioning during the tests. Each fixture was designed to retain 8 specimens at once.

In Figure II-14 the retaining fixture for CBS is shown. The specimens are positioned using a pin with a close clearance fit via the bolt hole and additionally held by clips.

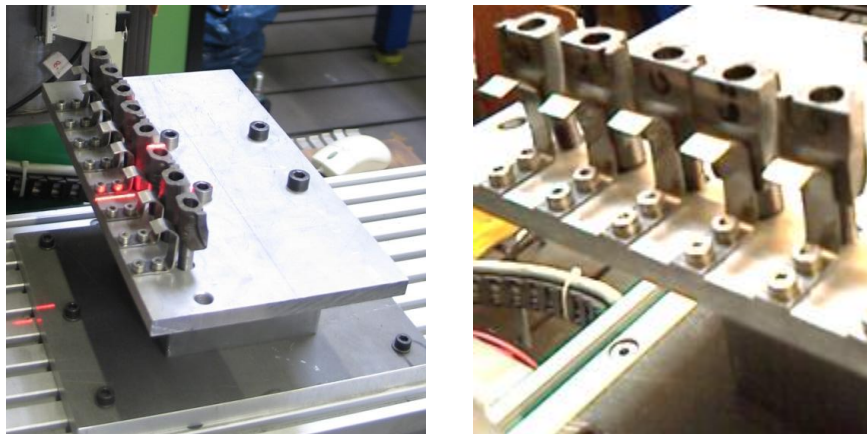


Figure II-14: Retaining fixture for CBS

In Figure II-15 the retaining fixture for con-rod bodies (left side of the picture) and con-rod caps (right side) is shown. For both kinds of specimen the same device has been used with minor changes.

⁷⁷ See Appendix II.4.3 for details about the data post-processing.

⁷⁸ Movement Speed = laser line thickness (50 μ m) x 0.6 x 30 pics/sec = 0.9 mm/sec



Figure II-15: Retaining fixture for con-rod body (left) and con-rod cap (right)

II.4.3 Laser Scanner Data Analysis

For the calculation of the spatial surface profile from the 2-D surface data, CCD⁷⁹ sensor data and an auxiliary matrix were used. This matrix contains the position of the brightest point per CCD row (“x-position” on the CCD sensor), the number of the row (“y-position” on the CCD sensor) as well as the difference between each adjacent time stamp. Additionally, the traverse speed was entered manually. With these data the true spatial coordinates of each data point were calculated using formulas and an additional set of calibration data delivered by Scansonic.

The next step of data processing was a rough filtering process. First, the average height and the standard deviation of all data were determined. All data that vary more than 10 times standard deviation from the average height were removed. After this rough filtering process the profile data still have a poor signal to noise ratio in the interval of very small wavelengths (see Figure II-16 lefthand).

⁷⁹ **CCD** = charge coupled device

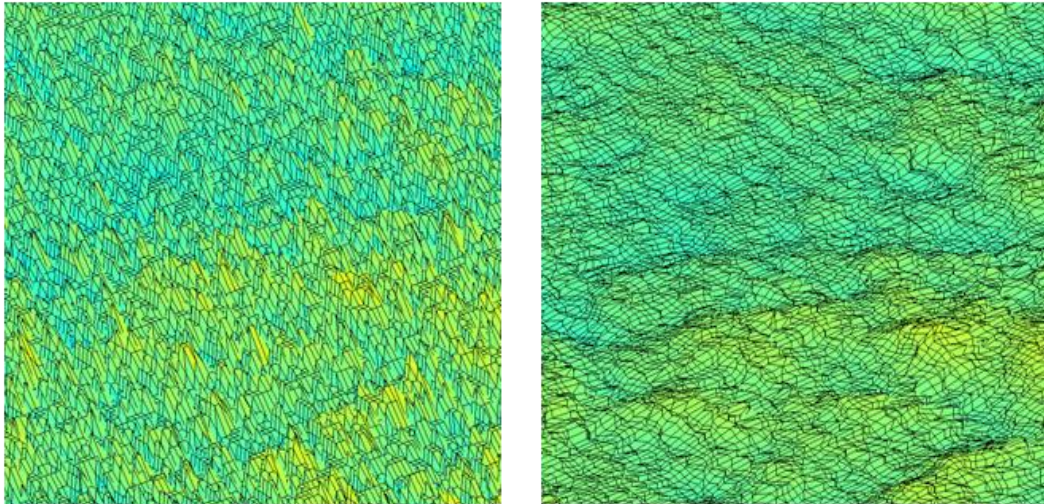


Figure II-16: Surface detail of a profile scan before (left) and after (right) smoothing

According to (ISO11562, 1998) the filtering process is closely related to the characteristic length of the profile. In case of a fractured surface this characteristic length is of a high magnitude due to the related roughness R_z ⁸⁰. Using such a filter would erase the majority of the fraction of small wavelengths. These, however, are needed for the further analysis process. As a result, a proprietary smoothing algorithm which consists of a 5x5 matrix of the surrounding data points was used to calculate a floating average value.

The next step of the data processing is the alignment of the surface scans into the origin of a 3-D Cartesian coordinate system which is unique for each pairing of fractured surfaces. The first step is to fit the surface scan into the x-y-layer (see Figure II-17). This is done by determining the deviation angle (dashed line in Figure II-17) as well as the distance and the direction of the displacement of the reference points P1 and P2 in Figure II-17. P1 is the upper left corner of the image and P2 is the target position of this corner in the origin of the coordinate system. This was performed for both surfaces of each pairing.

⁸⁰ R_z is a benchmark for the determination of the characteristic length of aperiodic profiles (for further details see (ISO4288, 1998))

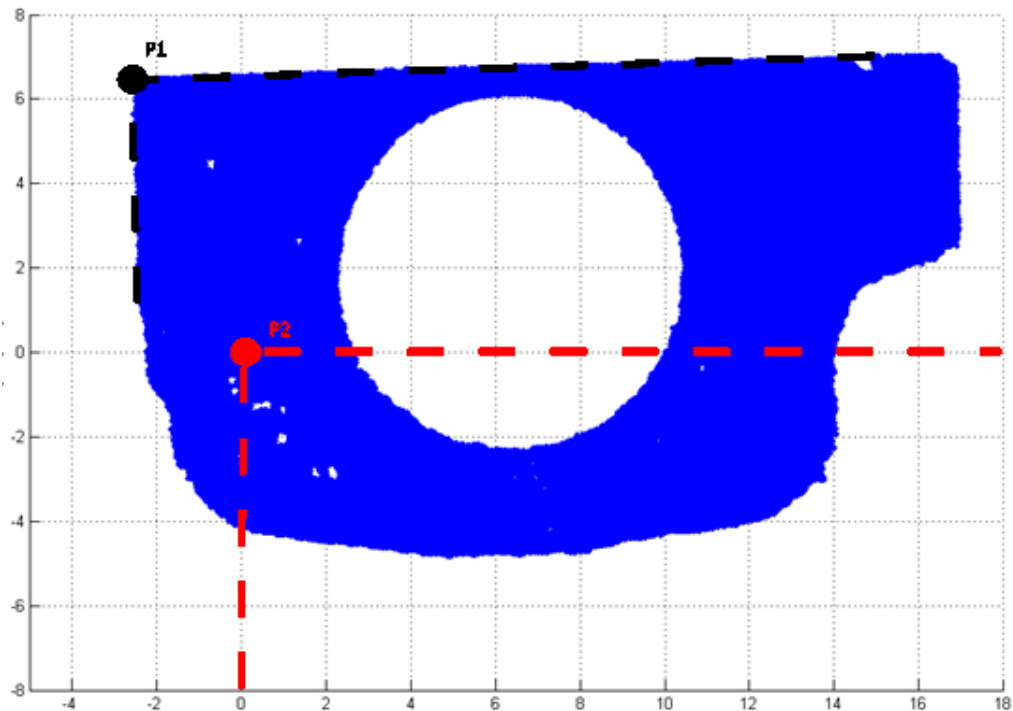


Figure II-17: Vertical orientation of a surface scan before alignment process (P1 and black dashed line) and target orientation (P2 and red dashed line)

After finishing the horizontal alignment, the surface scans were adjusted with respect to the vertical z-axis. The relative vertical alignment is performed by freezing the position of the lower surface. The upper surface is turned by 180° about the y-axis so that both surfaces face each other in the appropriate horizontal orientation. For the next step an auxiliary alignment matrix with an element size of $2\text{mm} \times 2\text{mm}$ is calculated. For each grit element the average vertical position of all included data points is calculated. The position of the center of each grit element and the corresponding average vertical position are written in an auxiliary matrix. The vertical alignment is performed by turning the upper surface about the x-axis and the y-axis so that the average distance of the vertical positions of the auxiliary matrices of both surfaces is minimal.

Due to the orientation process and measurement uncertainties the data grit of both surfaces is deformed. To finally enable a proper analysis for both surfaces the data grit needs to be revised by interpolation (see Figure II-18). This data grit has an element size of $50\ \mu\text{m}$ and is used for both surfaces.

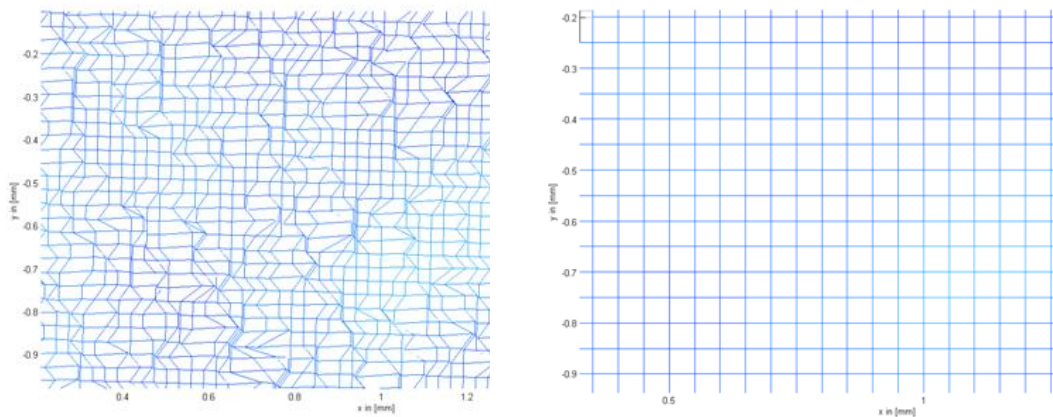


Figure II-18: Section of the data grit of a surface scan before (left) and after (right) revision by interpolation

II.4.4 Shear Load Test

The transferrable shear load tests have been conducted as quasi static shear tests at ambient temperature (22°C) and at con-rod operating temperature (150°C). The tests have been performed with a hydropulsor model Instron 8801. The hydropulsor was equipped with a proprietary shear loading device (see Appendix II.2) for the con-rod bolting specimens and a tube furnace from Thermoprozess Company. The shear loading device is shown in Figure II-19.

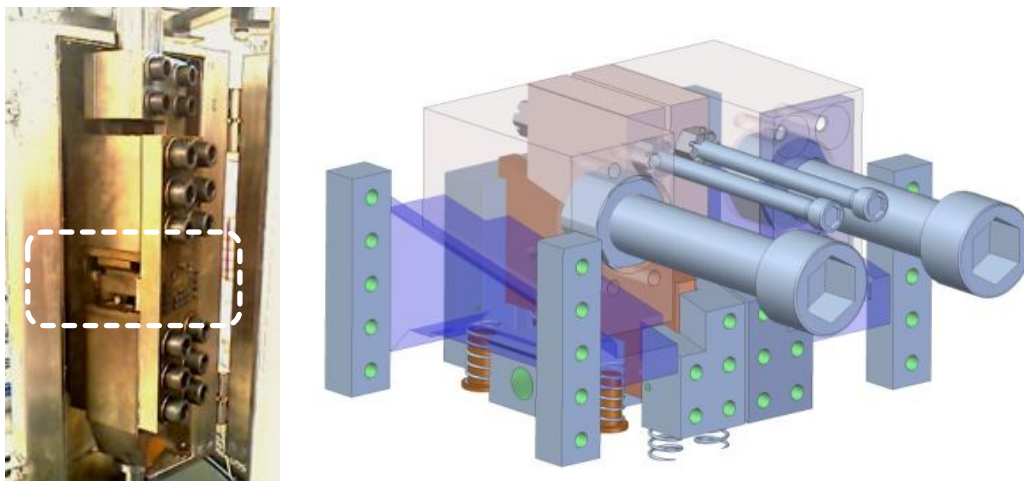


Figure II-19: Shear loading device for CBS inside the tube furnace at the hydropulsor (left) and sketched detail of the specimen fixture (right)

Prior to each single test run, the target elongation of each bolt for the desired pre-load was determined using the tensile testing machine (see Appendix II.2). Then a specimen was loosely assembled and placed into the shear loading device. There the bolt was engaged while the bolt elongation was measured online up to the de-

terminated target elongation. The specimen was then fixed in the device and the test started. The test ended when the specimen failed.

For tests at operating temperature (150°C) the tube furnace was mounted. For these tests, the specimens were assembled, yield controlled, and relaxed for 168h at 150°C. Prior to the shear load test the furnace was activated so that the tested specimen did not cool down between the relaxation and the shear loading phase.

II.4.5 Relaxation Test

The measurement of relaxation losses was performed at ambient temperature (22°C) as well as at operating temperature (150°C). In both cases the relaxation loss was measured using the ultrasonic bolt elongation measurement device Nor-bar USM III with permanently mounted transducers at the bolts (see Appendix II.2). The ultrasonic transducers used for the measurements were glued directly to the bolts⁸¹. For the relaxation tests at room temperature (22°C) the specimens were stored in an air-conditioned room to ensure a constant temperature. For the operating temperature tests a drying kiln was used (see Appendix II.2).

For the relaxation tests with particles, the particles were manufactured artificially. The particles were gained by sawing off a con-rod body and collecting the debris. The particles were sorted by weight from 4mg to 15mg. For test series Relax_1P one particle with the weight of 7mg was used. For test series Relax_3P three particles were taken with a total weight between 36mg and 37mg. The bolt was assembled up to yield strength ($30Nm + 90^\circ + X^\circ$), so that the turning angle prescribed by the manufacturer was exceeded by X° .

For each test up to 30 specimens of a test series were either placed in an air-conditioned room or in the drying kiln subsequent to the bolt assembly. Consequently, the specimens of all test series were tested in parallel except for the reference test series which was tested in two rounds. Every 10 specimens and a single bolt were connected with one multi channel scanner. The single bolt at each scanner was used for temperature adjustment. At the beginning of the storage phase and after 168h the overall bolt elongation of each specimen was measured. After storage the specimens were disassembled and the remaining plastic bolt elongation was measured. The specimens of test series Relax_T1 and Relax_T2 were stored

⁸¹ For further information about ultrasonic measurement see Appendix II.3

at different temperatures⁸². In these two test series at the start and the end of each storage phase the overall bolt elongation was measured.

II.5 Specimen Setup

In this section the procedure of the specimen setup is described.

1. Labeling of con-rods with a capital letter and a consecutive number with respect to their laser notch batch
2. Disassembly of bolts including measurement of breakaway torque
3. Separation of cap and body including measurement of separation force as described in Section 5.2
4. Short visual inspection of fractured surfaces in order to track surface anomalies such as material retractions, particles or particle tracks
5. REM survey of selected specimen only, as described in Section 5.4
6. Manufacture of standard connection bodies (see Appendix II.1)
7. Scan of fractured surfaces (see Appendix 4.4.1.2)
8. Preparation of bolt (see Appendix II.5.1)
9. Bolting process (see Appendix II.5.2)
10. Measurement of maximum bolt elongation
11. Execution of selected test (shear load test or relaxation test)
12. Measurement of final bolt elongation
13. Disassembly of bolts
14. Measurement of remaining plastic bolt elongation
15. Final surface inspection by macro photography of selected specimen (see Section 6.1.2 for relaxation tests and Section 6.2.2 for shear load tests)

In the following two sections the processes of bolt preparation and the bolting itself are described in detail.

II.5.1 Bolt Preparation

For the use with the ultrasonic measurement equipment the bolts needed to receive a special preparation. Bolt head and foot needed to be flattened for a proper use of the ultrasonic transducers. Furthermore, both flattened surfaces had to face parallel to minimize measurement errors. Prior to the flattening, the bolts were mounted into a machining plate to also ensure a uniform bolt length.

⁸² See Section 6.1.1 for further details

The machining plate was manufactured with 10 x 9 bolt holes. Each bolt hole had a diameter of 8.1mm which was about 0.1mm larger than the real bolt shaft diameter. At the end of each bolt hole a thread with a length of 5mm was manufactured. The machining plate was 47mm thick so that there was an excess length of the bolts after mounting in the plate of about 3mm (shaft length of each bolt was about 50mm).

After grinding the flattened bolts remained in the machining plate for the application of the piezo transducers. The transducers were connected to the bolts using two component glue HBM X 280, designed for use with strain gauges at high temperatures of up to 280°C. The transducers of all CBS bolts were connected to the bolt foot, the transducers for the con-rod bolts were connected to the bolt head. After applying the glue to the bolts, the transducers were placed on the glue and fixed by standard adhesive tape. After that the machining plate with the prepared bolts was put in a drying kiln at 80°C for two hours in order to harden the glue. Finally, the tape and glue residues were removed from the bolts.

II.5.2 Elongation Measurement Process

The correct ultrasonic measurement of the relaxation losses in a yield-controlled assembled bolted joint requires some understanding of the multi-dimensional stresses and the related elongations.

At the beginning of the assembly process, the bolt is free of any stress. During the assembly phase, the bolt is loaded with torsion stress introduced by the torque tool as well as with tension stress due to the axial elongation caused by the tightening of the bolt. At the end of the assembly phase the tension stress reached the yield strength of the material and the stress-strain-curve changes distinctly (see Figure II-20). Based on the van-Mises hypothesis⁸³ at this point the yield strength is not equal to the yield strength at the beginning of the assembly process. The increasing torsion stress appears also as a load to the bolt material, but it does not affect the bolt elongation. Instead, the effective yield strength is reduced. In short, the application of torque to the bolt changes the yield strength to a distinctly lower magnitude.

⁸³ see Section 7.3.1

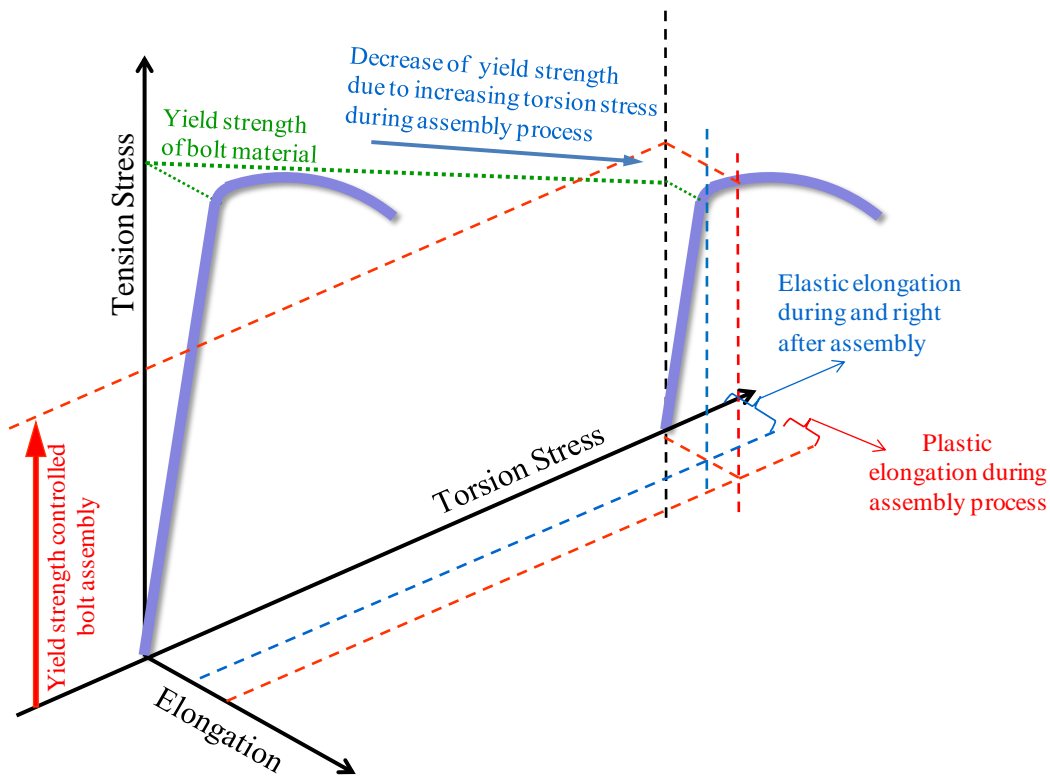


Figure II-20: Tension stress and torsion stress during a yield-controlled assembly of a bolted joint and some related important elongations – relaxation step 1

When the assembly phase is over and the torque tool is removed, the torsion stress in the bolt decreases instantly. Only a fraction of the highest torsion stress remains (see Figure II-21). Consequently, the materials yield strength increases again. Due to some remaining torsion stress, this actual yield strength is located somewhere between the magnitude before assembly (no torsion stress) and before the tool removal (maximum torsion stress).

Towards the end of the assembly process the yield-controlled tightening caused some plastic deformation of the bolt. Due to the rise of the yield strength after removal of the torque tool, the stress level in the bolt drops back to pure elastic loading. Consequently, additional plastic deformation is not expected to appear again.

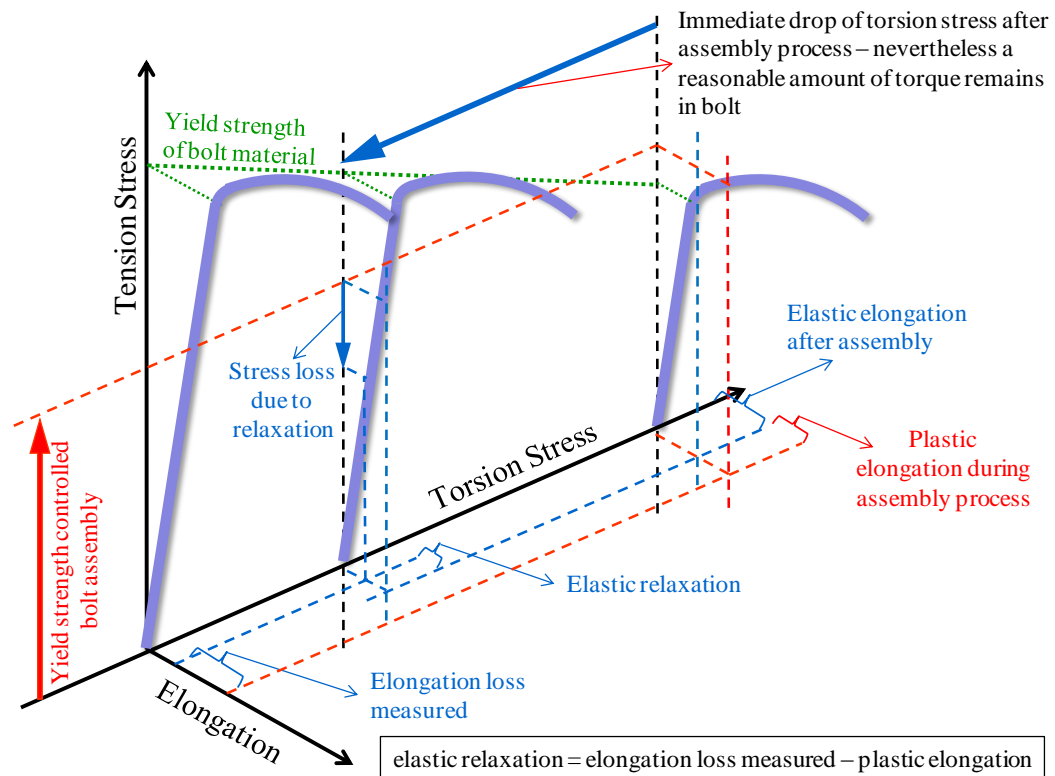


Figure II-21: Tension stress and torsion stress during and after a yield-controlled assembly of a bolted joint and some related elongations – relaxation step 2

The elongation measured by the ultrasonic measurement device is the sum of all elongations present at that time. In consequence, the measurement of the elastic elongation loss requires the subtraction of the plastic elongation from the indicated value.

The elongation measurement process involved the following steps:

1. Measurement of the initial unloaded bolt length
2. Assembly of the bolt into the specimen
3. Measurement of the maximum bolt length at the end of the tightening process
4. Test run
5. Measurement of the bolt length at the end of the test series
6. Disassembly of the specimen
7. Measurement of the remaining plastic bolt elongation

III. Detailed Test Results

This Chapter contains the detailed test results of the relaxation tests and the shear load tests.

III.1 Relaxation Test Results with CBS

In Figure III-1 a detailed summary of the test results of all relaxation tests with CBS is shown.

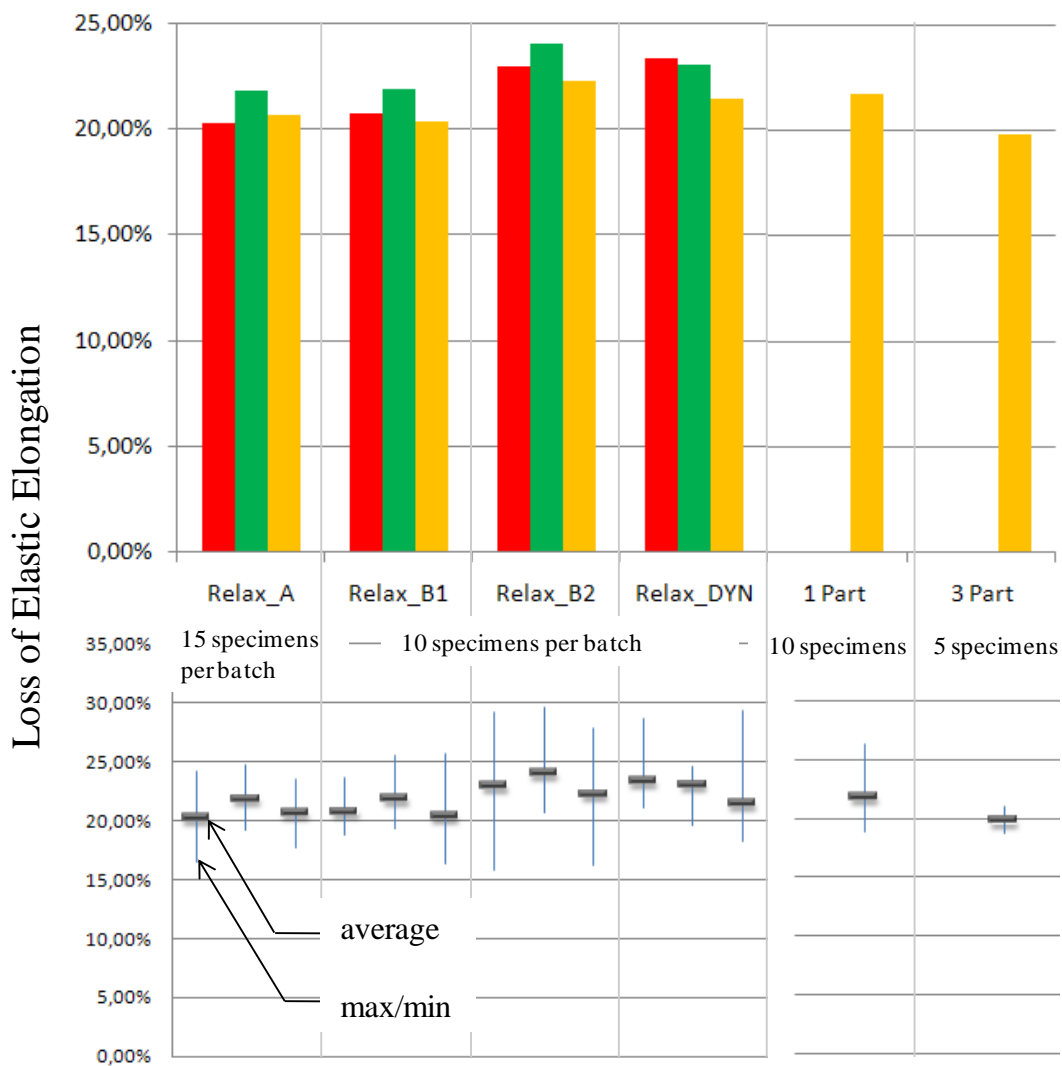


Figure III-1: Detailed summary of test results of the relaxation tests with CBS

Detailed Results

Test series Relax_Ref

No.	Batch	Con-Rod	Inner/Outer	Assembly		Start		End	
				Date/Time	L_max* [μm]	L_plastic [μm]	L_max [μm]	Date/Time	L_point* [μm]
1	R	47	O	19.10.08 17:51	310,2	31,4	278,8	28.10.08 11:43	242,7
2	R	28	O	19.10.08 17:17	289,3	15,3	274	28.10.08 11:37	225,5
3	R	34	O	19.10.08 17:30	321,3	38,2	283,1	28.10.08 11:39	256,1
4	R	17	O	19.10.08 17:27	315,5	34,6	280,9	28.10.08 11:39	252
5	R	26	O	19.10.08 17:55	307,8	35,4	272,4	28.10.08 11:44	249
6	R	6	O	19.10.08 16:30	295,6	30,7	264,9	28.10.08 11:32	239
7	R	36	O	19.10.08 17:49	303	37,9	265,1	28.10.08 11:42	248,2
8	R	14	O	19.10.08 17:20	300,3	38,4	261,9	28.10.08 11:38	246,6
9	R	31	O	19.10.08 16:47	301,4	17,2	284,2	28.10.08 11:34	246,1
10	R	19	O	19.10.08 16:39	294,5	23,8	270,7	28.10.08 11:34	243,4
11	R	20	O	19.10.08 17:53	308,2	32,4	275,8	28.10.08 11:43	257,3
12	R	37	O	19.10.08 17:22	291,4	31,7	259,7	28.10.08 11:38	244,1
13	R	43	O	19.10.08 17:58	303,6	30,3	273,3	28.10.08 11:44	255,9
14	R	3	O	19.10.08 16:36	276,5	23,1	253,4	28.10.08 11:33	233
15	R	2	O	19.10.08 16:33	286,4	26,1	260,3	28.10.08 11:33	243,4
16	G	41	O	28.10.08 13:40	307,2	29,8	277,4	4.11.08 11:35	238,5
17	G	33	O	28.10.08 13:42	302,9	27,8	275,1	4.11.08 11:36	238,1
18	G	20	O	28.10.08 13:44	309,1	39,5	269,6	4.11.08 11:37	246
19	G	28	O	28.10.08 13:35	300,3	32,6	267,7	4.11.08 11:34	239,5
20	G	10	O	28.10.08 13:43	302,6	20,1	282,5	4.11.08 11:36	238,5
21	G	3	O	28.10.08 13:24	292,8	28,8	264	4.11.08 11:30	233,4
22	G	35	O	28.10.08 13:38	307,9	32,8	275,1	4.11.08 11:34	247,2
23	G	29	O	28.10.08 13:30	302,1	32,2	269,9	4.11.08 11:32	243
24	G	26	O	28.10.08 13:26	306,9	30,1	276,8	4.11.08 11:30	246,9
25	G	1	O	28.10.08 13:31	302,8	32,4	270,4	4.11.08 11:32	245,2
26	G	31	O	28.10.08 13:33	297,1	27,2	269,9	4.11.08 11:33	241,1
27	G	17	O	28.10.08 13:34	305,3	33,4	271,9	4.11.08 11:33	249,8
28	G	45	O	28.10.08 13:28	294,8	25,8	269	4.11.08 11:31	241
29	G	47	O	28.10.08 13:41	301,5	36,5	265	4.11.08 11:35	249,4
30	G	4	O	28.10.08 13:27	285	25,4	259,6	4.11.08 11:31	235
31	Y	7	O	19.10.08 17:41	309,3	28,3	281	28.10.08 11:41	243
32	Y	23	O	19.10.08 16:16	297,7	23,3	274,4	28.10.08 11:31	233,5
33	y	42	O	19.10.08 17:05	315,2	26,6	288,6	28.10.08 11:37	250,1
34	Y	47	O	19.10.08 17:47	310,8	30,2	280,6	28.10.08 11:42	248
35	Y	15	O	19.10.08 16:11	301,1	29,8	271,3	28.10.08 11:31	241
36	Y	21	O	19.10.08 16:22	286,6	17,2	269,4	28.10.08 11:32	228,2
37	Y	6	O	19.10.08 17:36	293,2	34,2	259	28.10.08 11:40	238
38	Y	29	O	19.10.08 17:38	307,4	21,3	286,1	28.10.08 11:40	246,5
39	Y	26	O	19.10.08 17:03	293,4	31,8	261,6	28.10.08 11:36	238,7
40	Y	39	O	19.10.08 15:58	298	23,7	274,3	28.10.08 11:30	244,4
41	Y	31	O	19.10.08 16:58	282,1	26,9	255,2	28.10.08 11:35	235
42	Y	30	O	19.10.08 16:04	295,2	21,8	273,4	28.10.08 11:30	245
43	Y	46	O	19.10.08 17:01	280,4	23,1	257,3	28.10.08 11:36	233,7
44	Y	19	O	19.10.08 16:55	292,5	10,7	281,8	28.10.08 11:35	242,5
45	Y	2	O	19.10.08 17:44	298,3	34,2	264,1	28.10.08 11:41	251,6

Table III-1: Detailed results of test series Relax_Ref (test temperature 150°C)

Test Series Relax_T1

No.	Batch	Con-Rod	Inner/Outer	Assembly		Start		End of test @ 22°C		End of test @ 150°C	
				Date/Time	L_max* [μm]	L_plastic [μm]	L_max [μm]	Date/Time	L_point* [μm]	Date/Time	L_point* [μm]
1	R	42	O	30.9.08 13:40	318,2	29,1	289,1	11.11.08 14:32	292,4	20.11.08 12:12	263
2	R	33	O	30.9.08 13:34	321	27,2	293,8	11.11.08 14:31	300	20.11.08 12:11	251,3
3	R	21	O	30.9.08 13:43	318,5	27,9	290,6	11.11.08 14:32	287,3	20.11.08 12:12	250,2
4	R	9	O	30.9.08 13:30	324,3	30,3	294	11.11.08 14:30	300,4	20.11.08 12:10	264,2
5	R	8	O	30.9.08 13:37	313	26,3	286,7	11.11.08 14:31	286,2	20.11.08 12:11	249,3
6	R	12	O	30.9.08 13:48	301,9	19,8	282,1	11.11.08 14:33	280,2	20.11.08 12:13	246,1
7	R	38	O	30.9.08 13:58	313,5	34,7	278,8	11.11.08 14:34	293,2	20.11.08 12:14	259,2
8	R	15	O	30.9.08 13:27	317,6	34,7	282,9	11.11.08 14:30	300,3	20.11.08 12:10	264,3
9	R	4	O	30.9.08 13:53	306,3	34,5	271,8	11.11.08 14:33	286,2	20.11.08 12:13	250
10	R	25	O	30.9.08 13:55	312,2	24,1	288,1	11.11.08 14:34	290,7	20.11.08 12:14	256,7
11	G	38	O	30.9.08 14:16	321,7	33,8	287,9	11.11.08 14:27	296,7	20.11.08 12:27	248,2
12	G	5	O	30.9.08 15:24	311,6	30,3	281,3	11.11.08 14:29	284,7	20.11.08 12:29	241,3
13	G	11	O	30.9.08 14:26	301,5	32,5	269	11.11.08 14:28	283,8	20.11.08 12:28	241
14	G	9	O	30.9.08 14:14	324,8	36,1	288,7	11.11.08 14:26	297,1	20.11.08 12:26	263,2
15	G	16	O	30.9.08 14:36	310,6	28,5	282,1	11.11.08 14:29	286,7	20.11.08 12:29	255,2
16	G	6	O	30.9.08 14:08	314,2	35,2	279	11.11.08 14:25	290,2	20.11.08 12:25	254,6
17	G	13	O	30.9.08 14:05	313,2	33,2	280	11.11.08 14:25	292,8	20.11.08 12:25	257,1
18	G	27	O	30.9.08 15:30	316	29,4	286,6	11.11.08 14:28	290,2	20.11.08 12:28	254,2
19	G	37	O	30.9.08 14:20	310,3	30,5	279,8	11.11.08 14:27	288,1	20.11.08 12:27	248,3
20	G	46	O	30.9.08 14:10	319,8	31,8	288	11.11.08 14:26	297,2	20.11.08 12:26	264
21	Y	27	O	30.9.08 15:11	314,9	29,7	285,2	11.11.08 14:18	292,4	20.11.08 12:03	241,7
22	Y	40	O	30.9.08 14:50	308,4	34,1	274,3	11.11.08 14:15	284,8	20.11.08 12:00	246,3
23	Y	44	O	30.9.08 15:07	322,5	35,7	286,8	11.11.08 14:18	300,1	20.11.08 12:03	263,9
24	Y	4	O	30.9.08 14:58	306,2	33,1	273,1	11.11.08 14:16	288,2	20.11.08 12:01	249,2
25	Y	11	O	30.9.08 14:54	314	33,1	280,9	11.11.08 14:16	290,8	20.11.08 12:01	255,1
26	Y	22	O	30.9.08 15:05	308,5	37,3	271,2	11.11.08 14:17	286,7	20.11.08 12:02	255,1
27	Y	32	O	30.9.08 15:14	313,2	35,5	277,7	11.11.08 14:19	293,6	20.11.08 12:04	259,1
28	Y	3	O	30.9.08 14:52	305,5	33,8	271,7	11.11.08 14:15	284,6	20.11.08 12:00	254,7
29	Y	33	O	30.9.08 15:16	312,7	32,3	280,4	11.11.08 14:19	292,6	20.11.08 12:04	260,1
30	Y	28	O	30.9.08 15:03	290,4	24,8	265,6	11.11.08 14:17	281,1	20.11.08 12:02	247,1

Table III-2: Detailed results of test series Relax_T1 (test temperature 22°C & 150°C)

Detailed Results

Test Series Relax_T2

No.	Batch	Con-Rod	Inner/Outer	Assembly		Start		End of test @ 22°C		End of test @ 150°C	
				Date/Time	L_max* [μm]	L_plastic [μm]	L_max [μm]	Date/Time	L_point* [μm]	Date/Time	L_point* [μm]
				1	R	42	O	30.9.08 13:40	318,2	29,1	289,1
2	R	33	O	30.9.08 13:34	321	27,2	293,8	11.11.08 14:31	246,1	20.11.08 12:11	239,2
3	R	21	O	30.9.08 13:43	318,5	27,9	290,6	11.11.08 14:32	249,8	20.11.08 12:12	245,1
4	R	9	O	30.9.08 13:30	324,3	30,3	294	11.11.08 14:30	258,1	20.11.08 12:10	252,7
5	R	8	O	30.9.08 13:37	313	26,3	286,7	11.11.08 14:31	245,7	20.11.08 12:11	243,6
6	R	12	O	30.9.08 13:48	301,9	19,8	282,1	11.11.08 14:33	242,3	20.11.08 12:13	238,4
7	R	38	O	30.9.08 13:58	313,5	34,7	278,8	11.11.08 14:34	258,1	20.11.08 12:14	254,1
8	R	15	O	30.9.08 13:27	317,6	34,7	282,9	11.11.08 14:30	262,9	20.11.08 12:10	258,3
9	R	4	O	30.9.08 13:53	306,3	34,5	271,8	11.11.08 14:33	250,2	20.11.08 12:13	258,1
10	R	25	O	30.9.08 13:55	312,2	24,1	288,1	11.11.08 14:34	252,7	20.11.08 12:14	266,5
11	G	38	O	30.9.08 14:16	321,7	33,8	287,9	11.11.08 14:27	250,2	20.11.08 12:27	236,3
12	G	5	O	30.9.08 15:24	311,6	30,3	281,3	11.11.08 14:29	247,2	20.11.08 12:29	233,8
13	G	11	O	30.9.08 14:26	301,5	32,5	269	11.11.08 14:28	239,4	20.11.08 12:28	235,6
14	G	9	O	30.9.08 14:14	324,8	36,1	288,7	11.11.08 14:26	261,2	20.11.08 12:26	256,7
15	G	16	O	30.9.08 14:36	310,6	28,5	282,1	11.11.08 14:29	248,5	20.11.08 12:29	244,5
16	G	6	O	30.9.08 14:08	314,2	35,2	279	11.11.08 14:25	254,9	20.11.08 12:25	249,9
17	G	13	O	30.9.08 14:05	313,2	33,2	280	11.11.08 14:25	254,6	20.11.08 12:25	250,2
18	G	27	O	30.9.08 15:30	316	29,4	286,6	11.11.08 14:28	256,9	20.11.08 12:28	251,6
19	G	37	O	30.9.08 14:20	310,3	30,5	279,8	11.11.08 14:27	243,9	20.11.08 12:27	247,9
20	G	46	O	30.9.08 14:10	319,8	31,8	288	11.11.08 14:26	261,9	20.11.08 12:26	260,2
21	Y	27	O	30.9.08 15:11	314,9	29,7	285,2	11.11.08 14:18	242,8	20.11.08 12:03	235,5
22	Y	40	O	30.9.08 14:50	308,4	34,1	274,3	11.11.08 14:15	245,8	20.11.08 12:00	238,6
23	Y	44	O	30.9.08 15:07	322,5	35,7	286,8	11.11.08 14:18	261,2	20.11.08 12:03	256,1
24	Y	4	O	30.9.08 14:58	306,2	33,1	273,1	11.11.08 14:16	247,7	20.11.08 12:01	244,1
25	Y	11	O	30.9.08 14:54	314	33,1	280,9	11.11.08 14:16	254,2	20.11.08 12:01	253,1
26	Y	22	O	30.9.08 15:05	308,5	37,3	271,2	11.11.08 14:17	250,2	20.11.08 12:02	250,1
27	Y	32	O	30.9.08 15:14	313,2	35,5	277,7	11.11.08 14:19	257,4	20.11.08 12:04	254,1
28	Y	3	O	30.9.08 14:52	305,5	33,8	271,7	11.11.08 14:15	249,7	20.11.08 12:00	247,7
29	Y	33	O	30.9.08 15:16	312,7	32,3	280,4	11.11.08 14:19	258,1	20.11.08 12:04	253,8
30	Y	28	O	30.9.08 15:03	290,4	24,8	265,6	11.11.08 14:17	252,2	20.11.08 12:02	247,4

Table III-3: Detailed results of test series Relax_T2 (test temperature 22°C & 150°C)

Test Series Relax_Dyn

No.	Batch	Con-Rod	Inner/Outer	Assembly		Start		End	
				Date/Time	L_max* [μm]	L_plastic [μm]	L_max [μm]	Date/Time	L_point* [μm]
1	R	16	O	24.1.09 11:10	315,4	22,5	292,9	31.1.09 11:10	231,4
2	R	48	O	25.2.09 11:15	301,1	26,1	275	4.3.09 11:15	229
3	R	46	O	14.2.09 10:00	313,1	19,2	293,9	21.2.09 10:00	240,5
4	R	32	O	6.2.09 10:05	312,8	26,3	286,5	13.2.09 10:05	246,6
5	R	39	O	28.1.09 13:55	308,4	28,2	280	4.2.09 13:55	242,9
6	R	29	O	2.2.09 11:50	314,2	39	275,2	9.2.09 11:50	253,4
7	R	24	O	28.1.09 13:55	292,5	32,7	259,8	4.2.09 13:55	236,1
8	R	27	O	11.2.09 9:40	307,8	26,1	281,7	18.2.09 9:40	248
9	R	13	O	3.3.09 15:00	304,5	28,8	275,7	10.3.09 15:00	246,2
10	R	23	O	21.2.09 11:10	313,8	33,4	280,4	28.2.09 11:10	254,6
11	G	8	O	5.3.09 10:00	305,5	26	279,5	12.3.09 10:00	236,8
12	G	2	O	5.2.09 10:00	307,3	24	283,3	12.2.09 10:00	238,2
13	G	30	O	1.3.09 16:20	305,2	26	279,2	8.3.09 16:20	237,4
14	G	25	O	27.1.09 11:45	302,1	28,8	273,3	3.2.09 11:45	235,8
15	G	34	O	8.2.09 11:15	305,8	32,8	273	15.2.09 11:15	242,6
16	G	39	O	20.2.09 10:50	306,1	40	266,1	27.2.09 10:50	245,1
17	G	19	O	16.2.09 14:15	316	40,5	275,5	23.2.09 14:15	253,5
18	G	15	O	13.2.09 10:05	315,5	38,4	277,1	20.2.09 10:05	253,2
19	G	36	O	1.2.09 11:30	310,7	34,6	276,1	8.2.09 11:30	250,8
20	G	22	O	23.1.09 12:00	300,3	30,5	269,8	30.1.09 12:00	247,5
21	Y	41	O	4.2.09 10:00	310	9,1	300,9	11.2.09 10:00	221,6
22	Y	43	O	7.2.09 11:25	317,2	24,7	292,5	14.2.09 11:25	252
23	Y	8	O	15.2.09 12:00	302,7	35,3	267,4	22.2.09 12:00	244,3
24	Y	17	O	25.1.09 10:40	308,8	25,4	283,4	1.2.09 10:40	249,4
25	Y	10	O	22.2.09 10:50	307	36,1	270,9	1.3.09 10:50	250,5
26	Y	16	O	31.1.09 12:00	290,8	31,6	259,2	7.2.09 12:00	237,9
27	Y	25	O	19.2.09 11:00	302,3	30,5	271,8	26.2.09 11:00	247
28	Y	1	O	28.2.09 15:50	297,2	27,3	269,9	7.3.09 15:50	243,1
29	Y	14	O	22.1.09 10:00	313	14,6	298,4	29.1.09 10:00	253,2
30	Y	24	O	12.2.09 9:20	300,2	30,9	269,3	19.2.09 9:20	251,2

Table III-4: Detailed results of test series Relax_Dyn (test temperature 150°C)

Detailed Results

Test Series Relax_Plain

No.	Batch	Con-Rod	Inner/Outer	Assembly		Start		End	
				Date/Time	* [μm]	L_plastic [μm]	L_max [μm]	Date/Time	L_point* [μm]
1	R	10	O	5.9.09 12:48	297,2	24,3	272,9	12.9.09 15:40	239,2
2	R	22	O	5.9.09 12:53	300,8	28,7	272,1	12.9.09 15:42	248,8
3	R	35	O	5.9.09 12:56	303,2	33,1	270,1	12.9.09 15:44	248,6
4	R	40	O	5.9.09 12:59	314,1	35,1	279	12.9.09 15:46	257,4
5	R	44	O	5.9.09 13:02	300,1	27,1	273	12.9.09 15:48	245,1
6	R	45	O	5.9.09 13:05	305,2	26,4	278,8	12.9.09 15:50	247

Table III-5: Detailed results of test series Relax_Plain (test temperature 150°C)

Test Series Relax_MA

No.	Batch	Con-Rod	Inner/Outer	Assembly		Start		End	
				Date/Time	L_max * [μm]	L_plastic [μm]	L_max [μm]	Date/Time	L_point* [μm]
1	R	35	I	5.9.09 13:45	292,2	30,8	261,4	12.9.09 15:30	239,2
2	R	35	O	5.9.09 13:47	300,2	33,8	266,4	12.9.09 15:31	248,8
3	R	37	I	5.9.09 13:50	293,4	30,6	262,8	12.9.09 15:32	248,6
4	R	37	O	5.9.09 13:52	306,3	40,5	265,8	12.9.09 15:33	257,4
5	R	38	I	5.9.09 13:54	296,1	35,2	260,9	12.9.09 15:34	245,1
6	R	38	O	5.9.09 13:56	297,8	26,2	271,6	12.9.09 15:35	247

Table III-6: Detailed results of test series Relax_MA (test temperature 150°C)

Test Series Relax_1P

No.	Batch	Con-Rod	Inner/Outer	Assembly		Start		End	
				Date/Time	L_max* [μm]	L_plastic [μm]	L_max [μm]	Date/Time	L_point* [μm]
1	Y	43	I	29.5.09 16:20	302,5	34	268,5	8.6.09 10:00	252
2	Y	9	O	29.5.09 16:21	300,8	35,1	265,7	8.6.09 10:01	245
3	Y	18	O	29.5.09 16:22	307,9	36,9	271	8.6.09 10:02	248,5
4	Y	45	O	29.5.09 16:23	303,4	29,9	273,5	8.6.09 10:03	246,7
5	Y	36	O	29.5.09 16:24	304,2	34,5	269,7	8.6.09 10:04	249
6	Y	38	O	29.5.09 16:25	301,8	28,2	273,6	8.6.09 10:05	229,8
7	Y	35	O	29.5.09 16:26	299	33,2	265,8	8.6.09 10:06	243,1
8	Y	37	O	29.5.09 16:27	310,7	38,3	272,4	8.6.09 10:07	251,4
9	Y	5	O	29.5.09 16:28	310,2	37,8	272,4	8.6.09 10:08	249,3
10	Y	12	O	29.5.09 16:29	324	44,7	279,3	8.6.09 10:09	259,5

Table III-7: Detailed results of test series Relax_1P (test temperature 150°C)

Test Series Relax_3P

No.	Batch	Con-Rod	Inner/Outer	Assembly		Start		End	
				Date/Time	L_max* [μm]	L_plastic [μm]	L_max [μm]	Date/Time	L_point* [μm]
1	Y	16	O	1.6.09 12:50	300,4	35,5	264,9	8.6.09 10:10	249
2	Y	2	O	1.6.09 13:00	301,9	26,2	275,7	8.6.09 10:11	248,3
3	Y	36	O	1.6.09 13:07	300,5	31	269,5	8.6.09 10:12	245,8
4	Y	40	O	1.6.09 13:12	302,8	20	282,8	8.6.09 10:13	249,7
5	Y	32	O	1.6.09 13:18	307,6	45,2	262,4	8.6.09 10:14	252,6

Table III-8: Detailed results of test series Relax_3P (test temperature 150°C)

III.2 Shear Load Transfer Results with CBS

In Figure III-2 a detailed summary of the test results regarding the elastic limit of all shear load tests is shown.

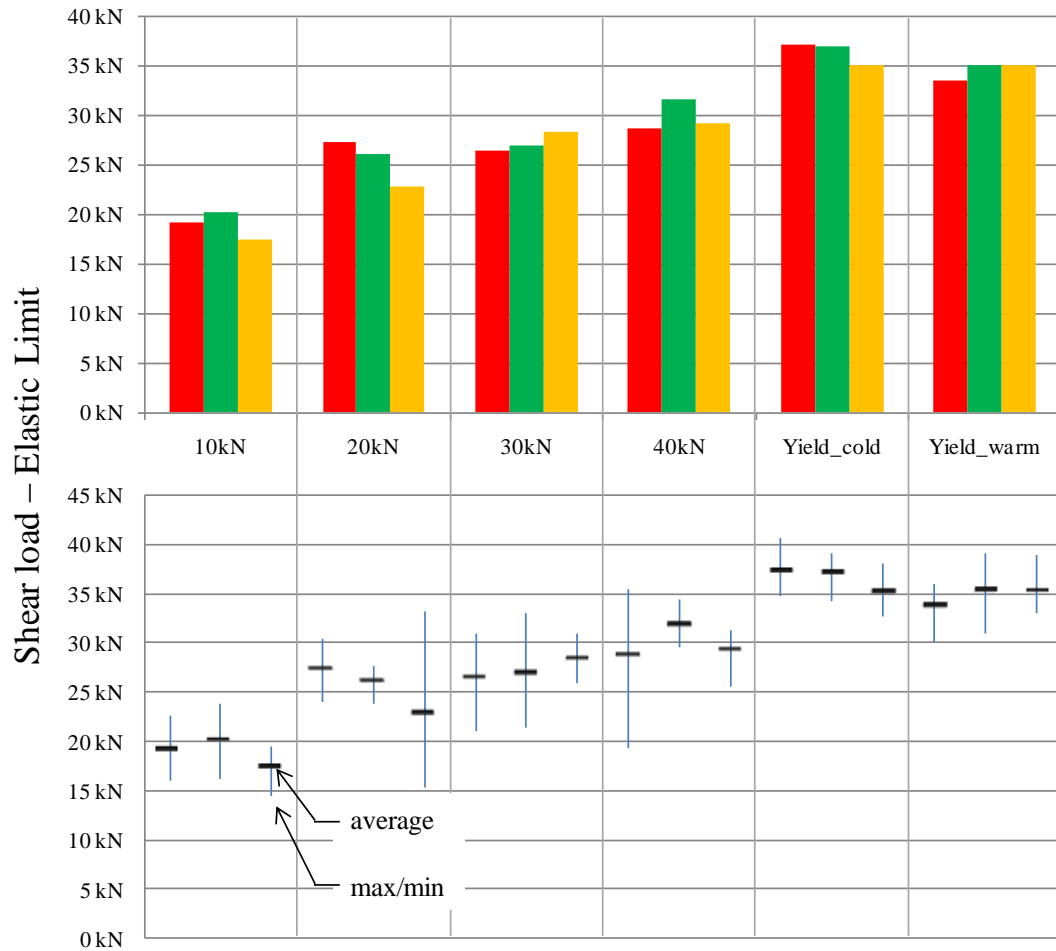


Figure III-2: Detailed summary of test results of the shear load tests regarding the elastic limit. In each test 5 specimens per batch were involved.

In Figure III-2 a detailed summary of the test results regarding the shear limit of all shear load tests is shown.

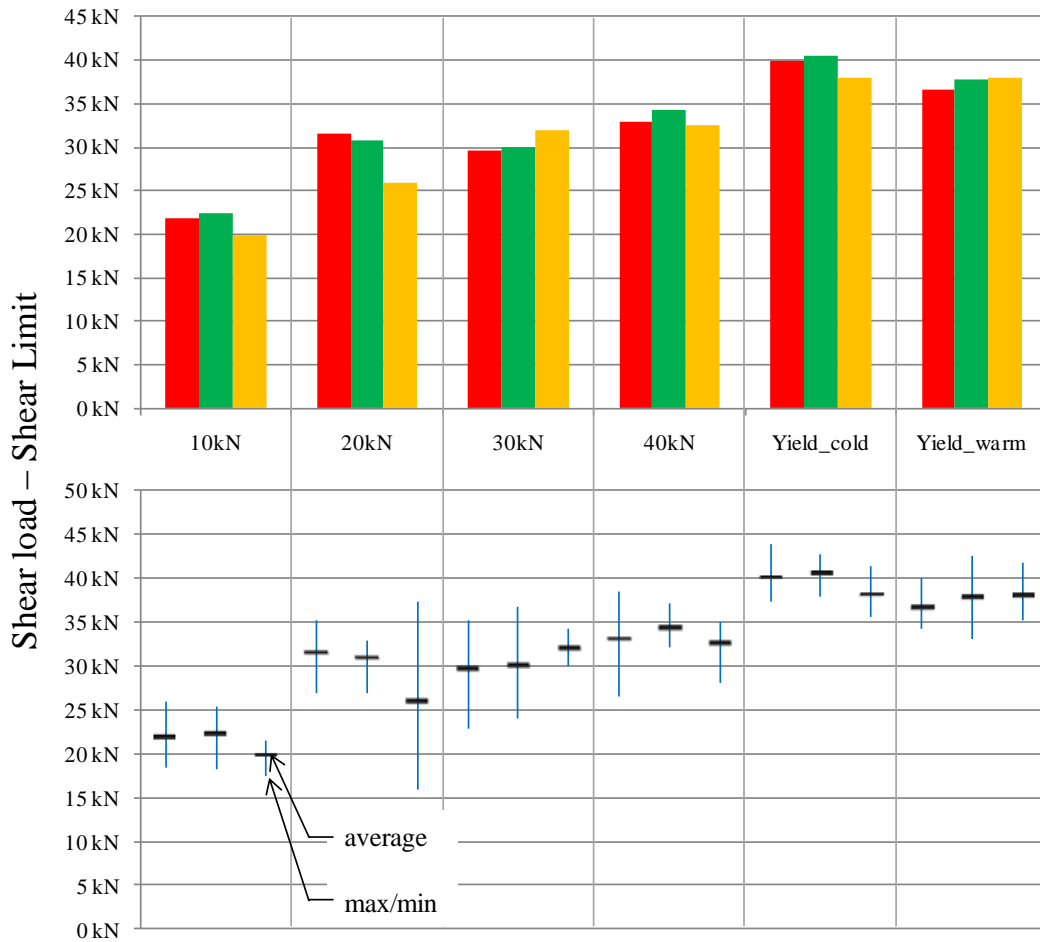


Figure III-3: Detailed summary of test results of the shear load tests regarding the shear limit. In each test 5 specimens per batch were involved.

III.3 Relaxation Test Results with Con-rods

In Figure III-4 a detailed summary of the test results of all relaxation tests with con-rods is shown.

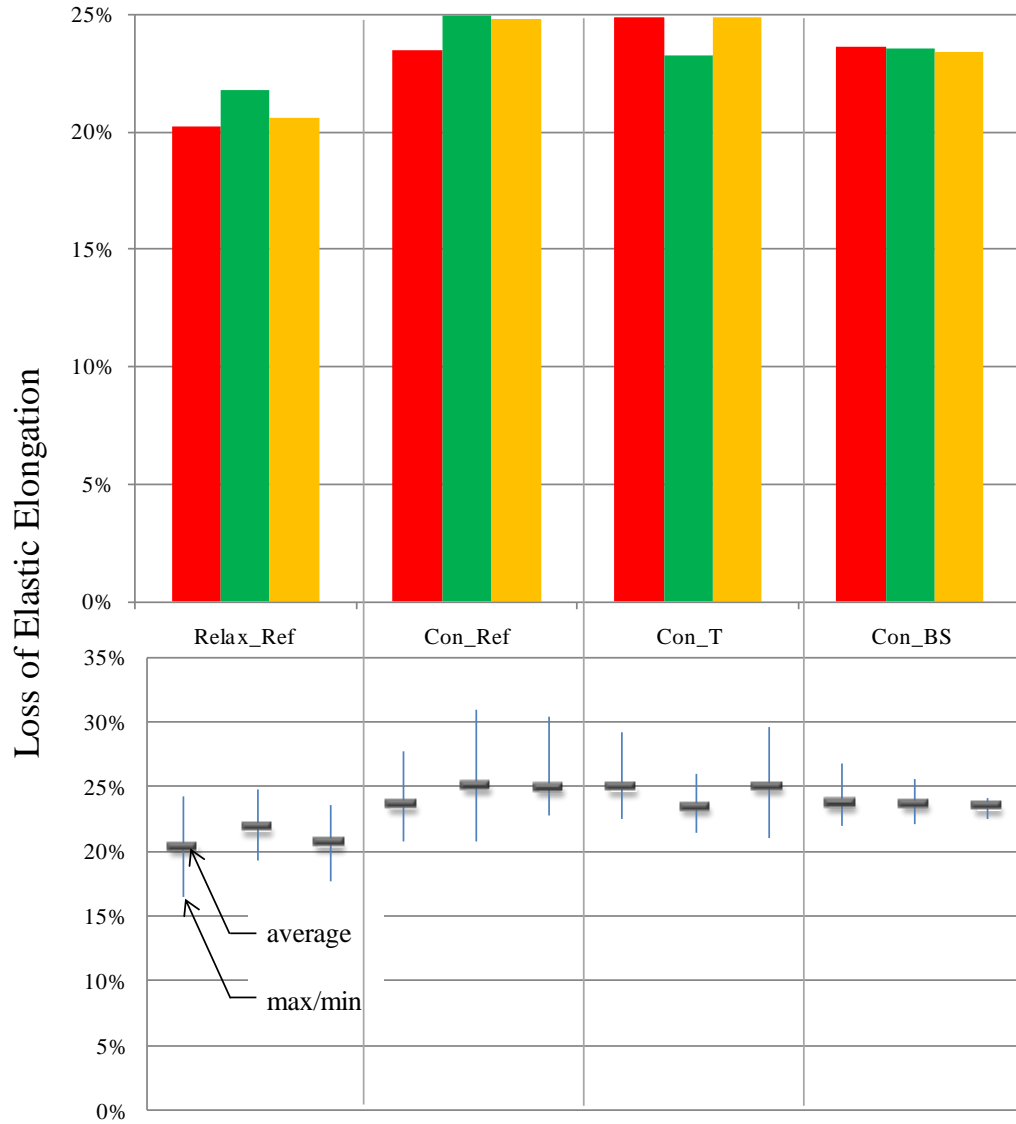


Figure III-4: Detailed summary of test results of the relaxation tests with con-rods

Test Series Con_Ref

No.	Batch	Con-Rod	Inner/Outer	Assembly		Start		End	
				Date/Time	L_max* [μm]	L_plastic [μm]	L_max [μm]	Date/Time	L_point* [μm]
1	G	52	I	24.04.2009 12:25	325,8	21,8	304	01.05.2009 18:00	233,6
2	G	52	O	24.04.2009 12:26	321,8	26	295,8	01.05.2009 18:01	232,4
3	G	54	I	24.04.2009 12:32	299,2	10,5	288,7	01.05.2009 18:02	228,8
4	G	54	O	24.04.2009 12:33	278,5	28,8	249,7	01.05.2009 18:03	213,8
5	G	53	I	24.04.2009 12:50	279,9	43,8	236,1	01.05.2009 18:04	207
6	G	53	O	24.04.2009 12:51	307,4	25,5	281,9	01.05.2009 18:05	242
7	G	56	I	24.04.2009 12:54	289,2	22,6	266,6	01.05.2009 18:06	232,4
8	G	56	O	24.04.2009 12:55	302,9	22,7	280,2	01.05.2009 18:07	242,4
9	G	55	I	24.04.2009 12:57	310,5	26,9	283,6	01.05.2009 18:08	252,5
10	G	55	O	24.04.2009 12:58	306,7	25,4	281,3	01.05.2009 18:09	246,5
11	R	51	I	24.04.2009 13:09	313,2	17,8	295,4	01.05.2009 18:10	246,8
12	R	51	O	24.04.2009 13:10	306	20,1	285,9	01.05.2009 18:11	246,8
13	R	54	I	24.04.2009 13:22	321	29,5	291,5	01.05.2009 18:12	255
14	R	54	O	24.04.2009 13:23	302,6	17,7	284,9	01.05.2009 18:13	241,4
15	R	60	I	24.04.2009 13:30	294	15	279	01.05.2009 18:14	216,8
16	R	60	O	24.04.2009 13:31	308,5	27,5	281	01.05.2009 18:15	241,8
17	R	59	I	24.04.2009 13:35	312,2	29,1	283,1	01.05.2009 18:16	242
18	R	59	O	24.04.2009 13:36	297,8	20,2	277,6	01.05.2009 18:17	233,6
19	R	62	I	24.04.2009 13:50	326	33,5	292,5	01.05.2009 18:18	252,3
20	R	62	O	24.04.2009 13:51	304,1	25,7	278,4	01.05.2009 18:19	239
21	Y	98	I	24.04.2009 14:02	328	14,8	313,2	01.05.2009 18:20	232,8
22	Y	98	O	24.04.2009 14:03	312,7	24,5	288,2	01.05.2009 18:21	239,2
23	Y	92	I	24.04.2009 14:13	290,5	23	267,5	01.05.2009 18:22	225,6
24	Y	92	O	24.04.2009 14:14	306,9	30,4	276,5	01.05.2009 18:23	241,3
25	Y	91	I	24.04.2009 14:16	320,6	17	303,6	01.05.2009 18:24	243,5
26	Y	91	O	24.04.2009 14:17	295,4	16,5	278,9	01.05.2009 18:25	228,2
27	Y	90	I	24.04.2009 14:30	319,3	24,1	295,2	01.05.2009 18:26	252,1
28	Y	90	O	24.04.2009 14:31	316,4	33,6	282,8	01.05.2009 18:27	249,1
29	Y	96	I	24.04.2009 14:35	326	30,5	295,5	01.05.2009 18:28	252,3
30	Y	96	O	24.04.2009 14:36	304,1	25,7	278,4	01.05.2009 18:29	239

Table III-9: Detailed results of test series Con_Ref (test temperature 150°C)

Detailed Results

Test Series Con_T

No.	Batch	Con-Rod	Inner/Outer	Assembly		Start		End of test @ 22°C		End of test @ 150°C	
				Date/Time	L_max* [μm]	L_plastic [μm]	L_max [μm]	Date/Time	L_point* [μm]	Date/Time	L_point* [μm]
1	G	61	I	24.04.2009 15:12	313,1	26,7	286,4	01.05.2009 18:30	281,2	12.05.2009 10:30	243,6
2	G	61	O	24.04.2009 15:13	289,7	21,1	268,6	01.05.2009 18:31	262	12.05.2009 10:31	232,2
3	G	62	I	24.04.2009 15:19	311,9	27,9	284	01.05.2009 18:32	280,2	12.05.2009 10:32	246,7
4	G	62	O	24.04.2009 15:20	305,3	22,7	282,6	01.05.2009 18:33	276,3	12.05.2009 10:33	240,7
5	G	58	I	24.04.2009 15:26	308,7	22,2	286,5	01.05.2009 18:34	274,8	12.05.2009 10:34	240,2
6	G	58	O	24.04.2009 15:27	306,3	25,7	280,6	01.05.2009 18:35	263,8	12.05.2009 10:35	233,3
7	G	59	I	24.04.2009 15:30	317,8	30,3	287,5	01.05.2009 18:36	287,3	12.05.2009 10:36	252,8
8	G	59	O	24.04.2009 15:31	309,7	27,6	282,1	01.05.2009 18:37	278,8	12.05.2009 10:37	246,3
9	G	60	I	24.04.2009 15:35	320,9	31,2	289,7	01.05.2009 18:38	281,6	12.05.2009 10:38	250,5
10	G	60	O	24.04.2009 15:36	302,7	32,5	270,2	01.05.2009 18:39	273	12.05.2009 10:39	242,6
11	R	52	I	24.04.2009 16:06	307,3	26,1	281,2	01.05.2009 18:50	279,2	12.05.2009 10:50	244
12	R	52	O	24.04.2009 16:07	316,5	33,1	283,4	01.05.2009 18:51	283,4	12.05.2009 10:51	251
13	R	56	I	24.04.2009 16:10	301,9	5,7	296,2	01.05.2009 18:52	265	12.05.2009 10:52	223,1
14	R	56	O	24.04.2009 16:11	316,8	26,5	290,3	01.05.2009 18:53	274,5	12.05.2009 10:53	242,3
15	R	53	I	24.04.2009 16:18	318	18	300	01.05.2009 18:54	273,9	12.05.2009 10:54	230,3
16	R	53	O	24.04.2009 16:19	319,4	31,8	287,6	01.05.2009 18:55	279,5	12.05.2009 10:55	248,5
17	R	55	I	24.04.2009 16:32	311,2	29,6	281,6	01.05.2009 18:56	274,9	12.05.2009 10:56	240,7
18	R	55	O	24.04.2009 16:33	313,3	35,1	278,2	01.05.2009 18:57	279	12.05.2009 10:57	245,8
19	R	61	I	24.04.2009 16:37	316,2	33,9	282,3	01.05.2009 18:58	285,1	12.05.2009 10:58	252,7
20	R	61	O	24.04.2009 16:38	319,9	41,2	278,7	01.05.2009 18:59	283,2	13.05.2009 10:58	249,3
21	Y	86	I	24.04.2009 15:40	306,5	24,8	281,7	01.05.2009 18:20	280	12.05.2009 10:40	246,1
22	Y	86	O	24.04.2009 15:41	302,3	25,7	276,6	01.05.2009 18:21	277,4	12.05.2009 10:41	244
23	Y	83	I	24.04.2009 15:46	315,1	29,2	285,9	01.05.2009 18:22	277	12.05.2009 10:42	241,8
24	Y	83	O	24.04.2009 15:47	319,6	6,9	312,7	01.05.2009 18:23	272	12.05.2009 10:43	227
25	Y	67	I	24.04.2009 15:52	309,7	25,6	284,1	01.05.2009 18:24	281,1	12.05.2009 10:44	241,8
26	Y	67	O	24.04.2009 15:53	302,3	20,8	281,5	01.05.2009 18:25	266,9	12.05.2009 10:45	232,8
27	Y	95	I	24.04.2009 15:56	318,2	34,7	283,5	01.05.2009 18:26	282,3	12.05.2009 10:46	245,7
28	Y	95	O	24.04.2009 15:57	325,1	41,4	283,7	01.05.2009 18:27	284,4	12.05.2009 10:47	249,1
29	Y	94	I	24.04.2009 16:01	316,1	30,7	285,4	01.05.2009 18:28	277	12.05.2009 10:48	243,9
30	Y	94	O	24.04.2009 16:02	329,1	35,9	293,2	01.05.2009 18:29	289,2	12.05.2009 10:49	255,2

Table III-10: Detailed results of test series Con_T (test temperature 22°C & 150°C)

Test Series Con_BS

No.	Batch	Con-Rod	Inner/Outer	Assembly		Start		End	
				Date/Time	L_max* [μm]	L_plastic [μm]	L_max [μm]	Date/Time	L_point* [μm]
1	R	63	I	11.09.2009 15:55	322,6	30,6	292	21.09.2009 17:05	256,2
2	R	63	O	11.09.2009 15:57	308,7	27,6	281,1	21.09.2009 17:06	233,6
3	R	69	I	11.09.2009 16:00	312,5	32,2	280,3	21.09.2009 17:07	245,7
4	R	69	O	11.09.2009 16:03	309,7	26,5	283,2	21.09.2009 17:08	245
5	R	80	I	11.09.2009 16:10	320,2	29,6	290,6	21.09.2009 17:09	256,5
6	R	80	O	11.09.2009 16:12	304,8	32	272,8	21.09.2009 17:10	237,6
7	R	84	I	11.09.2009 16:15	311,5	32,5	279	21.09.2009 17:11	245,4
8	R	84	O	11.09.2009 16:17	309,4	30,7	278,7	21.09.2009 17:12	248
9	R	86	I	11.09.2009 16:19	298,9	31,9	267	21.09.2009 17:13	234,2
10	R	86	O	11.09.2009 16:21	311,7	33,2	278,5	21.09.2009 17:14	245,6
11	G	63	I	11.09.2009 16:28	309,1	32,9	276,2	21.09.2009 17:15	243,4
12	G	63	O	11.09.2009 16:30	303,2	26,5	276,7	21.09.2009 17:16	232,3
13	G	64	I	11.09.2009 16:45	302,6	30,5	272,1	21.09.2009 17:17	240,6
14	G	64	O	11.09.2009 16:47	316,7	35,4	281,3	21.09.2009 17:18	251,5
15	G	71	I	11.09.2009 16:50	309	30,4	278,6	21.09.2009 17:19	247,4
16	G	71	O	11.09.2009 16:53	323	35,6	287,4	21.09.2009 17:20	253,2
17	G	76	I	11.09.2009 16:57	321,5	36,5	285	21.09.2009 17:21	251,8
18	G	76	O	11.09.2009 16:59	308,3	32,2	276,1	21.09.2009 17:22	244,1
19	G	77	I	11.09.2009 17:01	306,2	35,8	270,4	21.09.2009 17:23	243,8
20	G	77	O	11.09.2009 17:03	315,6	37,2	278,4	21.09.2009 17:24	250,9
21	Y	66	I	11.09.2009 17:06	310,2	36	274,2	21.09.2009 17:25	244,2
22	Y	66	O	11.09.2009 17:08	312,9	36,1	276,8	21.09.2009 17:26	247,4
23	Y	75	I	11.09.2009 17:10	307,8	30,2	277,6	21.09.2009 17:27	245,5
24	Y	75	O	11.09.2009 17:13	324,3	35,8	288,5	21.09.2009 17:28	255
25	Y	84	I	11.09.2009 17:20	297,8	25,1	272,7	21.09.2009 17:29	236
26	Y	84	O	11.09.2009 17:22	315,6	25,5	290,1	21.09.2009 17:30	248,8
27	Y	85	I	11.09.2009 17:24	300,9	28,2	272,7	21.09.2009 17:31	236,2
28	Y	85	O	11.09.2009 17:27	308,9	28,9	280	21.09.2009 17:32	243,1
29	Y	87	I	11.09.2009 17:30	315,2	34,6	280,6	21.09.2009 17:33	249
30	Y	87	O	11.09.2009 17:32	311,6	35,7	275,9	21.09.2009 17:34	247,6

Table III-11: Detailed results of test series Con_BS (test temperature 150°C)

III.4 Simplified FEM-Model by Alraheb

The introduction of the effective friction coefficient enabled the creation of a simplified FEM model as seen in the example shown in Figure III-5.

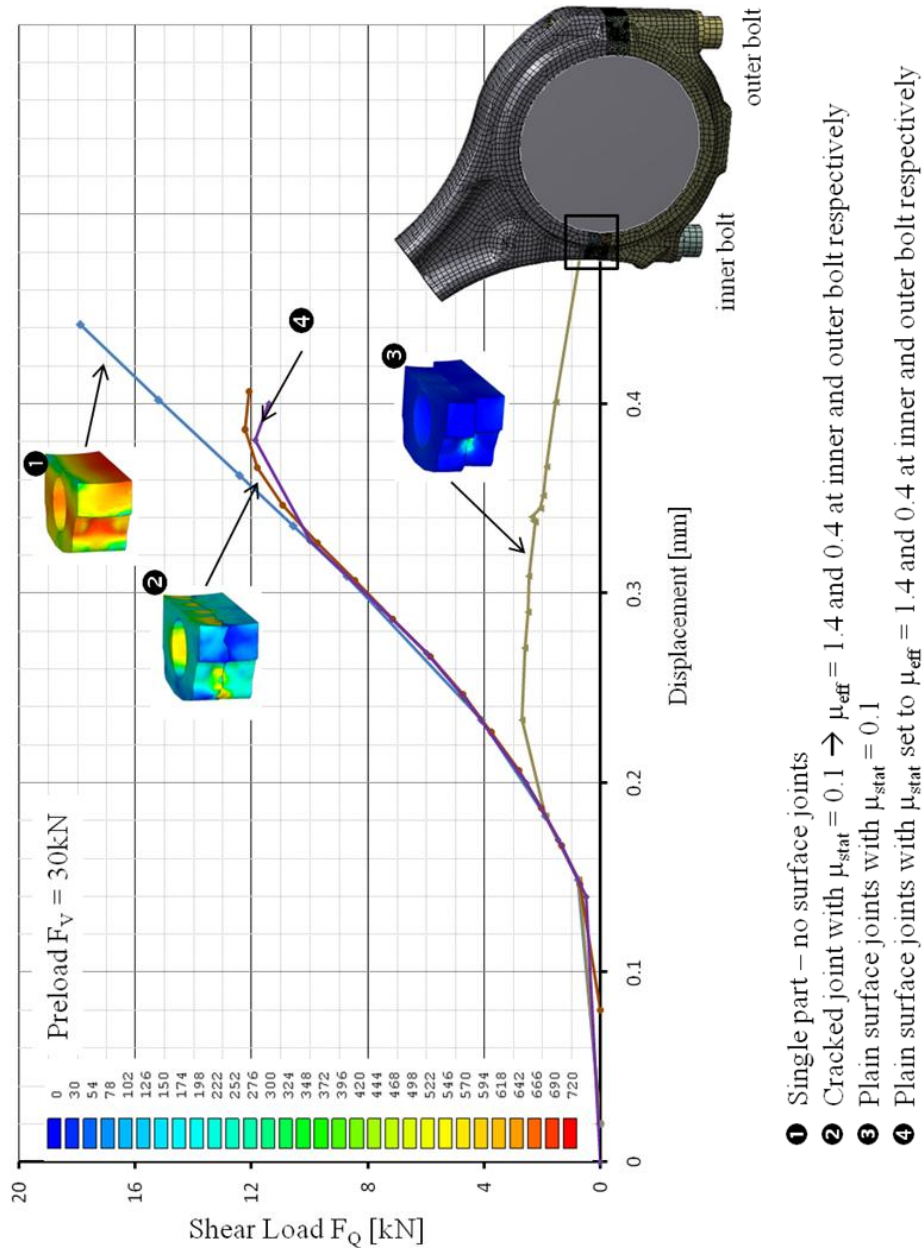


Figure III-5: Example of the simplified FEM-Model of a con-rod with cracked surfaces (calculation #4) in comparison to a con-rod with a plain joint (#3), a con-rod with a directly modelled cracked surface (#2) and an undivided single-body con-rod (#1) (displacement along con-rod shaft) (taken from (Lyszczan, et al., 2010))

The undivided con-rod simulated in calculation 1 shows the expected – and typical - behaviour of a metal part under tension load with pure elastic elongation.

In calculation 2 a con-rod with a directly modelled cracked surface joint with a static friction coefficient of $\mu_{\text{stat}} = 0.1$ is simulated. Up to a displacement of about 0.32mm the elastic deformation of the con-rod with cracked surface joint and the undivided con-rod share the same elastic deformation behaviour. Then the cracked surface starts to fail and its load curve starts to deviate from the curve of the undivided con-rod. The maximum transferrable shear load is about 12kN. At the first glance the amount of 12kN seems to be quite low with respect to the installed initial preload of 30kN. But the tension loading along the con-rod shaft decreases the actual clamping load of the joint. Consequently, at the point of the maximum transferrable shear load the actual clamping load in the cracked joint at the inner bolt is just about 8.6kN resulting in a value for $\mu_{\text{effective}}$ of 1.4.

In calculation 3 a con-rod with plain surface joints and a static friction coefficient of $\mu_{\text{stat}} = 0.1$ is simulated. The maximum transferrable shear load for this joint is less than 3kN at a deviation of less than 0.24mm. This distinct difference of performance in comparison to the cracked surface joint meets the common expectations.

In calculation 4 the same con-rod model used in calculation 3 was taken. The only difference was that instead of the static friction coefficient the effective friction coefficient calculated in calculation 2 was used ($\mu_{\text{effective}} = 1.4$). The run of the curve as well as the result of this calculation is very close to that of calculation 2.

This result indicates that the use of the effective friction coefficient in a FEM calculation instead of the static friction coefficient in combination with a simple surface joint model (plain surfaces) provides an effective way for an easy calculation the effect of cracked surface joints.